Characterisation of Low Impact Energy Induced Damage in Composite Plates with Embedded Optical Sensors

THÈSE N^{O} 5046 (2011)

PRÉSENTÉE LE 20 MAI 2011

À LA FACULTÉ SCIENCES ET TECHNIQUES DE L'INGÉNIEUR
LABORATOIRE DE MÉCANIQUE APPLIQUÉE ET D'ANALYSE DE FIABILITÉ
PROGRAMME DOCTORAL EN MÉCANIQUE

ÉCOLE POLYTECHNIQUE FÉDÉRALE DE LAUSANNE

POUR L'OBTENTION DU GRADE DE DOCTEUR ÈS SCIENCES

PAR

Jeannot FRIEDEN

acceptée sur proposition du jury:

Prof. J. Zhao, président du jury
Prof. I. Botsis, Prof. T. Gmür, directeurs de thèse
Prof. J. F. Dias Rodrigues, rapporteur
Prof. A. J. Mendes Ferreira, rapporteur
Prof. V. Michaud, rapporteur

ÉCOLE POLYTECHNIQUE
FÉDÉRALE DE LAUSANNE

Suisse
2011

Abstract

Fibre reinforced materials are increasingly employed in aerospace, naval and civil structures because of their low weight and high specific strength and stiffness. A major concern is the inherent susceptibility of composite laminates to barely visible damage induced by low velocity impacts. Non-destructive, in-situ inspection techniques are required to continuously control the integrity of such structures. Traditional non-destructive testing methods, like ultrasonic scanning, are time-consuming and require the withdraw from service of the tested part. Vibration-based structural health monitoring methods are reported to be a promising tool to check the structural integrity. In fact, damage leads to a local decrease of the structural stiffness and alters the wave propagation in a laminate. The stiffness modification results in a change of the modal characteristics of the structure. Numerous studies have shown that eigenfrequencies, damping ratios and curvature mode shapes of a laminated composite structure are sensitive to impact induced damage. Inverse numerical-experimental techniques based on modal characteristics have already demonstrated their applicability for the identification of mechanical properties of intact composite laminates. By using an adequate damage model, a similar method may be used for the identification of damage parameters.

In this work, a damage identification method based on signals obtained by an integrated sensing system is proposed. Fibre Bragg gratings (FBG), a recent sensor technology, are optical sensors allowing to measure internal strains in composite laminates. This type of sensor can be perfectly integrated in a structure, is maintenance-free and may last for the entire lifetime of a structure. A high rate FBG interrogation system based on intensity modulation is enhanced so that calibrated low-noise strain measurements can be performed with acquisition rates of up to 250 kHz. In this study, the FBG sensors are embedded in carbon fibre reinforced cross-ply plates made of 28 unidirectional plies. The sensors are used to capture the dynamic response of the plate to an impact event and to carry out experimental modal analysis. Moreover, acoustic waves originating from impacts are sensed with a high sensitivity and an acquisition rate of 1 GHz. The experimental results using several instrumented plates demonstrate the efficiency and accuracy of the interrogation

system.

Monitoring of the structural integrity of the composite plate consists of two stages, first impact localisation and second damage identification. The appearance of an eventual impact is detected by surveying the dynamic response of the FBG sensors and its location is predicted based on waves propagating from the impact to the sensors. The prediction is made via interpolation of a previously determined reference data set produced by non-destructive hammer impacts. The interpolation-based localisation method does neither require the knowledge of the wave propagation velocity nor the exact position of the sensors within the laminate. The prediction accuracy of the localisation method is evaluated with several numerical and experimental validation tests and is shown to be in the order of a few millimetres. The different potential error sources are identified and they are found to be mainly independent on the plate size.

Upon the detection and localisation of an impact, an eventual damage is identified using an inverse numerical-experimental optimisation method. A finite element model of the damaged plate is built based on three-dimensional characterisation of the damage pattern using high resolution X-ray computed tomography. The identification method utilises a homogenised damage model with an approximated damage shape and reduced transverse shear moduli. The damage surface and position are identified by minimising the discrepancy between the numerically calculated and experimentally determined eigenfrequency changes using a hybrid iterative and global search algorithm. The initial guess of the damage position required for the optimisation procedure needs to be sufficiently precise. Within this work, it consists of the predicted impact location obtained from the localisation method. The robustness of the algorithm to different initial guesses of the parameters is tested by numerical and experimental examples.

The impact localisation and damage identification method is summarised and demonstrated by a comprehensive experiment. Four FBG sensors are employed to detect and localise the impact and to determine the plate's eigenfrequencies. The damage surface is in general underestimated by approximately 20 % by the numerical-experimental optimisation algorithm and the distance between the identified and exact damage position corresponds to less than 10 % of the damage size.

Keywords: Composite materials, low-velocity impact, damage, numerical-experimental identification, fibre Bragg grating, dynamic strain measurements.

Resumé

Les matériaux composites fibreux sont de plus en plus utilisés dans l'industrie aérospatiale et navale et dans les infrastructures civiles. Le risque des stratifiés composites de subir des endommagements invisibles causés par des impacts à basses vitesses constitue par ailleurs une préoccupation importante lors de l'utilisation de ces matériaux. Des techniques non destructives d'inspection sont nécessaires pour contrôler de façon continue l'intégrité d'une structure. Les méthodes traditionnelles de contrôle non destructives, par exemple par ultrasons, sont en général coûteuses en temps et nécessitent la mise hors service des pièces testées. Des méthodes de surveillance basées sur le comportement vibratoire d'une structure peuvent présenter des solutions prometteuses pour contrôler de façon continue l'intégrité structurelle. En effet, un endommagement entraîne une diminution locale de la rigidité et modifie ainsi la propagation des ondes acoustiques dans le stratifié. Plusieurs études ont montré que les fréquences, les amortissements, ainsi que les modes propres, sont sensibles à des endommagements causés par des impacts à basses vitesses. Des méthodes inverses numériques-expérimentales s'appuyant sur le recalage modal et fréquentiel d'un composant ou d'une structure et permettant l'identification des propriétés mécaniques d'un matériau ont déjà été proposées. Par l'utilisation d'un modèle numérique approprié, une telle approche pourrait être appliquée à la caractérisation des paramètres d'endommagement.

Dans cette thèse, une nouvelle méthode d'identification de l'endommagement basée sur les signaux d'un système de capteurs intégrés est présentée. Des fibres optiques à réseau de Bragg sont utilisées pour mesurer les déformations à l'intérieur du stratifié. Ce type de capteur peut en effet être parfaitement intégré dans la structure et, de plus, ne demande pas d'entretien tout en dépassant généralement la durée de vie de la structure. Un système d'interrogation rapide, basé sur la modulation de l'intensité optique, est ici amélioré afin de permettre une mesure calibrée de déformation à une fréquence d'échantillonnage allant jusqu'à 250 kHz et avec un faible niveau de bruit. Durant les études expérimentales, les fibres à réseau de Bragg sont noyées dans des plaques en matériau composite renforcées par des fibres de carbone et formées de 28 plis unidirectionnels. Les capteurs sont utilisés

pour mesurer la réponse dynamique de la plaque à un impact et pour réaliser une analyse modale expérimentale. De plus, les ondes acoustiques provenant de l'impact sont mesurées avec une sensibilité élevée et une fréquence de 1 GHz. Les résultats expérimentaux extraits de différentes plaques instrumentées démontrent l'efficacité et la précision du système d'interrogation.

La surveillance de l'intégrité structurelle est entreprise en deux étapes : la localisation de l'impact et l'identification de l'endommagement. L'impact est détecté par surveillance de la réponse dynamique des réseaux de Bragg et sa position est prédite par recours à l'étude de la propagation des ondes acoustiques. La prédiction est réalisée grâce à l'interpolation des données de référence créées par des impacts non destructifs. Cette méthode de localisation ne nécessite ni la connaissance préalable des vitesses de propagation des ondes, ni la position exacte des capteurs à l'intérieur du stratifié. La précision de la méthode est évaluée par des tests numériques et expérimentaux et est de l'ordre de quelques millimètres seulement. Les sources d'erreur potentielles sont identifiées et il est montré qu'elles sont en majeure partie indépendantes de la taille de la plaque testée.

A la suite de la détection et de la localisation d'un impact, un endommagement éventuel est identifié en utilisant une méthode d'optimisation numérique-expérimentale. Un modèle d'éléments finis de la plaque endommagée est construit grâce à une caractérisation tridimensionnelle de la forme de l'endommagement, obtenue par tomographie par rayons X. La méthode d'identification utilise un modèle d'endommagement homogénéisé avec une forme d'endommagement approchée et des modules de cisaillement transverse réduits. La surface et la position de l'endommagement sont estimées en minimisant l'écart entre les changements de fréquence numériques et expérimentaux par une méthode d'optimisation hybride combinant un algorithme de recherche itérative à une approche globale. L'estimation initiale de la position de l'endommagement requise par la procédure d'identification doit être suffisamment précise. Dans ce travail, le point d'impact déterminé par la méthode de localisation sert d'estimation initiale. La robustesse et la convergence de l'algorithme sont étudiées au travers d'exemples numériques et expérimentaux.

La méthode complète de localisation de l'impact et d'identification de l'endommagement est résumée et illustrée par une expérience. Quatre réseaux de Bragg servent à localiser un impact et à déterminer les fréquences propres de la plaque avant et après l'impact. La surface d'endommagement est en général sous-estimée d'environ 20 % par la méthode d'optimisation numérique-expérimentale et la distance entre les positions exacte et identifiée de l'endommagement correspond à moins de 10 % de la taille de celui-ci.

Mots clés : Matériaux composites, impact à basses vitesses, identification numérique-expérimentale, fibre à réseau de Bragg, mesures de déformation dynamiques.

Acknowledgements

First of all, I would like to thank Prof. John Botsis, my thesis director, for giving me the opportunity and making available all the necessary means to complete this thesis at the laboratory of applied mechanics and reliability analysis (LMAF) of the EPFL. His regular supervision and the confidence he has placed in me beneficially affected the progression of my work. I would like to address the same acknowledgements to Prof. Thomas Gmür who has also been supervising my work. His accuracy and our interesting discussions on research, social and general matters have enriched my work and my workaday life. Special thanks go also to Dr. Joël Cugnoni for sharing his expertise in numerous fields and for contributing to my work with various comments and suggestions. I am grateful to these persons for their scientific as well as personal qualities, for offering me the possibility to start this thesis and for keeping my focus on the essential.

This work could not have been accomplished without the help and equipment obtained from other laboratories and their employees. I would like to thank Prof. Jan-Anders Månson and the staff of the LTC laboratory for placing the autoclave at my disposal. My gratitude is expressed to Prof. Jacques Giovanola and Dr. Alain Schorderet from LCSM laboratory for making available the scanning laser vibrometer system even in times of a loaded utilisation planning. I would like to thank Prof. Dominique Pioletti and his doctoral student Alireza for providing me the X-ray computed tomography scanner and the necessary assistance. I thank Prof. Jean-Pascal Reymondin for receiving me at HEIG-VD and for volunteering his time to assist me for the C-scan measurements. I thank Micron Optics Inc., in particular Mr. Todd Haber, for their collaboration in relation with the FBG interrogator. Furthermore, many thanks go to Marc Jeanneret as well as Nicolas and Stéphane of the workshop for their collaboration and effort to built the impact test facility and the patience exercised by them to carry out all the painful machining tasks I have been asking for. I would also like to greet the students who contributed to this thesis by their master projects.

At this place I would also like to thank the members of my jury for having undertaken the lecture of this document and for sharing their interesting comments.

I also acknowledge the financial support of the Swiss National Science Foundation (grants N° 200020-116715/1 and 200020-127183/1) that has enabled this research work.

My stay at EPFL has been very pleasant and therefore I would like to thank all my colleagues who have contributed to the enjoyable ambience and especially Marco and Samuel who both started their thesis almost at the time as me. As amusing as the shared working time has been the time we've all spent together having a drink while discussing science and similar topics.

Finally, many thanks go to my family, my friends and particularly to Lynn for their encouragement to start this thesis, their permanent support throughout all these years and for sharing the time with me.

Contents

List of Tables

List of Figures

List of Symbols

A_0	fundamental asymmetric Lamb wave mode
A	damage surface
$\boldsymbol{B}$	matrix composed of vector subspace
$\boldsymbol{C}$	stiffness matrix of an orthotropic material
c	phase velocity of Lamb waves
c_g	group velocity of Lamb waves
c_L	propagation speed of longitudinal waves
c_T	propagation speed of transverse shear waves
$\boldsymbol{d}$	search direction of optimisation algorithm
$\boldsymbol{D}$	damping matrix
$\boldsymbol{D}^0$	diagonalised damping matrix
d_i^0	i-th element of the diagonalised damping matrix
D_{23}, D_{13}	damage factors for transverse shear moduli G_{23} and G_{13}
E	Young's modulus of an isotropic material
E_1, E_2, E_3	Young's moduli of an orthotropic material
E_{crit}	estimation of critical energy for delamination initiation
$\bar{E}_a$	relative absorbed energy
$\boldsymbol{E}(\boldsymbol{\alpha})$	Error vector as a function of parameters $\boldsymbol{\alpha}$
f	excitation frequency
f_m^{num}	numerically calculated eigenfrequency of mode m
f_m^{exp}	experimentally measured eigenfrequency of mode m
$\bar{f}_m^{\text{exp}}$	relative experimental eigenfrequency change of mode m
$\bar{f}_m(\boldsymbol{\alpha})$	relative eigenfrequency change of mode m as a function of parameters $\boldsymbol{\alpha}$
$\boldsymbol{f}$	external force vector
$\boldsymbol{f}^0$	projection of external force vector in vector space $\boldsymbol{B}$
$F_s(j\omega)$	excitation spectrum of a DOF s
G	shear modulus of an isotropic material
G_{23}, G_{13}, G_{12}	shear moduli of an orthotropic material
G_{IIc}	critical energy release rate in mode II

$h_{rs}(j\omega)$	theoretical FRF between a DOF r and a DOF s
h	thickness of a plate
H_0	drop height of the impact weight
$\boldsymbol{H}$	matrix comprising shape functions
$I_{\mathrm{M}}(t)$	intensity signal of measuring arm
$\tilde{I}_{\mathrm{M}}(t)$	AC intensity signal of measuring arm
$I_{\mathrm{R}}(t)$	intensity signal of reference arm
$\tilde{I}_{\mathrm{R}}(t)$	AC intensity signal of measuring arm
$\bar{I}(t)$	intensity ratio signal
$\hat{I}(t)$	AC intensity signal with partially removed noise
$\bar{I}_i$	actual average intensity ratio
$\bar{I}_0$	target average intensity ratio
j	complex unitary number $\sqrt{-1}$
$\boldsymbol{J}$	Jacobian matrix
k	wave number
$\boldsymbol{K}$	stiffness matrix
$\boldsymbol{K}^0$	diagonalised stiffness matrix
k_i^0	i-th element of the diagonalised stiffness matrix
L_{kl}	isoline of the interpolated response surface $\widehat{\Delta t}_{kl}^{R}(x_1, x_2)$
$\boldsymbol{M}$	mass matrix
$\boldsymbol{M}^0$	diagonalised mass matrix
m_i^0	i-th element of the diagonalised mass matrix
n_{eff}	effective refractive index
n_R	number of reference points used by the localisation method
n_S	number of sensors used by the localisation method
n_3^e	number of finite elements in the through-the-thickness direction
$\boldsymbol{N}$	direction cosine matrix of a unitary normal vector
p_e	photo-elastic coefficient
$\boldsymbol{P}$	permutation matrix
$\boldsymbol{q}$	projection of the displacement vector $\boldsymbol{u}$ in the vector space $\boldsymbol{B}$
r_W	aspect ratio of rhombic damage shape
S_0	fundamental symmetric Lamb wave mode
S_k	sensor number k
$S_m\left(\alpha_j^0, \delta\alpha_j\right)$	sensitivity of the eigenfrequency m to a parameter α_j
$S^{\|\boldsymbol{E}\|}\left(\alpha_j^0, \delta\alpha_j\right)$	sensitivity of the error norm to a parameter α_j
t_k	arrival time of a wave at a sensor k
Δt_{kl}	arrival time delay between two sensors S_k and S_l
Δt_{kl}^R	arrival time delay associated to a reference point $\left(x_1^R, x_2^R\right)$

Δt_{kl}^{P}	arrival time delay used for the prediction of the impact location
$\widehat{\Delta t}_{kl}^{R}\left(x_1, x_2\right)$	interpolated arrival time response surface
$\boldsymbol{u}$	displacement vector
$\delta\boldsymbol{u}$	virtual displacement vector
$\dot{\boldsymbol{u}}$	velocity vector
$\ddot{\boldsymbol{u}}$	acceleration vector
$U_r\left(j\omega\right)$	response spectrum of a DOF r
U	drive voltage of FP filter
U_i	actual drive voltage of FP filter
ΔU_i	incremental update for the drive voltage of a FP filter
V_i	incident impact velocity
V_r	rebound velocity
W^e	general in-plane finite element size
W_1, W_2	damage sizes in the x_1 and x_2 directions
x_1	in-plane position coordinate
x_2	in-plane position coordinate
(x_1, x_2)	in-plane position
$\left(x_1^{\mathrm{d}}, x_2^{\mathrm{d}}\right)$	damage position
$\left(x_1^{R}, x_2^{R}\right)$	reference positions of localisation method
$\left(x_1^{S}, x_2^{S}\right)$	sensor positions of localisation method

α	coefficient of Rayleigh damping model
$\boldsymbol{\alpha}$	parameter vector
β	coefficient of Rayleigh damping model
$\boldsymbol{\beta}_i$	mode shape of mode i
$\bar{\varepsilon}_m^{f}$	relative error between num. and exp. eigenfrequencies of mode m
ε_1	longitudinal strain in the optical fibre
$\boldsymbol{\varepsilon}$	strain tensor (Voigt notation)
η_i	modal damping coefficient of mode i
$\bar{\eta}_m^{\mathrm{exp}}$	relative experimental damping change of mode m
θ	propagation direction of a wave
λ	Lamé constant
λ_{wave}	wavelength of a Lamb wave
λ_{B}	Bragg wavelength
λ_{B0}	initial Bragg wavelength of an unloaded FBG
$\Delta\lambda_{\mathrm{B}}$	Bragg wavelength shift
Λ	period of the modulation of the refractive index in an FBG

ν	Poisson's ratio of an isotropic material
$\nu_{23}, \nu_{13}, \nu_{12}$	Poisson's ratios of an orthotropic material
ρ	density of a material
$\boldsymbol{\sigma}$	stress tensor (Voigt notation)
ϕ	potential, scalar field
$\boldsymbol{\psi}$	divergence-free vector field
ω	angular excitation frequency
ω_i	eigenfrequency of mode i of the damped vibration system
ω_{0i}	eigenfrequency of mode i of the undamped vibration system
Ω	domain defined by the volume of a body
$\partial\Omega$	boundary of a domain Ω
${}^e\Omega$	volume of a finite element

∇	gradient operator
$\frac{\partial \cdot}{\partial x_i}$	partial derivative with respect to x_i
$(\cdot)^T$	transpose operation of a matrix
$\|\cdot\|_2$	Euclidean norm

List of Abbreviations

AE	acoustic emission
ANN	artificial neural network
BVID	barely visible impact damage
CP	cross-ply
CT	computed tomography
DOF	degree of freedom
DTL	delamination threshold load
FBG	fibre Bragg grating
FE	finite element
FP	Fabry-Pérot
FRF	frequency response function
FRP	fibre reinforced polymer
FSR	free spectral range
MAC	modal assurance criterion
MEMS	micro electromechanical system
MDOF	multiple degrees of freedom
NDT	non-destructive testing
PSDT	P-order shear deformation theory
SDOF	single degree of freedom
SHM	Structural health monitoring
SLDV	scanning laser Doppler vibrometer
UD	unidirectional
WDM	wavelength division multiplexing

Chapter 1

Introduction

1.1 Motivation

Fibre reinforced polymer (FRP) materials are used in many applications like sports goods, cars, construction engineering, navigation, aviation and aerospace. Especially in high-tech applications, they are extensively used because of their advantageous ratio between high stiffness and low weight as well as strength and weight. FRP composite materials are produced of thin reinforcement fibres surrounded by a matrix and are mostly used to produce shell type structures. During manufacturing of the composite, several laminae are assembled with a predefined stacking sequence allowing to customise the properties of the laminate in both in-plane directions.

A major concern in the use of such laminates is their inherent susceptibility to barely visible damage originating from transverse low velocity impacts. During manufacturing and in service, low energy impacts, as caused for example by a tool drop or runway debris, can lead to local damage in the material. Because of the low interlaminar strength, a commonly encountered failure mode is delamination, which is difficult to diagnose from outside the structure. In fact, the interface between the plies is usually ensured by the matrix only and therefore it fails more easily than the fibre reinforced plies themselves.

When damage is apparent in a structure, its strength is generally reduced drastically. Moreover, existing cracks may propagate because of static or fatigue loading. In order to prevent composite structures from premature and unexpected failure, their integrity needs to be controlled regularly. In practice, non-destructive testing (NDT) methods are required to detect and characterise an eventual damage, especially delamination damage, at an early stage. Where appropriate, the structure can be repaired or its remaining service life

accordingly be predicted. Ultrasonic inspection is one of the most common NDT methods employed nowadays for composite structures. Such a check is time-consuming and the part under test needs to be withdrawn from service. Moreover, scanning techniques generally need to be operated manually with external access to the structure. Especially in case of large or expensive structures, an increasing demand for continuous, in-situ structural health monitoring (SHM) techniques has arised. Thus, the requirement to integrate the surveying system in the structure for its whole lifetime leads to new sensing techniques and new evaluation methods.

Because of their light weight and minimal invasiveness, optical fibre sensors are extraordinary well suited to be integrated in composite laminates. Indeed, optical fibres have a small diameter of 125 µm and can therefore be embedded between the laminae during fabrication. Fibre Bragg grating (FBG) sensors are optical in-fibre filters allowing to measure deformations. When embedded into layered composite materials, they provide internal strain measurements with optimal load transfer conditions. This type of sensor can be perfectly integrated in a structure, is maintenance-free and may last for the entire lifetime of a structure. In quasi-static conditions, FBG sensors can be used to make local or distributed measurements of internal strains and are therefore attractive in experimental mechanics. The same sensor can be used for different purposes throughout the service life of a composite structure. Their use for dynamic strain measurements, which is very recent, offers opportunities for new developments and allows for new approaches in SHM.

For these damage detection techniques, new evaluation methods are required that are not based on full field measurements but rely on several single point measurements. Although, damage originating from impacts is locally concentrated, it influences its global dynamic response. In fact, damage results in a local decrease of the structural stiffness and therefore locally alters the propagation speed of mechanical waves. The change of the wave propagation affects the vibrational behaviour of the structure. Since the existence of modal testing, the influence of damage on the modal parameters of a structure has been investigated and confirmed initially by analytical and later by numerical methods.

Especially finite element (FE) methods permit an accurate modelling of laminated composite structures and the integration of various damage models. Inverse numerical-experimental optimisation methods have already shown their applicability for characterisation of material properties and may allow, in a similar way, for the identification of damage parameters. The use of an inverse damage identification method based on experimental data obtained from embedded FBG sensors may constitute a promising combination for the development of an integrated system for SHM.

1.2 State of the art

Fibre reinforced composite materials are commonly used to produce shell type structures with a relatively low thickness. Long fibre composite laminates consist of reinforcement fibres surrounded by a polymer matrix and are often used for high technology applications. The reinforcing fibres have a high Young's modulus and tensile strength. Depending on the application, they are generally made of carbon, glass or Kevlar®. Carbon fibres for example have a Young's modulus in the range of 200 to 400 GPa and a tensile strength in the range of 1 500 to 4 500 MPa. The role of the polymer matrix is to keep the fibres aligned and transfer the stresses to the fibres. It has a relatively low stiffness and strength compared to the fibres. The properties of the laminate can be tailored by the constituents of the composite, by the fibre volume fraction, interface, and the stacking orientation of the laminae. In case of unidirectional (UD) plies, the reinforcing fibres are aligned in one direction. In cross-ply (CP) laminates, the stiffness is more or less balanced in the two in-plane directions by alternatively changing the orientation of the plies (Figure 1.1). The resulting composite laminates have orthotropic material properties which are in general expressed in terms of three Young's moduli, three shear moduli and three Poisson's ratios in the principal directions of the composite lay-up [1].

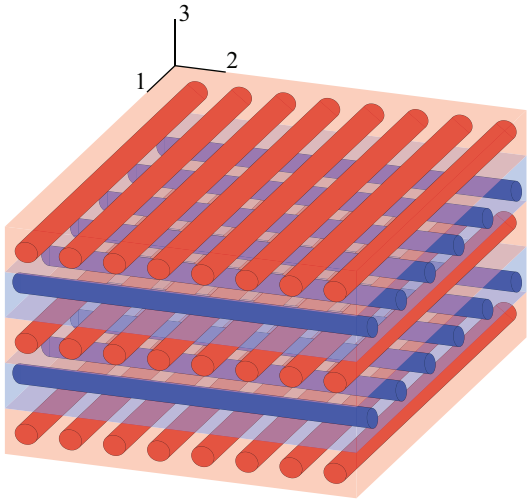

Figure 1.1: Illustration of a cross-ply composite.

1.2.1 Damage originating from low-velocity impacts

Low velocity impacts can occur during manufacturing or during the service of a structure. An impact is a dynamic event during which the structure is submitted to local contact

forces for a short period of time and the structural response is governed by propagating waves and a superposition of the first mode shapes [2]. In a composite plate with finite dimensions, the waves travel towards the boundaries where they are partially reflected. During such an impact, the stress field around the contact point may grow at such a level that the laminate may fail. Because of the extensive use of composite materials, researchers have been interested in understanding the failure mechanisms taking place during an impact. Many attempts have been made to establish models for the prediction of the damage onset and the resulting damage size. Besides all the work that is done to understand the failure modes of composite laminates and predict the damage, researchers are committed to improve the impact resistance of composites. Throughout innumerable experimental studies, the influence of material and laminate properties as well as the test configuration on the damage type and size are investigated. The residual properties of the composite materials are at all times an important issue because it determines whether a part can be kept in service after an impact or if it has to be repaired or replaced. A review of these studies is reported amongst other by Abrate [3, 4], Cantwell and Morton [5], Davies, Hitchings and Wang [6] as well as Richardson and Wisheart [7]. Once damage is apparent, it may grow due to static or fatigue loading. This phenomenon is reviewed by Degrieck and Van Paepegem [8]. With the appearance of high computational performance, impacts on composite materials and the initiation and propagation of damage can be simulated using explicit FE codes (a selection of available software is discussed by Nguyen et al. [9]) and many different failure criteria are proposed for composite materials. A comparison of these failure criteria is done by Daniel [10] and in an extensive collaboration initiated by Soden, Hinton and Kaddour [11, 12].

Four failure modes are mainly mentioned in conjunction with low velocity impacts:

- **Intralaminar matrix cracking**: Cracks occur parallel to the reinforcing fibres due to tension, compression or shear stresses.
- **Delamination**: The interface between adjacent plies fails because of interlaminar stresses.
- **Fibre breakage**: The fibres break on the face opposite to the impact because of tension stresses or fail on the contact side due to buckling.
- **Penetration**: The composite shell is completely perforated.

In case of low energy impacts, the first apparent failure modes are generally delamination damage and matrix cracking [2]. This is due to the low mechanical properties of the matrix compared to the reinforcing fibres. The interface between adjacent plies consists in general of resin only. The failure of this interface is mainly attributed to elevated transverse

shear stresses around the impact point [13]. The interlaminar shear stresses are even more pronounced when the adjacent plies have an unmatched stiffness or Poisson's ratio, like in case of different stacking orientations [14]. Delamination damage mostly appears between plies with a different lay-up orientation. The onset of the delamination can in general be related to a threshold impact force [6].

In laboratory experiments, different techniques are used to characterise the damage originating from low velocity impacts. A review of damage characterisation methods has been done by Abrate [2] and Adams and Cawley [15]. These techniques are generally classified in destructive and non-destructive methods. Most of them can only provide two-dimensional information on the damage pattern. Among the destructive methods, the most common are microscopic examination and the deply technique. By repeating the labour-intensive work on different planes, three-dimensional information can be obtained. A non-exhaustive list of non-destructive techniques to visualise the internal damage in composites comprises ultrasonic scanning methods [16], radiography with or without contrast liquid, thermography, shearography, backlighting and Eddy currents. X-ray computed tomography (CT) allows to obtain three-dimensional information on the damage pattern but it is a complex, time-consuming and expensive technique. Only a few works are published in literature where the entire three-dimensional damage pattern is presented [17, 18]. The use of X-ray CT did not always give satisfactory results because the resolution of the utilised device is of the order of 25 µm and does not allow the detection of delaminations with a small crack opening [19]. A major issue of CT is the large amount of accumulated data to have a sufficient resolution to detect small cracks within a large scanned region.

Delaminations are typically peanut shaped. In cross-ply plates, they spread alternatively in both in-plane directions and are generally oriented in the direction of the reinforcing fibres of the ply beneath the corresponding interface [20]. It is found that the damage pattern depends on the plate thickness. If the plate is relatively thick, the damage is concentrated above the neutral plane. In case of thin plates, the delaminations are present through the whole thickness of the plate and are increasing in size towards the opposite side of the impact [21]. In general, it is found in literature that delamination is the main damage type encountered during low energy impacts.

1.2.2 Structural health monitoring methods

The aforementioned damage characterisation techniques require the withdraw from service of the concerned part, are time-consuming and labour-intensive. Thus, researchers are looking into developing in-situ, continuous damage detection and characterisation methods. These systems are meant to be integrated in the structure for continuous monitoring of its

integrity. In general, they consist of at least two components, i.e. a built-in sensor system and software for interpretation of the measurements [22]. The purpose of these methods is the detection of damage and its characterisation. Afterwards the remaining lifetime of the structure may be predicted or, if required, the structural part be repaired or replaced. In case the structure itself and the integrated system are able to repair a damage on its own, it is called a self-healing structure [23]. An overview of different SHM methods is given in [24–26]. They can be classified in passive and active systems as detailed in the following sections.

Passive structural health monitoring systems

For passive diagnostic systems, only sensors are used to continuously monitor the structure in service. The structure is only subjected to excitation originating from operation and the sensor signals are analysed and checked against measurements from a healthy structure. The interpretation of such data is often difficult and the data base containing the reference measurements from the healthy structure needs to be large.

A structure in service is often submitted to dynamic mechanical excitations during operation. When the excitation signal is sufficiently well known or uniform over a given frequency range, long-time monitoring of the structural response can be used for detecting changes of the vibrational behaviour which can be related to the presence of damage. Operational modal analysis is proposed for damage monitoring of operating machinery or large structures [27].

Acoustic emission (AE) is an other well known passive technique for the detection of crack initiation and propagation [28]. Several, very sensitive sensors are needed so that the location of the crack can be determined. AE techniques give indication about the existence of damage and its location. Classification methods of the signal features may allow to differentiate between the damage mechanisms but it remains difficult to obtain comprehensible information about the damage size. A technique similar to AE permits to detect and localise an impact event. This method is also based on the propagation of guided waves, which are in this case excited by the impact itself. Piezoelectric sensors are generally used and the impact location can be predicted with an accuracy of several millimetres [29, 30].

Active structural health monitoring systems - wave propagation

For active diagnostic systems, the structure needs to be mechanically or non-mechanically loaded with transducers or actuators and the response of the structure is compared to the one of the healthy structure. Dynamic mechanical excitation of the structure is chosen by many researchers. Active detection methods mainly rely on the local changes of stiffness and damping or the appearance of non-linearities.

In case of high frequency excitation, often carried out by piezoelectric transducers, the damage detection method is based on guided wave propagation [31]. In plate structures, Lamb wave propagation modes are generally considered. The signals of waves travelling past a damage or reflected from a damage are compared to reference data recorded when the structure has been intact. Based on various signal analysis methods, the existence of the damage is established. The location can also be determined based on waves reflected from the damage [32]. The signal processing methods can be feature extraction, Fourier or short-time Fourier transform, wavelet analysis or pattern recognition. Artificial neural networks (ANN) are more and more used for classification of the large amount of data that can be recorded but are difficult to interpret. A disadvantage of this method is the high required number of sensors and the high analogue-to-digital conversion rate needed for the acquisition of the high frequency signals.

Active structural health monitoring systems - vibration-based

In case of low excitation frequencies, the SHM methods are often called vibration-based damage detection techniques. The modal response or parameters of the structure are compared to the ones of a reference state. An extensive review is made by Döbling et al. [33], Zou et al. [34] and Della et al. [35]. Different data exploitation methods are used to treat the experimental measurements. The effect of damage on the frequency response function (FRF) itself or modal parameters, i.e. eigenfrequencies, damping factors or mode shapes, are analysed. Different evaluation methods are proposed to relate the experimental data to a damage indicator. Damage evaluation methods can for example be based on ANNs, damage indexing methods, or inverse numerical-experimental optimisation [36].

The frequency response transfer function can be directly employed to detect and locate a damage [37–39]. Damage is known to alter the dynamic response of a structure which is represented by the FRFs. Non-linear effects induced by damage can also be noticed in the transfer function because of the appearance of harmonics. This phenomenon may serve to identify damage [40]. It is mainly caused by the various dissipation modes at the delamination and the opening and closing of cracks.

The damage identification can also be based on the modal parameters. The influence of damage on eigenfrequencies, damping factors and mode shapes of a panel or structure have been investigated. While changes of the displacement mode shapes are less noticeable [41], curvature mode shapes are shown to be sensitive to a local stiffness reduction [38]. In fact, the curvature of a bending mode is related to the bending stiffness of a composite shell which can be drastically reduced by the presence of damage. A detailed measurement of the curvature shapes allows to identify and locate a structural damage. To obtain the normalised curvature mode shapes with a sufficient precision, a very fine measurement grid is needed. This is a major disadvantage of this approach and may be the main reason why experimental measurements are often done with a scanning laser Doppler vibrometer (SLDV) [42–44], and several validation examples are based on numerical data [41, 43–46]. Strain gages, PZT or PVDF film sensors allow for a direct measurement of the strain mode shapes which have the same sensitivity to damage as the curvature mode shapes [42, 45, 46]. Damage indexing methods like the strain energy based criterion allow a direct identification of the damage position [46, 47]. Here again, a coarse measurement grid limits the quality of the prediction.

The local stiffness reduction not only affects the mode shapes but also the eigenfrequencies of a structure, which can generally be determined with very good precision. The sensitivity of natural frequencies to structural damage is already perceived with the early use of experimental and numerical modal analysis and modal parameter extraction [48]. Several numerical and experimental studies confirm these findings [49, 50]. In a work from Tracy et al. [51], a single central delamination spreading over one third of a laminated composite beam reduced the eigenfrequencies of the first four modes by up to 20 %. In construction engineering this method is commonly proposed to monitor the state of bridges [52]. Also in application fields of composite materials, for example airplane wings or wind-turbine blades, the sensitivity of the resonance frequencies to damage is studied [53]. Only few sensors are needed and the importance of the sensor positioning is of a second order because the sensors do not need to be placed close to the damage to detect the eigenfrequency changes. It is however observed that the first eigenfrequencies of a structure are not affected considerably when the damage is small compared to the size of the structure. In the case of a large structure, the eigenfrequencies which are sensitive to damage correspond to higher order modes and the excitation frequencies and the response measurements need to be adapted appropriatly. Otherwise a damage with a relatively small critical size might not be detectable.

The inverse problem, namely a damage identification and characterisation based on experimentally measured eigenfrequency changes, is often missed or validated by few experimental tests only. Finite element model updating is however a promising technique

to identify damage based on eigenfrequencies [54]. Recently, inverse damage identification based on eigenfrequency changes and displacement mode shapes obtained by a scanning laser vibrometer is successfully accomplished and validated by experimental tests [44]. When the experimental data are limited to a few eigenfrequency measurements, the damage model needs to be simple in order to limit the number of parameters compared to the number of input data for the identification procedure.

As mentioned before, the damping of composite structures is also influenced by damage, particularly delamination damage. Several studies confirm the sensitivity of modal damping ratios to damage [49, 55–59]. In general, the damping ratios increase and relative changes of up to a factor three are observed. A direct damage localisation method relying on a damping damage indicator, which is function of the strain mode shapes and relative damping changes, is proposed by Montalvão et al. [60]. It is however noticed by several authors that no systematic trend of the damping factors could be observed with increasing delamination size [58, 61].

1.2.3 Fibre Bragg gratings

A fibre Bragg grating is an optical fibre filter, first demonstrated in 1978 [62] and can be used for strain or temperature measurements.[1] Initially, FBG interrogation methods have been limited in speed and only quasi-static strain measurements could be carried out. When embedded into a composite, they are capable of measuring internal local and distributed strains. Therefore, they have become increasingly used in experimental mechanics and their use for damage detection methods is investigated. Recent developments in optics permit a dynamic acquisition of strains and hence pave the way for new applications. Different high rate interrogation methods have been developed recently and are presented in this section. The applicability of FBG sensors within various SHM methods is investigated by many researchers. A general overview of the possible usage of FBG sensors is given in a book by Measures [63] and a review article by Majumder [64].

Fibre Bragg gratings in structural health monitoring

At the beginning of the FBG technology, the interrogation methods have been limited to quasi static strain acquisition. The curing process of composite aircraft structures, the real-time evolution of internal strains and quasi-static strains close to bonded joints of loaded structures have been monitored [65, 66]. Long Bragg gratings allow to make

[1] The working principle of FBG sensors is detailed in Section 2.3.

distributed static strain measurements by which the residual stresses in a fibre reinforced composite could be characterized [67]. The strain evolution around a delamination damage or a delaminated bond can be captured when the sensor is placed within a distance of 2 – 3 times the damage radius [68, 69]. When long FBG sensors are placed close to the damage, small matrix cracks can also be located and the crack propagation under quasi-static load can be monitored [70, 71]. Multiplexed FBG sensors are employed to characterise Mode-I and Mode-II delamination propagation in double cantilever beam specimens [72].

Since new interrogation methods allow dynamic signal acquisitions, FBG sensors are for instance used to replace traditional sensors within the SHM methods presented in the previous section. As a replacement to commonly employed piezoelectric sensors, FBG sensors are used for detecting acoustic waves in composite structures and hence for localising a dynamic excitation source. Several research projects have demonstrated that Lamb waves originating from a PZT transducers can be captured and in some of the works the excitation source could be successfully localised [73–76]. The first attempts to locate a real impact are also reported [77–79]. In this case, the sensor configuration is similar to the one used in case of a piezoelectric excitation source but the signal processing and localisation methods have to be adapted to the lower excitation frequencies. Experimental modal analysis for vibration-based SHM has also been carried out recently with FBG sensors [78, 80–82].

Since researchers have been aware of the interesting usage of FBG sensors for internal strain measurements in laminated composite materials, they have studied the influence of the optical fibre on the impact resistance of a laminate. In fact, the optical fibre which has a diameter of 125 µm constitutes an inclusion in the composite and therefore acts as a stress concentrator. When the fibre is embedded parallel to the reinforcing fibres towards the opposite side of an eventual impact, the reduction of the laminate's impact resistance is found to be negligible [83, 84]. In this case, no resin accumulation forms around the optical fibre as it would do in case the fibre is embedded perpendicular to the reinforcing fibres [84].

High rate interrogation methods for FBG sensors

Strain measurements with FBG sensors are based on optical wavelength measurements. At the early use of FBG sensors, the wavelength measurements were performed using optical spectrum analysers which are limited in speed. Lately, fast spectrum analysers are for example based on a tunable laser light source which is harmonically swept over a range of up to 70 nm. These recent developments push the interrogation rate to 20 kHz [78, 85]. A major advantage of this kind of interrogation device is their capability for wavelength division multiplexing (WDM). Several Bragg gratings, having different nominal

Bragg wavelengths, within a single optical fibre can be interrogated almost simultaneously. Distributed strain measurement with long FBG sensors are generally done using optical low coherence reflectometry (OLCR) [67] or optical frequency domain reflectometry [86]. This interrogation principles are however limited in speed to a few Hz.

The following overview is limited to high rate FBG interrogation methods allowing acquisition speeds of up to 100 kHz or more. These interrogation principles allow local strain measurements with short FBG sensors. A general comparison of high rate FBG interrogation methods is reported by Todd et al. [87].

Many interrogation methods are based on intensity modulation of the Bragg wavelength shift. The Bragg reflection peak is thereby coupled through an optical filter with a decaying transmission spectrum or the incident light is limited to a wavelength band that is small compared to the bandwidth of the FBG. The intensity acquisition is in general made by simple photodiodes and the sampling rate of the analogue-to-digital conversion is only limited by the acquisition card or oscilloscope and the photodiodes response time.

- The group of Cusano, Capoluongo et al. uses an optical filter based on a chirped Bragg grating for the intensity demodulation of the Bragg wavelength shift [80]. It has a linear attenuation over a bandwidth of 5 nm. Reference measurements account for fluctuations of the broadband light source and losses in the light guides. The FBG sensor's nominal Bragg wavelength has to be situated within the bandwidth of the linear attenuation filter.

- Chen and Shin use a tunable thin-film filter with a bandwidth of 1.2 nm. The filter is placed between the broadband light source and the FBG sensor and no reference intensity measurements are made [79]. Such reference measurements are however needed to create a reproducible calibration of the strain measurements.

- Park et al. use a device from Micron Optics (model si920) [88]. The intensity demodulation is carried out by a tuneable Fabry-Pérot (FP) filter which can be matched to the nominal Bragg wavelength of the FBG. Reference measurements account for fluctuations of the light source and losses in the light guides. The strain range and sensitivity is given by the finesse of the FP filter. Interrogation speeds of several hundred kHz are demonstrated.

- In the work of Tsuda et al., the intensity demodulation is achieved with an auxiliary FBG grating. The Bragg wavelength of the auxiliary grating has to be adjusted to the one of the measuring grating. Calibrated measurements with acquisition rates of 100 MHz have been carried out [89].

- In the work of Betz et al., the light source consists of a tunable laser which is set

to the full width at half-maximum of the Bragg reflection peak [74]. The sensitivity and measurable wavelength range depend on the bandwidth of the FBG sensor. Very sensitive and calibrated measurements over a relatively small but almost linear range of 40 $\mu\varepsilon$ with low noise are demonstrated [90]. Reference measurements compensate for fluctuations of the light source intensity but losses in the waveguides cannot be accounted for and may falsify the calibrated measurements.

Very recent works report the development of high rate full spectrum analysers. In general, these devices are scanning a certain wavelength range with a very high sweeping rate.

- Vella et al. have developed a full spectrum analysers using a sweeping micro electromechanical system (MEMS) filter [91]. Depending on the sweeping range a drive frequency of up to 100 kHz and an analogue-to-digital sampling rate of 100 Megasamples/second is used. Because of the harmonic sweeping of the filter a non-uniform wavelength resolution of several picometres is obtained.
- Fu et al. discuss a high rate interrogation principle based on a dispersion compensation module [92]. The wavelength offset of the monitored FBG to a reference grating is transformed into a time delay. The coefficient of time shift against strain is 0.202 $^{ps}/_{\mu\varepsilon}$. A very high analogue-to-digital conversion rate (several GHz) is needed to have a sufficient time resolution.
- A high rate interrogation method capable of WDM is proposed by Lee et al. [93]. A spectrometer disperses the reflected light on an array of photodiodes. An acquisition rate of 100 kHz is demonstrated.

1.2.4 Conclusions

With the increasing use of composite materials in different engineering fields, characterisation of low impact energy induced damage is now more of concern than ever. Dynamic analysis of the composite structure is shown to be a promising method for damage detection. Several research studies have pointed out the sensitivity of the vibrational behaviour of composite structures to damage. The exploitation of modal parameters appears to be a promising approach for the assessment of damage and inverse numerical-experimental techniques for damage identification are proposed by a few authors. A consistent implementation of the identification method with a damage model based on a few comprehensible parameters and validated by extensive experimental results is, however, often missing.

The strong interest in dynamic strain measurements with FBG sensors manifested by many authors over the past years and during the present work confirms the attractiveness

of such sensors for experimental mechanics and SHM. These optical sensors represent a recent technology and their applicability is being investigated under different forms. Their full potential of replacing existing sensors or offering new opportunities for further development is not yet tapped. At the beginning of this work, the acquisition rates have been limited, the signal-to-noise ratio has been moderate, the versatility of measurement range and sensitivity have not been ensured and a calibration of the interrogation devices has often been missing. As pointed out by the very recent studies in the previous overview, considerable improvement has also been achieved by other authors during the time of this work.

1.3 Objectives

The main objective of this work is the development of an integrated impact localisation and damage identification method in composite plates with embedded FBG sensors. The proposed method relies on the dynamic sensing capabilities of FBG sensors and an inverse numerical-experimental optimisation algorithm for damage identification. The research work involves the following developments and novelties:

- Enhance a high rate FBG interrogation method based on intensity modulation to enable calibrated and low noise strain measurements and highly sensitive acoustic wave sensing with FBG sensors.
- Characterize the three-dimensional damage pattern originating from low-velocity impacts and produce an experimentally validated damage model based on few parameters.
- Predict the position of a real low energy impact on a composite laminate with embedded FBG sensors based on an interpolation-based localisation method.
- Develop a numerical-experimental damage identification method based on dynamic signals obtained from embedded FBG sensors.

The actual state of knowledge in optical sensing technology and on the effect of damage on composite laminates leads us to the following postulate:

> "It is possible to localise a low-velocity impact event and identify damage in a composite plate with dynamic strain measurements from embedded FBG sensors."

In order to achieve this objective, the work is divided into six tasks:

- Design of an impact testing facility
- Adaptation and validation of a high rate FBG interrogation method for dynamic strain measurements
- Development of an impact localisation method with FBG sensors
- Characterisation of impact damage and its effect on the modal parameters of a plate
- Construction and validation of an efficient damage model
- Implementation of a numerical-experimental identification algorithm

As a result of the various numerical and experimental methods applied to carry out these tasks, the structure of this document is divided according to the different topics. Chapter 2 gives an overview of the experimental and numerical methods used throughout the work. Chapter 3 concentrates on optics and details the high rate FBG interrogation method. Chapter 4 is dedicated to the physics of wave propagation and the impact localisation method. The accuracy of the localisation method is tested with numerical and experimental data. In Chapter 5, the damage in a composite laminate originating from low velocity impacts is characterised and its influence on the vibrational behaviour of the plate is characterised. Based on these findings, a numerical damage model is built and validated with experimental results. In Chapter 6, this damage model is parametrised and its sensitivity to the parameters is analysed. Based on the conclusions drawn from the sensitivity analysis, a numerical-experimental optimisation algorithm for damage identification is proposed and is validated by numerical and experimental examples. Lastly, Chapter 7 summarises the experimental approach and the implementation of the developed impact localisation and damage identification method and demonstrates its applicability by a comprehensive experiment.

Chapter 2

Methods

2.1 Preface

Throughout this work, miscellaneous experimental and numerical studies are carried out. In this chapter, the analysis methods are described and preliminary results are presented in the corresponding sections. The composite plate processing as well as the characterisation of the composite material and its elastic properties are described. The working principle of the FBG sensors and their use as strain gages in laminated composite materials is introduced. The concept of the test facility for low velocity impacts is also developed in this chapter. The testing rig is built on purpose and is instrumented with the necessary measuring sensors. Preliminary results are presented in order to attest reproducibility of the impact tests and data collected during impacts with varying incident energies are discussed.

The fundamentals of experimental and numerical modal analysis are described in detail to have a thorough understanding of the analysis methods which underlie the damage identification procedure proposed in Chapter 6. Finally, a brief theoretical background on the numerical resolution of a transient dynamic problem with an explicit time-integration scheme is given. Such a numerical model is used to simulate a non-destructive impact and, in Chapter 3, to validate the strain measurements carried out with FBG sensors.

2.2 Composite processing and characterisation

2.2.1 Composite plate processing

The composite plates used throughout the experiments are T700 carbon fibre reinforced epoxy plates with a fibre volume of 60 %. The preimpregnated plies are purchased from EPO GmbH with a FT109 resine and can be stored over a duration of up to 2 years at a temperature of −25 °C. The prepregs have unidirectional (UD) reinforcing fibres that are kept aligned by nylon fibres oriented in an oblique direction. The plates are manufactured from 28 UD plies with a nominal thickness of 150 µm resulting in a plate thickness of 4.2 mm. The prepregs are cut to a square size of 300 mm × 300 mm. In general, cross-ply (CP) plates with a symmetric $[0\,^\circ_2, 90\,^\circ_2, 0\,^\circ_2, 90\,^\circ_2, 0\,^\circ_2, 90\,^\circ_2, 0\,^\circ_2]_s$ stacking sequence are produced. For the characterisation of the single plie, UD plates with a $[0\,^\circ_{14}]_s$ lay-up sequence are prepared.

When an optical fibre is embedded, it is placed between the ultimate and penultimate ply parallel to the direction of the reinforcing fibres on the opposite side of the impact. The fibre is placed far away from the neutral plane of the plate so that the FBG sensor is very sensitive to longitudinal strains from bending. The polyimide coated fibre is uncoated at the location of the grating and a few millimetres beyond on each side. At the entrance of the optical fibre into the prepreg stack, a Teflon® tube prevents the resin from flowing along the fibre and protects the fibre from breaking.

The prepreg layup is wrapped with Teflon® sheets on the upper and lower side (cf. Figure 2.1) to facilitate the demoulding and obtain a reproducible fibre volume fraction. Bundles of carbon fibres are inserted between the overlapping Teflon® sheets to allow the air to be evacuated. The laminate is placed together with the Teflon® sheets on an aluminium base plate in an aluminium frame. Another aluminium plate with dimensions of 297 mm × 297 mm covers the stack to achieve a good planarity and a good surface quality. Finally the laminate and the frame are covered by a vacuum bag with sealant tape between the bag and the base plate.

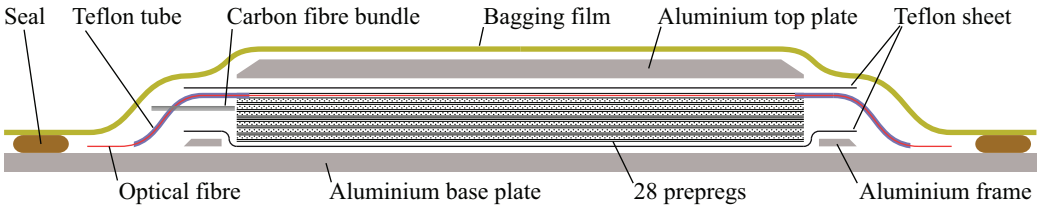

Figure 2.1: Schematic of the plate processing.

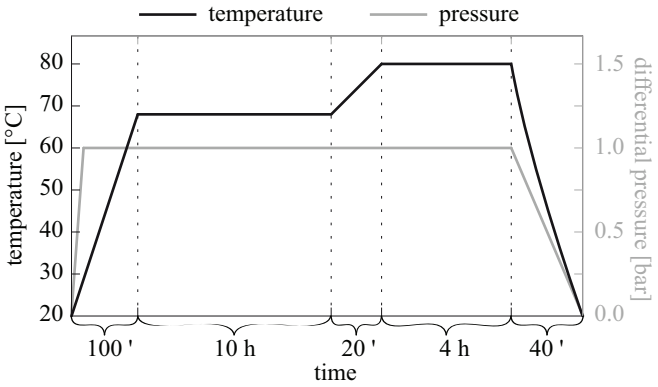

Figure 2.2: Curing cycle of CFRP plate in autoclave.

The plate is cured in an autoclave with a pressure of 1 bar using a curing cycle of almost 17 h at up to 80 °C (Figure 2.2). During the whole curing cycle a vacuum is maintained. The epoxy resin is cured at the lowest possible temperature given by the specifications of the manufacturer. This reduces the residual stresses in the plate and prevents the resin from flowing out of the mould because of low viscosity.

If not stated differently, the square plates are cut into two pieces in order to obtain two plates with a width of 140 mm and a length of 300 mm (Figure 2.3). During the cutting process, a strip of approximately 10 mm is cut off along the border of the square plate, where the material is less uniform. The cut is performed with a diamond cutting wheel. Holes with a diameter of 11 mm are drilled along the two short sides of the final plate to pass the bolts of the fixture. During the drilling process, the laminate is clamped between two wooden plates to prevent the carbon fibres from being pulled out and to reduce matrix

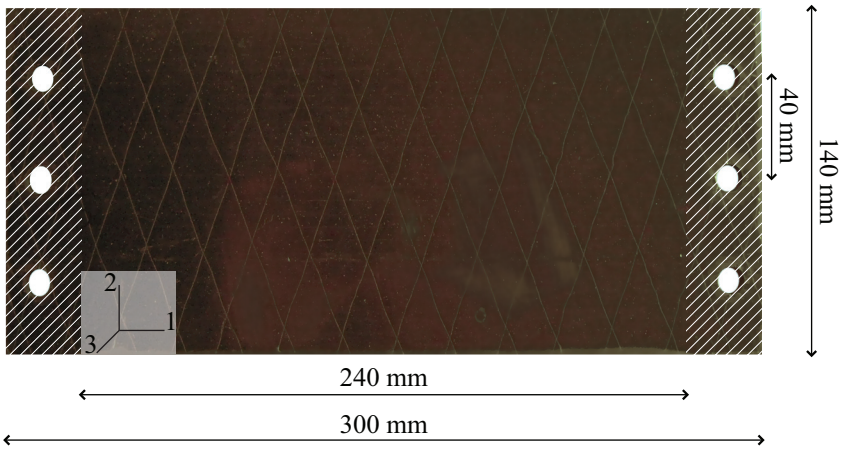

Figure 2.3: Picture of a plate.

cracking to a minimum. The convention adopted for the axis system in this work is also illustrated in Figure 2.3. The x_1 direction is oriented in the direction of the span and the x_3 axis is normal to the plate.

2.2.2 Characterisation of the material and the plate

The fibre volume fraction and the porosity are determined using micrography. At the same time the integration of the optical fibre is checked. The characterisation of the plate consists in measuring the final thickness of the plate and verifying its planarity. The final density of the cured composite material is measured and the mechanical properties of the UD lamina and the cross-ply plate are determined using a modal identification method.

Fibre volume and porosity

Microscopic images are produced to determine the fibre volume fraction and the porosity of the cured CFRP. Therefore, a UD plate is sectioned, enclosed in an epoxy resin and polished. Porosity appears as black spots in the image (Figure 2.4). They are rare and mainly located next to nylon fibres oriented diagonal to the reinforcing fibres. The volumetric fraction of porosity is below 1 %. The fibre volume is determined via image treatment of microscopic images. They are converted to black and white images with a threshold method so that the reinforcing fibres appear as white spots. The fibre volume fraction is calculated by the ratio between the surface occupied by fibres and the total surface of the cross-section. A fibre volume fraction of 58 % (±1.6 %) is found and is slightly lower than

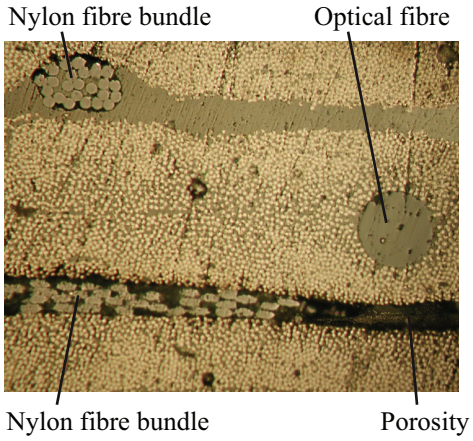

Figure 2.4: Microscopic image of sectioned composite plate with embedded optical fibre.

the nominal specification of the prepregs (60 %). These measurements are reproducible for different specimens.

Integration of embedded fibre

In order to limit its invasiveness, the optical fibre is always embedded parallel to the reinforcing fibres. In this way, the integration of the optical fibre is best because no resin accumulation forms around the fibre, as seen in Figure 2.4. Around the nylon fibres, resin accumulations or porosities are more frequent.

Planarity of plate

When a numerical model of the plate is created, its geometry needs to be known precisely. Especially the thickness has to be measured with good precision because of its high influence on the bending stiffness of the plate. After manufacturing and cutting the plate, its thickness is determined with a micrometer at 12 places and an average value of 4.2 mm is found for the plates. It is however noticed that the thickness may vary by up to 0.4 mm over a plate. Therefore, the planarity is determined using a coordinate measuring machine (GAMMA from D.E.A.). The surface coordinates of both sides of the plate are measured

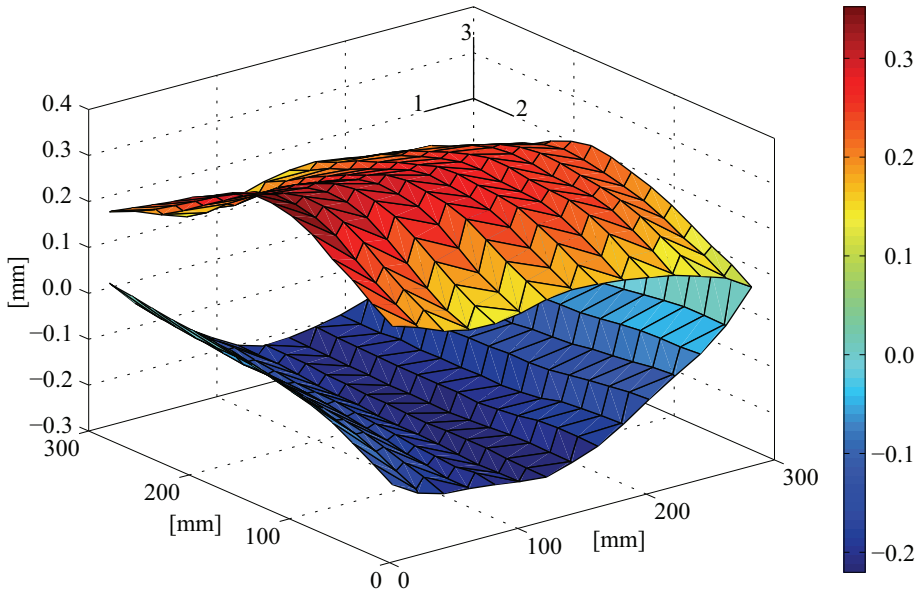

Figure 2.5: Illustration of the planarity of the CFRP plate. The graph indicates the variation of the thickness relative to the smallest thickness of the plate.

on a regular mesh having a distance of 20 mm between measurement points. The shape of both surfaces is illustrated in Figure 2.5. The laminate's surfaces are slightly curved due to the fact that the base and top plates are presumably bending in the autoclave.

2.2.3 Elastic properties of the laminate

The CFRP plates are orthotropic and thus, 9 independent elastic coefficients need to be determined. The linear constitutive equations of an orthotropic homogeneous media define the relation between a state of stress and a state of strain within the body. The stress and strain fields are each determined by 6 independent values. When the coordinate system is aligned with the symmetry planes of the orthotropic material properties, the linear relation between the stress $\boldsymbol{\sigma}$ and strain $\boldsymbol{\varepsilon}$ is defined by [1]

$$\boldsymbol{\sigma} = \boldsymbol{C}\boldsymbol{\varepsilon} \tag{2.1}$$

or in the expanded notation

$$\begin{bmatrix} \sigma_{11} \\ \sigma_{22} \\ \sigma_{33} \\ \sigma_{23} \\ \sigma_{31} \\ \sigma_{12} \end{bmatrix} = \begin{bmatrix} C_{11} & C_{12} & C_{13} & 0 & 0 & 0 \\ C_{12} & C_{22} & C_{23} & 0 & 0 & 0 \\ C_{13} & C_{23} & C_{33} & 0 & 0 & 0 \\ 0 & 0 & 0 & C_{44} & 0 & 0 \\ 0 & 0 & 0 & 0 & C_{55} & 0 \\ 0 & 0 & 0 & 0 & 0 & C_{66} \end{bmatrix} \begin{bmatrix} \varepsilon_{11} \\ \varepsilon_{22} \\ \varepsilon_{33} \\ \varepsilon_{23} \\ \varepsilon_{31} \\ \varepsilon_{12} \end{bmatrix} \tag{2.2}$$

In these equations, $\boldsymbol{C}$ is the stiffness matrix and C_{ij} are the elastic coefficients. The elastic coefficients C_{ij} are related to the engineering constants E_i, ν_{ij} and G_{ij}, called Young's moduli, Poisson's ratios and shear moduli, respectively

$$\begin{gathered} C_{11} = E_1 \cdot \frac{1-\nu_{23}\nu_{32}}{A},\ C_{22} = E_2 \cdot \frac{1-\nu_{13}\nu_{31}}{A},\ C_{33} = E_3 \cdot \frac{1-\nu_{12}\nu_{21}}{A} \\ C_{23} = E_2 \cdot \frac{\nu_{32}-\nu_{12}\nu_{31}}{A},\ C_{13} = E_1 \cdot \frac{\nu_{31}-\nu_{21}\nu_{32}}{A},\ C_{12} = E_1 \cdot \frac{\nu_{21}-\nu_{31}\nu_{23}}{A} \\ C_{44} = G_{23},\ C_{55} = G_{13},\ C_{66} = G_{12} \\ A = 1-\nu_{12}\nu_{21}-\nu_{23}\nu_{32}-\nu_{31}\nu_{13}-2\nu_{21}\nu_{32}\nu_{13} \end{gathered} \tag{2.3}$$

The following relation is additionally verified between the Poisson's ratios ν_{ij} and ν_{ji} and the Young's moduli E_i and E_j

$$\frac{\nu_{ij}}{E_i} = \frac{\nu_{ji}}{E_j} \tag{2.4}$$

The material properties of UD plates and through-the-thickness homogenised properties of CP plates are determined using modal identification [94–96]. The elastic properties are

identified by reducing the discrepancy between experimentally measured and numerically calculated eigenfrequencies and mode shapes of the plate. The error norm minimised by the Levenberg-Marquardt algorithm is based on several criteria. The error vector comprises the difference between numerical and experimental eigenfrequencies and the correspondence of the nodal displacement lines. Moreover, the diagonal and off-diagonal mode shape correlation coefficients associated to the classical modal assurance criterion (MAC) are taken into account.

The modal analysis of the plate is performed with quasi-free boundary conditions. The plate is therefore suspended on two thin nylon yarns. The excitation is performed with a loudspeaker (Bose) and measured by a microphone (Earthworks M30BX). The response of the plate is recorded using a scanning laser Doppler vibrometer (SLDV) (model PSV200 from Polytec). Details on experimental modal analysis and modal parameter extraction are given in Section 2.5. Depending on the quality of the experimental data, the first 12 – 14 eigenmodes are considered for the identification. The experimental mesh size used for these measurements is regular and the distance between measurement points is approximately 10 mm. A reflective tape (Scotchlite™ EG 3210 from 3M) is pasted on one side of the plate because the SLDV needs a reflective surface to measure the transverse velocity of the plate. The reflective film increases the mass of the plate but its contribution to the stiffness of the plate is found to be negligible. The additional mass is comprised in the density of the plate's FE model used for numerical-experimental identification of the elastic properties. The mechanical properties are only accurate if the density of the material is known with a good precision. It is determined by weighting specimens with a known geometry and, hence, a known volume.

The numerical modal analysis is performed with the finite element software MAFE[1] considering variable p-order shear deformation theory (PSDT) shell elements [97]. A regular mesh is generated with an element size of approximately 10 mm × 10 mm. This mesh is found to be sufficiently fine after studying the influence of the mesh size on the identification results. It can be shown that the model is not very sensitive to the transverse Young's modulus E_3 and transverse Poisson's ratios ν_{23} and ν_{31}. In case of a UD plate, the transverse Young's modulus E_3 is set equal to the value of E_2 by assuming transverse isotropy of a UD laminate. For the same reason, the Poisson's ratio ν_{13} is similar to ν_{12}, which can be identified with a good precision because of its influence on the shape of the nodal displacement lines. Because the reinforcing fibres are oriented in the x_1 direction, the longitudinal Young's modulus E_1 is expected to be much higher than E_3. Therefore, the Poisson's ratio ν_{31} is set to the small value of 0.03. The Poisson's ratio ν_{23} is fixed to a value of 0.3 because in this plane this material parameter is mainly dominated by the

[1]Modal analysis by finite elements

Name	Length [mm]	Width [mm]	Thickness [mm]	Density [kg/m³]
UD 1	121.0	121.1	4.39	1450.3
UD 2	159.3	120.8	4.42	1448.6
CP 1	200.9	132.3	4.19	1458.1
CP 2	76.0	132.3	4.19	1461.8

Table 2.1: Dimensions and densities of plates used for the identification of the mechanical properties.

properties of the matrix. In case of a CP plate, the transverse Young's modulus E_3 is set to the same value as in the UD laminate and both Poisson's ratios ν_{23} and ν_{31} are fixed to a value of 0.03.

The properties of a single ply are determined using UD plates and, for the CP plates, through-the-thickness homogenised properties are identified.Specimens with different sizes are cut from distinct plates. The geometry of the plates is carefully chosen so that their eigenfrequencies are uniformly distributed over the lower frequency range. The sizes of the UD plates are 160 mm × 120 mm and 120 mm × 120 mm. The geometries chosen for the CP plate are 200 mm × 130 mm and 75 mm × 130 mm. Note that the latter plate has a small length-to-thickness ratio in both in-plane directions. This allows the identification procedure to be more sensitive to the transverse shear moduli G_{23} and G_{31}. Table 2.1 summarizes the precise dimensions of the specimens and the measured densities of the plates without the reflective sheets. The reflective sheet increases the mass per unit area by 282 g/m² and hence the density by approximately 67 kg/m³.

The results of the mixed numerical-experimental identification are listed in Table 2.2. A small standard deviation is obtained for the different plates and the optimisation results are reproducible when different initial guesses of the properties are chosen for the identification procedure. It could be shown that the results do not change considerably when the values

	E_1 [GPa]	E_2 [GPa]	E_3 [GPa]	ν_{23} [-]	ν_{31} [-]	ν_{12} [-]	G_{23} [GPa]	G_{31} [GPa]	G_{12} [GPa]
UD	96.00	8.67	8.70	0.30	0.03	0.38	2.24	3.59	4.04
	±0.06	±0.04	fixed	fixed	fixed	±0.03	±0.24	±0.08	±0.02
CP	65.89	44.93	8.70	0.03	0.03	0.12	2.55	2.54	4.23
	±1.42	±0.33	fixed	fixed	fixed	±0.04	±0.08	±0.49	±0.08

Table 2.2: Mechanical properties of UD and CP plates.

of the fixed parameters are changed by 30 %.

2.3 Strain measurements using FBG sensors

One of the objectives in this work is to use embedded FBG sensors to measure dynamic strain signals in laminated composite plates. This section gives an overview on the working principle of FBG sensors and their specific use for strain measurements in laminated composite materials.

2.3.1 Working principle of FBG sensors

A Bragg grating is an optical interference pattern written in the core of an optical fibre (Figure 2.6). The fibre, which usually has a cladding diameter of 125 µm, is in general protected from breakage and humidity by a polymer coating. In this work, polyimide coated fibres with an outer coating diameter of approximately 150 µm are employed. The refraction index of the photosensitive core is changed by UV irradiation and the regular pattern is obtained by irradiating through a phase mask.

If broadband light is coupled into the optical fibre, a narrow wavelength band is reflected. The peak wavelength of this reflection band, called Bragg wavelength λ_B, depends on the period Λ of the modulation of the refractive index along the fibre core and the effective refractive index n_{eff}

$$\lambda_B = 2 n_{eff} \Lambda \tag{2.5}$$

In this work, FBG sensors with a Bragg wavelength λ_B of 1 550 nm and a grating length

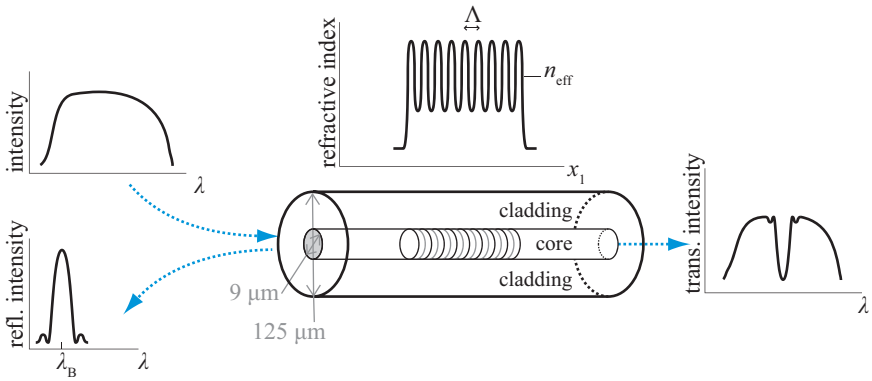

Figure 2.6: Working principle of FBG sensor.

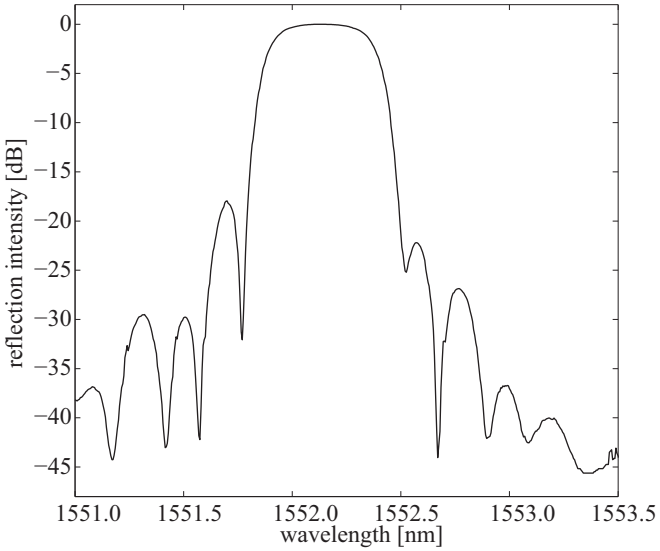

Figure 2.7: Reflection spectrum of FBG sensor.

of 3 mm are used. The gratings are written in SMF-28 optical fibres by Avensys Inc. The reflection spectrum of the FBG has a bandwidth of 0.5 nm (at −3 dB) and a reflectivity of 90 % and is shown in Figure 2.7.

If the grating is submitted to longitudinal strain ε_1, the Bragg wavelength λ_B shifts by an amount $\Delta\lambda_\mathrm{B}$

$$\frac{\Delta\lambda_\mathrm{B}}{\lambda_{\mathrm{B}0}} = (1 - p_e)\,\varepsilon_1 \tag{2.6}$$

where $\lambda_{\mathrm{B}0}$ is the initial Bragg wavelength. This relation is true under the condition of homogeneous longitudinal strain along the optical fibre axis and considering no temperature changes. The wavelength shift is related to the longitudinal strain ε_1 via the photo-elastic coefficient p_e, which depends on the optical fibre and can be experimentally determined. In standard SMF-28 optical fibres p_e has a value of 0.22. In case of a nominal Bragg wavelength $\lambda_{\mathrm{B}0}$ of 1 550 nm, the term $(1 - p_e)\,\lambda_{\mathrm{B}0}$ takes a value of 1.2 $^{\mathrm{pm}}/_{\mu\varepsilon}$. The general formulation of the Bragg wavelength shift $\Delta\lambda_\mathrm{B}$ is dependent on the three-dimensional strain field around the optical fibre and on temperature [98]. When the grating is submitted to uni-axial load and the temperature is not taken into account, the general formulation of the Bragg wavelength shift is reduced to Equation 2.6. The photo-elastic coefficient p_e accounts for the longitudinal strains and the transverse strains due to the Poisson effect.

2.3.2 Integration of FBG sensors

The optical fibres are embedded in a way that the sensors are mostly sensitive to longitudinal strains. When the optical fibres are embedded parallel to the reinforcing fibres, little resin accumulates around the optical fibre as seen in Figure 2.4. In the direction of the optical fibre an isostrain condition is assumed within the optical fibre and the surrounding layers. The transfer of longitudinal strains from the surrounding layers to the optical fibre is good because its Young's modulus (96 GPa) is higher than the one of the glass fibre. In the direction transverse to the optical fibre an isostress condition is assumed in the optical fibre and the surrounding layers. In this direction, the Young's modulus of the surrounding orthotropic material is 10 times lower than the one of the glass fibre and hence, the strain felt by the fibre is small. When the optical fibres would be embedded perpendicular to the reinforcing fibres they are surrounded by elliptic resin accumulations and the impact resistance of the laminate diminishes [83].

The optical fibre can also be glued on the surface of the plate. Rapid epoxy resin (Araldite®) is applied with a syringe over a length of approximately 20 mm (Figure 2.8). The uncoated sensor is placed close to the plate to reduce the epoxy layer between the plate and the sensor. The sensor is however covered by a 2 mm wide and 1 mm thick layer of epoxy resin to maximise the strain transfer from the plate to the sensor [99, 100].

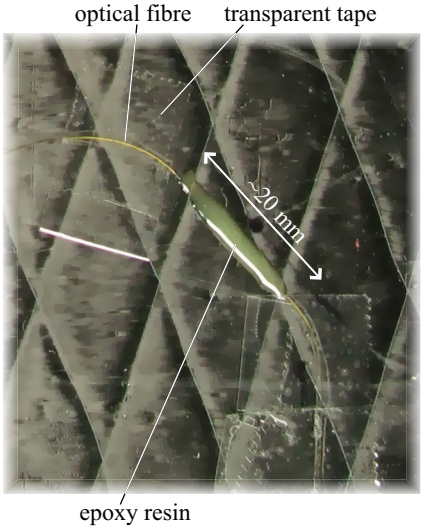

Figure 2.8: Photo of surface-glued optical fibre.

2.3.3 Dynamic strain acquisition

The Bragg wavelength λ_B is commonly determined with optical spectrum analysers whose acquisition rates are limited to a few hundred Hertz. Fast interrogation of the Bragg wavelength (several kHz) would make FBG sensors suitable for monitoring internal strains in structures submitted to dynamic excitations like impact or vibration loads.

The high speed interrogation principle of the Bragg gratings adopted in this work is described in Chapter 3. It is based on a prototype device from Micron Optics Inc. (model MO si920), which is enhanced to suite the requirements for allowing quantitative low noise dynamic strain measurements. A total of four optical fibres each on with an FBG sensor can be interrogated simultaneously. The interrogation device has four optical channels, whereof two with a strain range of 10 000 µε and two with a smaller range of 2 000 µε but an increased sensitivity. When all four optical channels are used, a synchronous acquisition rate of 250 kHz is feasible.

2.4 Impact testing

The impact tests carried out in this work are low velocity impacts on carbon fibre reinforced laminates. The objective of these tests is the creation of a reproducible, barely visible damage in the CFRP plates. To carry out these tests, a custom impact test facility is designed and instrumented. The composite plates are mounted in the clamping fixture of the impact testing facility during the impact and the subsequent tests for damage characterisation.

2.4.1 Impact test facility

In literature, low velocity impacts are generally performed using a drop weight tower. The drop height range and the impact mass are given by the specification of the impact tower. The fixture for the composite specimen and its geometry are also predetermined. Commercially available drop weight towers are generally built to test the impact resistance of composite laminates and often allow to cover a large range of impact energies. The specimens most usually have a circular geometry and a small diameter of 120 mm or less. In this work, a custom basis and fixture for the composite plates is designed in order to study the behaviour in service of a composite panel with a more realistic geometry. The drop weight, its guiding rail and instrumentation are also custom-built.

In order to define the design of the impact tower and the performance specifications, some parameters need to be studied and estimated in advance. The main specifications to be fixed for the design of the facility are

- the range of impact weights,
- the range of drop heights,
- the shape and size of the impact tip,
- the size and geometry of the specimen,
- the configuration of the clamping,
- the type of instrumentation.

Clamping mechanism

The geometry of the composite plate is chosen to be different from those that are traditionally used to test the impact resistance of the laminates. The size of the specimens is bigger to represent more realistically a panel that is part of a real structure. The plates are rectangular with one dimension being 300 mm. The width of the plate can vary but is limited to 300 mm. The fixture is designed to have two edges of the plate clamped and two edges free. The span of the clamped plate is 240 mm. In terms of test reproducibility and easiness for modelling, the optimal clamping fixture and basis have to be rigid and heavy. On each side, the plate is tightened with bolts between two steel blocks with a thickness of 30 mm over a clamping width of 30 mm (cf. Figure 2.9). The distance between the bolts is 40 mm. The upper and lower blocks are kept aligned with a precision of $^1/_{100}$ mm using guiding pins. This assembly is fixed on a 50 mm thick steel base plate.

Drop weight and height

The threshold impact energy necessary to initiate delamination damage can be estimated using analytical models [13]. It has been shown that the onset of damage depends on the maximum impact force. In simple damage initiation and propagation models it is assumed that the onset of delamination damage is due to the transverse shear stresses around the impact point and is related to the interlaminar shear strength of the laminate [13]. In an isotropic plate, the energy release rate at the boundary of a circular delamination is independent of the delamination radius and can be related to the transverse force. The delamination threshold load (DTL) is defined as the impact load required to produce a

significant amount of delamination within the laminate [101]

$$\mathrm{DTL}^2 = \frac{8\pi^2 E h^3 G_{\mathrm{IIc}}}{9\,(1-\nu^2)} \tag{2.7}$$

In this equation, G_{IIc} is the critical energy release rate in mode II, h the thickness of the plate, E the Young's modulus of the material and ν its Poisson's ratio. Supposing a critical energy release rate of about $500\,\mathrm{J/m^2}$ [102], the DTL is approximately 3.5 kN. The average value of the in-plane Young's moduli of the cross-ply plate characterised in Section 2.2.3 and a thickness h of 4.2 mm are considered for this estimation.

The maximum contact force encountered during an impact is related to the plate's stiffness, the contact stiffness between impactor tip and plate, the impact weight and incident velocity. The critical energy E_{crit} can be estimated from the DTL (2.7) by using a simple spring-mass model [103]

$$E_{\mathrm{crit}} = \frac{\mathrm{DTL}^2}{2k} \tag{2.8}$$

In this equation, k is the apparent stiffness of the plate with a central loading. Using FE modelling, the linear stiffness of the composite plate is calculated by the ratio between the central load and the corresponding deflection and has a value of about $700\,\mathrm{kN/m}$. A critical impact energy of 8.8 J can hence be estimated. The estimation of this critical energy is based on many assumptions and should only be considered as a guideline for the conception of the testing facility. It is shown in literature that the damage due to low velocity impacts is a function of energy alone and not velocity or mass separately [104]. For practical reasons, the maximum drop height is limited to 2 m. A drop weight of 860 g is designed, which aims at incident impact energies in a range of 0.8 – 17 J.

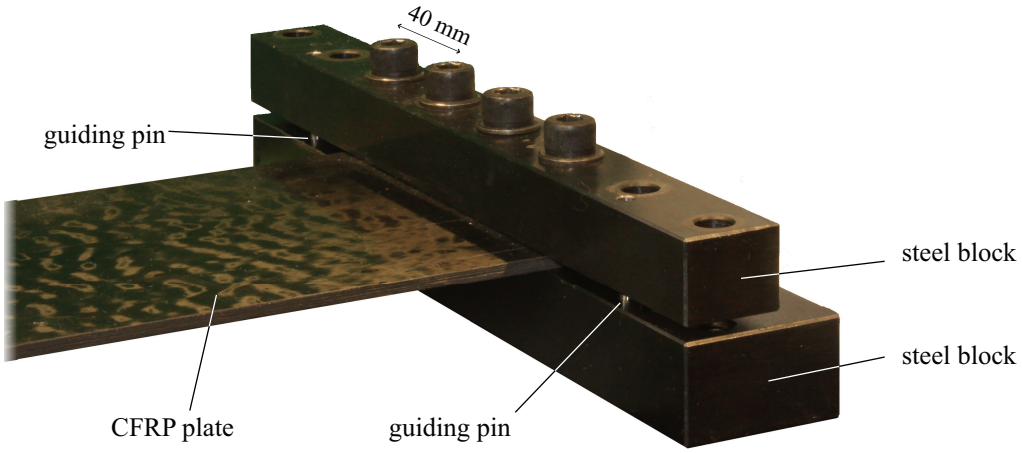

Figure 2.9: Photo of clamping mechanism.

Design of the impact facility

The impact tower consists of a base plate with the fixture mechanism and a frame supporting the guide for a drop weight (Figure 2.10). The base plate and frame are made of massive steel parts to restrain the vibrations travelling through the tower. The drop weight is machined from a solid aluminium block and is designed to have maximal stiffness and a mass of 860 g. The impactor tip is made of steel and has a hemispherical shape with a diameter of 12.7 mm. Additional weight can optionally be bolted to the top of the carriage. The impactor is guided by four wheels along two precision shafts from SFERAX SA. The axis-centre distance between the wheels is fine adjusted using eccentric axes. Before carrying out an impact, the impactor is arrested by a locking pin sliding in one of the evenly spaced holes along the centreline of the guiding rail. The holes are prefabricated with a regular spacing of 50 mm, with the lowest corresponding to a drop height of 55 mm and the highest of 1 855 mm. The impact position can be modified in one direction by choosing a different position of the plate in the clamping fixture and in the other direction by translating the guiding rail of the drop weight.

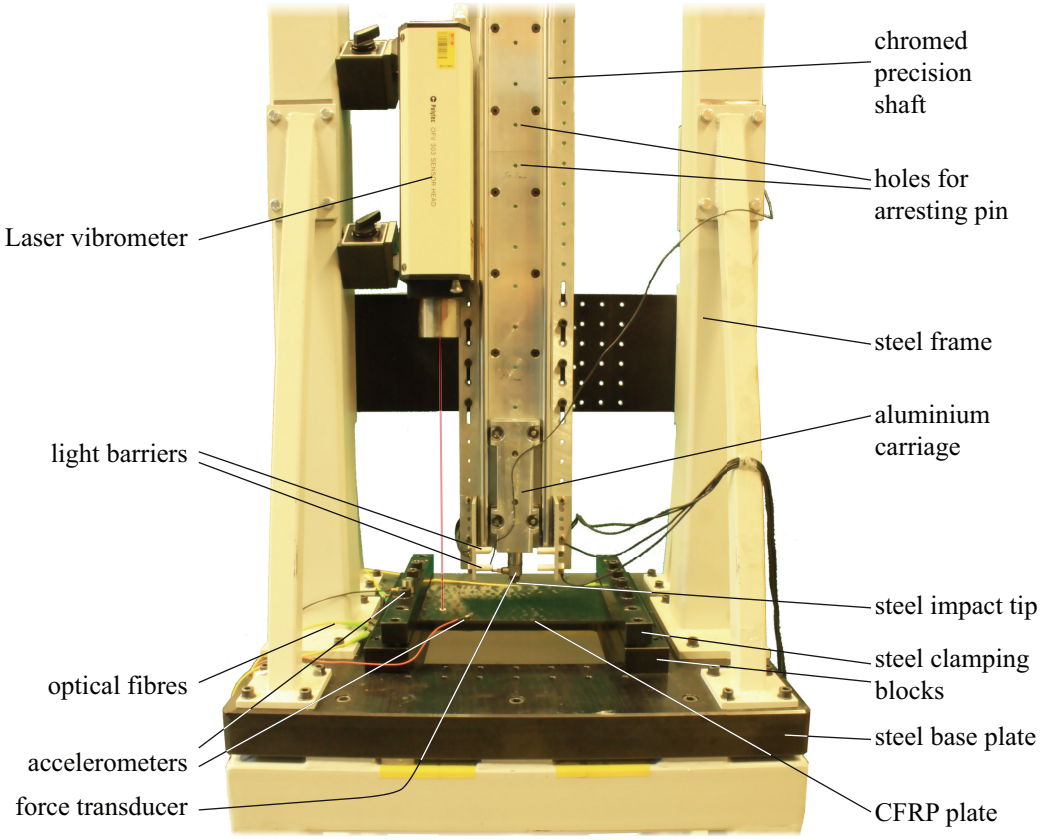

Figure 2.10: Photo of impact tower and instrumentation.

Instrumentation of impact facility

The impact tower is instrumented with all necessary sensors to monitor the impact force, the dynamic response of the plate and the incident and rebound velocities (Figure 2.10). The tip of the impactor is equipped with a piezoelectric force transducer B&K type 8230-003 in order to monitor the contact force. A laser Doppler vibrometer head (OFV 303 from Polytec), capable of measuring a single point velocity response, is mounted on the frame of the tower. The base of the tower is also equipped with an accelerometer. Two light barriers are mounted on the guiding rail in order to trigger the acquisition devices and measure the incident and rebound velocity of the drop weight. When the impact weight disrupts the light beam of a photoelectric sensor, the voltage at the output transistor shifts from 0 V to +5 V. The distance between the two sensors is 24 mm. When the impactor crosses the lower barrier, the impact tip is at a distance of 4 mm from the plate.

The force, velocity and light barrier signals are recorded using a dynamic signal acquisition card from National Instruments (NI DSA PCI-4474). A LabVIEW 8.6 user interface is built to control the number of analogue input channels and the parameters of the analogue-to-digital conversion. During impact loading the card's maximum sampling rate of 100 kHz is used. The high acquisition rate allows to capture short time features in the signal during the impact. Moreover, the time needed by the impact carriage to pass by the two light barriers can be determined with a resolution of ±10 µs. The light barriers have a high responsivity and therefore the rising time of the signal from 0 V to +5 V only takes the time that elapses during the acquisition of one or two samples.

2.4.2 Preliminary results from the impact tests

In this section, preparatory studies on impact testing and preliminary results obtained from a series of impact tests with varying energies are presented. The objective is to characterise the components of the testing facility and analyse the repeatability of the impact tests. In order to carry out an impact, the drop weight is released from a given height by pulling the locking pin. A multiple impact is prevented by catching the rebounding impactor manually.

In this section, the stiffness of the impactor is evaluated by studying its dynamic response during an impact. Furthermore it is verified that the incident impact velocity can be analytically estimated by assuming a free fall of the impact weight. Finally, the impact force and the absorbed energy are studied for a range of impact energies.

Stiffness of the impact weight

The impact weight is instrumented with an accelerometer on its upper surface in order to measure the frequency response function of the impactor carriage during an impact. The first vertical traction-compression vibration mode of the impactor appears at a frequency above 13 kHz. This frequency is considerably higher than the eigenfrequencies of the plate, excited during the impact. Hence the impactor is considered to be rigid during subsequent analysis and numerical modelling.

Incident impact velocity

The repeatability of the impact velocity is tested for a range of drop heights varying from 55 to 1 105 mm. For each drop height, 5 experimental tests are performed. Moreover, the experimentally measured velocity is compared to the analytical formula expressing the incident velocity as a function of drop height H_0 in case of a free fall

$$V_i = \sqrt{2gH_0} \tag{2.9}$$

In this equation, g is the gravity equal to 9.81 $^{\mathrm{m}}/_{\mathrm{s}^2}$.

The effective velocity is measured using the two light barriers. The duration needed by the impactor to pass from the first to the second photoelectric sensor is easily determined

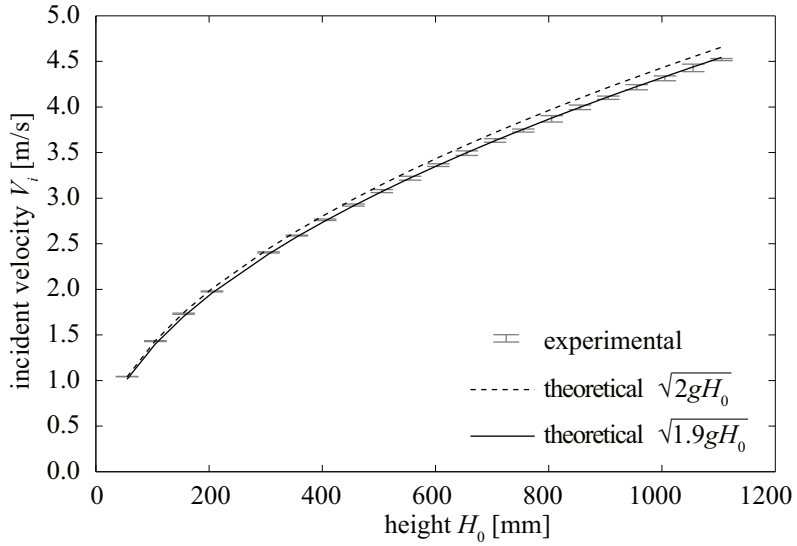

Figure 2.11: Experimentally measured and theoretical impact velocity as a function of drop height.

from the rectangular signals. The velocity is not assumed to be constant during this laps of time but it is considered to increase linearly with time because the distance between the two light barriers is large compared to small drop heights.

Figure 2.11 shows the experimentally measured velocity as a function of drop height and compares it to the theoretical velocity calculated supposing a free fall without friction and aerodynamic resistance. For a given drop height, the incident velocity before impact shows a very good reproducibility. Over the range of tested drop heights, the experimentally measured velocity is 2.5 % lower than the theoretical value.

Contact force

Throughout the present work, the contact force is acquired during all the impacts because it gives useful information about the onset of damage. Figure 2.12 shows the force-time history for selected impacts with incident energies ranging from 1.7 to 6.8 J. In these cases, distinct cross-ply plates with dimensions of 300 mm × 140 mm are impacted at the central location. The signals are similar in shape but have different amplitudes. It can be noticed that damage is occurring during the first millisecond of high energy impacts because high frequency oscillations can be noticed. The maximum impact force is shown as a function of incident impact energy in Figure 2.13. The observed trend may not be generalised to different impact positions because the apparent stiffness of the plate is assumed to differ with respect to the impact position. Moreover it may vary with increasing deflections because of non-linear geometry effects.

Absorbed energy

The energy absorbed during the impact can be determined by measuring the incident velocity V_i and rebound velocity V_r of the drop weight with the use of the light barriers. The absorbed energy is defined as the total incident energy minus the rebound energy and hence, the relative absorbed energy can be expressed in terms of a ratio between both velocities

$$\bar{E}_a = 1 - \left(\frac{V_r}{V_i}\right)^2 \tag{2.10}$$

The absorbed energy comprises the energy dissipated by the damage mechanisms, elasto-dynamic damping and damping at the clamping fixture. In the studied range of incident impact energies, the energy absorbed during a central impact is around 35 % (Figure 2.13).

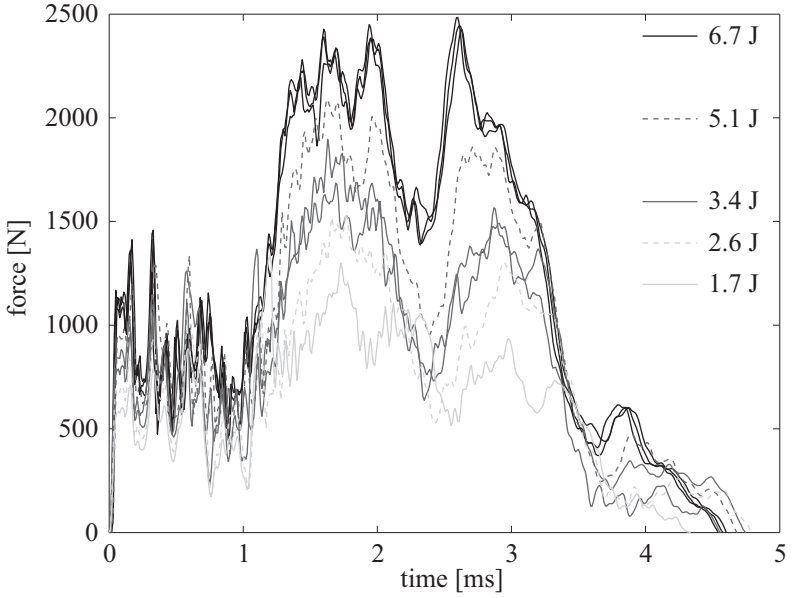

Figure 2.12: Impact force signals for different impact energies.

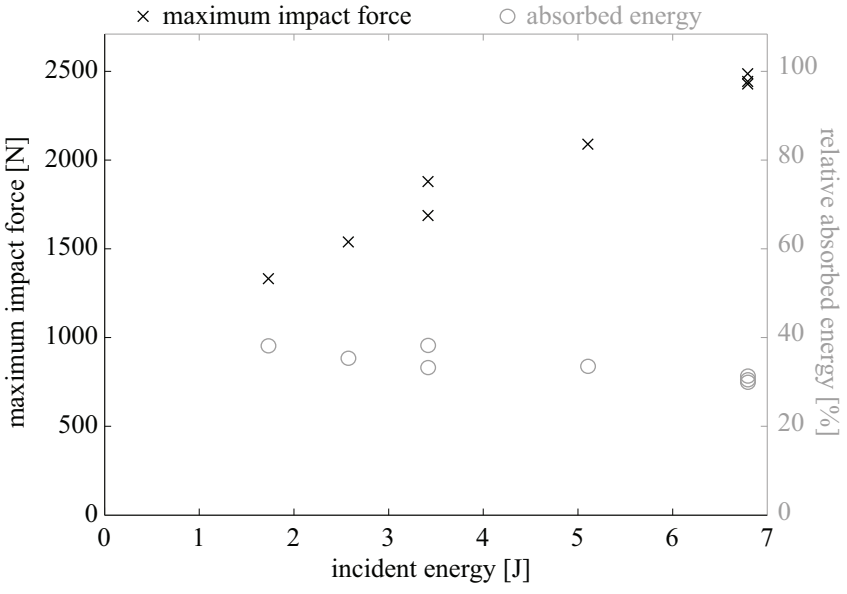

Figure 2.13: Maximum impact force and absorbed energy as a function of incident energy.

2.5 Experimental modal analysis

Within this work, experimental modal analysis is used for different purposes. It serves for material properties characterisation (Section 2.2.3) via numerical-experimental modal identification, numerical model validation (Section 2.6.1), characterisation of the clamping fixture and for damage identification (Chapter 6). The parameters extracted during modal analysis are the eigenfrequencies, mode shapes and modal damping ratios. In this section, the theoretical background for experimental modal analysis is introduced and the experimental approach is presented.

2.5.1 Theory

The dynamic equations of a discrete vibration model with n_{DOF} degrees of freedom (DOF) subjected to an external force vector $\boldsymbol{f}(t)$ is written

$$\boldsymbol{M}\ddot{\boldsymbol{u}} + \boldsymbol{D}\dot{\boldsymbol{u}} + \boldsymbol{K}\boldsymbol{u} = \boldsymbol{f}(t) \tag{2.11}$$

where $\boldsymbol{M}$, $\boldsymbol{D}$ and $\boldsymbol{K}$ are the mass, damping and stiffness matrices of the system. The displacement vector is denoted by $\boldsymbol{u}$ and the velocity and acceleration by $\dot{\boldsymbol{u}}$ and $\ddot{\boldsymbol{u}}$, respectively.

First, the free vibration is studied and the previous equation system (2.11) is considered without external forces (homogeneous solution). Assuming a harmonic solution $\boldsymbol{u} = \boldsymbol{\beta}\cos(\omega t + \phi) = \mathfrak{Re}\left[\boldsymbol{\beta}\mathrm{e}^{j(\omega t+\phi)}\right]$, a generalised eigenvalue problem is obtained

$$\left[-\omega_i^2\boldsymbol{M} + j\omega_i\boldsymbol{D} + \boldsymbol{K}\right]\boldsymbol{\beta}_i = 0 \tag{2.12}$$

where ω_i are the damped eigenfrequencies, $\boldsymbol{\beta}_i$ the eigenvectors and $j = \sqrt{-1}$ the complex unitary number. $\mathfrak{Re}$ designates the real part of a complex value. Under certain conditions (Caughey), it exists a matrix $\boldsymbol{B}$ representing a vector basis in which the projections of $\boldsymbol{M}$, $\boldsymbol{D}$ and $\boldsymbol{K}$ are diagonal matrices.

$$\begin{aligned} \boldsymbol{M}^0 &= \boldsymbol{B}^T\boldsymbol{M}\boldsymbol{B} \\ \boldsymbol{D}^0 &= \boldsymbol{B}^T\boldsymbol{D}\boldsymbol{B} \\ \boldsymbol{K}^0 &= \boldsymbol{B}^T\boldsymbol{K}\boldsymbol{B} \end{aligned} \tag{2.13}$$

In case off non-proportional damping, the small off-diagonal coupling coefficients of the projected damping matrix may be neglected. The displacement vector can also be projected in the vector space $\boldsymbol{B}$

$$\boldsymbol{u} = \boldsymbol{B}\boldsymbol{q} \tag{2.14}$$

After diagonalisation of the matrices, the system of equations (2.11) can be rewritten as a system of n_{DOF} uncoupled equations

$$m_i^0 \ddot{q}_i + d_i^0 \dot{q}_i + k_i^0 q_i = f_i^0 (t) \tag{2.15}$$

where m_i^0, d_i^0 and k_i^0 are the i^{th} elements of the diagonal matrices $\boldsymbol{M}^0$, $\boldsymbol{D}^0$ and $\boldsymbol{K}^0$, respectively. The projection of the excitation force vector $\boldsymbol{f}$ in the vector space $\boldsymbol{B}$ is denoted by $\boldsymbol{f}^0 = \boldsymbol{B}^T \boldsymbol{f}$. The undamped and damped eigenfrequencies ω_{0i} and ω_i and modal damping ratios η_i are then easily obtained from each of the equations

$$\begin{aligned} \omega_{0i} &= \sqrt{\frac{k_i^0}{m_i^0}} \\ \eta_i &= \frac{d_i^0}{2 m_i^0 \omega_{0i}} \\ \omega_i &= \omega_{0i} \sqrt{1 - \eta_i^2} \end{aligned} \tag{2.16}$$

The dynamic response of a degree of freedom r to an excitation on a position s as a function of the excitation frequency ω is finally expressed as a superposition of the response of n_{DOF} elementary oscillators with eigenfrequencies ω_i and eigenmodes $\boldsymbol{\beta}_i$. The complex frequency response function (FRF), which is the response spectrum $U_r (j\omega)$ normalised by the excitation spectrum $F_s (j\omega)$, is hence

$$h_{rs} (j\omega) = \frac{U_r (j\omega)}{F_s (j\omega)} = \sum_i \frac{\beta_{ri} \beta_{si}}{m_i^0 (\omega_{0i}^2 + 2j\eta_i \omega_{0i} \omega - \omega^2)} \tag{2.17}$$

where β_{si} and β_{ri} are the modal displacements of mode i for an excitation at a degree of freedom s and a response on a degree of freedom r. When the excitation frequency ω is equal or close to an eigenfrequency ω_{0k} and modes are well separated, the value of the FRF defined by (2.17) is dominated by the eigenmode k (SDOF method)

$$h_{rs} (j\omega_{0k}) = \sum_i \frac{\beta_{ri} \beta_{si}}{m_i^0 (\omega_{0i}^2 + 2j\eta_i \omega_{0i} \omega_{0k} - \omega_{0k}^2)} \approx \frac{\beta_{rk} \beta_{sk}}{2j m_k^0 \eta_k \omega_{0k}^2} \tag{2.18}$$

In this case, each component of the eigenvector $\boldsymbol{\beta}_k$ is proportional to the value of the FRF $h_{rs} (j\omega_{0k})$ which is almost purely imaginary. Due to the symmetry of expression (2.18), the knowledge of a single row or column of the matrix formed by $h_{rs} (j\omega_{0k})$ is sufficient to determine the shape of the eigenvector $\boldsymbol{\beta}_k$.

In practice it is therefore common to dynamically excite the different DOFs and to measure the dynamic response always on the same position.[2] When the excitation spectrum

[2]It is also possible to have the excitation on the same point and measure the response on the different DOFs, as it is done for example with an SLDV.

$F_s(j\omega)$ has an almost constant amplitude over the frequency range of interest, a response-only transfer function can be calculated. This can be useful when the exact excitation signal is unknown or cannot be simultaneously acquired. If a reproducible triggering of the response acquisition is not guaranteed, the response spectra will each comprise a different phase shift. In this case, the obtained eigenmodes will most probably be falsified and complex but the eigenfrequencies can still be easily identified. When the excitation signal is close to a Dirac signal, the phase delay is almost linear and could be corrected.

2.5.2 Experimental approach

In experimental modal analysis, the structure is spatially discretised and n_{DOF} DOFs are defined. The structure needs to be dynamically excited and the excitation signals recorded. Either a fixed point is chosen for the response measurement and the excitation is performed on all the DOFs of interest, or the excitation point remains the same and the response is measured on each one of the DOFs. An analogue low-pass filter (anti-aliasing filter) is used to limit the frequency range of interest and the acquisition rate of the signals has to be at least twice the stop-band frequency of this filter. The discrete Fourier transforms of the excitation and response signals are computed after the signals are made periodic by applying windowing functions. The FRF of each DOF is the ratio of the corresponding response and excitation spectra. The eigenfrequencies, damping factors and eigenmodes are identified by the modal curve fitting software ME'scope from Vibrant Technology. A polynomial curve fitting method, adjusting a superposition of single DOF transfer functions (2.17) to the experimentally determined FRFs is applied (MDOF method).

Two different types of boundary conditions (BC) are considered within this work. The free plate condition is obtained by suspending it on two thin nylon yarns and the clamped plate is mounted on the basis of the impact testing facility, as described in Section 2.4.1. The type of excitation is chosen so that at least the frequency range of interest is excited. Different excitation techniques are used generally in experimental modal analysis. The most common are hammer excitation or forced excitation with a electrodynamic shaker, loudspeaker, piezoelectric transducer or eccentric rotating wheel. The excitation signals received by these devices can be random frequency signals or frequency sweep signals. In this work, the plates with free BCs are excited without contact by loudspeakers actuated with frequency sweep signals and the plates with clamped BCs are excited using an instrumented hammer.

A large choice of sensors exists to measure the dynamic response of a structure. In this work, velocity measurements with a laser Doppler vibrometer are used as reference measurements of the modal parameters. The dynamic range of the vibrometer is very

high and a good signal-to-noise ratio is obtained. In Chapter 3 it is also shown that dynamic strain signals from FBG sensors can be used for experimental modal analysis. The position of the sensors needs to be chosen so that the sensors are sufficiently sensitive to the measured eigenmodes. Considering a viscous damping model, the velocity resonance frequency of the structure is theoretically the same as the undamped eigenfrequency but different from the damped displacement (or strain) resonance frequency. However, in this work, damped displacement resonance frequencies are nevertheless considered to be equal to velocity resonance frequencies. The corresponding error is less than $6.4{\cdot}10^{-5}$ with regard to the small modal damping ratios observed (less than 0.8 %). Table 2.3 summarises the different experimental configurations used for modal analysis in this work.

BC	Excitation type and measurement	Response measurement
free	loudspeaker (BOSE) microphone (Earthworks M30BX)	scanning laser Doppler vibrometer (Polytec PSV200)
clamped	instrumented hammer (Brüel & Kjær type 8206)	single point laser Doppler vibrometer (Polytec PSV OFV 303)
clamped	instrumented hammer (Brüel & Kjær type 8206)	FBG sensor

Table 2.3: Configuration of experimental modal analysis.

Throughout different experiments, the repeatability of the eigenfrequency and damping measurements is checked. Therefore, the modal analysis is carried out several times under the same conditions. The accuracy of the results mainly depends on the signal-to-noise ratio of the dynamic signals and the acquisition time, which is directly related to the frequency resolution of the discrete Fourier transform.

2.5.3 Results and discussion of repeatability

The convention to denote the eigenmodes is based on the displacement mode shapes and the number of nodal displacement lines. The letter designates a bending (B) or a torsion (T) mode. The first/second number indicates the number of nodal lines in the x_1/x_2 direction. Figure 2.14 show the first 10 experimentally measured displacement mode shapes of a plate with clamped BC and the respective notation of the modes. The eigenfrequencies of a free CP plate with dimensions of 140 mm × 300 mm and the relative standard deviation of the results throughout 4 different measurements are shown in Table 2.4. The frequencies are determined with an SLDV on a grid of 6 × 5 points. The repeatability of the eigenfrequency measurements on a single plate is very good and the maximum relative standard deviation

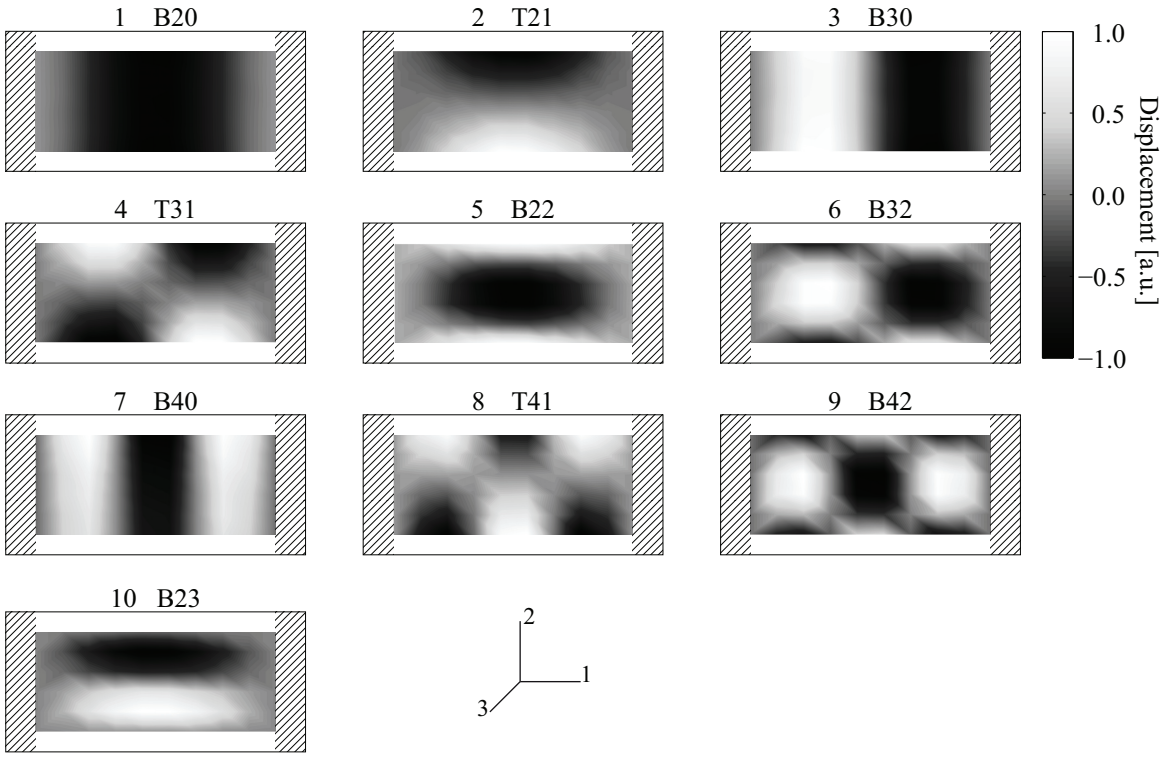

Figure 2.14: Experimental normalised displacement mode shapes of a clamped plate.

of the measured eigenfrequencies is 0.03 %. The repeatability of the measurements of the clamped plate is also good (see Table 2.5) having a maximum standard deviation of 0.06 %. Even when the plate is dismounted between experiments, it is shown that the maximum relative standard deviation is less than 0.2 %.

The modal damping factors of three different intact plates with clamped and free BCs are shown in Figures 2.15a and 2.15b. Prior to the impact they are similar for the different plates and, as indicated by error bars, the repeatability of the damping measurements on a single intact plate is good. For plates with free BC, modal damping ratios between 0.05 % and 0.4 % are found for the first 18 modes. The damping of the same plates with clamped BC is slightly higher because of the dissipation at the fixture. The relative standard deviation of the damping measurements on a single clamped plate is less than 16 %.

Overall, it can be retained that the eigenfrequencies can be determined with a high accuracy in the order of 0.06 % if the plate is not dismounted inbetween measurements. The damping factors of the intact plates can be determined with a precision better than 16 %. In Chapter 5, the influence of the damage on the modal parameters is studied. The relative variation of the parameters due to damage needs to be higher than the measurement accuracy in order to use these data within a damage identification procedure. In Chapter 3,

		Plate 1		Plate 2		Plate 3	
	Mode	Avg. freq.	RSD*	Avg. freq.	RSD*	Avg. freq.	RSD*
Mode	Shape	[Hz]	[%]	[Hz]	[%]	[Hz]	[%]
1	T11	173.25	0.016	176.26	0.000	174.59	0.045
2	B20	314.47	0.001	322.03	0.003	320.43	0.000
3	T21	465.75	0.008	475.96	0.029	471.86	0.021
4	B30	839.77	0.000	860.72	0.005	856.20	0.001
5	T31	982.11	0.001	1005.32	0.026	997.91	0.007
6	B02	1101.93	0.003	1161.44	0.011	1141.89	0.005
7	T12	1157.54	0.003	1188.31	0.019	1169.28	0.007
8	B22	1339.70	0.018	1385.13	0.029	1364.92	0.015
9	B40	1603.84	0.001	1648.99	0.007	1637.81	0.003
10	T41	1743.49	0.003	1778.34	0.003	1768.74	0.008
11	B32	1726.95	0.006	1777.70	0.037	1751.78	0.033
12	B42	2366.95	0.000	2428.79	0.018	2402.75	0.014
13	B50	2572.88	0.011	2653.86	0.035	2630.15	0.026
14	T51	2723.04	0.010	2770.86	0.015	2759.41	0.001
15	B03	2854.63	0.004	3066.99	0.014	3013.79	0.004
16	T13	3036.77	0.013	3079.25	0.020	3025.69	0.007
17	B23	3206.54	0.002	3318.81	0.014	3263.40	0.007
18	B52	3253.54	0.033	3335.20	0.029	3302.51	0.006

* : Relative standard deviation

Table 2.4: Repeatability of eigenfrequency measurements of free plates.

		Plate 1		Plate 2		Plate 3	
	Mode	Avg. freq.	RSD*	Avg. freq.	RSD*	Avg. freq.	RSD*
Mode	Shape	[Hz]	[%]	[Hz]	[%]	[Hz]	[%]
1	B20	423.10	0.029	434.71	0.035	432.36	0.007
2	T21	475.32	0.021	485.33	0.016	482.61	0.000
3	B30	1154.45	0.032	1191.03	0.007	1185.40	0.021
4	T31	1236.29	0.004	1268.11	0.012	1262.06	0.003
5	B22	1309.28	0.007	1353.54	0.001	1332.20	0.000
6	B32	1855.94	0.003	1913.12	0.009	1886.33	0.062
7	B40	2253.42	0.059	2322.82	0.035	2308.31	0.030
8	T41	2381.28	0.013	2416.57	0.064	2407.59	0.030
9	B42	2837.76	0.006	2904.31	0.036	2875.29	0.001
10	B23	3209.86	0.015	3320.68	0.004	3266.27	0.009

* : Relative standard deviation

Table 2.5: Repeatability of eigenfrequency measurements of clamped plates.

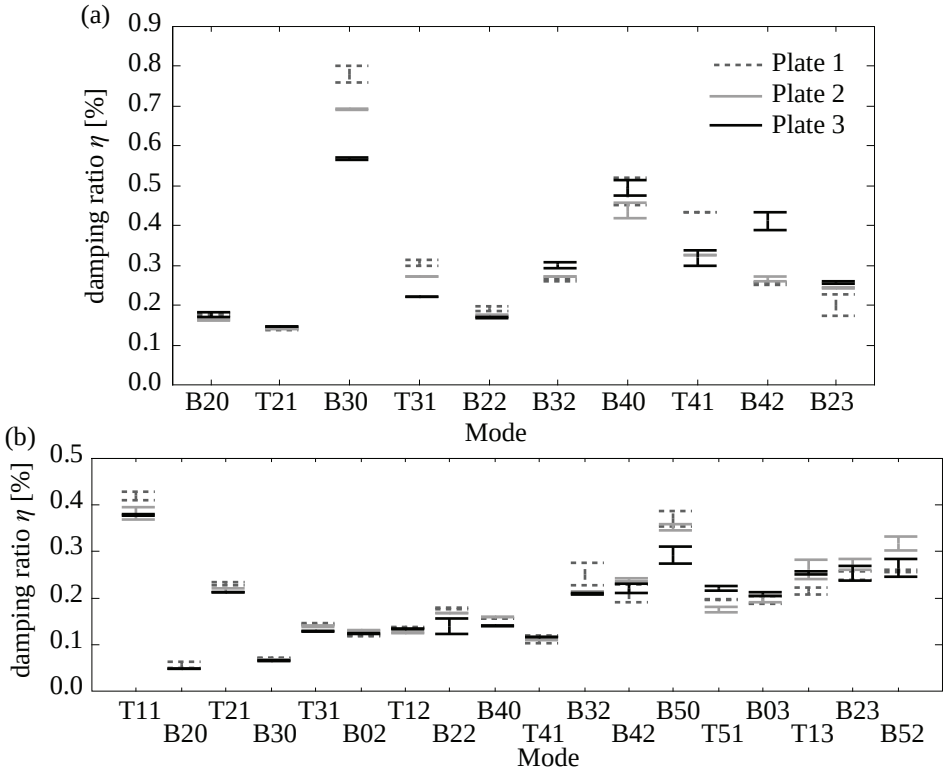

Figure 2.15: Modal damping factors of three different plates with (a) clamped and (b) free BC.

the same study is carried out for experimental modal analysis with FBG senors.

2.6 Numerical modelling

The finite element (FE) method is used for numerical modal analysis, which is performed using the Lanczos eigenvalue extraction method, and to calculate the transient response of a plate to a transverse low-velocity impact via an explicit integration scheme. The commercial FE software Abaqus FEA 6.8-2 is employed in both cases. This section gives an overview on the FE theory and details the development and validation of these two different applications. Numerical modal analysis is carried out in the particular case of a CFRP CP plate having the same dimensions as the one in the previous section. The eigenfrequencies and mode shapes of the plate are calculated for two different experimental configurations (free/clamped). These two configurations allow to disclose successively the possible error sources in the model. Whereas the first configuration allows to validate the material properties, the geometry and the mesh of the plate, the latter reveals the quality

of the clamping fixture. Such a numerical model is later used (Chapter 5) to study the influence of damage on the modal parameters of a plate and in the numerical-experimental damage identification method (Chapter 6). The transient response of a clamped plate to a non-destructive impact is simulated using Abaqus/Explicit. This numerical model is validated by experimental data acquired during the impact. This model is later used to validate the experimental strain response of an embedded FBG sensor (Chapter 3).

2.6.1 Numerical modal analysis

Theory

In numerical modal analysis, the elastodynamic equation of a solid with a volume Ω is solved to obtain its free vibration modes. In case of an anisotropic solid, the dynamic equation for the displacement vector $\boldsymbol{u}$ and the conditions on the boundary of the domain $\partial\Omega = \partial\Omega_u \cup \partial\Omega_\sigma$ are defined in [105]

$$\boldsymbol{\nabla}^T \boldsymbol{C}\, \boldsymbol{\nabla}\boldsymbol{u} = \rho\ddot{\boldsymbol{u}} \qquad \text{in } \Omega \tag{2.19}$$

$$\boldsymbol{u} = \hat{\boldsymbol{u}} \qquad \text{on } \partial\Omega_u \tag{2.20}$$

$$\boldsymbol{N}^T \boldsymbol{C}\, \boldsymbol{\nabla}\boldsymbol{u} = \boldsymbol{\sigma}_N \qquad \text{on } \partial\Omega_\sigma \tag{2.21}$$

where the density of the material is denoted ρ and $\ddot{\boldsymbol{u}}$ is the second derivative of the displacement field with respect to time. The operator $\boldsymbol{\nabla}$ is defined by

$$\boldsymbol{\nabla} = \begin{bmatrix} \partial/\partial x_1 & 0 & 0 \\ 0 & \partial/\partial x_2 & 0 \\ 0 & 0 & \partial/\partial x_3 \\ 0 & \partial/\partial x_3 & \partial/\partial x_2 \\ \partial/\partial x_3 & 0 & \partial/\partial x_1 \\ \partial/\partial x_2 & \partial/\partial x_1 & 0 \end{bmatrix} \tag{2.22}$$

and the direction cosine matrix $\boldsymbol{N}$ of the unitary vector $n = [n_1, n_2, n_3]^T$ normal to the boundary surface is defined in a similar way

$$\boldsymbol{N} = \begin{bmatrix} n_1 & 0 & 0 \\ 0 & n_2 & 0 \\ 0 & 0 & n_3 \\ 0 & n_3 & n_2 \\ n_3 & 0 & n_1 \\ n_2 & n_1 & 0 \end{bmatrix} \tag{2.23}$$

For the problem to be uniquely defined, the BCs have to be specified along the entire boundary of the domain. Either essential (2.20) or natural (2.21) BCs exist which means that either the displacement field $\hat{\boldsymbol{u}}$ or the surface tractions $\boldsymbol{\sigma}_N$ is specified. In the present work, the two kinds of BCs are encountered. The plate may be clamped (essential BCs) and hence the displacement field at the clamping surface is zero, or the surface is free and the stress components normal to the surface are zero (natural BCs).

In order to find a numerical solution to Equation (2.19), the weak form is expressed by

$$\int_{\Omega} \left[(\boldsymbol{\nabla}\delta\boldsymbol{u})^T \boldsymbol{C}\, \boldsymbol{\nabla}\boldsymbol{u} + \rho\delta\boldsymbol{u}^T\ddot{\boldsymbol{u}} \right] d\Omega - \int_{\partial\omega} \boldsymbol{N}^T\boldsymbol{C}\, \boldsymbol{\nabla}\boldsymbol{u}\delta\boldsymbol{u}\, d\partial\Omega = 0 \quad \forall\delta\boldsymbol{u} \tag{2.24}$$

In this integral equation, $\delta\boldsymbol{u}$ is an admissible virtual displacement field and Ω denotes the entire domain of the structure. When looking for a solution $\boldsymbol{u}$ to this equation, functions of the Sobolev space $H^1(\Omega)$ are considered and the essential BCs have to be verified. For the virtual displacement field $\delta\boldsymbol{u}$ to be admissible, it has to be equal to zero at the boundaries with essential conditions. The stress vector normal to a boundary surface with free BCs is also equal to zero. The second term of Equation (2.24) is hence zero in both cases of free and clamped boundaries.

The integral form of Equation (2.24) can be rewritten as a sum of integrals over elementary domains ${}^e\Omega$. This means that the structure can be spatially discretised using a finite number of subdomains, called finite elements. Within an element, the displacement field is approximated by

$${}^e\boldsymbol{u} \approx \boldsymbol{H}\ {}^e\boldsymbol{q} \tag{2.25}$$

where $\boldsymbol{H}$ consists of a matrix containing usually ${}^en$ orthogonal polynomial functions and ${}^e\boldsymbol{q}$ is a vector containing the nodal displacement fields of an element. The ${}^en$ nodes and shape functions are chosen so that the functions form a function subspace with each of them taking a unitary value on one node and zero on all the others. The virtual displacement field ${}^e\delta\boldsymbol{u}$ is approximated by the same subspace of functions.

$${}^e\delta\boldsymbol{u} \approx \boldsymbol{H}\ {}^e\delta\boldsymbol{q} \tag{2.26}$$

Introducing the approximation (2.25) in (2.24) leads to a system of equations for the vector $\boldsymbol{q}$ assembled from the elementary displacement vector ${}^e\boldsymbol{q}$ which comprises the nodal displacements of all the nodes

$$\boldsymbol{M}\ddot{\boldsymbol{q}}(t) + \boldsymbol{K}\boldsymbol{q}(t) = 0 \tag{2.27}$$

In this equation, the mass matrix $\boldsymbol{M}$ and the stiffness matrix $\boldsymbol{K}$ are obtained by assembling

the elementary matrices ${}^e\boldsymbol{M}$ and ${}^e\boldsymbol{K}$ defined by

$$
\begin{aligned}
{}^e\boldsymbol{M} &= \int_{{}^e\Omega} \rho \boldsymbol{H}^T \boldsymbol{H} \, d^e\Omega \\
{}^e\boldsymbol{K} &= \int_{{}^e\Omega} \boldsymbol{\nabla} \boldsymbol{H}^T \boldsymbol{C} \, \boldsymbol{\nabla} \boldsymbol{H} \, d^e\Omega
\end{aligned}
\tag{2.28}
$$

In order to solve the free vibration equation, a harmonic time-dependency with an angular frequency ω is assumed for $\boldsymbol{q}(t)$ and Equation (2.27) can be formulated in the frequency domain

$$
\left[-\omega^2 \boldsymbol{M} + \boldsymbol{K}\right] \boldsymbol{\beta} = 0 \tag{2.29}
$$

This eigenvalue problem is numerically solved using the iterative Lanczos solver. For more details, the reader is referred to [105].

Geometry, mesh and boundary conditions

The spatial discretisation of the rectangular plate is done using quadratic brick elements having 20 nodes. The elements have a reduced integration scheme and are denoted C3D20R in the Abaqus/Standard element library. These elements do not suffer from shear locking. In order to allow for a good convergence of the shear deformations, more than a single element in the through-the-thickness direction is needed because otherwise the transverse shear strain would be approximated by a constant value. When too much elements are used in the through-the-thickness direction compared to the in-plane direction, the aspect ratio of the element is high and the element's stiffness matrices may become ill-conditioned. Given that the geometry of the plate is simple, a regular mesh with brick elements can easily be produced and the thickness-to-length ratio of the elements is easily controlled.

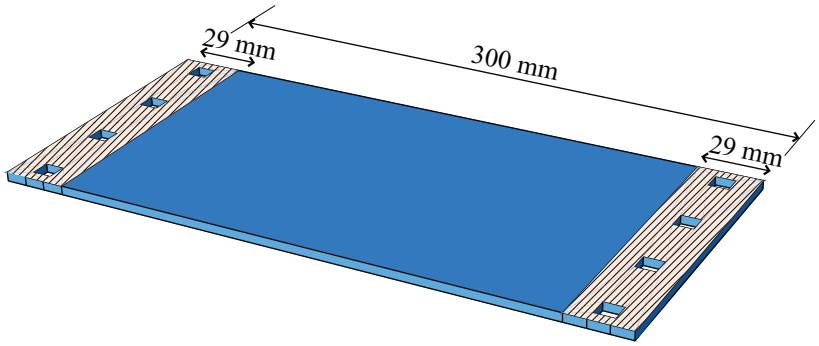

Figure 2.16: Geometry of the plate's FE model.

The geometry of the model is a rectangular plate with dimensions of 300 mm × 140 mm and a thickness of 4.2 mm. For simplification of the meshing strategy, the holes, drilled in the plates for the clamping mechanism, are modelled by square holes with an equivalent surface. The clamped BCs are introduced by fixing the three translational DOFs of the nodes at the lower and upper clamping surface. In order to account for the imperfect contact in the corner of the real clamping fixtures, the effective span between the fixtures is increased by 1 mm on each side. The phenomena that are hereby taken into consideration are eventual slipping of the plate in the fixture, contact opening and closing and a non-infinite stiffness of the fixture and the base. This offset value of 1 mm is identified empirically. On the two short sides of the plate, a surface with a width of 29 mm is partitioned (Figure 2.16) to model the clamping.

Material properties

The CP plate is either modelled ply-by-ply or with through-the-thickness homogenised properties. Mechanical properties of the UD plies and CP plates are determined in Section 2.2.3 with an inverse numerical-experimental modal identification method. The ply-by-ply modelling of the plate causes a very fine mesh and, consequently, a system of equations with a lot of DOFs needs to be solved. The use of homogenised material properties allows to reduce the number of elements in the through-the-thickness direction independently of the number of plies in the composite.

Mesh convergence study

A mesh convergence study of the FE model with through-the-thickness homogenised properties is carried out. The in-plane element size W^e is varied from 20 mm to 2 mm and the number of elements in the through-the-thickness direction n_3^e is varied from 3 to 6 elements. Figure 2.17 shows the different normalised eigenfrequencies as a function of the number of elements. The eigenfrequencies obtained using a mesh with an element size W^e equal to 7 mm and a number n_3^e of 3 elements in the through-the-thickness direction — hence a total of 2 400 elements — differ by up to 0.6 % from the results with the finest mesh. This mesh may, however, be sufficiently fine to study the relative effect of different damage stages on the output of the model while maintaining a similar mesh throughout the analysis. A convergence study of the relative eigenfrequency change is carried out for the damage model in Section 5.4.2. The results presented in the following section are obtained using a mesh with approximately 3 × 40 × 20 elements.

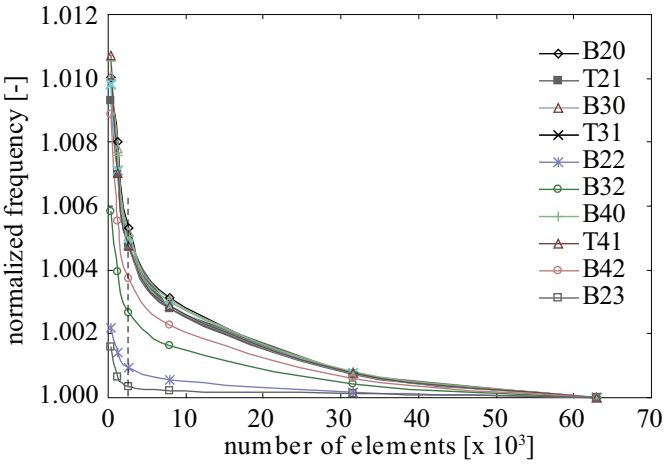

Figure 2.17: Mesh convergence analysis of the FE model.

Validation of the numerical model

The results of the numerical modal analysis are compared to the experimental results obtained in Section 2.5. The normalised frequency error of each eigenmode m is defined by

$$\bar{\varepsilon}_m^f = \frac{f_m^{\text{num}} - f_m^{\text{exp}}}{f_m^{\text{exp}}} \tag{2.30}$$

where f_m^{num} and f_m^{exp} are the numerical and experimental eigenfrequencies, respectively.

The experimental eigenfrequencies of four different intact plates are compared to the numerical eigenfrequencies. Figure 2.18 shows the range of errors between numerical results and experimental eigenfrequencies of the four different plates in the case of free BCs. The normalised frequency errors of the first 18 modes are within a range of -3 to $+5\,\%$. The experimental results show a scattering because the plate processing is not exactly reproducible and consequently the plate thickness and the material properties vary from plate to plate. The numerical model does not account for this uncertainties. In average, the accuracy of the numerical model is however good.

The eigenfrequencies of the same plates with clamped BC (as described in Section 2.5) are also used to validate the corresponding numerical model. The first bending frequencies are overestimated by the model because the plates have a slightly smaller thickness close to the clamping fixture compared to the average thickness (see Section 2.2.2). Figure 2.19 shows that in average the numerical model is a good representation of the plate and its clamping. The numerical model appears to be sufficiently accurate even with the assumption of a uniform thickness of the plate. The imperfection of the clamping fixture is well accounted for.

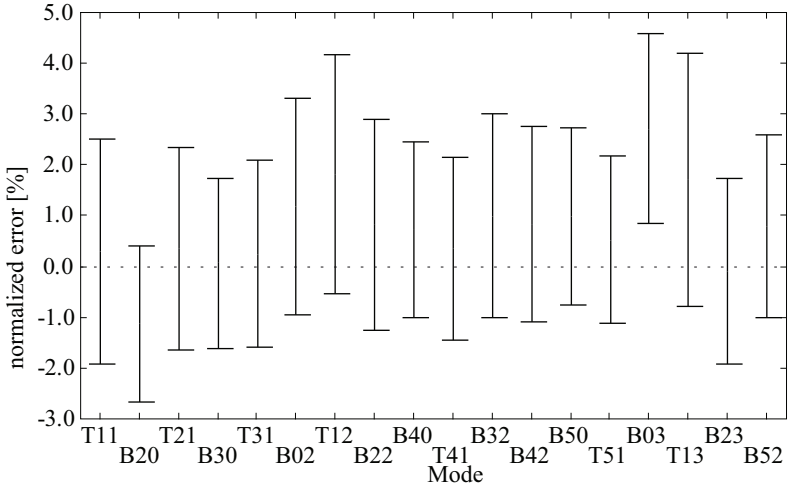

Figure 2.18: Normalised differences between the numerical eigenfrequencies of a plate with free BCs and the experimental data of a set of plates. Results are obtained using a mesh with $3 \times 40 \times 20$ elements.

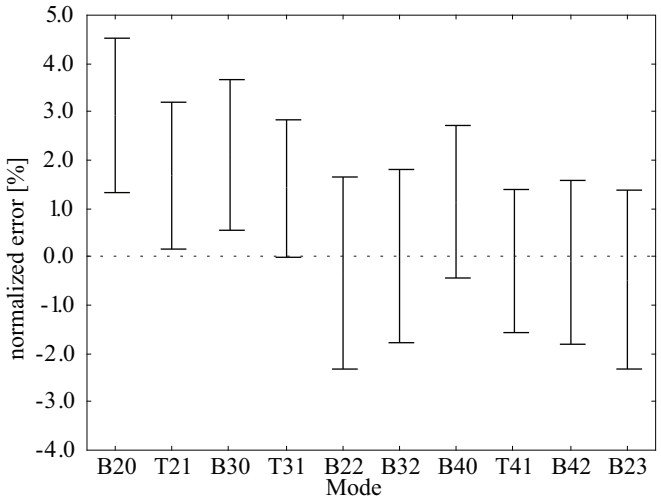

Figure 2.19: Normalised differences between the numerical eigenfrequencies of a plate with clamped BCs and the experimental data of a set of plates. Results are obtained using a mesh with $3 \times 40 \times 20$ elements.

2.6.2 Simulation of impact loading

Another FE model is created to simulate the dynamic response of a plate to a non-destructive impact. The objective of this model is to extract the local strain data and compare it to an experimental strain signal obtained by an FBG sensor. A non-destructive impact is chosen to reduce the modelling difficulties and uncertainties related to damage initiation and propagation and, hence, the accuracy of the numerical results.

Theoretical background

Such dynamic problems can be solved by explicit or implicit integration of the elastodynamic equations or via modal superposition. The modal superposition method is based on the assumption of linearity and therefore no contacts can be simulated. Explicit time-integration solvers are best suited for short time transient problems [106] involving high accelerations and large gradients of the displacement field.

In Abaqus/Explicit a lumped mass matrix is used and its inverse is easily computed to calculate the nodal acceleration field from force equilibrium at each iteration step. The equations of motion are then integrated using the explicit central difference integration rule. The nodal forces are finally computed from the displacement field and stiffness matrix.

The explicit integration procedure is conditionally stable. The integration time step needs to be sufficiently small — smaller than half of the period of the highest frequency of the model. This implies that the integration time step becomes shorter when the mesh is finer and the number of DOFs is higher.

The main dissipation model available in Abaqus/Explicit is Rayleigh damping. The damping matrix $\boldsymbol{D}$ is written as a linear combination of the mass and the stiffness matrix

$$\boldsymbol{D} = \alpha \boldsymbol{M} + \beta \boldsymbol{K} \tag{2.31}$$

The coefficients α and β have been adjusted empirically in such a way that the amplitude decay of the numerical transient response corresponds to the one of the experimental results. The values retained for α and β are 40 and $1{\cdot}10^{-7}$, respectively. Attention is paid to keep the coefficient β low. In fact, increasing the part of the damping proportional to the stiffness matrix diminishes the stable integration time step and unnecessarily increases the computation time. Indeed, the damping model is not in the scope of the present work and has a negligible influence on the amplitude of the strain signal during the first milliseconds of the transient response. When $\beta \boldsymbol{K}$ is small, the high frequencies will indeed be less damped than the low frequencies. In Abaqus/Explicit a bulk viscosity model is

implemented to suppress ringing of the elements at their highest frequency. This dissipation model strongly damps high frequency pressure modes in order to obtain more physically sound solutions.

Description of the model

The CFRP CP plate and part of the impactor are modelled in Abaqus FEA 6.8-2. The dimensions of the CP plate are identical to the ones considered for numerical modal analysis. Also the partitioning of the plate is the same and the width of the clamping surface is again reduced to 29 mm to account for the imperfections of the real clamping. Through-the-thickness homogenised material properties given in Table 2.2 are used. The steel part of the impactor is modelled and the mass of the remaining aluminium carriage is added as punctual mass coupled to the upper surface of the impactor tip. Due to the high stiffness of the carriage, it is supposed to be rigid. The impactor tip has a mass of 74 g and the carriage of 786 g.

Linear finite elements are used in Abaqus/Explicit and are denoted C3D8R. The plate is discretised using a regular mesh. The mesh should not be too fine to keep a reasonable integration time step. A minimum number of elements is nevertheless required in the through-the-thickness direction to have a faithful representation of the strain profile despite the usage of linear elements. A total of 6 elements through-the-thickness is found to be sufficient. The local refinement in the thickness of the plate is chosen in the way that the outer elements have a thickness of two composite plies. The strain can then be extracted from the central integration point which is at the same distance from the neutral plane of the plate than the FBG sensor. A refined mesh is used at the contact surface of the plate and the impactor. The mesh of the plate and the impactor tip are illustrated in Figure 2.20. The integration time step employed by the solver is 1 µs.

A linear contact law is inserted between the impactor tip and the plate. Compared

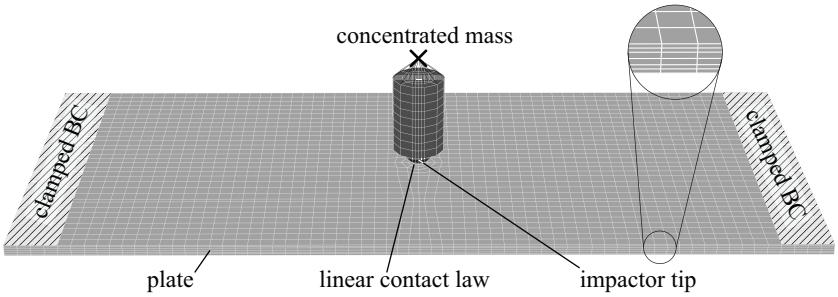

Figure 2.20: Geometry and mesh of the FE model used for impact simulation.

to a hard contact law, the convergence of the explicit solver is better and parasitic high frequencies are restrained during the contact formation. The stiffness constant is, besides the secondary damping parameters, the only parameter that remains to be adjusted to fit the model to the experimental results. The stiffness constant is chosen so that the numerical contact stiffness fits to the experimental one. With values between $1{\cdot}10^8$ and $1{\cdot}10^{12}$, a good agreement is obtained. It has to be noticed that the stiffness constant represents the stiffness of a virtual spring between a node of the master surface (impactor tip) and the slave surface (plate). Therefore, for a selected stiffness constant, the stiffness of the entire contact depends on the mesh and the number of nodes involved in the contact definition.

Initial conditions need to be specified before the dynamic equations can be solved. The drop height used in the experiment is 305 mm. The impactor tip is initially placed close to the plate with a initial velocity of 2.45 $^{\mathrm{m}}/_{\mathrm{s}}$.

Validation of the model

The experimental contact force is measured by a force transducer in the tip of the impactor. The amplitude, shape and duration of the numerical and experimental signals agree well. Both signals can be seen in Figure 2.21. The global stiffness of the FE model is verified by comparing the numerical resonance frequencies to the experimental ones. The acceleration spectrum of a node in the model is compared to the experimentally measured acceleration

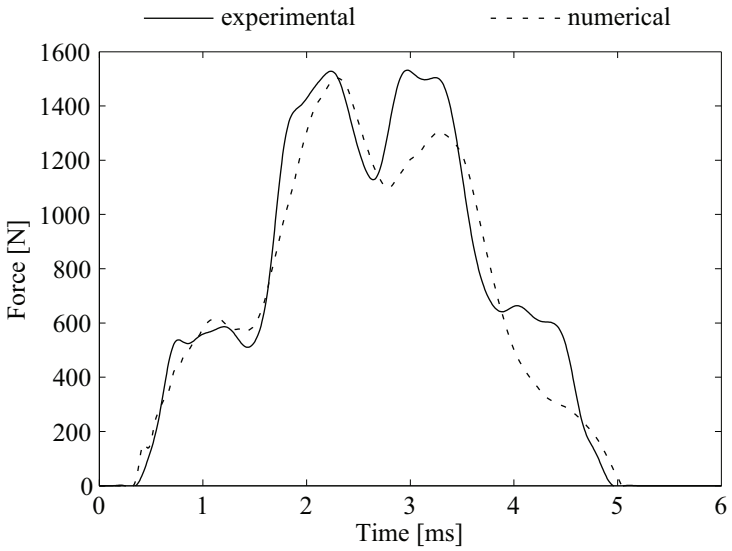

Figure 2.21: Comparison of numerical and experimental contact force.

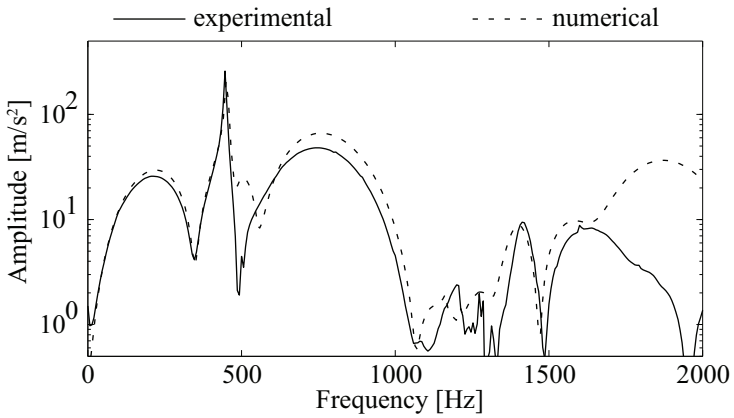

Figure 2.22: Comparison of numerical and experimental acceleration response spectra.

spectrum. The first modes that are excited by the central impact are the symmetric bending modes B20 ($\sim$ 450 Hz) and B22 ($\sim$ 1 300 Hz). The frequencies of the numerical and experimental signals are very similar. It is also noticed that the response amplitudes of the corresponding frequencies compare very well. The numerical and experimental response spectra are shown in Figure 2.22. Overall, a good agreement between the numerical and experimental results is obtained.

2.7 Summary

Within this chapter, various numerical and experimental methods as well as the corresponding results are presented. The composite material and plate are characterised and the elastic properties are determined. The working principle of FBG sensors is detailed and it has been found that the optical fibre is well integrated between the UD composite plies. The impact testing method is explained and preliminary results demonstrate the good reproducibility of the impact tests. A theoretical background of experimental modal analysis is given. The reproducibility of the eigenfrequency measurements of a composite plate is checked and a relative precision of 0.06 % can be attributed when the composite plate is not dismounted inbetween measurements.

Finally, two different numerical models are built and validated by experiments. The results of the FE model used for numerical modal analysis are shown to be in good agreement with the first 10 – 18 experimentally measured eigenfrequencies. The numerical simulation of a non-destructive impact is successfully validated by comparing numerical to experimental contact forces and acceleration signals.

Chapter 3

High rate FBG interrogation

3.1 Preface

One of the objectives of this work is to use embedded FBGs for monitoring the dynamic response of a plate. The performance specifications of the sensors and the interrogation method should allow the realisation of the following three tasks:

- Quantitative measurements of internal strains in a composite plate subjected to impact load
- Sensing acoustic waves with a high sampling rate and sensitivity
- Experimental modal analysis based on dynamic strain response measurements with a good signal-to-noise ratio

The FBG interrogation method used in this work is based on intensity modulation obtained via a Fabry-Pérot (FP) filter. From the intensity measurements either the Bragg wavelength shift or the axial strain is calculated. Remember that the wavelength shift $\Delta\lambda_B$ is related to the strain ε_1 by the linear relation (2.6). The equipment is based on a prototype from Micron Optics (model MO si920) [107]. The device is modified to enhance the quality of the acquired signals and to adapt it to the specific use. Hardware and software changes are implemented to allow for the previously enumerated requirements. Amongst numerous modifications, two different acquisition modes, which can be used simultaneously, are proposed. The first interrogation mode permits quantitative dynamic strain measurements at a rate of several 100 kHz. The second mode enables acquisition of qualitative intensity signals at a sampling rate of 1 GHz and is sensitive to low amplitude perturbations. Whereas the first acquisition mode allows to acquire calibrated strain

signals during impact events, the second allows to monitor acoustic waves.

3.2 Fast FBG interrogation method

3.2.1 Assumptions

The FBG interrogation method for calibrated strain measurements is based on a few assumptions. These assumptions have to be made because the entire Bragg reflection spectrum is not recorded and analysed during the measurements. The measurements are mainly based on the central wavelength of the Bragg reflection.

- The strain in the FBG has to be uni-axial and oriented in the longitudinal direction to the optical fibre. Transverse strains lead to an additional shift of the Bragg wavelength which cannot be distinguished from the shift arising from the longitudinal strain. Moreover, if the the strains in the two direction normal to the optical fibre are not the same, birefringence is induced. This assumption is verified in Section 3.3.1.
- The strain field along the grating has to be uniform so that the Bragg reflection spectrum is not distorted. In the case of non-uniform strains, the grating becomes chirped and the narrow reflection spectrum widens. This assumption is verified as long as the wavelength of the vibration mode is sufficiently long compared to the length of the Bragg grating. Therefore, short FBG sensors are employed.

These assumptions are only necessary in case of calibrated strain measurements. During the time when the signal is dominated by waves propagating through the gratings, the assumption of uniform strains may not apply. During this very short time, the interest relies on the fast qualitative measurements of the intensity signals.

3.2.2 Working principle

The interrogation is based on modulation of the Bragg wavelength shift into an intensity variation by using a tunable Fabry-Pérot (FP) filter. A FP filter is an optical interferometer with a cavity and two reflective surfaces and whose transmission spectrum has multiple peaks. The width of the peaks, defined by the fineness, is controlled by the reflectivity and planarity of the reflective surfaces. The distance between the peaks in the transmission spectrum, called free spectral range (FSR), is determined by the gap of the cavity. The spectrum range of interest is limited to the slope of a single transmission peak. Its wavelength has to be situated around 1 550 nm, the nominal wavelength of the FBG.

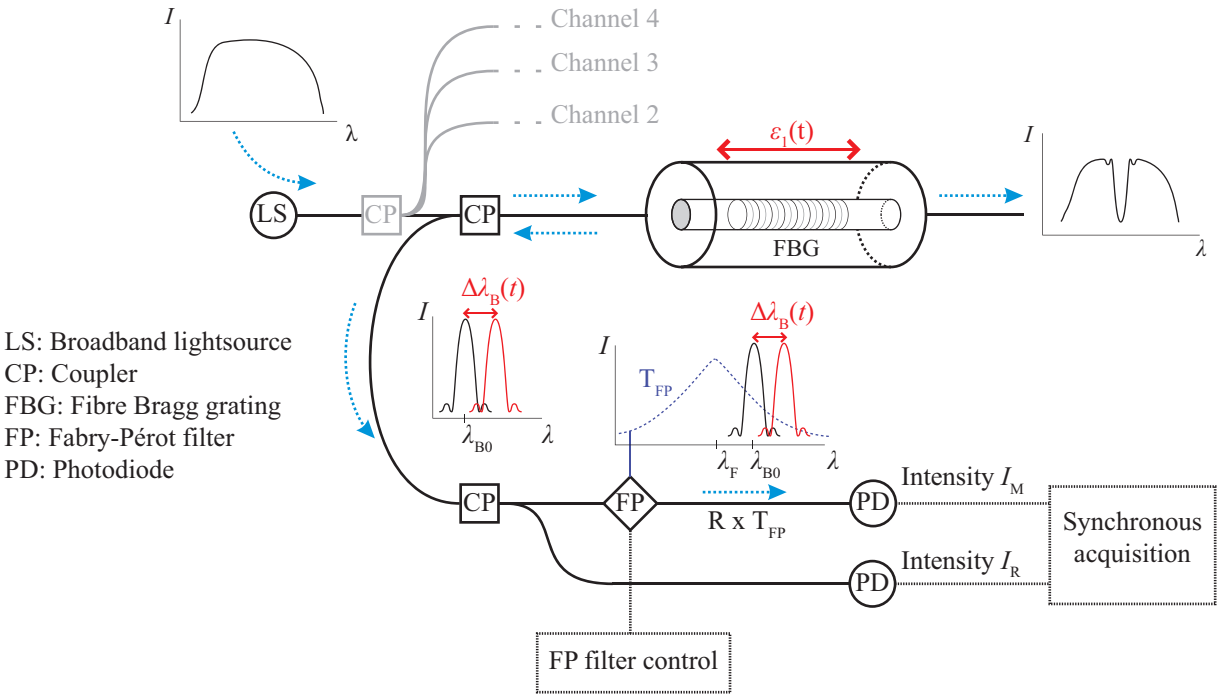

Figure 3.1: Schematic of interrogation principle.

The working principle of the interrogation method explained hereafter is demonstrated on the basis of a single optical channel allowing to interrogate one short FBG sensor. Broadband light is coupled into the FBG sensor. The voltage for the broadband light source is provided by a stabilised power supply in order to reduce light fluctuations to a maximum. The Bragg reflection peak, with a nominal wavelength λ_{B0}, is split by a coupler into a measuring arm and a reference arm. In the reference arm, the integral intensity I_R of the reflection peak is measured with a photodiode. In the measuring arm, the Bragg reflection is coupled through a FP filter with a very smooth filter edge. The filtered intensity I_M is also measured with a photodiode. The configuration is illustrated in Figure 3.1. This setup, with exception of the light source, has to be replicated for each additional optical channel. In this work, four optical channels are available.

The reference intensity I_R is measured to account for fluctuations of the light source and losses in the optical fibres. The intensity in the measuring arm is normalised by the reference intensity and the intensity ratio

$$\bar{I}(t) = \frac{I_M(t)}{I_R(t)} \tag{3.1}$$

is defined. When the wavelength of the Bragg reflection shifts by an amount $\Delta\lambda_B$, the intensity I_M in the measuring arm and hence the intensity ratio $\bar{I}$ vary. Due to the shape

of the FP filter edge and the shape of the Bragg reflection spectrum, the relation between the intensity ratio $\bar{I}$ and the Bragg wavelengths shift $\Delta\lambda_B$ is non-linear and cannot be expressed by means of a single proportionality factor. A calibration curve needs to be elaborated to convert the intensity ratio to a Bragg wavelengths shift or axial strain. The relation between axial strain ε_1, Bragg wavelengths shift $\Delta\lambda_B$ and intensity ratio $\bar{I}$ is shown in Figure 3.2 and typical data originating from a harmonic strain signal are illustrated.

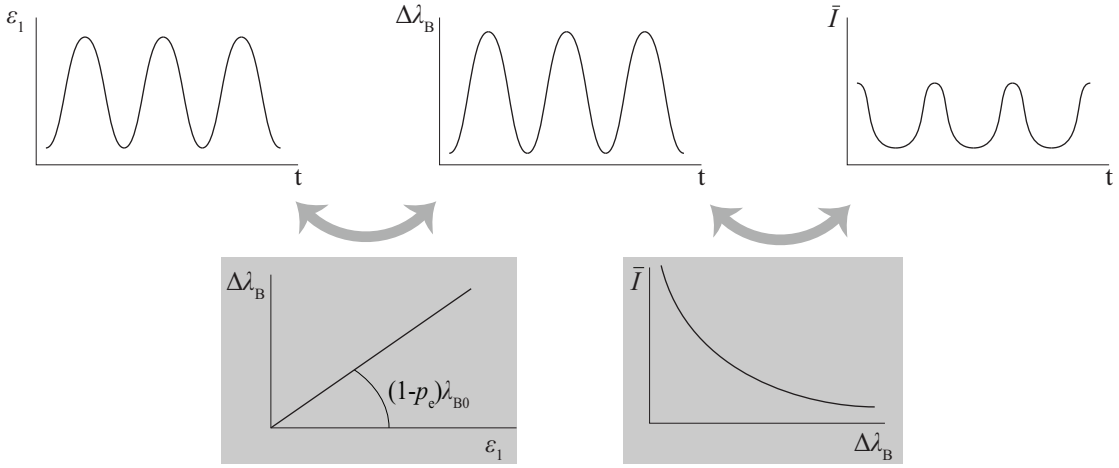

Figure 3.2: Typical signals involved in dynamic FGB interrogation.

The steeper the slope of the FP filter transmission spectrum, the more sensitive are the intensity variations to a wavelength shift. The width of the transmission peak is inversely related to the slope and defines the wavelength range of the measurement method.

3.2.3 Acquisition of data

The photodiodes from JDS Uniphase Corporation (Series EPM 705) used for the measurement of the intensities are highly responsive. A common amplifier from Linear Technology (LTC6241 Dual CMOS Op Amp) is used for the two photodiodes on the measuring and reference arm. In this way, the electric noise is almost the same in both reference and measuring intensity signals $I_R(t)$ and $I_M(t)$ and thus it is partially cancelled within the intensity ratio $\bar{I}(t)$.

Two different kinds of acquisition modes are used within this work. With the first acquisition mode, calibrated strain measurements can be performed at a rate of up to 250 kHz. The second acquisition mode allows to acquire only the variable part of the intensity signals with a sampling rate of 1 GHz per optical channel.

Calibrated strain measurements

The acquisition of the calibrated strain measurements is done using an acquisition card from United Electronic Industries (model PD2-MFS-8-2M/14). A maximum sampling rate of 2 Megasamples per second shared by eight analogue input channels is available. Remember that each optical channel requires two analogue input channels to sample the intensities of the measuring and reference arm. The data acquisition card allows a synchronous analogue-to-digital conversion using the hold and sample technique. The card has no built-in anti-aliasing filters so that the signals have to be digitised at a high rate. Thereafter they can be digitally low-pass filtered and decimated.

When an optical channel is active, the voltage of its two photodiodes is recorded simultaneously. The DC voltage is acquired with an asymmetric input range of 0 – 5 V. This range is optimised for the output of the photodiodes' amplifiers and consequently reduces the electrical noise to a minimum. The intensity ratio $\bar{I}$ is directly calculated as the ratio between both voltage signals. The axial strain data is finally calculated from the intensity ratio $\bar{I}$ using the data from the calibration described in Section 3.2.4. The scope of this acquisition mode is to get quantitative strain signals during dynamic loading.

Fast intensity measurements

A faster and more sensitive acquisition of the intensity signals can be made simultaneously to the calibrated strain measurements. The photodiodes' AC voltage is acquired using a small analogue input range of ±50 mV to maximise the sensitivity. The variable parts $\tilde{I}_{\mathrm{M}}$ and $\tilde{I}_{\mathrm{R}}$ of the intensity signal at the photodiodes of the measuring and reference arm are measured with a high sampling rate. The entire signal is not of interest and therefore it is unimportant if the signal is partially out of range. The analogue-to-digital conversion is performed with an oscilloscope (Lecroy Wavesurfer 434) at a rate of 1 GHz per channel.

Let us recall that the noise in the signals of the measuring and reference arm are similar because both photodiodes share a common amplifier. The amplitudes of the noise in the recorded AC signals are almost proportional to their DC voltage. In order to eliminate the noise in the intensity signal, the variable intensity signal is defined by the difference

$$\hat{I}(t) = \tilde{I}_{\mathrm{M}}(t) - \alpha_{\mathrm{I}} \tilde{I}_{\mathrm{R}}(t) \tag{3.2}$$

where α_{I} is the ratio between the DC voltages of the measuring and reference arm. It is not possible to calculate the strain data from the variable intensity signal $\hat{I}$ by means of a calibration. The scope of this acquisition method is to detect the arrival time of acoustic

waves at the sensors with high precision and to use this information for impact localisation as described in Chapter 4.

3.2.4 Calibration

A basic requirement to carry out quantitative strain measurements is an accurate and reliable calibration. The objective of this section is to establish a calibration curve between measured intensity ratio $\bar{I}$ and strain ε_1. The strain can thereafter be determined from the measured intensity ratio via interpolation of the calibration curve. For the calibration test, the tunable FP filter is set so that the Bragg reflection peak is initially in the middle of the slope of the FP filter transmission spectrum. The tuning of the FP filter is explained in Section 3.2.5.

The calibration curve is determined by a traction test on an unembedded FBG. In order to verify the calibration, it is carried out with respect to longitudinal strain ε_1 and Bragg wavelength shift $\Delta\lambda_\mathrm{B}$. Both calibration curves are thereafter compared. They should be similar up to a factor of $1.2\,{}^{\mathrm{pm}}/_{\mu\varepsilon}$ in accordance to the relation (2.6).

Materials and method

Throughout the present study FBG sensors with 3 mm gauge length are used. The gratings are written in SMF-28 optical fibres with polyimide coating that is removed along the FBG length and beyond by a few mm on each side. The described calibration is carried out for each of the four optical channels. The calibration data of an optical channel can thereafter be used for different gratings. The following specifications of the FBG, however, have to be met in order to guarantee for correct results:

- The nominal Bragg wavelength of the grating is around 1 550 nm.
- The reflectivity is at least 90 %.
- The bandwidth of the Bragg reflection peak is 500 pm. The bandwidth of the Bragg reflection must be smaller than half the FSR of the FP filter.

Using a specially prepared cardboard frame, the optical fibre is clamped with a span of $l_0 = 100\,\mathrm{mm}$ on an electro-mechanical traction test machine (Bose ElectroForce® 3200) that is equipped with a force transducer (maximum range of 220 N) and a linear variable differential transformer (LVDT) for displacement measurements (Figure 3.3). The fibre is prestressed with a force of 1 N and loaded with a sinusoidal force. Since the relation of the

intensity ratio to the wavelength shift is independent of the frequency of the signal, the test can be carried out at a low frequency of 0.5 Hz.

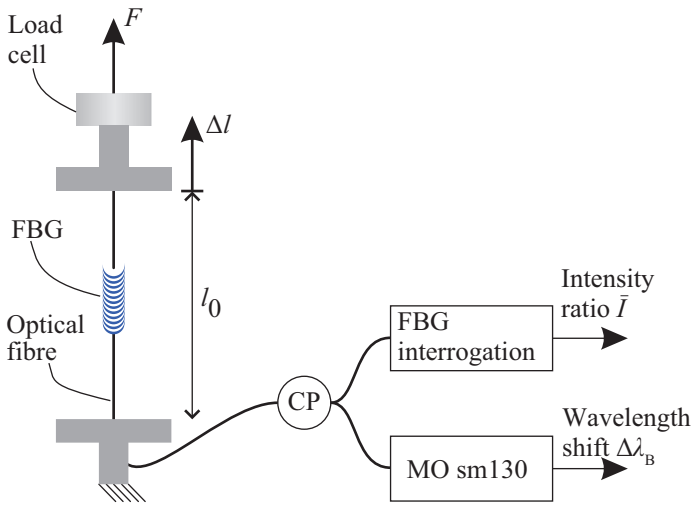

Figure 3.3: Experimental setup for the calibration of the FBG interrogation.

For each channel, a first calibration test is carried out where the excitation force F, the displacement Δl, and the intensity ratio $\bar{I}$ are measured. The signal are simultaneously acquired and plotted in Figure 3.4a. From the force-strain curve in Figure 3.4b it is possible to determine the apparent Young's modulus E of the optical fibre. It can then be compared to the Young's modulus of glass to check the force and displacement measurements. Supposing a cross-section diameter of the uncoated fibre of 125 µm, the apparent Young's modulus of the uncoated fibre is 71.3 GPa (typical modulus of fused silica glass is 72.4 GPa [108]) and thus, it confirms the accuracy of the measurements. Traction tests on polyimide coated fibres have shown a negligible increase of their apparent stiffness by 1.2 %. Eventual slipping of the fibre in the grips would be easily detected in the load-displacement curve but this can be excluded.

By plotting the strain signal as a function of the intensity ratio (Figure 3.5) it is shown that the calibration curve is reproduced reliably over multiple loading cycles. The calibration curve is finally decimated to 100 data points. This number of data points is a reasonable compromise between required computational power for signal treatment and accurate conversion of intensity ratio to strain when a spline interpolation function is used.

A second calibration test with a similar configuration is produced in order to verify the results of optical channels 3 and 4. Simultaneously to the intensity ratio measurement, the Bragg wavelength shift $\Delta\lambda_B$ is measured with a low rate FBG interrogator from Micron Optics (model sm130) during the sinusoidal traction of the FBG. The acquired signals are

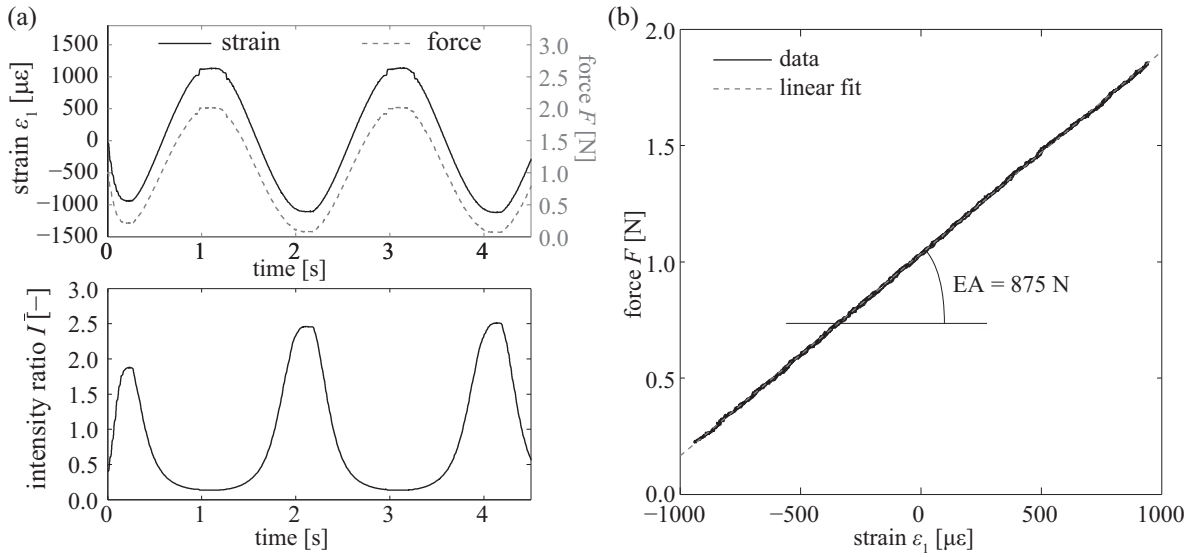

Figure 3.4: (a) Strain, force and intensity ratio acquired during the calibration test (b) Force-strain curve.

shown in Figure 3.6.[1] The intensity ratio $\bar{I}$ saturates during this test at a value of 2. This happens when the Bragg wavelengths λ_B approaches the central frequency λ_F of the FP filter. It can be noticed that the intensity ratio is more sensitive to a wavelength shift when the intensity ratio is high. In this case the variation of the intensity ratio is high compared to the variation of the wavelength (cf. Figure 3.5).

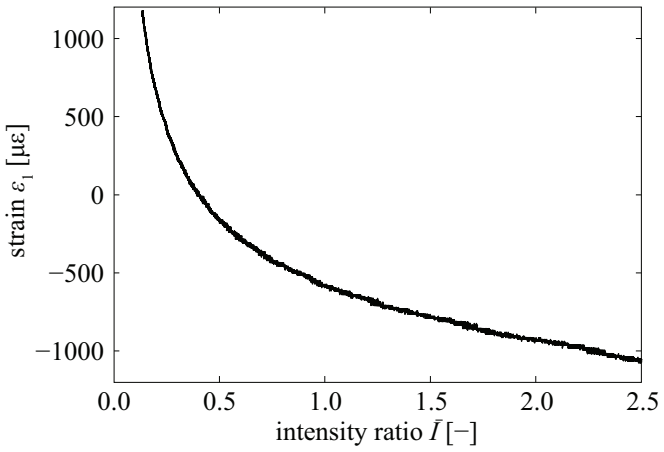

Figure 3.5: Relation between strain and intensity ratio (optical channel 3) signals.

[1]Note here that in the present case the coupler, splitting the reflection peak into the measuring and reference arms, is not a 50:50 coupler but a 67:33 coupler. Therefore, the intensity ratio equals 2 when the Bragg reflection peak is aligned with the maximum transmission peak of the FP filter.

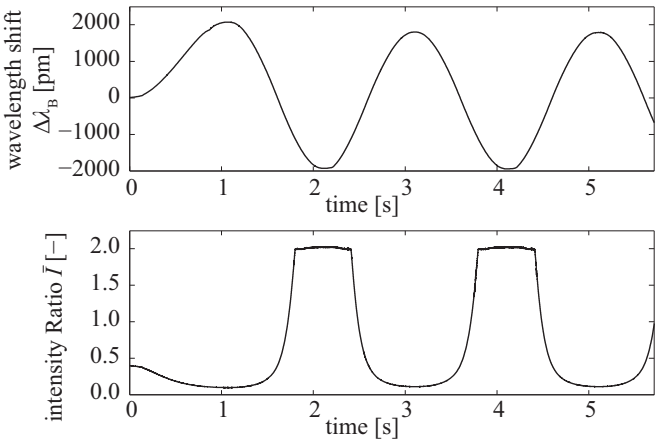

Figure 3.6: Intensity ratio and Bragg wavelength shift acquired during the calibration test of optical channel 3.

The calibration curves of the four optical channels are displayed in Figure 3.7. Figure 3.7b shows the two superimposed calibration curves of channel 3 and 4 determined throughout two independent calibration tests. It is demonstrated that the shape of the calibration curves is well reproduced and the ratio between strain amplitude and wavelength shift corresponds to the expected value of $1.2\,^{\mathrm{pm}}/_{\mu\varepsilon}$. It can be noticed that the calibration curve of channel 4 is oriented in a different way than the others. Here, the Bragg reflection peak is located on the other side of the FP filter's transmission spectrum (to the right side in Figure 3.8).

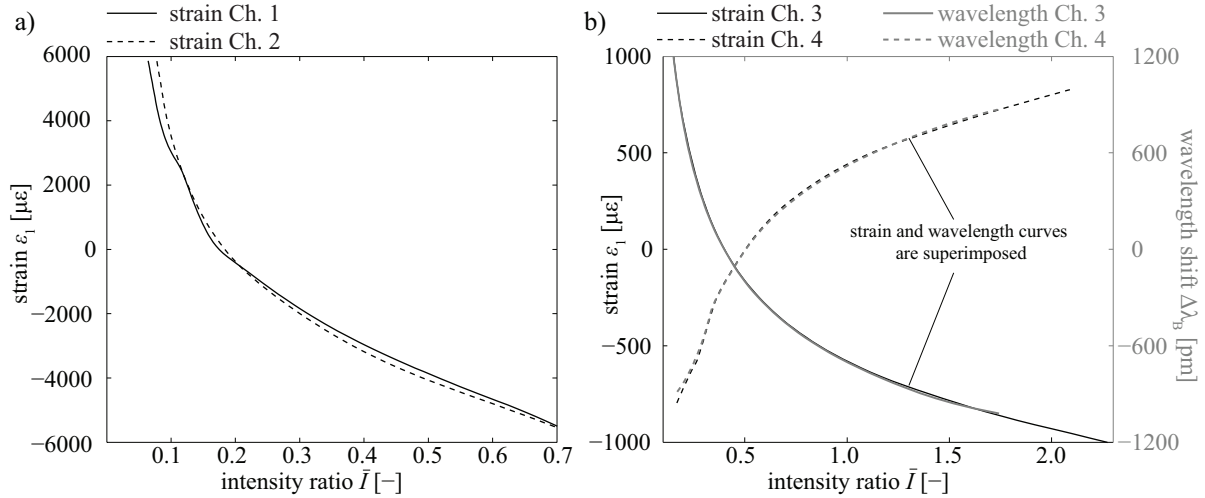

Figure 3.7: (a) Calibration curves as a function of strain of channels 1 and 2 (b) Calibration curves as a function of strain and Bragg wavelength shift of channels 3 and 4.

3.2.5 Fabry-Pérot filter tuning

The objective of the FP filter tuning is to adjust the central frequency of the FP filter prior to a measurement so that the Bragg reflection peak is situated on a smooth edge of the FP filter's transmission spectrum. The wavelength λ_F of the FP filter is biased to the nominal Bragg wavelength λ_{B0}, which has to be around 1 550 nm (Figure 3.8). The objective of the filter tuning is to obtain a predefined target intensity ratio

$$\bar{I}_0 = \frac{\int_{t_1}^{t_2} I_M(t)dt}{\int_{t_1}^{t_2} I_R(t)dt} \tag{3.3}$$

where $[t_1, t_2]$ is a short time interval. The tuning permits the compatibility of the FP filter to distinct FBG sensors. It also acts as a filter for very low frequency shifts of the Bragg wavelength due to temperature changes or static loads.

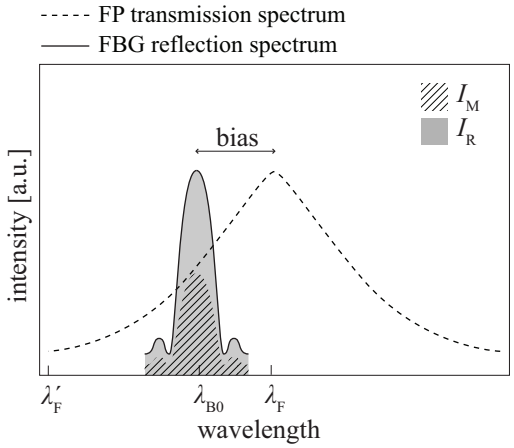

Figure 3.8: Illustration of the bias between the FP filter transmission spectrum and the Bragg reflection peak.

The Bragg reflection peak must stay on the slope of the FP transmission spectrum when the Bragg wavelength is shifting during the measurements. The Bragg reflection peak must not cross the central wavelength λ_F of the FP filter. When the Bragg reflection peak shifts towards a wavelength λ'_F at the valley of the transmission spectrum, the sensitivity tends to zero. Both wavelengths λ_F and λ'_F define the wavelength range that can be covered by the Bragg wavelength λ_B during a measurement. In this work, two FP filters with a usable range of approximately 12 000 pm and two with a range of 2 400 pm are employed. They correspond to strain ranges of 10 000 µε and 2 000 µε, as seen on the calibration curves in Figure 3.7.

The target intensity ratio $\bar{I}_0$ to which the FP filter is tuned determines where the initial Bragg wavelength λ_{B0} is situated between λ_F and λ'_F. The user can thereby chose if he wants a symmetric strain range or a range that allows to measure more compression or traction strains. When the measurements should be optimised for high sensitivity, the central FP wavelength λ_F should initially be set close to the nominal Bragg wavelength λ_{B0}. A high target intensity ratio is used in this case.

By default, the software uses a target ratio $\bar{I}_0^d$ such that the strain range will be symmetric. In case of the optical channel 3 for example, the default target intensity ratio $\bar{I}_0^d$ is equal to 0.4. Within the user interface, the operator can easily influence these settings by directly indicating the null position of the strain range. By choosing for example a strain offset ε_0 of -750 µε, a target intensity ratio $\bar{I}_0$ of 1.4 is determined by means of the calibration curve as indicated in Figure 3.9. The resulting strain range in this case would then be $[-250\,\mu\varepsilon;+1\,750\,\mu\varepsilon]$. In this example, the sensitivity of the interrogation channel is enhanced.

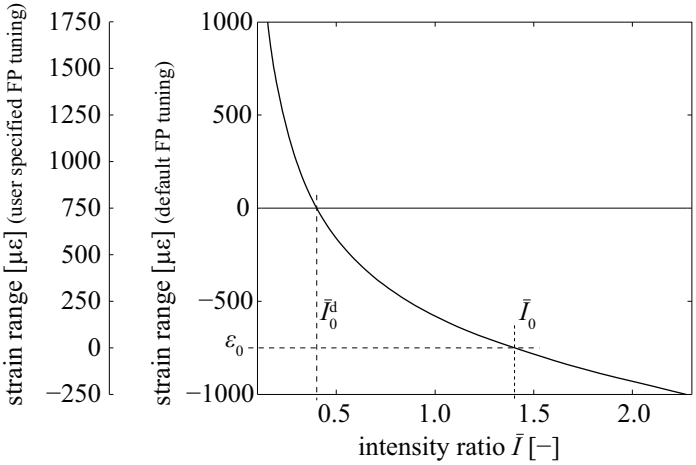

Figure 3.9: Illustration of the influence of the target intensity ratio on the strain range based on the calibration curve of channel 3.

The wavelength of the FP filter is tuned using a PZT actuator. The DC drive voltage U is supplied by a data acquisition card with four 16 bits analogue outputs with an output range of $[-10\,V;+10\,V]$ (NI PCI-6229). An electric resistance limits the current to 5 mA to protect the electrical circuit of the acquisition card. The drive voltage of the filter is controlled in a closed loop on user-demand. When the actual drive voltage U_i is changed, the voltage on the PZT actuator increases with small retardation due to the capacitor effect of the PZT. This hysteresis behaviour is accounted for by reducing the control speed adequately.

During the execution of the control loop, intensity measurements have to be done at

each iteration in order to calculate the actual mean intensity ratio $\bar{I}_i$. Therefore, a few hundred samples are acquired on the reference and measuring arm and their average is taken. The actual intensity ratio $\bar{I}_i$ is then compared to the target intensity ratio $\bar{I}_0$. The tolerance is set to a value of $2{\cdot}10^{-4}$ for the high range channels and $4{\cdot}10^{-4}$ for the low range channels. If the tolerance criterion is not met, a voltage increment ΔU_i is estimated and the DC drive voltage for the FP filter is updated. Figure 3.10 illustrates the implementation of the control loop. After completed tuning, the FP filter can be locked or the tuning can persist continuously during subsequent acquisitions. A constant voltage is applied to the PZT actuator when the FP filter is locked, but the filter may drift off after a while. It is nevertheless stable during a time of about 60 s.

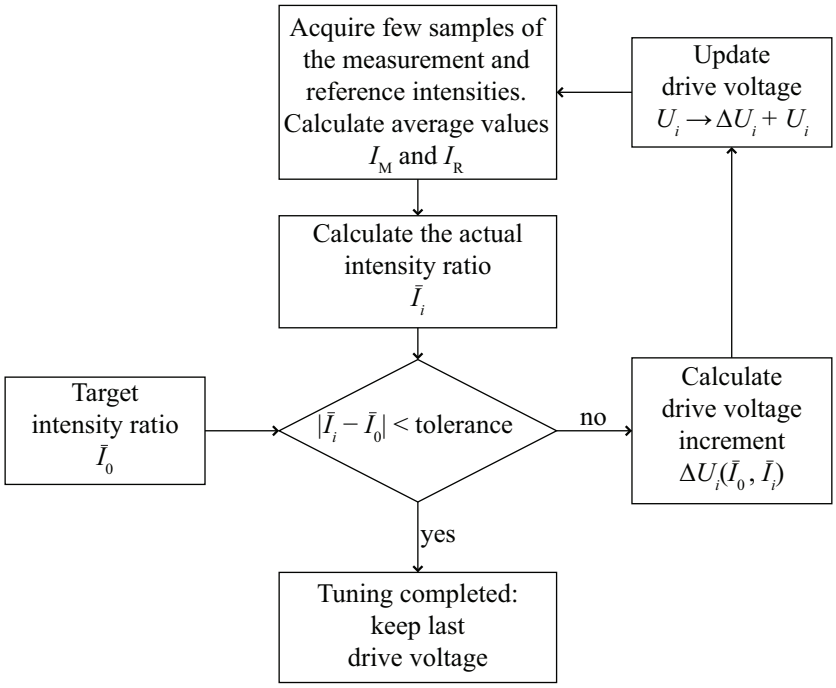

Figure 3.10: Block diagram of the control loop for the FP filter.

The tuning of the filter by a proportional controller is difficult because the relation between drive voltage U and resulting intensity ratio $\bar{I}$ is strongly non-linear. The optimal voltage increment ΔU_i cannot be estimated easily by a multiple of the error $\left(\bar{I}_0 - \bar{I}_i\right)$ between the target and actual intensity ratios. An example of a response curve of the intensity ratio as a function of drive voltage is given in Figure 3.11. The shape of this curve is always identical for a given FP filter, as long as the Bragg reflection spectrum of the used FBG sensor has a bandwidth of about 0.5 nm. The curve is simply offset by a constant voltage when the nominal Bragg wavelength λ_{B0} of the FBG is different.

In order to account for the non-linearity between the drive voltage U and the intensity

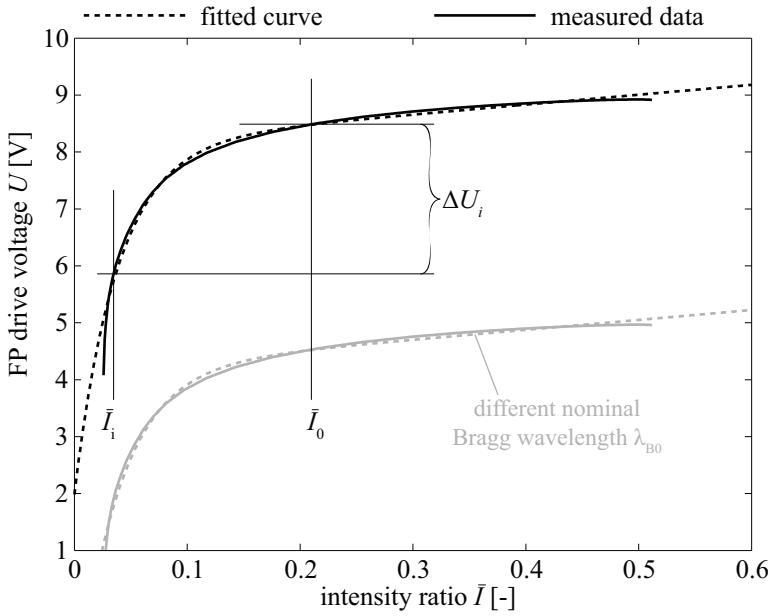

Figure 3.11: Non-linear response curve of intensity ratio to FP drive voltage.

ratio $\bar{I}$, an analytical curve is adjusted to the measured data. An empirical formula based on three parameters γ_1, γ_2 and γ_3 and an irrelevant constant fits the curve well

$$U = \gamma_1 \mathrm{e}^{-\gamma_2 \bar{I}} + \gamma_3 \bar{I} + \mathrm{cst} \tag{3.4}$$

Such a fitted curve is also displayed in Figure 3.11. The parameters identified by least square optimisation are listed in Table 3.1. It can be noticed that the response curve of the Fabry-Pérot filter 4 is oriented in the opposite way than the others. This is again due to the fact that the Bragg reflection peak is located on the other side of the Fabry-Pérot's transmission spectrum (to the right side in Figure 3.8).

	γ_1 [V^{-1}]	γ_2 [-]	γ_3 [V^{-1}]
FP filter 1	6.154	26.30	1.736
FP filter 2	4.690	18.69	1.742
FP filter 3	7.142	20.28	1.295
FP filter 4	-5.063	13.8	-0.812

Table 3.1: Parameters identified for the model of the FP filter drive voltage.

A voltage increment ΔU_i is now calculated from this analytical formula. In order to avoid an overshoot of the control, the voltage increment is estimated to be a fraction of

the theoretical voltage difference.

$$\Delta U_i = 0.2\,(U_0 - U_i) = 0.2\left[\gamma_1\left(e^{-\gamma_2 \bar{I}_0} - e^{-\gamma_2 \bar{I}_i}\right) + \gamma_3\left(\bar{I}_0 - \bar{I}_i\right)\right] \tag{3.5}$$

The updated drive voltage $U_{i+1} = U_i + \Delta U_i$ is forced to stay within a range of $[-2\,\mathrm{V};+10\,\mathrm{V}]$. The upper limit of 10 V corresponds to the maximum voltage supplied by the analogue output pin of the card. The lower limit protects the PZT actuator from sustaining damage. The control based on this calculation allows a fast, robust and precise tuning of the FP filter.

3.2.6 User interface

The parameters for the acquisition and the FP filter tuning are user-selectable via a LabVIEW 8.6 virtual interface (VI) to enhance the versatility of the device. The acquisition rate, the number of active channels and the analogue input range of the data acquisition card can be specified by the user. The user can also influence the settings of the FP filter tuning. Depending on the operation purpose, he can opt for maximising the measurement range or maximising the sensitivity.

Instead of choosing the initial intensity ratio to calibrate the FP filter, the user indicates the offset ε_0 of the null strain position. A symmetric strain range is obtained with a zero strain offset ε_0 or the range can be shifted to more compressive or tension strain. The effective range can however diminish because the analogue input channel of the measuring arm saturates. Let's consider the optical channel 3 for example. The calibration curve is defined over a strain range of $2\,000\,\mu\varepsilon$ and the corresponding intensity ratio may vary between 0.1 and 2.2 (cf. Figure 3.9). When the reference voltage is higher than 2.3 V and the intensity ratio tends towards a value of 2.2, this means that the voltage on the measuring arm exceeds 5.0 V. This is however the upper limit of the default analogue input range. The software accounts for this event and indicates the remaining measurement range. An interface also allows to monitor the average intensity of the reference arm while setting up the FBG sensors on the interrogation channels. An attenuator may be needed to regulate the total reflected light in order to avoid saturation of the photodiodes.

The acquisition, the data treatment and the FP filter control are performed by individual LabVIEW routines. Triggered and continuous acquisitions are feasible. In this work, the acquisition is in general triggered by an external signal to synchronise it with a dynamic event. The continuous acquisition is not explained in detail because its working principle is similar to the one of the triggered acquisition mode except that the acquisition start does not wait for a trigger signal and the data is not stored.

Triggered acquisition

When the user initiates a triggered acquisition, the following operations are executed:

- The user confirms the summary of settings or changes them if desired.
- The user chooses if the FP filters are tuned anew or locked to the actual drive voltage.
- The FP filters are tuned if this operation is selected by the user. The target intensity ratio for each FP filter is deduced from the strain offset ε_0 provided by the user via the calibration curves.
- When the FP filters are ready, the user is informed and the acquisition card waits for an external trigger signal.
- Immediately after the trigger signal is given, the required number of samples are acquired on the measuring and reference arm.
- The intensity ratio signal is converted to a strain signal by means of the calibration curve.
- The data is saved to a file and folder selected by the user. Finally the data of each active channel are plotted.

The sequence of operations is shown in a block diagram in Figure 3.12.

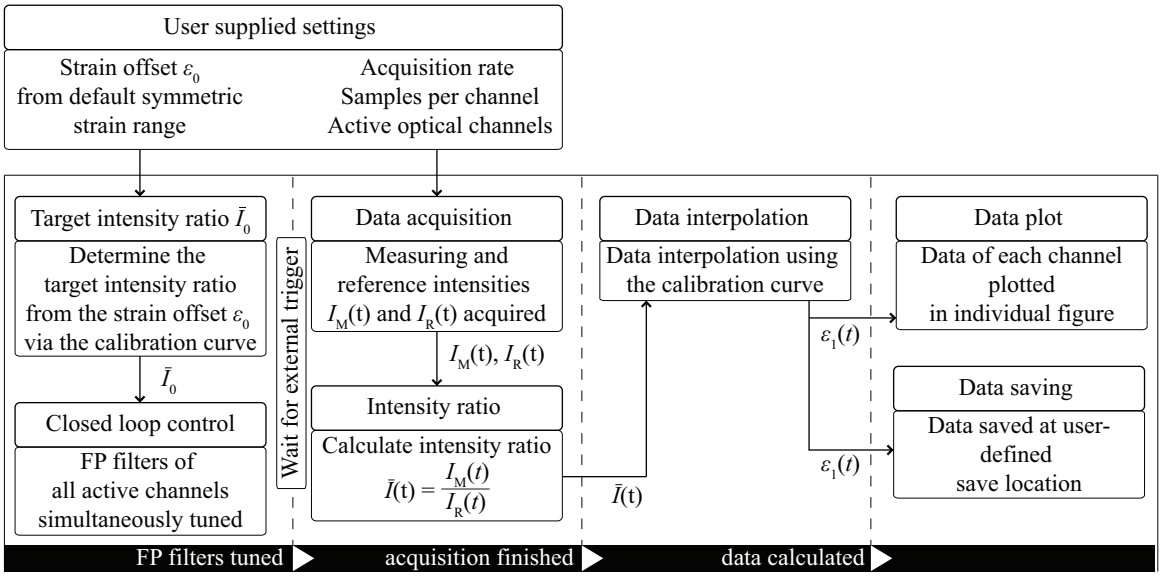

Figure 3.12: Sequence of operations during a triggered acquisition.

Note

The fast intensity acquisition method is not yet controllable via the LabVIEW interface because this acquisition is performed by an external oscilloscope. When this interrogation method is used, the FP filter tuning is controlled by the LabVIEW software and the acquisition of the AC intensity signals is performed independently by the oscilloscope.

3.3 Validation of the FBG interrogation method

The calibrated acquisition mode is used to monitor the strain responses of CFRP CP plates to low-velocity impacts. For validation purpose, the amplitude of a strain signal acquired during a non-destructive impact is compared to numerical results. Furthermore, strain signals from impacts with varying energies and destructive impacts are also presented. The calibrated acquisition mode is also used to carry out experimental modal analysis. In order to validate the use of FBG sensors for experimental modal analysis, the signal-to-noise ratio is analysed, the repeatability of the measurements is tested and the results are compared to experimental results obtained from velocity measurements.

The fast intensity acquisition mode can be used simultaneously to the calibrated strain measurement. It is used to detect the arrival time of acoustic waves originating from an impact and is validated in Chapter 4.

3.3.1 Strain measurement during non-destructive impact

Experimental method

A CP plate with a symmetric stacking sequence and a resulting thickness of 4.2 mm is produced as described in Section 2.2.2. An optical fibre is embedded between the ultimate and penultimate ply parallel to the direction of the reinforcing fibres. The plate is cured in autoclave and cut to dimensions of 300 mm × 140 mm. The optical fibre is located at a distance of 40 mm from the plate's free edge and at 1.95 mm from the neutral plane of the plate (Figure 3.13). The longitudinal position of the FBG along the optical fibre is equidistant between the two clamping fixtures and is verified using optical low coherence reflectometry measurements. It is found to be 124 mm from one side and 116 mm from the other side of the clamping fixture.

The composite plate is clamped on the base of the impact tower and oriented in the

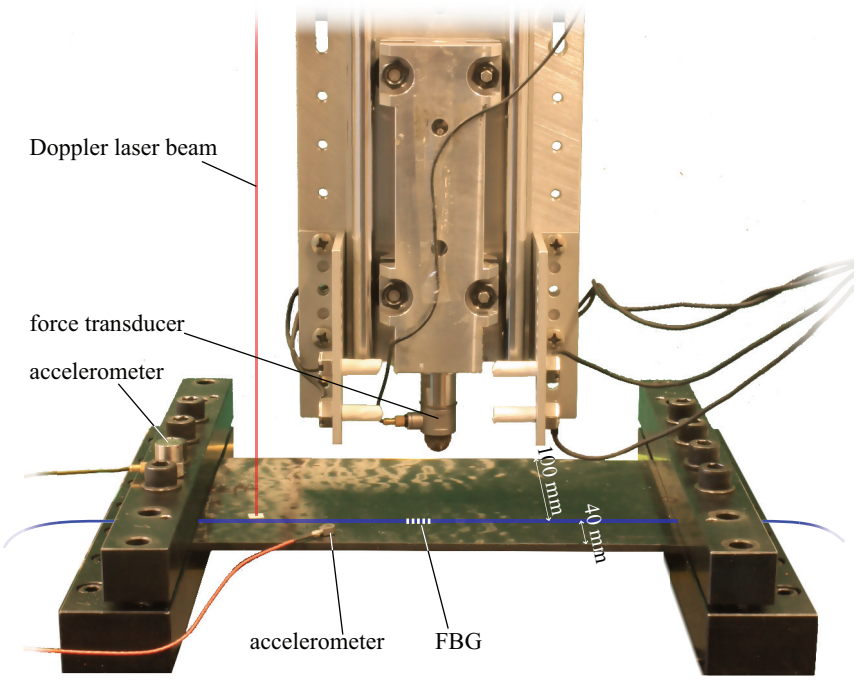

Figure 3.13: Photo of experimental setup for impact test.

way that the optical fibre is in the longitudinal direction at the opposite side of the impact point. The drop weight is 860 g and its tip is equipped with a piezoelectric force transducer (B&K type 8230-003) in order to monitor the impact force. The response of the plate is measured with an accelerometer and a laser Doppler vibrometer head from Polytec (OFV 303) capable of measuring a single point velocity response. Light barriers are mounted on the guiding rails in order to trigger the acquisition device and measure the incident velocity of the drop weight. The acquisition of the force, velocity and acceleration signals is carried out using an NI 4474 DSA card.

A low energy, quasi non-destructive impact test is performed. The composite plate is impacted at its central location with an energy of 2.6 J. The FBG strain response is acquired at a rate of 100 kHz using the calibrated interrogation method. In order to validate the numerical model, the contact force signal and the acceleration spectrum of the plate are measured.

Numerical method

The FE model of the plate presented and validated in Section 2.6.2 is used to calculate the transient response of the plate. The plate is modelled using through-the-thickness

homogenised material properties and linear brick elements. The dynamic equations are solved using Abaqus/Explicit. For an improved representation of the strain distribution along the plate thickness but still a reasonable time increment of the solver, 6 elements are used to mesh the plate thickness (Figure 3.14). A non-uniform thickness of the elements is chosen in the way that the outer elements have a thickness of two composite plies. The strain can then be extracted from the central integration point, which is at the same distance from the neutral plane of the plate than the FBG sensor. The steel tip of the impact weight is modelled using solid elements and a mass representing the impact carriage, considered as a rigid body, is added on the upper surface of the steel tip.

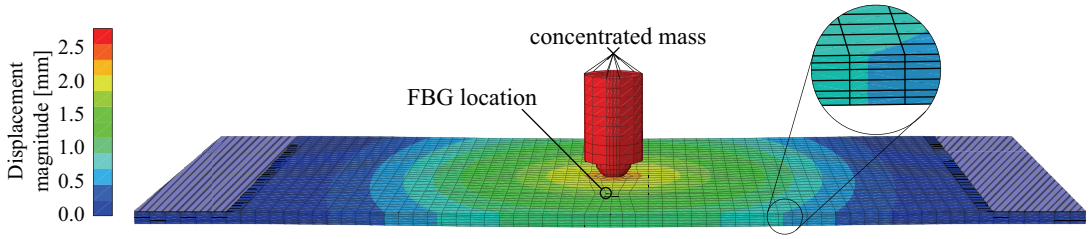

Figure 3.14: Impact simulation using Abaqus/Explicit.

For the validation of the FBG data, only the longitudinal strains are considered and the transverse strains are neglected. To validate this assumption the plate is submitted to bending and the amount of transverse strains transferred to the FBG is checked in a refined sub-model. In this model, a 20 mm × 20 mm rectangular part of the plate is meshed ply-by-ply and UD material properties are considered in the appropriate stacking orientation. This part of the plate is submitted to a bending moment in the x_1 direction. The strain component ε_2 perpendicular to the optical fibre is plotted in Figure 3.15. The data show that the transverse strain felt by the optical fibre is 6 times smaller than the surrounding transverse strain, attributed to a transverse bending or a transverse traction. This means that longitudinal strains dominate in the optical fibre and that birefringence and hence splitting of the Bragg reflection peak is not expected when the FBG sensor is embedded parallel to the surrounding UD plies.

Results

Figure 3.16 demonstrates the good agreement between the FBG strain response and the numerical strain results obtained from an integration point at the location of the FBG. The good resolution and accuracy in amplitude allows to capture the maximum local deformation during the impact. As it could be observed on the spectra of the signals in Figure 3.16, the transient response after impact is a superposition of the first and third

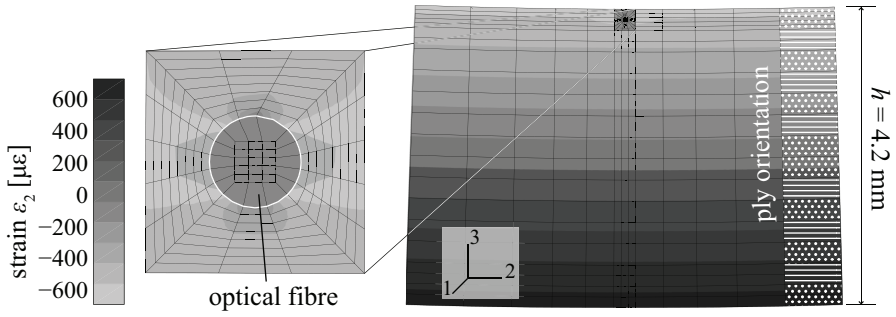

Figure 3.15: Strain component ε_2 around the optical fibre in a partial cross-section of the plate. The plate is submitted to bending in the x_1 direction.

longitudinal bending modes, which can be identified on both experimental and numerical results. It is demonstrated that FBG sensors can be employed to monitor local strain signals during an impact event.

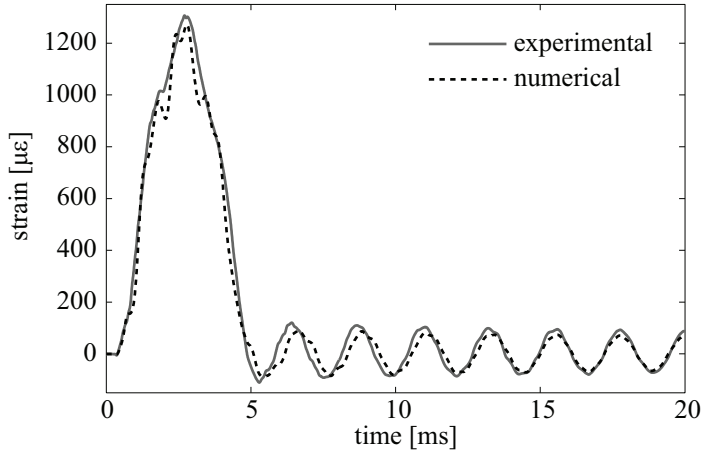

Figure 3.16: Comparison between numerical and experimental strain signal.

3.3.2 Strain signals as a function of impact energy

In order to study the evaluation of the strain impulse with increasing incident impact energy, the previously described plate is consecutively impacted with energies varying from 0.46 J to 3.00 J with increasing steps of 422 mJ. The dynamic strain responses are measured during the impact tests and are shown in Figure 3.17a.

It is noticed that the maximum strain amplitude varies proportionally to the square root of the impact energy (Figure 3.17b). Such a relation is expected when the impact of a

mass on a plate is studied as a single degree of freedom oscillator. The impact duration is, however, not constant but decreases with increasing impact energies. This may be due to a stiffening of the plate with increasing deflection because of non-linear geometry effects.

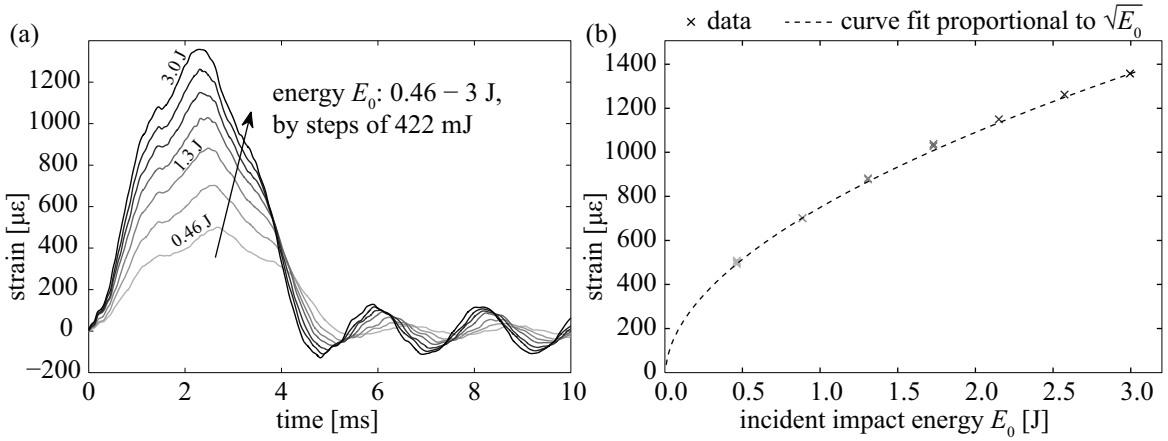

Figure 3.17: (a) Strain signals as a function of incident impact energy (b) Maximum strain as a function of incident impact energy.

Such a strain impulse gives evidence about the appearance of an impact event, which is characterised by a high contact force of short duration. It is proposed to trigger the acquisition procedure after the appearance of a dynamic strain impulse that exceeds a certain threshold value. A high-pass filter should be used to eliminate the strain response to quasi static loads or in-service vibrations. The measured strain amplitudes naturally depend on the impact energy, but also on the impact and measurement positions, the laminate itself and the boundary conditions. Such a criterion may be very conservative because it only triggers the acquisition procedure. In Chapter 5, computed tomography images show that delamination damage already occurs during transverse impacts with an energy of 1.7 J and a maximum contact force beyond 1 000 N. For the present plate, a threshold value of 200 $\mu\varepsilon$ is proposed. If no experiments can be made to estimate the strain criterion, a numerical FE model, as described in Section 2.6.2, may be employed.

3.3.3 Strain measurement during destructive impact

Finally FBG sensors are used to monitor dynamic strains during an impact with sufficiently high energy to create considerable damage. A distinct plate with two embedded FBG sensors is impacted at its centre with an incident kinetic energy of 6.8 J (the same configuration as shown in Figure 3.19 is used). It is shown by micrographic images that multiple delamination cracks occur at this energy (cf. Chapter 5). During the impact, the

FBG strain response is acquired at a rate of 100 kHz without filtering and during a time of 2 seconds.

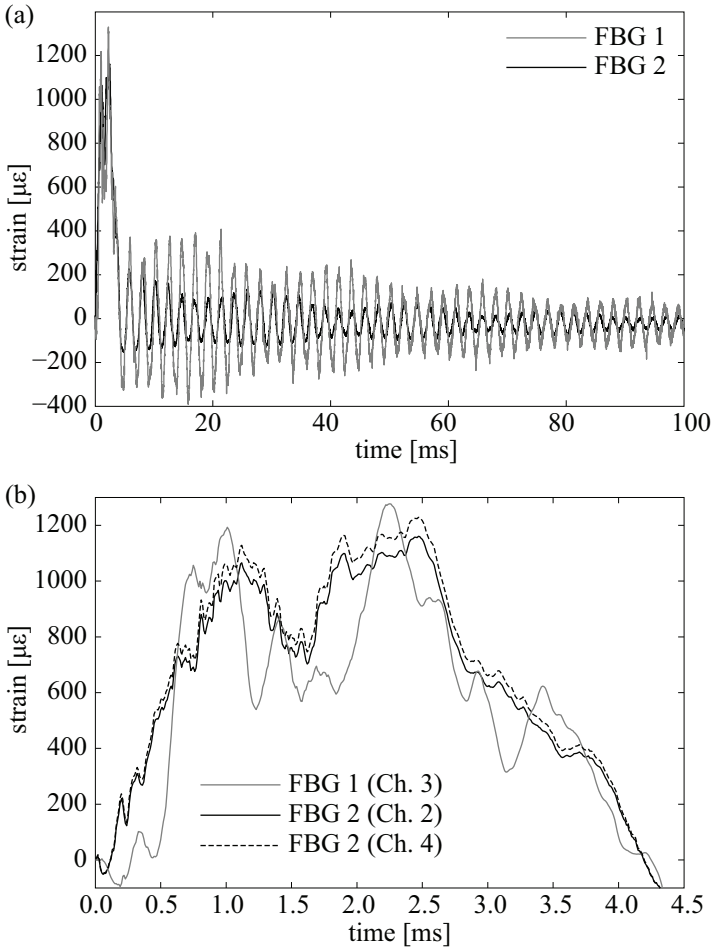

Figure 3.18: (a) Strain signals during destructive impact (b) First 4.5 ms of the strain signal.

The transient strain response (Figure 3.18a) of the plate can be accurately and entirely monitored and an excellent spectral resolution of the plate response is obtained. The signal recorded during this experiment again confirms the good signal-to-noise ratio of the strain measurements. The beating in the harmonic strain response is due to a superposition of the first bending and first torsion modes whose eigenfrequencies are close. Because of the high acquisition rate, the short-time deformation at the location of the FBG can be accurately captured during the impact and the high spectral content of the strain response is reliably represented (Figure 3.18b). The fluctuation of the signal of FBG 2, which is closest to the impact point, is attributed to waves issued during damage formation and crack propagation. The amplitude of this fluctuation is considerably higher than the noise

level of 2 µε observed on this interrogation channel.

The preceding calibration allows to have a quantitative measurement of the local strain amplitudes reached during the impact. An impact duration of 4.5 ms and a maximum deformation of 1 200 µε at the locations of the two FBG sensors can be observed in Figure 3.18b. The signal of FBG 2 is simultaneously interrogated with two different optical channels (Channel 2 and 4). It is expected from these measurements that the signals interrogated with two distinct optical channels having a different strain range (10 000 µε and 2 000 µε, respectively) are the same. The shape of the signals is indeed the same and the amplitude only differs by less than 5 %. The accurate calibration carried out prior to this experiment makes the knowledge of the strains a valuable and appropriate indicator for the evaluation of the impact severity.

3.3.4 Experimental modal analysis using FBG sensors

Two FBG sensors are used to carry out a multi-reference experimental modal analysis using hammer excitation. When the FP filter is biased towards high intensity ratios, accurate and sensitive strain measurements of low amplitude signals can be done. The signals are analysed and the measured eigenfrequencies are compared to results obtained by laser vibrometer measurements. Remember that the displacement resonance frequencies and the velocity resonance frequencies are almost the same in case of very small damping.

Experimental method

A CP plate with dimensions of 300 mm × 140 mm is clamped on the two short sides. Two FBG sensors are embedded between the ultimate and penultimate ply in the direction of the reinforcing fibres at locations optimized to be sensitive to the first vibration modes (Figure 3.19). The plate is dynamically excited by a hammer on a grid of 15 points. The FBG sensors are interrogated at a rate of 100 kHz and are decimated to a rate of 10 kHz after appropriate digital low-pass filtering.

Results

Figure 3.20 shows the strain response of the two FBG sensors to a hammer excitation on one of the points. By analysing these signals in detail as well as the signal obtained from an unloaded FBG sensor, a low noise level of only 2 µε can be observed. A dynamic range

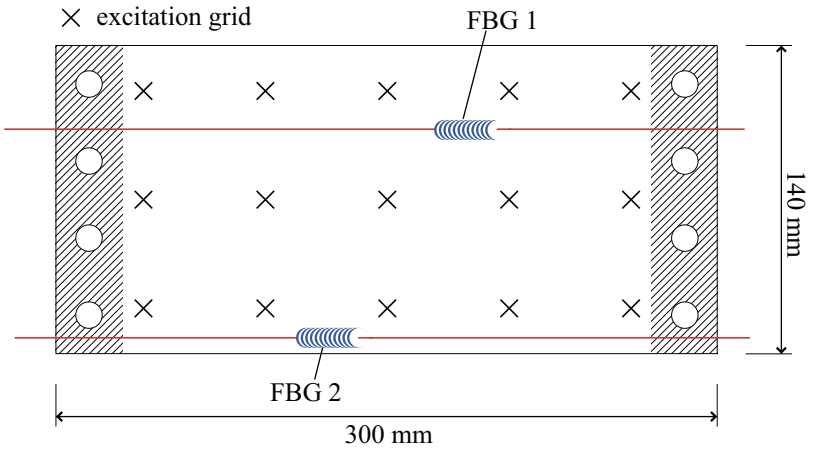

Figure 3.19: Schematic of plate with two embedded FBG sensors prepared for experimental modal analysis.

of ∼60 dB is calculated when the amplitude of the noise floor of each channel is compared to its respective measurement range.

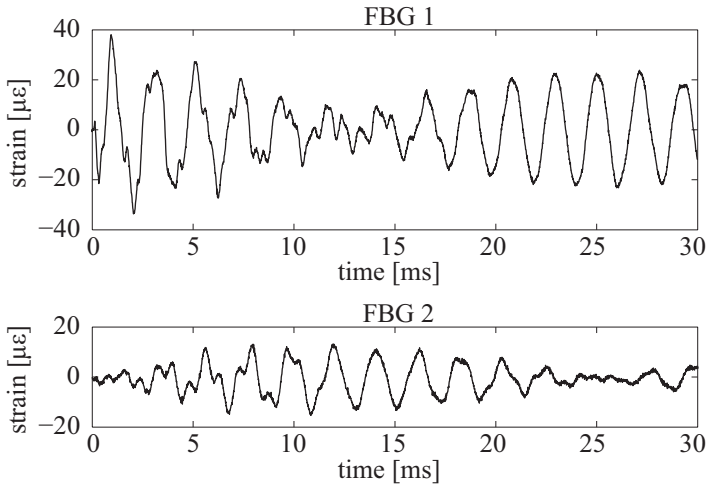

Figure 3.20: Strain responses of two FBG sensors to hammer excitation on one of the excitation points.

The FRFs are computed with the modal curve fitting software ME'scope (Vibrant Technology, California). Each FRF is computed as an average of a set of three different hits. The global averaged frequency response function (Figure 3.21a) presents a sufficiently high dynamic range for proper identification of the natural frequencies. When the excitation has a uniform spectrum over the frequency range of interest, the frequency response function can also be computed from the response signals only. In the low frequency range the exci-

tation spectrum is relatively flat, when the dynamic excitation is done by a non-destructive hammer impact. The use of an FBG sensor for experimental modal analysis leads to the strain mode shapes shown in Figure 3.21b. It has to be mentioned that the mode shapes shown on this figure are asymmetric because of a slightly non-uniform thickness of the plate.

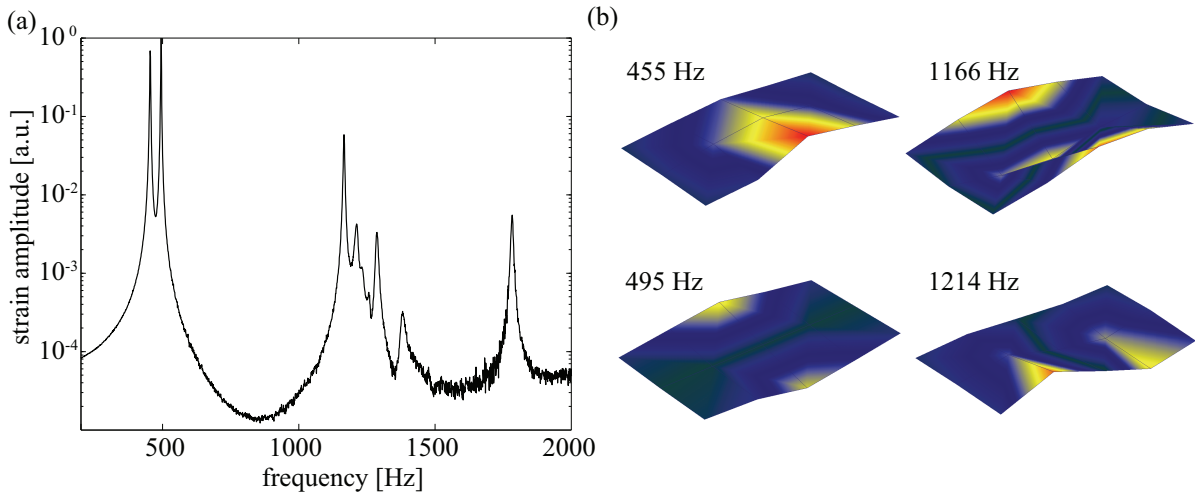

Figure 3.21: (a) Average FRF obtained with FBG sensors (b) Strain mode shapes of the first four eigenmodes.

This experiment also highlights the importance of a prior calibration of the device for a precise modal analysis since the non-linearity of the FP filter function can introduce distortions on the intensity signal and thus deform its spectrum due to the appearance of false harmonics. For example, a sinusoidal strain signal applied to the FBG sensor results in a sinusoidal variation of the Bragg wavelength. Because the shape of the FP filter function has a non-linear relation between wavelength and attenuation, the intensity signal measured at the photodiodes is a periodic signal whose positive and negative lobes are either flattened or tapered (cf. Figure 3.2). Thus a non-linear calibration function is needed to correctly recover the initial sinusoidal signal and thus avoid false harmonics in the measurement spectrum.

Validation of the eigenfrequency measurements

The repeatability of the eigenfrequency determination is studied. Therefore, the entire experimental modal analysis is realised several times and MDOF modal curve fitting is carried out separately on the two sets of responses from FBG 1 and FBG 2. Additionally, the problem is treated as a multi-reference modal analysis using jointly the responses of

both FBG sensors. The results of the modal fitting are the same for all the different measurement sets. The relative standard deviation of the eigenfrequencies obtained during repeated experiments is only 0.07 %. The repeatability achieved with the FBG sensors is thus similar to the one obtained by traditional sensors (cf. Section 2.5). Both FBG sensor positions are found to be appropriate for a precise identification of the natural frequencies because they are both located sufficiently far from nodal displacement lines.

The eigenfrequencies obtained by experimental modal analysis with FBG sensors are also compared to results based on velocity response measurements. This test is carried out on the same plate under the same conditions and the velocity response is measured with a laser vibrometer from Polytec (OFV 303). The maximum relative difference in eigenfrequencies between both measurement methods, based on strain or velocity response, is 0.11 % for the first ten natural frequencies. Table 3.2 shows the average natural frequencies obtained from the measurement sets generated with FBG sensors and their relative standard deviation from the results obtained using velocity response measurements.

Mode shape	Frequency [Hz]	RSD* [%]
B20	455	0.01
T21	495	0.01
B22	1166	0.02
B30	1214	0.05
T31	1287	0.11
B32	1783	0.04
B40	2360	0.10
B23	2779	0.00
B42	2836	0.03
B33	3171	0.05

* Relative standard deviation

Table 3.2: Eigenfrequencies determined with FBG and their relative standard deviation from velocity measurements.

3.4 Summary and conclusion

The presented interrogation method is based on a prototype device from Micron Optics (MO si920). The FBG interrogation method is patented under US patent number

20080106745 [107]. Major modifications are made to the device in order to permit the use of FBG sensors for dynamic measurements within this work.

- The noise level in the quantitative strain signals is reduced by a factor ten:
  - A low noise amplitude of about 2 µε is obtained with the interrogation channels having a range of 2 000 µε. The optical channels with a range of 10 000 µε have a noise level that is approximately 5 times higher.
  - The FP filters can be tuned for maximum sensitivity.
  - The analogue input range of the data acquisition card is chosen appropriately.
  - The voltage source of the broadband light source has an independent stabilised power supply.
- The device is calibrated with accurateness:
  - Detailed non-linear calibration curves, expressed as a function of strain and Bragg wavelength shift, are created and validated.
  - The calculation of the strain data is made via spline interpolation.
  - A precise calibration is necessary to obtain quantitative strain data and prevent false harmonics from appearing in the signal spectrum.
- The tuning of the FP filters is reengineered:
  - Control parameters can be influenced by the user. He can opt for maximising the measurement range or maximising the sensitivity of an optical channel.
  - The drive voltage is supplied by analogue outputs of a data acquisition card with a 16 bit resolution. A precise bias of the FP filter can be regulated.
  - The closed loop control software for the FP filter tuning is new. The tuning is faster and more stable because the non-linear response of the FP filter to the drive voltage is taken into account.
- The software of the device is modified:
  - The acquisition rate, number of samples and input range of the channels can be user-specified.
  - The available strain range of each channel is indicated by the software taking into account an eventual saturation of the photodiodes.
  - Instantaneous external triggering of the device is feasible on demand.

  - The data saving management is more flexible.
  - The continuous acquisition mode is faster.
- A fast and sensitive acquisition of intensity signals for wave sensing is implemented:
  - Acquisition rates of 1 GHz per channel are feasible.
  - The analogue input range is optimised for maximum sensitivity.
  - The electrical noise can partially be removed from the intensity signal via the reference measurements.

As a result of these modifications on the device, FBG sensors can be used for precise acquisition of quantitative dynamic strain signals. The high acquisition rate allows to capture the high frequency content of the signals during the impact. The short strain impulse, a typical response to an impact, can be used to detect an impact event and trigger the acquisition procedure. It is shown that FBG sensors can also be used for experimental modal analysis. Because the signal-to-noise ratio is sufficiently high, they can be used to determine the eigenfrequencies of a structure with a similar precision as the one obtained by traditional sensors.

Chapter 4

Impact localisation

4.1 Preface

The knowledge about the existence and position of an impact event on a composite structure is useful preliminary information for subsequent characterisation of an eventual damage. When the position of the impact event is known with a certain precision, the inspection of the laminate can be limited to this region. This information may significantly reduce the complexity of the damage identification problem. Localisation of an impact event based on mechanical wave propagation in plate-type structures has been continuously studied over the last decades and has evolved with the use of miscellaneous sensors, signal processing methods and triangulation methods. The following overview gives a state-of-the art in this field.

In experimental impact and/or damage detection methods, piezoelectric (e.g. PZT [109] and PVDF [110]) sensors and Doppler laser velocimetry are used for sensing acoustic waves in structures. More recently, FBG sensors are shown to have a sufficiently high sensitivity for sensing acoustic waves [73, 75–78, 111–113]. However, the orientation of the sensor with respect to the propagation direction of the wave is of concern. The dependence of the FBG orientation on the wave propagation direction has been studied and its sensitivity turned out to be sufficient when the incident angle of the wave is within $\pm 45\,^\circ$ – $60\,^\circ$ to the optical fibre orientation [74, 76, 79].

A first step in determining the source of acoustic waves in a structure is the determination of the arrival time of the waves at the sensor by analysing the corresponding signals. In general, the sensor signals are filtered using either amplifier built-in analogous or more conveniently adjustable digital low-pass or band-pass filters. The filtering considerably re-

duces the noise in the signals and partially accounts for the dispersive character of flexural waves in plate-type structures by limiting the signal content to a narrow frequency band. A commonly used signal processing method for the identification of the wave arrival time in commercially available acoustic emission (AE) equipment is the threshold method. Here, the appearance of the impulse is detected whenever the amplitude of the signal exceeds a value bigger than the noise level. A more complex method accounting for the dispersive character of Lamb waves is based on wavelet analysis [114] which relies on maximum cross-correlation between the filtered signal and a wavelet with a known frequency. With this method, the prediction accuracy of the acoustic source location is improved when the source excites a large frequency spectrum. This is for example the case for a lead break experiment or an acoustic emission source emulated by a piezoelectric transducer, which can cover a large range of excitation frequencies. The arrival time delays between couples of sensors can also be determined using signal cross-correlation [115]. Therefore, the signal spectra have to be reduced to a certain frequency band, the signals need to be similar and the impulse shape must not significantly change due to the dispersive character of the wave propagation.

Once the arrival times of the waves at different sensor positions are known, triangulation techniques are employed to locate the source of the waves. The early triangulation methods are valid for isotropic materials only because a uniform wave propagation velocity is assumed [116]. These methods are based on the wave arrival time at a minimum of three different sensors. Later, they are also adapted to anisotropic wave propagation. Based on a priori knowledge of the wave speed profile, the problem is solved by expressing the equations to be solved as a minimisation problem [29, 30, 117]. The objective function often presents several local minima and a Simplex or gradient-descent optimisation algorithm may not converge to the absolute minimum. However, modifications to the objective function and customised minimisation algorithms allow for a prediction of the impact position. The impact position can also be predicted from arrival time delays and other signal features by using an artificial neural network (ANN) and ignoring the wave propagation formulation [109, 118]. An inherent issue of this method is the optimal design of a network with an appropriate amount of layers and neurons to obtain a good generalisation and regularisation of the problem. Moreover, it needs an extremely large set of reference data for training of the ANN.

In most of the research studies for impact localisation, the acoustic emission source is emulated by a lead break or by a piezoelectric transducer. During a low-velocity impact, however, the excitation frequencies are generally low and in the range of 100 kHz. In only a few works, the localisation and especially the signal processing methods are validated by real transverse impact tests [77, 118, 119]. Within this work, the objective is to develop an

easily implementable technique allowing the detection and localisation of real low-velocity transverse impacts on laminated composite structures with the use of short FBG sensors.

In this chapter, the high speed interrogation method presented in Chapter 3 is used to obtain qualitative intensity signals from the optical sensors at a rate of 1 GHz. The interpolation-based localisation method presented herein can be easily adapted to different orthotropic structures and does not need the knowledge of the wave propagation profile. First, the error caused by the data interpolation is evaluated and the necessary number and position of the reference data points and sensors are studied. For validation purpose, the method is tested using data from piezoelectric accelerometers and, finally, using intensity signals from FBG sensors.

4.2 Theory of wave propagation

The theoretical analysis of the wave propagation phenomena caused by a low energy impact is complex because of the different kinds of waves that may be initiated during this event. Moreover, in case of a composite plate, the wave equations need to be expressed in terms of orthotropic material properties. Besides longitudinal and transverse shear waves, Lamb waves are most commonly considered to be the main wave propagation type in plates and their usage in the field of damage detection has been studied. This section gives a short overview on wave propagation theory in plates. The main goal is to identify the type of waves that are initiated during a transverse impact and to estimate their velocity. For simplicity reasons, the development of the theory is done for the case of isotropic plates and the results are generalised for the case of orthotropic plates. A detailed formulation of the wave propagation problem in thin composite plates can be found in [120]. Details on elasticity theory of orthotropic materials are found in Section 2.2.3.

4.2.1 Longitudinal and transverse shear waves

The elastodynamic equation for a solid, isotropic and homogeneous medium without applied body forces is written

$$G\frac{\partial^2 u_i}{\partial x_j \partial x_j} + (\lambda + G)\frac{\partial^2 u_i}{\partial x_j \partial x_i} = \rho \ddot{u}_i \;\; (i,j = 1,2,3) \tag{4.1}$$

In this equations, u_i is the displacement in the x_i direction and λ, G, ρ are the first Lamé constant, shear modulus and density, respectively. The boundary conditions of the domain

are given by setting equal to zero each stress component in the x_3 direction at the free upper and lower surface of the plate with a thickness h

$$\begin{aligned} \sigma_{13}\left(x_3 = \pm h/2\right) &= 0 \\ \sigma_{23}\left(x_3 = \pm h/2\right) &= 0 \\ \sigma_{33}\left(x_3 = \pm h/2\right) &= 0 \end{aligned} \tag{4.2}$$

The plate is considered to be infinitely long in the x_1 and x_2 directions and the waves are supposed to propagate in the x_1 directions. A plane strain assumption is made which results in zero displacement and zero variation of any parameter in the x_2 direction

$$\begin{aligned} u_2 &= 0 \\ \frac{\partial \cdot}{\partial x_2} &= 0 \end{aligned} \tag{4.3}$$

Searching for a general solution of Equation (4.1), it is rewritten in the frequency domain by assuming a harmonic time-dependency of the displacement with an angular frequency ω. Based on the Helmholtz theorem, the displacement vector field is decomposed into the sum of the gradient of a scalar field ϕ and the rotational of a divergence-free vector field $\boldsymbol{\psi}$. Accounting for the plane strain assumption defined by (4.3), the only remaining component of vector $\boldsymbol{\psi}$ is written ψ and the displacement field is expressed by

$$\begin{aligned} u_1 &= \frac{\partial \phi}{\partial x_1} + \frac{\partial \psi}{\partial x_3} \\ u_2 &= 0 \\ u_3 &= \frac{\partial \phi}{\partial x_3} - \frac{\partial \psi}{\partial x_1} \end{aligned} \tag{4.4}$$

This allows to decompose Equation (4.1) in two parts, with the first governing the pressure wave modes and the second the transverse shear wave modes which are supposed to not interact in a plate of infinite dimensions,

$$\begin{aligned} \frac{\partial^2 \phi}{\partial x_1^2} + \frac{\partial^2 \phi}{\partial x_3^2} &= \frac{1}{c_L^2} \frac{\partial^2 \phi}{\partial t^2} \quad \text{longitudinal wave modes} \\ \frac{\partial^2 \psi}{\partial x_1^2} + \frac{\partial^2 \psi}{\partial x_3^2} &= \frac{1}{c_T^2} \frac{\partial^2 \psi}{\partial t^2} \quad \text{transverse wave modes} \end{aligned} \tag{4.5}$$

In these equations, c_L and c_T are the propagation speeds of the longitudinal and transverse

waves, which are written as follows in the case of an isotropic material

$$c_L = \sqrt{\frac{2E\,(1-\nu)}{\rho\,(1+\nu)\,(1-2\nu)}}$$
$$c_T = \sqrt{\frac{G}{\rho}} \tag{4.6}$$

where $E = 2G\,(1+\nu)$ is the Young's modulus of the isotropic material and ν and G are the Poisson's ratio and the shear modulus, respectively.

In case of an anisotropic material, the pressure wave and transverse shear velocities in the x_1 and x_2 directions are given by

$$c_{L1} = \sqrt{\frac{c_{11}}{\rho}} \quad c_{L2} = \sqrt{\frac{c_{22}}{\rho}}$$
$$c_{T1} = \sqrt{\frac{c_{55}}{\rho}} \quad c_{T2} = \sqrt{\frac{c_{44}}{\rho}} \tag{4.7}$$

with c_{11} and c_{22} being the first and second elements of the diagonal of the stiffness matrix $\boldsymbol{C}$. The coefficients c_{44} and c_{55} are the fourth and fifth elements of the stiffness tensor's diagonal and correspond to the shear moduli G_{23} and G_{13}, respectively. Considering the material properties of the cross-ply plate presented in Table 2.2, the theoretical longitudinal and transverse shear velocities in the x_1 and x_2 direction are given in Table 4.1. Whereas the longitudinal wave velocities are different in both propagation directions, the shear wave velocities are only depending on the corresponding shear moduli which are almost equal.

	c_L [m/s]	c_T [m/s]
x_1 - direction	6731	1326
x_2 - direction	5595	1323

Table 4.1: Theoretical longitudinal and transverse wave propagation velocities along x_1 and x_2 direction of the CFRP plate.

4.2.2 Lamb waves

The wave equations for Lamb waves are obtained from the eigenvalue problem derived from equations (4.5) considering a general solution for waves propagating in the x_1 direction, obtained by separation of variables (4.4), and accounting for the free lower and upper

boundary conditions (4.2)

$$\frac{\tan(qh)}{q} + \frac{4k^2 p \tan(ph)}{(k^2 - q^2)^2} = 0$$
$$q\tan(qh) + \frac{(k^2 - q^2)^2 \tan(ph)}{4k^2 p} = 0 \tag{4.8}$$

where $k = \omega/c$ is the wave number, $\omega = 2\pi f$ the angular frequency and c the Lamb wave velocity in the x_1 direction. The variable substitutions p and q are defined by

$$p^2 = \frac{\omega^2}{c_L^2} - k^2$$
$$q^2 = \frac{\omega^2}{c_T^2} - k^2 \tag{4.9}$$

The first equation of (4.8) governs symmetric mode shapes and the second antisymmetric mode shapes. The phase velocity of Lamb waves depends on their frequency ω and plate thickness h and an infinite number of symmetric and antisymmetric modes can exist. The dispersion curves of the fundamental symmetric and antisymmetric Lamb wave modes S_0 and A_0 are given as a function of the frequency-thickness product in Figure 4.2 for the laminate characterised in Section 2.2.2. The shapes of the fundamental modes S_0 and A_0 are illustrated in Figure 4.1.

The reason why only the fundamental Lamb wave modes are considered in this theoretical analysis is substantiated by some preliminary experimental results and findings from other researchers. When the frequency-thickness product is below 1 000 Hz m, only the fundamental modes S_0 and A_0 can propagate in fibre reinforced composite plates. This limit is called the cut-off frequency of higher-order modes. During a transverse low-energy impact on a plate, the range of the excited frequencies is relatively low and does not exceed the cut-off frequency of higher-order modes [117]. Spectral analysis from experimental results in Section 4.4.1 confirms that the spectral content of the signal obtained with FBG sensors is within 100 kHz.

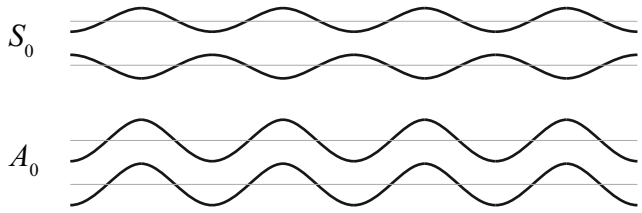

Figure 4.1: Mode shapes of the fundamental Lamb wave modes S_0 and A_0.

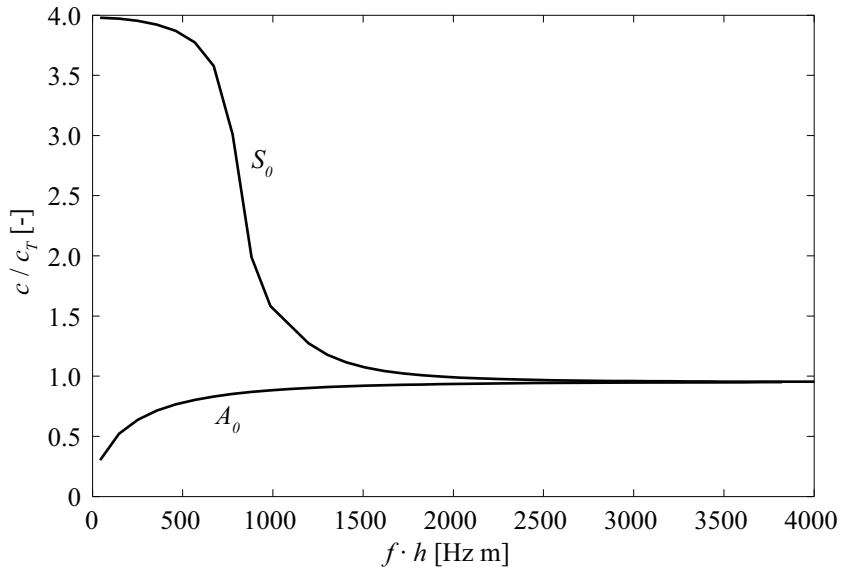

Figure 4.2: Normalised phase velocities of first order symmetric (S_0) and antisymmetric (A_0) Lamb waves.

In general, the amplitude of S_0 wave modes is considerably lower than the one of the A_0 modes [120]. Moreover, a transverse impact will preferentially excite the A_0 mode and not the S_0 mode because of the symmetric shape of the latter. The propagation time of S_0 waves from the excitation source to a sensor is considerably smaller compared to the one of A_0 waves, since they propagate approximately 4 times faster in the low frequency range. Therefore, the S_0 mode is easily distinguished from the A_0 mode when it is present in a signal and excited with a sufficient amplitude. It can be noticed throughout impact tests, as it has been by other authors [117], that the signal of the faster symmetric Lamb waves cannot, or extremely difficult, to be distinguished from the noise level in the measurements because of their low amplitude.

4.2.3 Group velocity

The group velocity c_g is the velocity with which the overall shape of a wave impulse propagates through a plate. It is the actual velocity captured in experiments and the velocity of wave energy transportation [120]. It has to be mentioned that the shape of the impulse may vary with time due to the dispersive character of the Lamb wave propagation. The phase velocity c is the propagation speed of the phase of a wave with a given frequency

ω. The phase velocity of a wave with a frequency ω is related to the wavelength λ_{wave} by

$$c = \omega \frac{\lambda_{\text{wave}}}{2\pi} \tag{4.10}$$

The wave number k is related to the wavelength by $k = {}^{2\pi}/_{\lambda_{\text{wave}}}$. The group velocity c_g is calculated from the phase velocity by this formula

$$c_g = \frac{\partial \omega}{\partial k} \tag{4.11}$$

The wave number k can be substituted by ${}^{\omega}/_{c}$. The group velocity is dependent on the central frequency $f = {}^{\omega}/_{2\pi}$ and plate thickness h [121]

$$c_g\left(f \cdot h\right) = c^2 \left[c - \left(f \cdot h\right) \frac{dc}{d\left(f \cdot h\right)}\right]^{-1} \tag{4.12}$$

In Figure 4.3, it can be seen that the group velocity of the fundamental antisymmetric mode A_0 is almost constant over a large range of frequencies and has an upper bound that is slightly higher than the shear wave velocity. The determination of the arrival time of the wavefront will rely on the first appearance of the fundamental antisymmetric Lamb wave A_0.

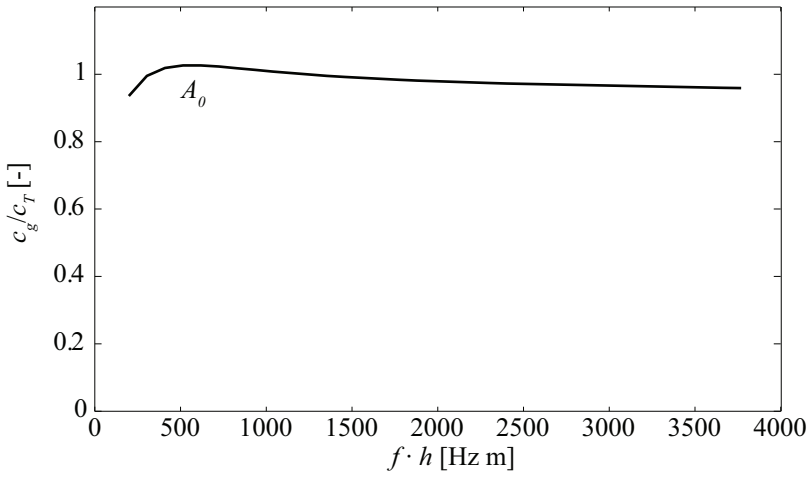

Figure 4.3: Normalised group velocity of first order antisymmetric (A_0) Lamb waves.

4.3 Materials and methods

4.3.1 Materials

The impact localisation method proposed in this chapter is tested for the case of transverse impacts on CFRP CP plates. The impacts are non-destructive and carried out using an instrumented hammer from Brüel & Kjær (B&K) (type 8206; weight: 100 g) and the acquisition is triggered by the signal of the load cell. The size of the plate is 300 mm × 300 mm and it is clamped on two sides resulting in span of 240 mm. The method proposed hereafter is based on acoustic wave propagation and is experimentally validated with two types of sensors, i.e. accelerometers and FBG sensors.

Four sensitive accelerometers from B&K (type 4517-C) are pasted on the CFRP plate with a thin layer of wax in each corner of the plate at a distance of 20 mm to the free edge and at a distance of 30 mm to the clamping in the way to delimit a domain of 180 mm × 260 mm (Figure 4.4). The acquisition of the accelerometer signal is done with a sampling rate of 1 MHz using a 300 MHz bandwidth oscilloscope from Agilent (Type DSO 6034A) and a 4-channel charge amplifier from B&K (type 2692).

The FBG sensors are glued on the lower side of a distinct plate. The gratings are orientated in the 45° direction in order to have a sufficient sensitivity of the sensors to incident

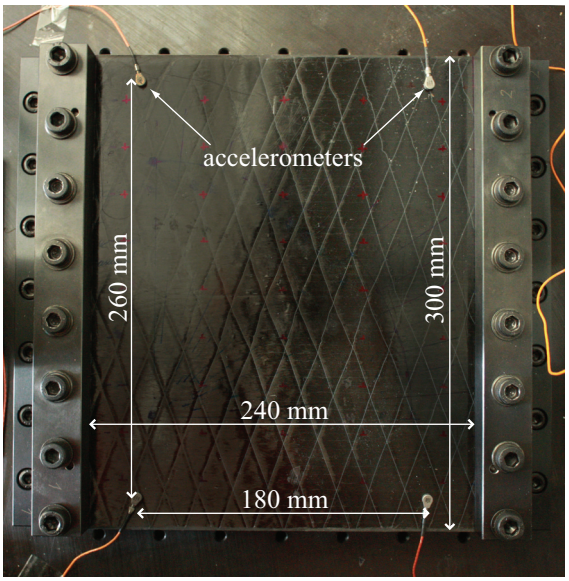

Figure 4.4: Picture of the clamped CFRP plate with four accelerometers for impact localisation.

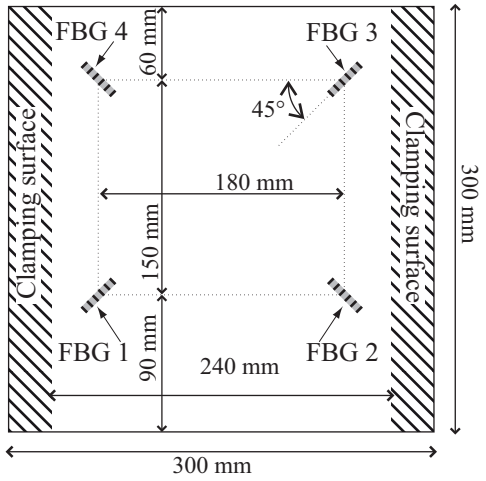

Figure 4.5: Schematic of the clamped CFRP plate with four surface-glued FBG sensors for impact localisation.

bending waves originating from a rectangular domain with a size of 180 mm × 150 mm (Figure 4.5). The present configuration allows the waves emitted within this domain to arrive on all four sensors at an angle in-between ±45 °.

The interrogation of the FBG sensors is performed using the high rate intensity acquisition mode. The acquisition of the reflected intensity on the measurement arm as well as on the reference arm is done using a Lecroy Wavesurfer 434 oscilloscope at a rate of 1 GHz over a duration of 1 ms. The recorded signals are digitally low-pass filtered and decimated to a rate of 1 MHz. Only two optical channels with sufficient sensitivity are available within this work and therefore each non-destructive impact test is carried out separately for each pair of sensors.

4.3.2 Experimental characterisation of acoustic waves

Prior to the development of the localisation method, the wave propagation in the CFRP plates is characterised and compared to theory. The wave speed is measured as a function of propagation direction using a pair of highly sensitive accelerometers (B&K type 4517-C) aligned at an angle varying from 0 ° – 90 ° to the longitudinal direction of the plate. The impact position for each of the propagation directions is aligned with the sensors and located beyond the two sensors (Figure 4.6), in the way that the same wave front passes by the two sensors. The wave speed can though be easily determined as the ratio of the distance between the sensors (120 mm) and the time of propagation between the sensors. This time of propagation is called arrival time delay and is defined in the next section.

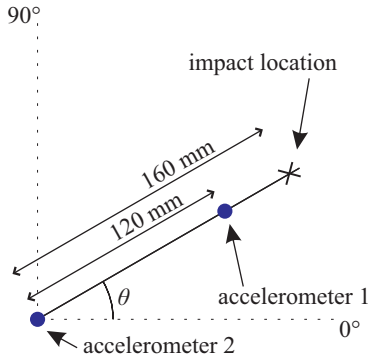

Figure 4.6: Schematic of the sensor configuration for wave velocity measurements.

Also classical PZT sensors are used to characterise the frequency content of the propagating waves. Therefore, two Nano-30 PZTs from Physical Acoustics Corporation are arranged in the same way as the accelerometers in Figure 4.6. The sensors are connected to a 1220A PAC preamplifier having a built-in band-pass filter and the acquisition is made with the DSO 6034A oscilloscope from Agilent. In comparison to standard accelerometers which have a frequency range of 1 Hz – 50 kHz, the signal from PZT sensors are amplified in a frequency range between 100 and 300 kHz. This experiment allows to verify the conclusions drawn from the experiments with accelerometers and FBG sensors.

4.4 Impact localisation method

4.4.1 Signal processing

The following signal analysis and previous findings in the theoretical section will lead to a choice of an appropriate method for determining the wave arrival time at a sensor, *i.e.* the threshold method, the signal cross-correlation or the wavelet analysis. The choice of the signal processing method is related to the amount of apparent wave modes and their shape as well as to the frequency content and similarity of the recorded signals.

Wave signal observed with accelerometers

Due to the dispersive character of antisymmetric Lamb waves and the damping of the CFRP composite, the shape of the wave impulse is expected to change while propagating through the plate. Figure 4.7 shows the signal measured by two accelerometers placed with a spacing of 120 mm and in-line with the excitation source (cf. Figure 4.6). The impact

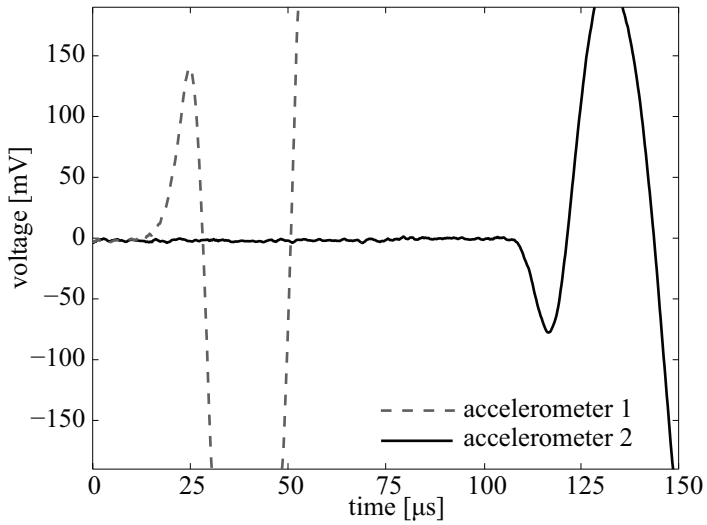

Figure 4.7: Signal originating from a wave propagating in the 45 ° direction and measured by two accelerometers.

point is outlying the two sensors, so that the same waves travel by both sensors. It can be noticed from the temporal signal that if symmetric S_0 Lamb waves propagate, their amplitude is smaller than the noise level. Otherwise the curve of accelerometer 2 would feature a non-zero signal far ahead of the signal at 105 µs. Moreover, a distortion of the impulse shape due to the dispersive characteristic of antisymmetric Lamb waves at low frequencies can be noticed.

Wave signal observed with PZT sensors

In the same way, no apparent signal originating from faster symmetric S_0 Lamb waves can be detected in the signals obtained from the PZT sensors (Figure 4.8). The signal arriving at sensor PZT 2 is smaller in amplitude as compared to the one measured on the sensor close to the impact point because of internal damping of the material. Also the shape of the signal is distorted due to the dispersive character of Lamb waves. The frequency content of the PZT signals is largely different from the one obtained by accelerometers because of the built-in band-pass filter in the PZT's preamplifiers and the reduced sensitivity of the accelerometers to frequencies beyond 50 kHz.

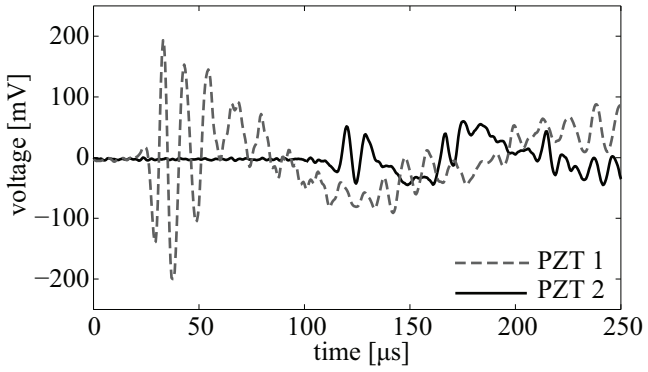

Figure 4.8: Signal originating from a wave propagating in the 45 ° direction and measured by two PZT sensors.

Frequency content of the wave signals

The frequency spectrum of the waves propagating in the structure depends on the excitation source. The excitation spectrum mainly depends on the contact stiffness and impact weight. In case of a destructive impact, waves also originate from damage initiation and propagation. The acoustic waves originating from damage initiation and propagation are expected to have low amplitude compared to the waves caused by the impact. The impact duration, which depends on the structural stiffness and the impact weight, is in the order of a few milliseconds and therefore longer than the on-way propagation time of an acoustic wave within the structure. This implies that a Fourier transformation of the entire excitation impulse does not directly disclose the frequency content of the propagating waves.

Wave signal observed with FBG sensors

The frequency content measured by accelerometers or FBG sensors during the first millisecond of the impact can be distinguished from the noise within a range of 100 kHz or less. In Figure 4.9, it can be seen that the noise floor of the FBG sensor signals is at around -60 dB. The FBG is less sensitive to waves at higher frequencies than the accelerometer. Consider a flexural wave with a given displacement amplitude and a frequency ω. The amplitude of the acceleration is proportional to ω^2. Assuming classical laminated plate theory, the measured strain amplitude is proportional to the square of the local curvature and hence inversely proportional to the square of its wavelength $\lambda_{\text{wave}} = {}^{2\pi c}/_{\omega}$. The phase velocity c of a Lamb wave depends on its frequency ω. In the low frequency range, the phase velocity of fundamental asymmetric A_0 Lamb waves is often approximated by the phase velocity

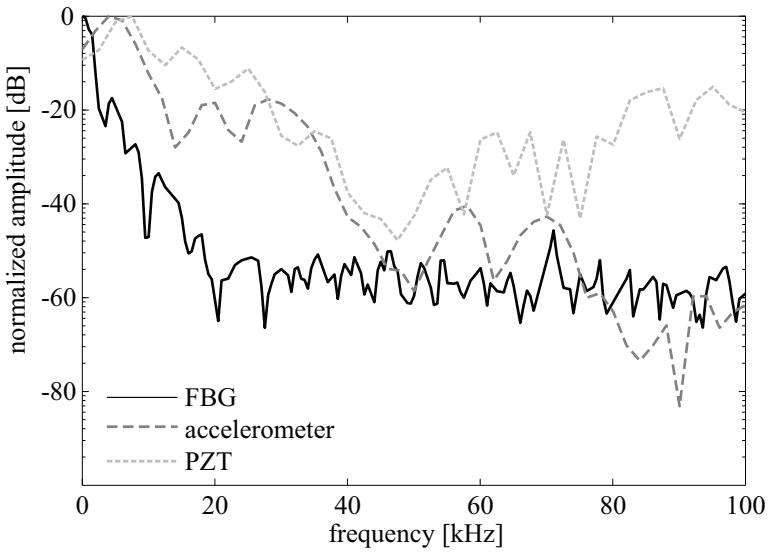

Figure 4.9: Spectral content of accelerometer, FBG sensor and PZT sensor signals during the first millisecond of a wave passing by the sensors.

of bending waves which is proportional to $\sqrt{\omega}$. The measured strain amplitude is hence proportional to ω. Strain measurements are consequently less sensitive to high frequency waves than acceleration measurements. Throughout these experiments, higher frequencies components are found to be rare in the FBG signals and cannot be distinguished from the noise level. The peak recorded at ∼70 kHz with the FBG (Figure 4.9) is not reproducible for different impact positions or energies. Because of the absence of higher frequency components a cross-correlation method with a Morlet wavelet is not feasible.

Figure 4.10a shows typical signals of two FBG sensors (FBG 3 and FBG 4 in Figure 4.5) recorded over a longer duration of 4.5 ms after a hammer excitation at a distance of 80 mm to FBG 3 and 150 mm to FBG 4. In general, the signals observed on different sensors are not sufficiently similar to use a maximum cross-correlation method to determine the arrival time delay between two sensors even if a band-pass filter would be applied. This absence of similarity can be attributed to the dispersive behaviour of Lamb waves and the different reflections from the clamping fixture close to the sensor. It can also be observed that a few milliseconds after the impact, the signals resemble a superposition of modal responses.

Signal processing method

The following method and signal processing is based on the assumption that only the fundamental antisymmetric A_0 Lamb waves are visible in the signals and that the frequencies

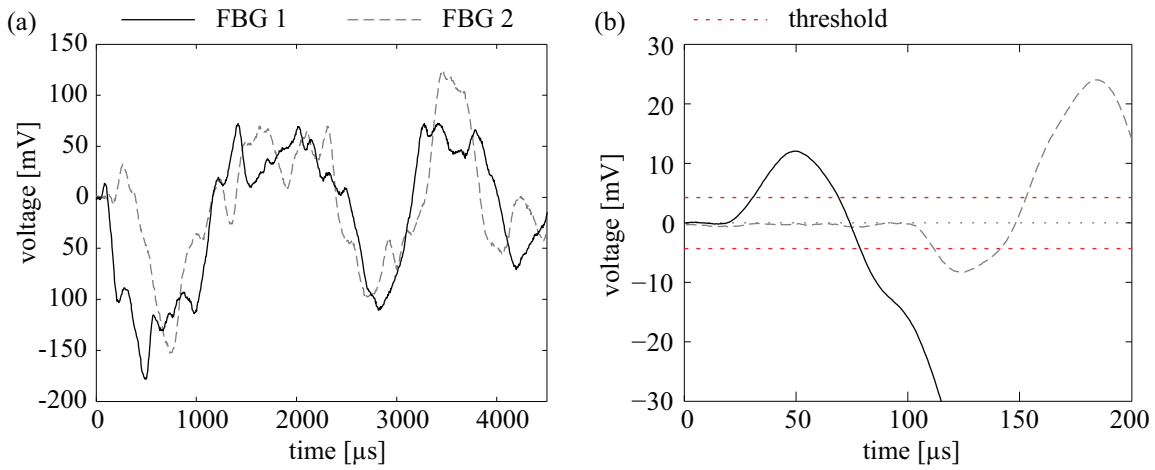

Figure 4.10: Signals from synchronous acquisition of two FBG sensors during a transverse non-destructive impact. (a) Acquisition during 4.5 ms (b) Zoom-in on first 200 µs.

of these waves are low. As presented in the theoretical Section 4.2.3, the group velocity of antisymmetric Lamb waves has an upper bound almost equal to the shear wave velocity. The wave arrival time t_k of a wave at a sensor S_k is therefore based on the first appearance of the impulse at a sensor and is determined using a threshold method. The threshold value needs to be higher than the noise level and is defined as a fraction of the maximum amplitude of the signal. It is verified that, throughout a range of threshold levels reaching from 2 % to 5 % of the maximum amplitude, the arrival time delay results in approximatly the same value (Figure 4.10b). If this is not the case, outliers are discarded and the other values are averaged. In order to reduce the noise in the signals and eliminate quasi-static deformations or low-frequency vibrations, a digital band-pass filter with a range of 1.5 – 50 kHz is applied to the signals prior to the threshold method.

The arrival time delay between two sensors S_k and S_l is defined as follows,

$$\Delta t_{kl} = t_k - t_l \tag{4.13}$$

At each impact, an array $[\Delta t_{kl}]$ is obtained, with $k = 1, \ldots, n_S$ and $l = 1, \ldots, n_S$, where n_S is the number of sensors. During the experiments, the non-destructive impact is repeated three or four times at each location in order to check the repeatability and the accuracy at which the arrival time delay can be determined.

4.4.2 Prediction of impact location

A localisation method based on interpolation of a known data set is proposed. This method does not require the knowledge of the wave propagation velocity as a function of propagation angle. However, a reference data set denoted by

$$\left\{ \left[\Delta t_{kl}^{R} \right] ; \left(x_1^R, x_2^R \right) \right\} \tag{4.14}$$

which consists of n_R arrays of arrival time delays $\left[\Delta t_{kl}^{R}\right]$ and n_R known locations $\left(x_1^R, x_2^R\right)$ is required for the interpolation. Thus, an interpolated response surface denoted by

$$\widehat{\Delta t}_{kl}^{R}\left(x_1, x_2\right) \tag{4.15}$$

is created as a function of the impact position for each arrival time delay over the domain defined by the reference points $\left(x_1^R, x_2^R\right)$ as shown in Figure 4.11.

For the prediction of the impact location, the array of arrival time delays $\left[\Delta t_{kl}^{P}\right]$ is required as an input for the localisation method. The isolines L_{kl} are the lines where the interpolated response surfaces $\widehat{\Delta t}_{kl}^{R}\left(x_1, x_2\right)$ take the values of the arrival time delays $\left[\Delta t_{kl}^{P}\right]$. The intersection between two isoline L_{kl} and L_{rs} is denoted $\left(x_1, x_2\right)_{klrs}$. Under optimal conditions the intersection of all of these isolines should correspond to the exact location $\left(x_1^P, x_2^P\right)$ of the impact. The intersections of the isolines may though be distinct due to interpolation or experimental errors. The experimentally determined reference data set $\left\{ \left[\Delta t_{kl}^{R} \right] ; \left(x_1^R, x_2^R \right) \right\}$ and the array of arrival time delays $\left[\Delta t_{kl}^{P}\right]$ for the prediction may be subject to errors. The predicted location $\left(x_1^P, x_2^P\right)$ is therefore calculated as a geometrical average of the intersections $\left(x_1, x_2\right)_{klrs}$.

Alternatively it is recommended to have a weighting average in which the contribution of an intersection is weighted by the product of two confidence factors $w_{kl}\left(x_1, x_2\right)$ and $w_{rs}\left(x_1, x_2\right)$ attributed each to a pair of sensors and thus to isolines L_{kl} and L_{rs}. A weight factor w_{kl} attributed to an isoline L_{kl} depends on the sensor pair $\left(S_k, S_l\right)$ and on the position $\left(x_1, x_2\right)_{klrs}$ where the intersection is found. Typically, for a given sensor pair $\left(S_k, S_l\right)$, the confidence factor $w_{kl}\left(x_1, x_2\right)$ may be a plane surface having a value 1 on the line joining the two sensors S_k and S_l and linearly decreasing with increasing distance from this line. In case of experimental data, the confidence factors account for the higher uncertainties in the determination of the arrival time delay when the acoustic source is far away from a pair of sensors.

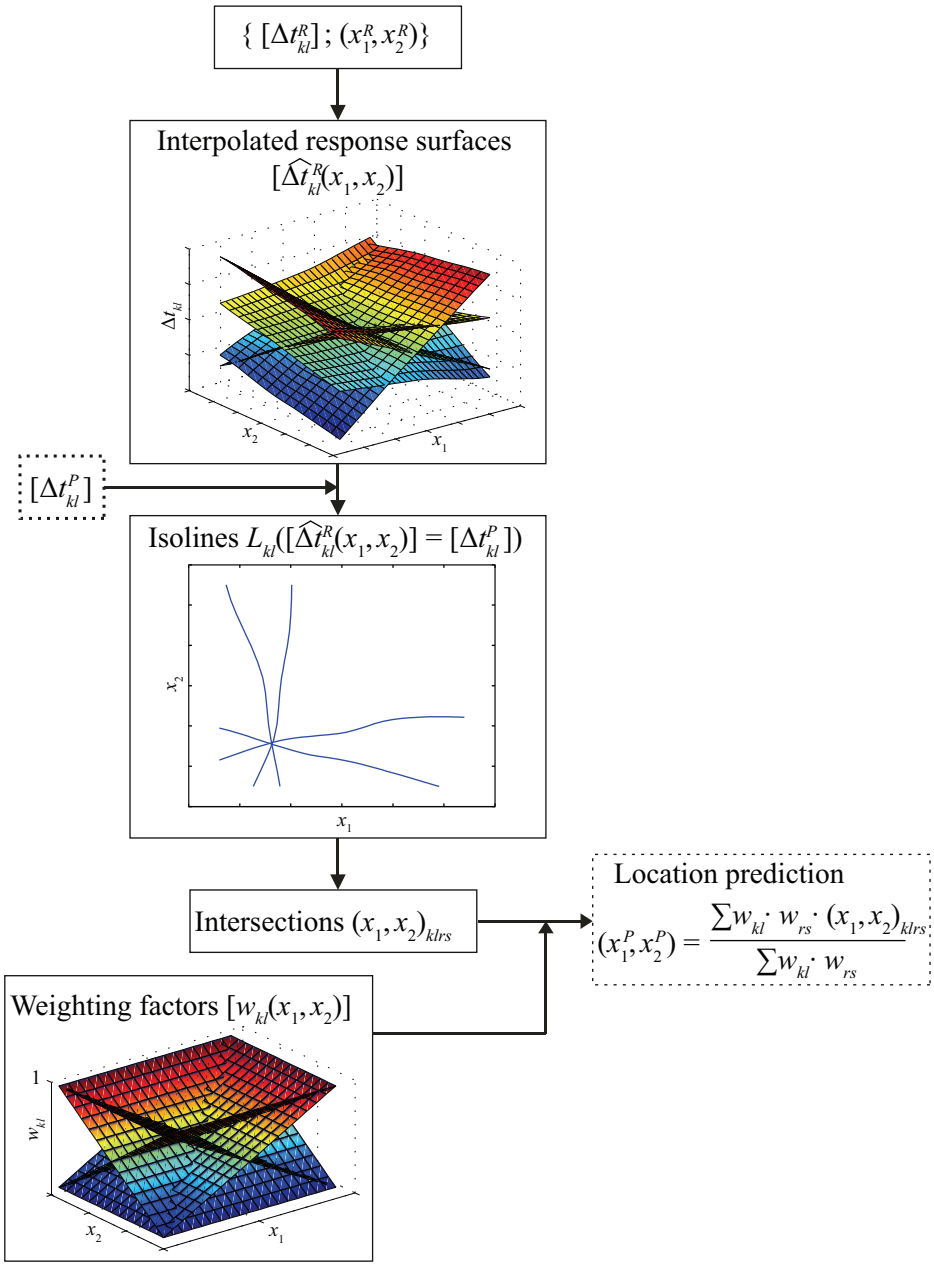

Figure 4.11: Block diagram of interpolation-based localisation method.

4.4.3 Validation of the impact localisation method

The localisation method described in the previous section is validated by means of numerical and experimental data. The predicted impact location is therefore compared to the exact location and the error is expressed in terms of a radius. The prediction error, related to the interpolation of the reference data, is evaluated using numerically generated data for the reference set as well as for the prediction. In the framework of two experimental tests, the locations of non-destructive impacts on a CFRP plate are predicted using the described method. The experiment is first carried out using accelerometers and, second, using surface-glued FBG sensors. By means of these validation tests, the error is decomposed in a proportion relative to a characteristic size and an absolute contribution independent from the plate size.

Numerical evaluation of the interpolation error

In order to verify the localisation method, it is tested with a numerically generated data set $\left\{\left[\Delta t_{kl}^{R}\right],\left(x_1^R, x_2^R\right)\right\}$ which does not comprise any errors related to the determination of arrival time delays $\left[\Delta t_{kl}^{R}\right]$ or inexact reference positions $\left(x_1^R, x_2^R\right)$. The time of propagation t_k of a wave initiated at a position (x_1, x_2) and arriving at a sensor S_k at the position $(x_1, x_2)_{Sk}$ is defined by

$$t_k = \frac{\left\|(x_1, x_2) - (x_1, x_2)_{Sk}\right\|_2}{c\left(\theta_k\right)} \tag{4.16}$$

where $\|\cdot\|_2$ is the Euclidean norm and $c\left(\theta_k\right)$ is the wave velocity in the propagation direction θ_k defined by the impact location (x_1, x_2) and the position of sensor S_k. The arrival time delay Δt_{kl} between to sensors S_k and S_l is defined by Equation (4.13). No reflections at the border of the domain are taken into account. Also in case of orthotropic wave velocity, the fastest way for a wave to propagate from its source to a sensor is considered to be the shortest one.

Several aspects and the influence of different parameters on the accuracy of the interpolation method are tested in this section. (a) The influence of the number of reference points n_R and hence the size of the reference data set $\left\{\left[\Delta t_{kl}^{R}\right],\left(x_1^R, x_2^R\right)\right\}$ is tested. (b) An isotropic material with a constant wave velocity and an orthotropic material having a wave propagation speed profile typical for an anisotropic composite plate are considered. (c) The number of sensors n_S is studied. (d) The influence of the combinations of different pairs of sensors (S_k, S_l) to calculate different arrival time delays is studied. When n_S sensors are used $n_S - 1$ independent arrival time delays can be calculated and a maximum of $n\left(n+1\right)/2$ sensor pairs (S_k, S_l) can be combined. (e) For each arrival time delay, an iso-

line L_{kl} at the value $\left[\Delta t_{kl}^{P}\right]$ can be computed. The feasibility of calculating all the possible intersections of these isolines is studied.

Following cases are studied to investigate the influence of the different parameters:

- Four sensors delimit a rectangular domain with a size of 180 mm × 150 mm. The accuracy of the method is evaluated when only 3 sensors are present.
- The reference data set for interpolation is generated on a grid of 3 × 3 points. A refined grid in the x_1 direction is also tested.
- The plate is considered to be made of isotropic material with a constant wave speed of 1 300 m/s.[1] The method is tested using anisotropic wave velocity profile with velocities of 1 600 m/s, 1 400 m/s, 1 700 m/s in the 0 °, 45 ° and 90 ° directions, respectively.[2]
- Four arrival time delays between the pairs of sensors (S_1, S_2), (S_2, S_3), (S_3, S_4) and (S_4, S_1) are considered and hence four isolines L_{12}, L_{23}, L_{34} and L_{41} can be computed. Other arrival time delays can be calculated by combining sensors (S_1, S_3) and (S_2, S_4).
- The four isolines L_{12}, L_{23}, L_{34} and L_{41} may result in 6 intersection points but only four intersections between the isolines (L_{12}, L_{23}), (L_{23}, L_{34}), (L_{34}, L_{41}) and (L_{41}, L_{12}) are computed. This pairs of isolines are almost perpendicular to each other. When the vector $\boldsymbol{x}_{S_k - S_l}$, defined by the positions of the two sensors S_k and S_l, is parallel to the vector $\boldsymbol{x}_{S_r - S_s}$, the corresponding isolines L_{kl} and L_{rs} risk to be almost parallel and their intersection may be far away from the exact location.
- The predicted location is the weighted average of the intersections $(x_1, x_2)_{klrs}$ with weighting factors w_{kl} and w_{rs} attributed to isolines L_{kl} and L_{rs}. The weighting factor w_{kl} is defined by a plane surface having the value 1.0 at the line connecting the sensors S_k and S_l and linearly decreasing to a value of 0.1 at the edge of the opposite border of the domain. The quality of these results are compared to the intersections found by a geometrical average.

Experimental validation

The previously described localisation method is used for the prediction of the known location of a non-destructive impact. The localisation method is applied to signals obtained from accelerometers and FBG sensors. For the experimental test with accelerometers, the sensor configuration of Figure 4.4 is employed. The reference data set for interpolation is

[1] The average wave speed measured in Section 4.5.2 is approximately 1 300 m/s.

[2] Wave propagation profile measured by Kundu et al.[29]

produced on a grid of 3 × 3 points. On each location of the reference data set, the array of arrival time delays is calculated as an average from three hits. The impact locations are predicted on 45 different points, with 3 hits at each location. Thus the error as well as the repeatability can be evaluated over the whole domain.

Finally, four surface-glued FBG sensors (cf. Figure 4.5) are used for localising a non-destructive impact. Again, a reference data set is produced on a grid of 3 × 3 points and serves for the prediction of five randomly selected impact locations. At each of these five locations, the impact is performed twice to test the repeatability of the method. The arrival time delay array for a single hit could not be produced at once because only two sufficiently sensitive optical channels were available for FBG interrogation. Therefore, the array of arrival time delays is assembled by carrying out a non-destructive impact for each sensor pair.

4.5 Results and discussion

4.5.1 Signal processing

The arrival time delays obtained from the accelerometer/FBG signals have a maximum standard deviation at one location of 10.3/12.4 µs and an average standard deviation for all measurements of 2.3/3.2 µs, respectively. Considering a wave speed of 1 300 m/s, this uncertainty in arrival time delay corresponds to a maximum uncertainty in position of 16 mm at one location and an average uncertainty of 4.2 mm. An uncertainty in location of approximately 2 mm can be attributed to a lack of precision during the manual excitation with the hammer. The higher imprecision of the arrival time delays obtained from FBG signal is due to the higher noise level. Larger deviations are due to a bad choice of the threshold value and a relatively high noise level in the signals. Throughout the experiments, the sensitivity of the FBG sensors was found to be sufficient when the incident waves arrived at an angle within ±45 °.

4.5.2 Wave speed measurements

The propagation speed is almost independent of propagation direction with an average value of 1 300 m/s (±100 m/s). The maximum relative standard deviation for three repeated tests in one propagation direction is 5 %. The wave speed as a function of propagation direction is shown in Figure 4.12. It agrees very well with the theoretical group velocity of the zero-order antisymmetric A_0 Lamb waves determined in Table 4.1 of Section 4.2.3.

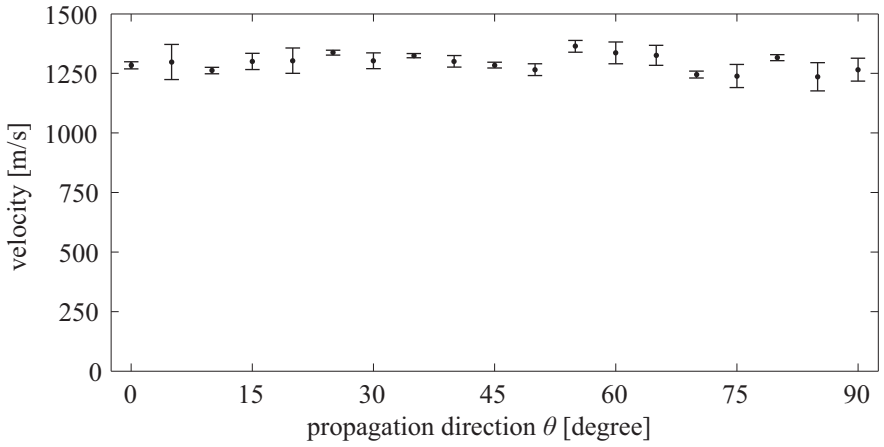

Figure 4.12: Experimentally measured wave velocity as a function of propagation direction. The error bars indicate the standard deviation of the measurements.

4.5.3 Numerical evaluation of interpolation error

The interpolation error is numerically evaluated over the whole domain and is expressed in terms of a radius between the exact position and the predicted position. Figure 4.13 shows the distribution of the error over the domain and an example of four arrival time delay isolines. A maximum error of 8.4 mm and an average error of 3.3 mm over the considered domain are obtained. Table 4.2 shows the influence of several parameters on the precision of the location prediction.

- When using a reference data set defined on a grid of 5×3 points, the average precision can be enhanced in the x_1 direction. The average error relative to a characteristic size of the reference grid is shown to be constant and is approximately 4 % of the distance between the reference points. In fact, the average error in Figure 4.13 is

Case	n_R	n_S	$n_{\text{intersections}}$	Location computation	Wave velocity	Prediction error [mm] maximum	average
1	3×3	4	4	weighted average	isotropic	8.4	3.3
2	5×3	4	4	weighted average	isotropic	7.1	2.3
3	3×3	3	3	weighted average	isotropic	11.8	4.6
4	3×3	4	8	weighted average	isotropic	7.0	3.0
5	3×3	4	4	geom. average	isotropic	6.2	2.9
6	3×3	4	4	weighted average	anisotropic	7.7	3.5
7	5×3	4	4	weighted average	anisotropic	6.9	2.7

Table 4.2: Numerically evaluated precision of the impact location prediction.

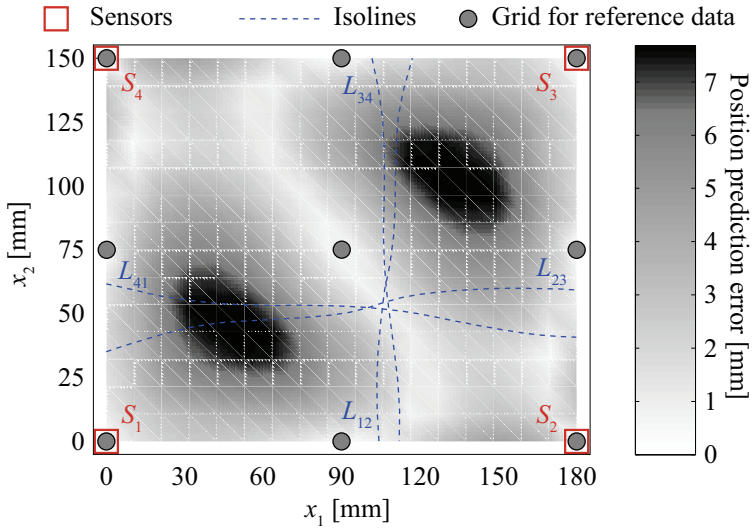

Figure 4.13: Localisation error due to numerical interpolation. An example of a set of arrival time delay isolines is given.

3.3 mm which is compared to a distance between the reference points of 90 mm and 75 mm in the x_1 and x_2 direction, respectively. It is reasonable in practice to have a similar spacing of the reference grid in both direction.

- The results confirm that the precision is worse when fewer sensors are used. The use of only 3 sensors yields to a maximum error of 11.8 mm and some of the predicted locations are found to be out of the bounds of the reference data. The fourth row in Table 4.2 shows that the prediction is only slightly enhanced when 8 intersections of a total of 6 isolines (in case of four sensors, a maximum of six pairs of sensors can be formed) are computed.

- This validation test confirms that the intersection between two isolines should only be taken into account if the isolines are far from being parallel to each other.

- Under the condition of an errorless reference data set, the geometrical average of the intersections gives a better prediction than a weighted average. The influence of confidence factors is also tested with experimental data in the next section.

- The interpolation method also gives accurate predictions in case of an orthotropic wave speed profile. Predictions can be slightly improved using a finer reference grid.

- Beyond the domain delimited by the sensors a prediction of the location is possible. However for each pair of sensors (S_k, S_l), the response surface $\left[\widehat{\Delta t}^{R}_{kl}(x_1, x_2)\right]$ takes a constant value on the semi-infinite long lines aligned with both sensors S_k and S_l

and located outside of the domain delimited by the two sensors. When the impact is located beyond the sensors, the predicted location might not be unique or can be less accurate.

4.5.4 Experimental validation

Accelerometers are used to experimentally validate the signal processing and localisation method. Figure 4.14 shows the predicted locations compared to the exact positions. The average prediction error is 6 mm and can mainly be attributed to the interpolation error which is related to the spacing between the reference points. The maximum prediction error of 32 mm is due to an outlier whose arrival time delay determination is erroneous because of abnormally noisy signals. Using a reference data set of 5 × 3 could slightly

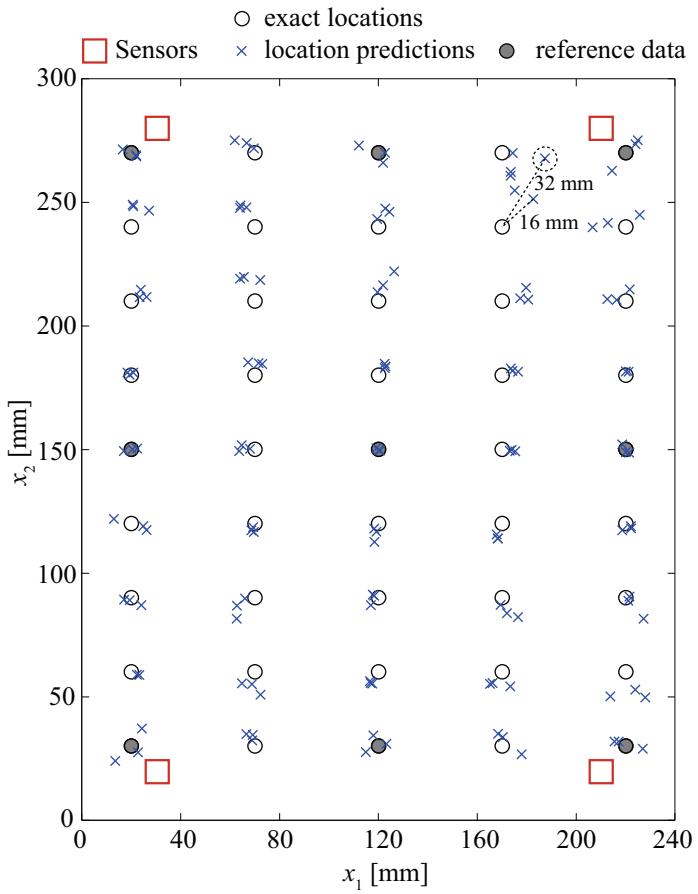

Figure 4.14: Experimentally predicted impact locations using accelerometer signals and interpolation-based localisation method.

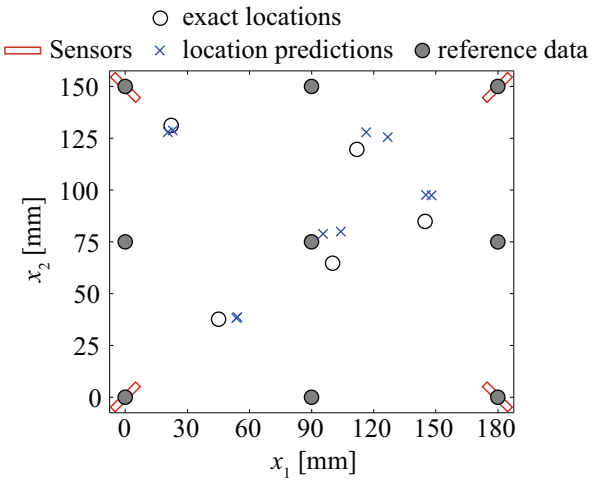

Figure 4.15: Experimentally predicted impact locations using four FBG sensors and interpolation-based localisation method.

improve the average prediction error to 5 mm, whereas the maximum error of the outlier could not be improved.

The average prediction error in the experiment with the FBG sensors is 10.1 mm and the maximum error is 15.5 mm (Figure 4.15). These values are attained using confidence factors which can reduce errors due to badly determined arrival time delays in case the impact is located far away from a sensor pair. The amplitude of a wave diminishes with increasing travelling distance and, consequently, it is difficult to determine the wave front because the signal-to-noise ratio becomes smaller.

The prediction accuracy difference between results obtained from FBG signals and accelerometer signals is also attributed to a higher uncertainty in determining the arrival time delays in case of FBG measurements. Furthermore, the arrival time delay arrays have not been produced simultaneously but have been assembled from different tests and, hence, uncertainties are accumulated.

If errors are present in the reference data set, either in terms of imprecise arrival time delays or inaccurate reference positions, these are directly reflected in the location prediction. Therefore, particular care must be taken when the reference data set is produced. It is suggested to repeat and average the reference measurements on each position. It is found that an average over 2 – 4 hits allows to identify erroneous data and reduce errors.

4.6 Summary and conclusion

FBG sensors can be used to determine the arrival time of a wave initiated by a low velocity impact. The precision of the arrival time delays could be enhanced by further improving the signal-to-noise ratio of the FBG interrogation. The data obtained from FBG sensors can be used to predict the location of a non-destructive impact. The presented interpolation-based localisation method is versatile and does neither require the knowledge of the wave propagation profile nor the exact positions of the sensors.

The FBG sensors should be placed at the periphery of the region monitored for impacts. Outside of the domain delimited by the sensors, the accuracy of the impact location prediction diminishes. A distance of a couple of centimetres should be kept to the edge of the plate or the fixture. Close to this discontinuities, the wavefront originating from the impact may interfere with reflections from the boundary and the arrival time of the wave is difficult to determine.

A minimum of three sensors is theoretically needed for the impact localisation technique. It is however shown that a fourth sensor can considerably improve the prediction accuracy. When the region monitored for impacts is larger, it is useful to use additional sensors because the amplitude of the wave diminishes with propagation distance. The amplitude decreases because of viscoelastic dissipation and because the radius of the circular wave front increases. When the signal-to-noise ratio becomes too small, the arrival time of the wave is difficult to determine.

Although the method is experimentally validated for plates with a low wave velocity anisotropy, numerical validation of the method supports its applicability to structures with orthotropic velocity profiles. In the latter case, the predictions can be enhanced by using a finer reference grid for the interpolation points.

Regarding the impact location, an average/maximum prediction error of 10 mm/16 mm is obtained and it is shown that this error is independent of the plate size. Numerical and experimental validation of the method has allowed for the identification of the error sources. Part of the error is due to the interpolation error and is relative to the spacing in the reference data set. If the size of the plate is larger, more reference points are needed to keep the same order of error. Another part of the error is due to uncertainties in determining the arrival time of a wave at the sensors. This contribution to the error depends on the signal processing. It is independent of the plate size and presents a considerable fraction of the error when the localisation is based on FBG signals. The accuracy of the prediction may be enhanced by further improving the sensitivity of the optical FBG interrogation channels and thereby the signal-to-noise ratio.

The predicted impact location will serve as an initial guess for the damage position identification. Regarding the low uncertainty of less than 16 mm of the impact localisation method, the identification of the damage position can be limited to a circular region within a radius of ∼20 mm apart from the predicted location.

Chapter 5

Damage characterisation and modelling

5.1 Objective

Delamination damage is the first apparent failure mode in composite laminates under low-energy impact, followed by intralaminar matrix cracking. Such damage is difficult to characterised in laminates because delamination cracks are nearly invisible at the surface. Delamination propagates at the interface of adjacent plies having a different orientation [2]. In general, delaminations are peanut shaped [14, 122, 123], increasing in size towards the opposite side of the impact and alternatively spreading in both in-plane directions. In laboratory tests, the most common damage characterisation techniques are ultrasonic scanning, microscopic examination, X-ray photography, deplying, visual inspection, thermography, back lightening, shearography or eddy currents [3]. Some of these damage techniques are destructive, but in laboratory the main objective is a detailed mapping of the damage without the need to preserve the structure or specimen. The recent developments in computational power, reconstruction software, high-resolution and high-sensitivity sensors permit the use of microscale X-ray computed tomography (CT) for three-dimensional imaging of composites with defects.

The objective of this chapter is the characterisation and modelling of the damage observed in composite plates with a stacking sequence of $[0\,^\circ_2, 90\,^\circ_2, 0\,^\circ_2, 90\,^\circ_2, 0\,^\circ_2, 90\,^\circ_2, 0\,^\circ_2]_s$. The processing of the plates with dimensions of 300 mm × 140 mm is detailed in Section 2.2.2 and the material properties are given in Table 2.2. In each plate, the damage is produced by a centrally located low-velocity impact with energy ranging from 1.7 – 6.8 J. Different experimental techniques are employed to obtain detailed information on the dam-

age pattern and to validate such data. Among those, high resolution X-ray CT is used to create a three-dimensional image from the damaged zone. Microscopic images of sectioned plates are taken to confirm the distribution of the damage in the through-the-thickness direction and its extent in the in-plane directions. Ultrasonic C-scan images confirm the size and shape of the projected damage surface. Also visual inspection of the plate's opposite face is considered as a simple and rapid method to estimate the projected damage surface.

The study focuses on a detailed analysis of the damage type, its shape and extent in order to establish a faithful numerical model of the damaged plate. The scope is to achieve an extensive understanding of the observed damage, its influence on the local stiffness and damping of the laminate and, hence, its effect on the vibrational behaviour of the plate. Two different FE models of the damaged plates are constructed. The first model comprises the detailed, experimentally obtained information of the damage pattern and is mainly supposed to substantiate the findings from the experimental damage analysis. The second model is a simplified and faster model based on continuum damage mechanics and is intended to be used in the inverse numerical-experimental damage identification method presented in the next chapter. In this model, the shape of the damage is approximated and material properties and damage are homogenised. The parameters of the continuum damage model are determined for several experimentally measured damage sizes and, finally, the model is validated.

In order to study the influence of damage on the vibrational behaviour of the plate, the modal parameters of the plates are determined experimentally before and after impact. Experimental modal analysis is carried out under free and clamped BCs to understand and isolate the effect of the damage and exclude an influence of the clamping. Besides the influence of the damage on the eigenfrequencies of the plate, the change of the modal damping ratios as well as modifications of the mode shapes are investigated. The results from experimental modal analysis also serve for validation of the numerical models.

5.2 Sensitivity of the modal parameters to damage

Laminated composite plates are prepared and experimental modal analysis is carried out under free and clamped BC using Doppler laser vibrometry. Such data are also used to carry out a modal analysis after a central impact in order to reveal any change of the modal parameters. The equipment used for the modal analysis and the experimental procedure is detailed in Section 2.5. For selected plates, embedded FBG sensors are used to perform the modal analysis of the clamped plate.

To study the reproducibility of the test and investigate the influence of the impact energy on the modal parameters of an impacted plate, a series of experimental results is collected by reproducing the same experimental procedure on nine different plates as follows. Prior to each test, the modal parameters of the intact composite plates are determined under free and clamped BC. Then each plate is impacted with energy ranging from 1.7 to 6.8 J, followed again by a subsequent modal analysis under clamped and free BC. The effect of the damage on the eigenfrequencies, the damping coefficients as well as the mode shapes is studied within a frequency range of 3 500 Hz, which comprises 10 and 18 modes under clamped and free BC, respectively. The relative change of the natural frequency of mode m due to damage is defined by

$$\bar{f}_m^{\text{exp}} = \frac{f_m^{\text{damaged}} - f_m^{\text{intact}}}{f_m^{\text{intact}}} \tag{5.1}$$

where f_m^{intact} and f_m^{damaged} are the experimentally measured eigenfrequencies of the intact and damaged plate, respectively. The relative change of the modal damping ratio of mode m is defined by

$$\bar{\eta}_m^{\text{exp}} = \frac{\eta_m^{\text{damaged}} - \eta_m^{\text{intact}}}{\eta_m^{\text{intact}}} \tag{5.2}$$

where η_m^{intact} and η_m^{damaged} are the experimentally measured modal damping ratios of the intact and damaged plate, respectively.

The sequence of the frequencies of the damaged plate is reordered with respect to the eigenfrequencies of the intact plate using the modal assurance criterion (MAC). The MAC between an eigenmode $\boldsymbol{\beta}_i^{\text{intact}}$ and $\boldsymbol{\beta}_j^{\text{damaged}}$ is written

$$\text{MAC}_{ij} = \frac{\left(\boldsymbol{\beta}_i^{\text{intact}} \cdot \boldsymbol{\beta}_j^{\text{damaged}}\right)^2}{\left(\boldsymbol{\beta}_i^{\text{intact}} \cdot \boldsymbol{\beta}_i^{\text{intact}}\right)\left(\boldsymbol{\beta}_j^{\text{damaged}} \cdot \boldsymbol{\beta}_j^{\text{damaged}}\right)} \tag{5.3}$$

In this equation the operation $(\,\cdot\,)$ is the scalar product between two vectors. When MAC_{ij} is close to one, the shape of the eigenmodes are similar and the modes are considered to coincide. When the MAC is close to zero, the modes are considered to be orthogonal.

5.2.1 Sensitivity of the eigenfrequencies to damage

Figures 5.1a and 5.1b illustrate how the natural frequencies of selected modes systematically change with increasing impact energy. The asymmetric bending modes, where the damage zone is located on a nodal line, are most affected by the shear stiffness reduction caused by delamination. In case of 6.8 J impact energy, the first affected eigenfrequencies,

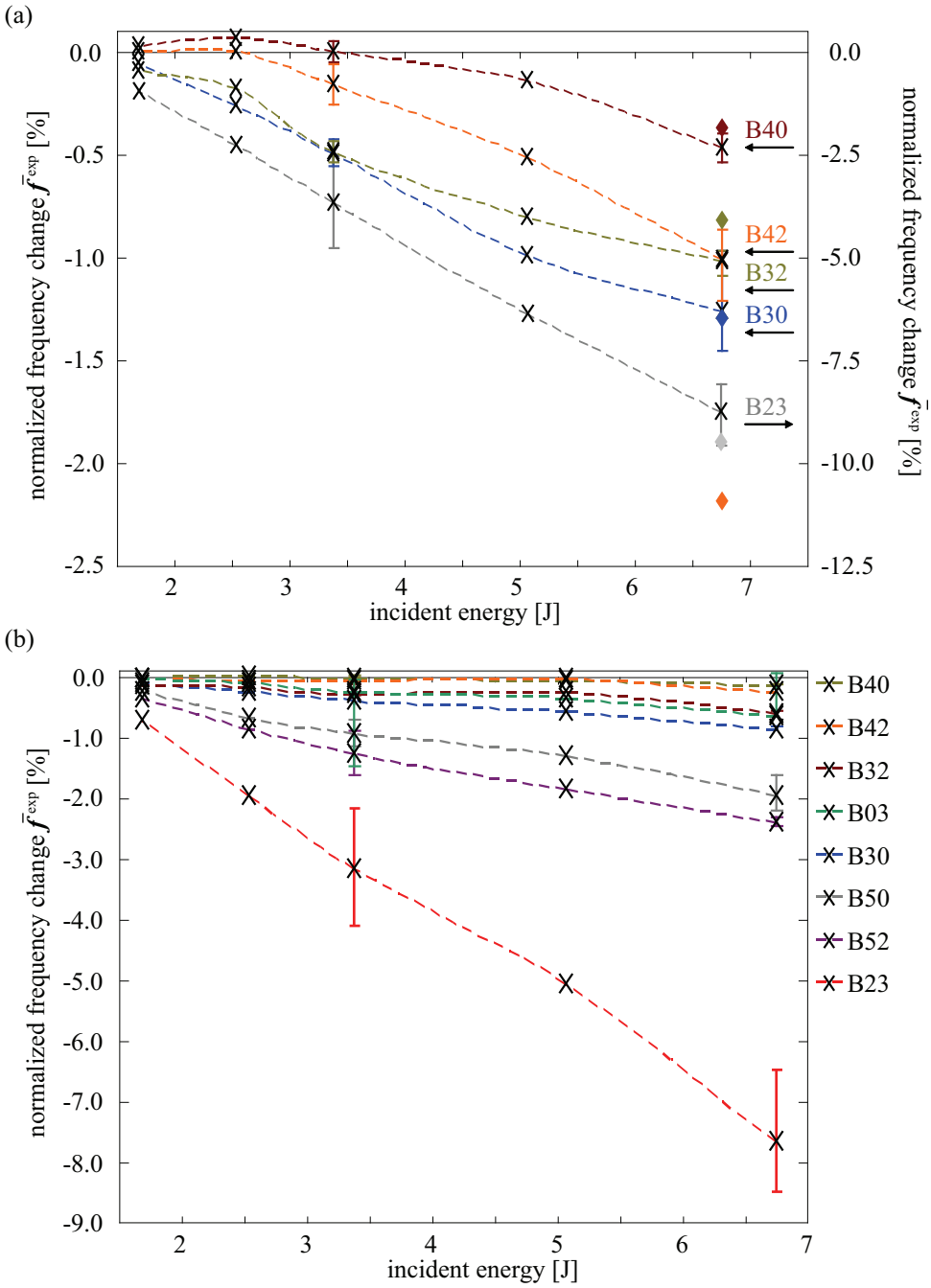

Figure 5.1: Experimentally measured normalised eigenfrequency changes of impacted plates with (a) clamped and (b) free BC. The convention to denote the eigenmodes is defined in Section 2.5.3.

which are lower than about 3 kHz, decrease by up to 2 % whereas higher eigenfrequencies, situated around 3.3 kHz, drop by 9 %. With high impact energies the natural frequencies of symmetric modes (e.g. B40)[1] also decrease. In case of low energies a small increase of the eigenfrequencies is apparent because the thickness of the plate slightly increases at the location of the damage and causes a local gain in bending stiffness.

The reproducibility of these tests is examined for impact energies of 3.4 J and 6.8 J and a small scattering of the eigenfrequency changes is found. Characterisation of the damage based on high resolution X-ray computed tomography indicates that the scatter of the relative change of the natural frequencies for a given impact energy can be explained by the different size of the damage area. Overall, a good correlation is found between the level of incident impact energy and the frequency change of asymmetric bending modes. Moreover, the frequency change of the modes that are the most sensitive to damage is significant and clearly much higher than the frequency resolution of the FBG or laser vibrometer based modal analysis.

5.2.2 Sensitivity of the damping ratios to damage

After the impact, no systematic change of the modal damping factors is observed with increasing impact energies. The modal damping factors of plates impacted with energy of 6.8 J change drastically by up to 150 %, but the observed changes are not reproducible for the three different plates. In Figure 5.2 it can be seen that the increase or decrease of the damping factors is high, but the standard deviation of the measurements is almost as high as the change itself. The measurements are non-reproducible for clamped plates and also for plates with free BC so that the absence of reproducibility cannot be entirely associated to a change of dissipation at the clamping.

The increase of the damping is partially explained by the friction occurring at the interfaces of the delamination. The amount of additional damping may not be reproducible because this friction depends on the nature of the fracture surface, the amplitude of the vibrations and the stresses that are opening or closing the delaminations.

5.2.3 Sensitivity of the mode shapes to damage

The mode shapes of the free plate are measured with an SLDV. The displacement mode shape is defined up to a scalar factor and can be directly deduced from the velocity measurements. When the spatial discretisation of the plate is coarse, e.g. a measurement grid

[1] The convention to denote the eigenmodes is defined in Section 2.5.3.

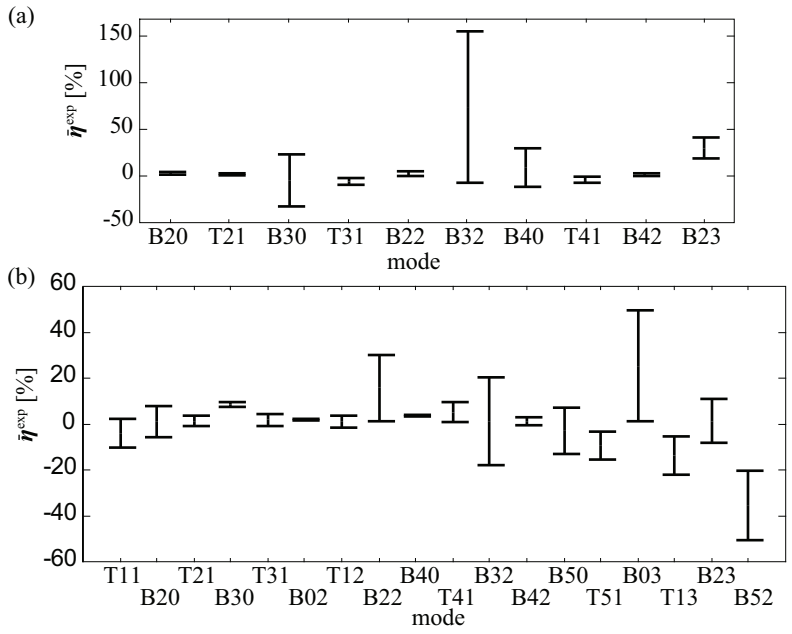

Figure 5.2: Normalised change of modal damping ratios measured with (a) clamped and (b) free BC for three different plates impacted with an energy of 6.8 J. The convention to denote the eigenmodes is defined in Section 2.5.3.

of 12 × 12 points is used, the displacement mode shapes of the damaged plate are almost identical to the displacement mode shapes of the intact plate.

The curvature mode shapes are analysed by scanning a segment of 500 points along the symmetry line of the free plate in the x_1 direction as shown in Figure 5.3b. The curvature shape is calculated from the smoothed displacement mode shape by double differentiation. In Figure 5.3a, the central damage in the plate becomes locally noticeable in the curvature shape of mode 4 (B30). Scans along alternative lines confirm that the change of the curvature is considerable only in a region slightly bigger than the damage area.

The numerical model presented in Section 5.4.1 confirms that the local changes of the curvature mode shapes are either due to a local stiffness degradation or to the appearance of locally dominant modes. When plies close to the plate's surface are delaminated over a sufficiently large area, local bending modes of this separated laminae appear. Hence, the transverse displacement of all points in the through-the-thickness direction is not unique in all the plies and thus, it is not always possible to capture these local mode shapes with embedded sensors.

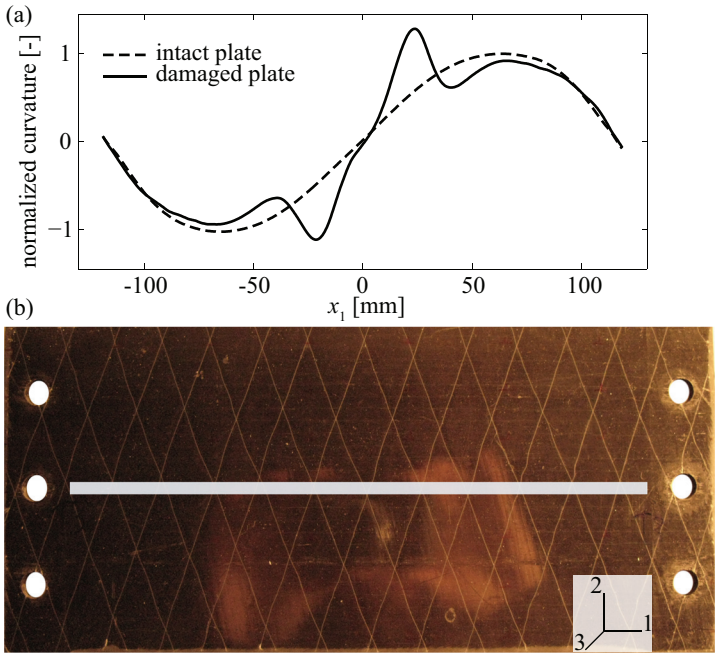

Figure 5.3: (a) Curvature shape of mode 4 (B30) along the central line of a plate with free BC and previously impacted with energy of 6.8 J. (b) Plate with a strip of reflective tape.

5.2.4 Discussion of the experimental sensitivity analysis

This experimental study shows that the eigenfrequencies as well as the modal damping factors and curvature mode shapes are sensitive to damage originating from low-velocity impacts. In the investigated impact energy range some eigenfrequencies see a relative decrease of up to -9 %, which is considerable compared to the measurement precision of the frequencies (0.06 %). The changes of the eigenfrequencies are due to a local stiffness degradation of the laminate.

Although the changes of the modal damping factors are large, the scattering of the data is high and no reproducible trend can be observed. The change of the damping is mainly attributed to energy dissipation by friction at the interfaces of the delamination. This dissipation mechanism is expected to depend on the transverse stresses at the delamination's interfaces and to be a non-linear phenomena with respect to the vibration amplitude.

A coarse measurement of the displacement mode shapes does not reveal any considerable change due to the damage. The computation of the curvature shape from velocity measurements along a fine grid manifests a change that is mainly limited to a region as large as the damage zone. When considering classical plate theory, the strain mode shapes are proportional to the curvature mode shapes. The modifications in the strain mode shapes

may be detected by direct measurements of the strain, but only if distributed measurements or many local strain measurements can be done. Because the mode shape vectors are defined up to a scalar factor, a few local measurements are not sufficient to highlight a change of the vector. Also the MAC, which allows to check the consistency between normalised eigenvectors, has a limited suitability to quantify the dissimilarity between to mode shapes [124].

From all modal parameters, the eigenfrequency measurements are retained for FE model validation and damage identification because a monotonic, almost linear relation is found between the eigenfrequency changes and the incident impact energy.

5.3 Damage characterisation

5.3.1 X-ray computed tomography

A detailed characterisation of the damage pattern is obtained by X-ray computed tomography which is carried out with a high resolution scanner from SkyScan, model 1076. A resolution of 9 µm per voxel[2] is used for scanning a part or the entire damage zone of a plate. Part of the plate containing the damage is cut in order to reduce the X-ray absorption in the in-plane direction of the plate. For the scan, an aluminium filter of 1 mm thickness is employed and the X-ray source voltage is set to 100 kV at maximum power of 10 W. The best contrast for the projected images is obtained at an exposure time of 1 750 ms and an average of 3 projected images is taken. A complete scan takes approximately 12 hours with an additional reconstruction time of about 12 hours on a cluster with two computers (2 Intel Xeon 5160 3.00 GHz with 3 GB RAM).

A cross-section of the three-dimensional image obtained from the computed tomography reconstruction software is shown in Figure 5.4. It can be seen that delamination cracks dominate the damage and intralaminar cracks are limited to a region located just beneath the impact point. A priori the exact extent of a delamination cannot be determined on one single cross-section. Due to its high resolution, the X-ray scanner produces cross-section images at intervals of 9 µm. A moving average over 50 cross-sections along the image stack in the x_1 direction allows to reduce the noise level and better distinguish a crack from the surrounding material.

To further treat the X-ray data, the cross-section images are converted to black and white ones using a grey level threshold of 0.6. The interfaces between plies are then

[2] volumetric picture element

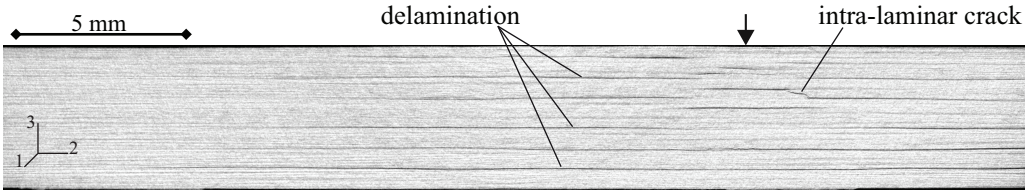

Figure 5.4: Cross-section image obtained by tomography reconstruction software from a plate impacted with energy of 5.1 J. Arrow indicates the impact point.

projected on a plane parallel to the plate in order to delimit the surface of each delamination as shown in Figure 5.5. The extent of each delamination can be identified accurately and is indicated by a diagonally patterned surface on the images. Thus, the surface of each delamination can be digitised. The oblique zones with black spots on each of these images are due to the presence of nylon fibres that keep the carbon fibres of the UD prepregs aligned while the resin is not cured.

Finally a complete three-dimensional representation of the delaminations is constructed as illustrated in Figure 5.6. It can be noticed that the delamination spreads in the x_1 and x_2 directions. In general, the size of the delaminations increases towards the opposite side of the impact location, whereas the delamination at the last interface is considerably longer

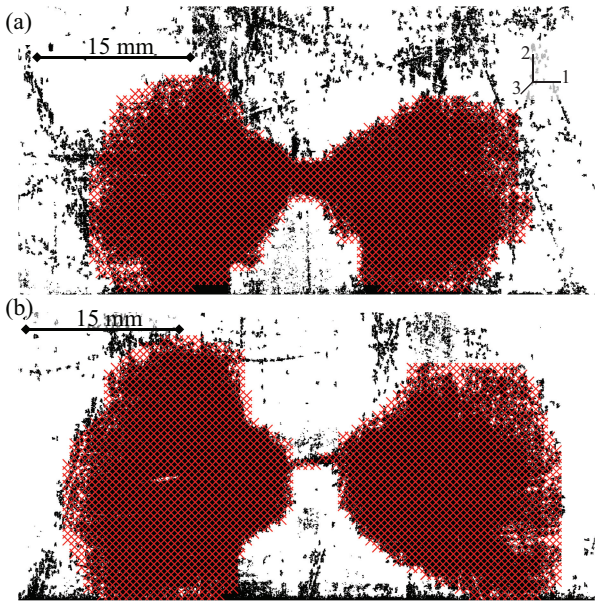

Figure 5.5: Top view projection of delaminations located at the fourth (a) and ninth (b) interface of the plate impacted with energy of 5.1 J. The diagonal textured surface is retained as effective delaminated surface.

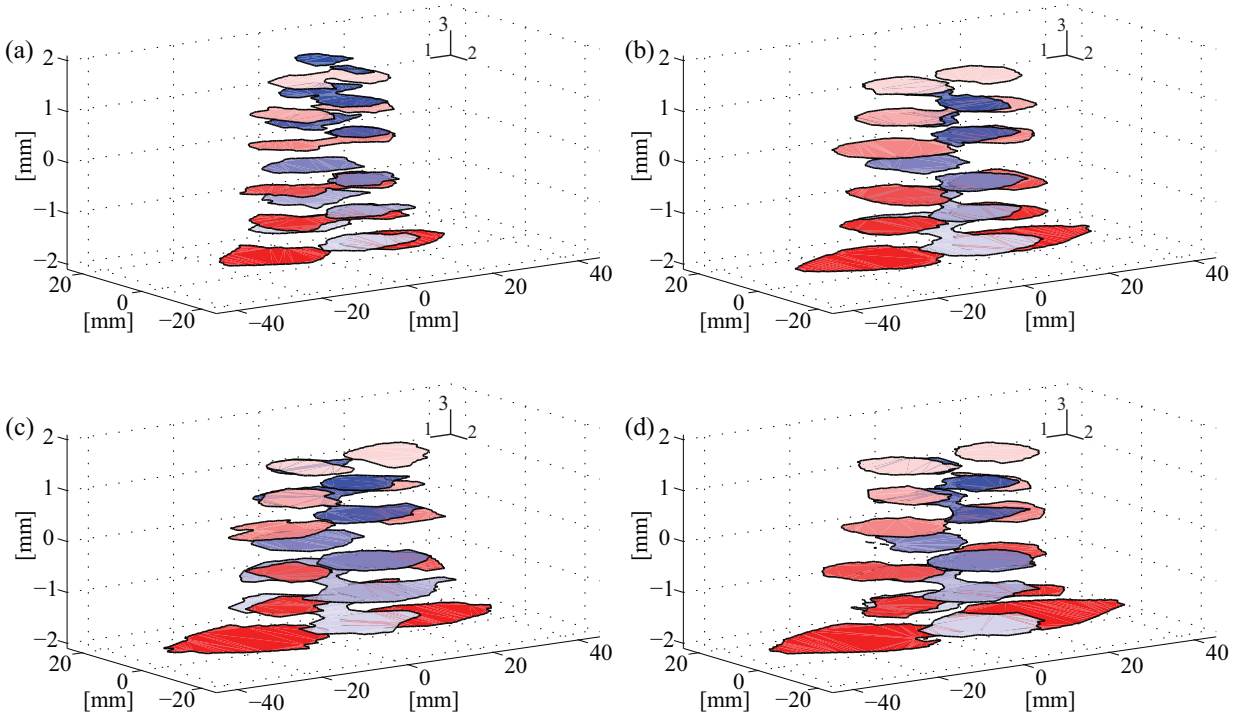

Figure 5.6: Three-dimensional damage pattern obtained from X-ray CT images of plates impacted with energies of 3.4 J (a), 5.1 J (b) and 6.8 J (c) & (d).

than the ones at the other interfaces. No delamination is apparent in-between the four plies in the middle of the symmetric plate because their fibres are all oriented in the same longitudinal direction.

The total delaminated surface is plotted as a function of absorbed energy in Figure 5.7a. A fit of a linear curve to these data points results in an absorbed energy per unit of delamination area of $280\,\mathrm{J/m^2}$. The damage pattern is then projected on a plane parallel to the plate. Figure 5.7b shows a plot of the projected damage surface as a function of the incident impact energy. Overall, a good affine relationship is observed between the total delaminated surface and the absorbed energy, but also between the projected damage surface and the incident energy. Because the projected damage area and the eigenfrequency changes have an almost linear relation to the incident impact energy, it can be concluded that the eigenfrequency changes have an almost linear relation to the damage surface.

Referring to the projected shape of the damage, shown in Figure 5.8, it is reasonable to approximate it by a rhombic area. The size of the rhomb is calculated so that the area of the approximated shape and the projected, experimentally measured, shape are equal.

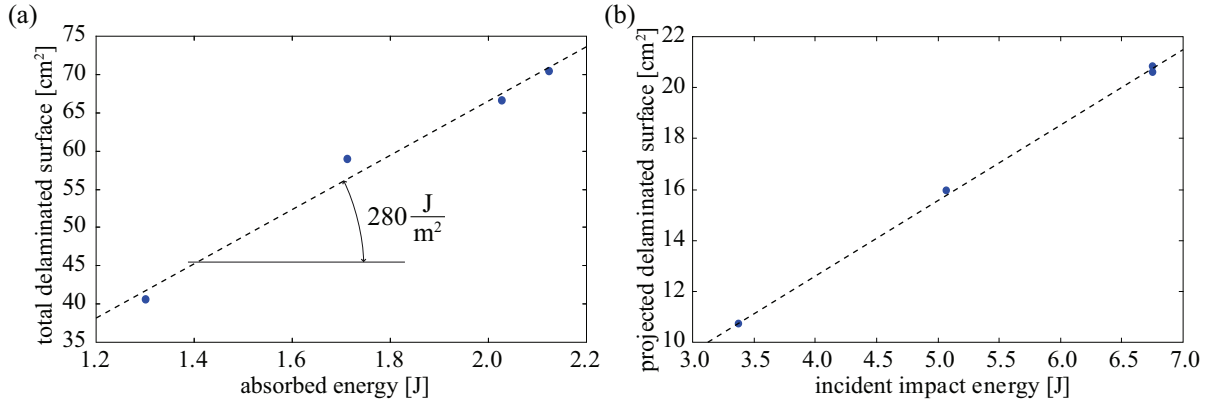

Figure 5.7: (a) Total delamination area as a function of absorbed energy. (b) Projected delamination area as a function of incident impact energy.

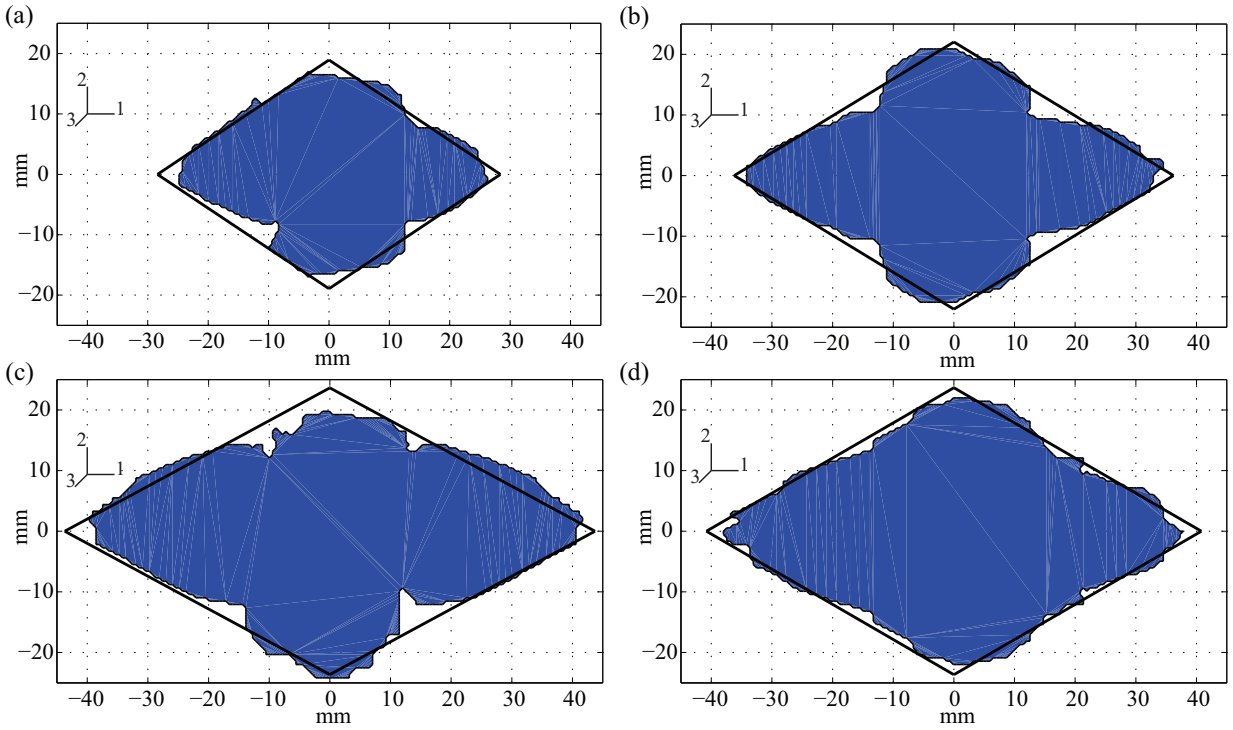

Figure 5.8: Projection of all delaminated interfaces on a common plane and rhombic approximated shape. Obtained from X-ray CT images of plates impacted with energies of 3.4 J (a), 5.1 J (b) and 6.8 J (c) & (d).

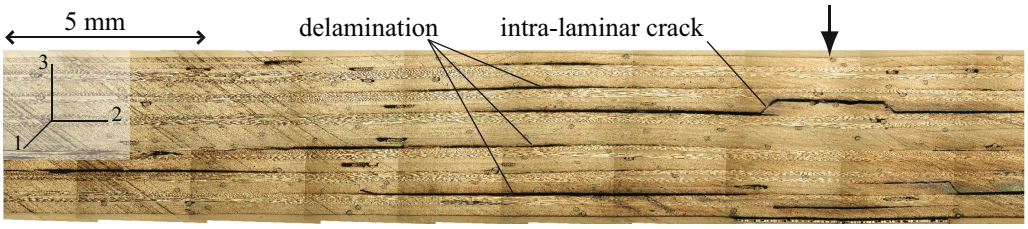

Figure 5.9: Microscopic image of a cross-section of a plate impacted with energy of 6.8 J. Arrow indicates impact point.

5.3.2 Microscopic images

Microscopic images are taken from selected plates impacted with different energies to validate the distribution and the extent of the cracks. The damaged plate is sectioned, embedded in epoxy resin and polished. The final image, shown in Figure 5.9 is assembled from multiple microscopic images. It confirms that intralaminar cracks are rare and that mainly delamination damage is present. The in-plane extent of the delaminations agrees well with the values obtained from the three-dimensional CT images. No delaminations propagate between plies oriented in the same direction and delaminations are only present at every second interface where the lay-up orientation changes.

5.3.3 Ultrasonic C-scan

Images obtained from ultrasonic C-scan are used to check the shape and size of the projected damage surface obtained from X-ray CT (Figure 5.8). Therefore, the composite plates are immersed in water and placed on blocks over a steel plate at a distance of 4 mm. A pulse echo system with a 2 MHz probe is used to scan a region of 100 mm × 80 mm over the plate. Instead of measuring the acoustic reflections from each crack in the material, the reflection peak of the steel plate is monitored. If delaminations are present, the acoustic reflection peak of the steel plate is not apparent in the signal, because most of the energy of the ultrasonic pulse is reflected or absorbed by the delamination. This method does not allow to estimate the through-the-thickness location of a delamination but it gives an accurate picture of the projected damage surface.

Figure 5.10 compares the C-scan image to the projected damage shape obtained from X-ray CT. The four squares at the corner of the scan are due to square reflective patches glued on the plate for the SLDV measurements. The damage area observed on the X-ray CT images is slightly underestimated and/or the one of the ultrasonic C-scan image is overestimated. Towards the end of a typical crack, the crack opening is very small and

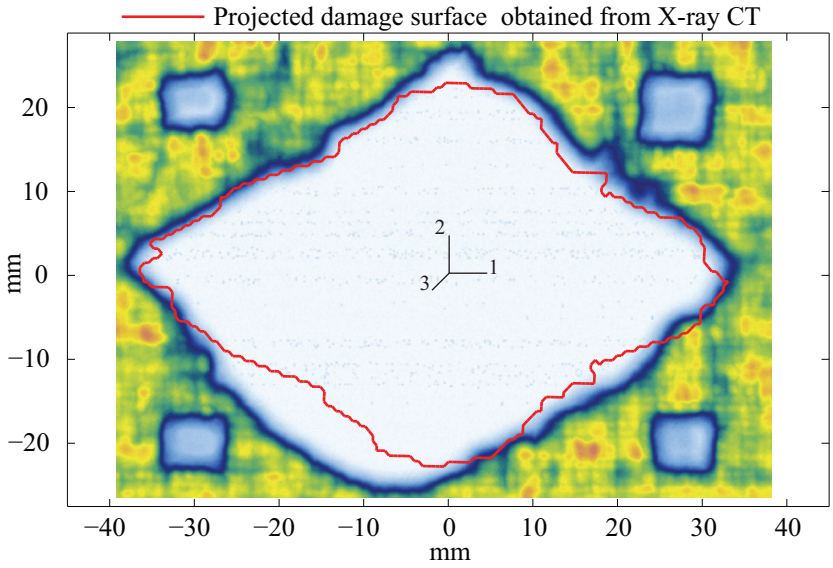

Figure 5.10: C-scan image of a plate impacted with energy of 6.8 J. The results are compared to the projected damage shape obtained from X-ray CT (thin line).

may therefore not be visible on the X-ray images. Overall, the agreement between both measurements is very good.

5.3.4 Visual inspection

It is noticed in the microscopic image of Figure 5.9 that a total crack opening of several micrometer ($\sim 20 - 50\,\mu m$) arises at a delamination thereby increasing the global thickness of the laminate. Moreover, the delaminations are increasing in size towards the opposite side of the impact (Figure 5.6). A blister visible to the naked eye forms on the plate's side opposite to the impact. The shape of the blister can be outlined along the edge where a discontinuity of the angle of light reflection is clearly visible. The length and the width of the rhombic shaped damage zone can afterwards be measured with a precision of approximately 2 mm, which results in a precision of about 10 % in terms of the damage area.

5.3.5 Summary of damage characterisation results

It can be observed in this study, that X-ray CT provides very detailed information on the damage pattern. Mainly delamination damage is found in the laminate after impact. The

total delaminated surface is almost proportional to the absorbed impact energy. The delaminations are peanut shaped and spread alternatively in the longitudinal and transverse direction only between plies having a different stacking orientation. Intralaminar cracks are rare and no fibre breakage is observed.

The shape of the projected damage can be approximated by a rhomb. The projected damage surface has an almost linear relation to the incident impact energy. It is found in Section 5.2 that the experimentally measured eigenfrequencies vary proportionally to the impact energy. As a result, the eigenfrequency changes have an almost linear relation to the damage size. These findings, i.e. the type of damage, its shape and size, are validated by microscopic and C-scan images. It is found that the size of the projected damage can also be estimated by visual inspection because a blister forms on the plate's surface opposite to the impact.

5.4 Damage models

In this section, numerical models are constructed to investigate the effect of damage on the modal parameters of a plate. The experimentally measured frequency changes presented in Section 5.2 are used to validate the numerical models. Two different models are presented whereof the first comprises the detailed three-dimensional information obtained from X-ray CT images. The second model is a simplified model based on homogenisation of damage and material properties. A general description of the approach in FE modelling is given in Section 2.6.

5.4.1 Detailed delamination model

The composite plate is modelled with the FE software Abaqus 6.8-2 using a regular mesh. Solid quadratic finite elements with a reduced integration scheme (C3D20R) are employed. In the thickness direction, the plate is meshed with 14 elements in order to include the stacking orientation of the plate lay-up in the model definition and the in-plane element size is set to 7 mm. At the centre of the plate, a cruciform region having a refined mesh with in-plane element dimensions of 2 mm $\times$ 2 mm is defined for a more detailed reproduction of the damage shape (Figure 5.11a). The final mesh consists of 31 500 elements and is identical for the intact and the damaged plate. The material properties of a UD carbon fibre reinforced polymer ply listed in Table 2.2 are implemented. Two bands with a width of 29 mm are partitioned at each end of the plate in order to block displacements in every direction in the case of clamped BC. Under these conditions a numerical modal analysis is

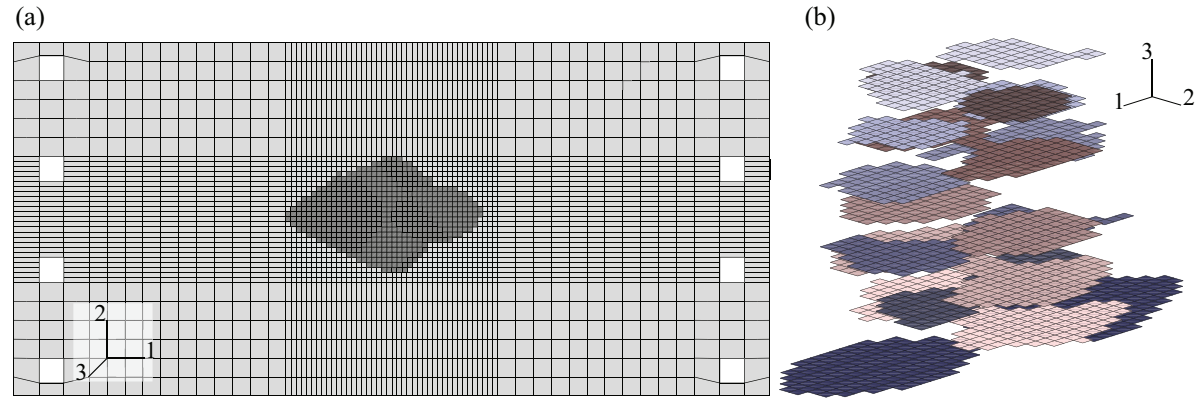

Figure 5.11: a) Mesh of the detailed damage model with the projected damage indicated by the dark grey colour. (b) Approximated three-dimensional shape of the delaminations.

performed to obtain the reference values of the natural frequencies of the intact plate with free and clamped BC.

In the detailed model of the damaged plate, only the effect of the delaminations between the plies having a different stacking orientation is accounted for. Based on the X-ray CT images, the three-dimensional representation of the delamination pattern is introduced in the FE model of the plate and the delaminated surfaces are approximated by a 2 mm × 2 mm grid (Figure 5.11b). At the location of the delaminations, the nodes at the interface of two plies are duplicated and disconnected. Thus, the numerical modal analysis with free and clamped BC simulates the influence of the delaminations on the natural frequencies of the composite plate. No contact is considered between the delaminated interfaces because numerical modal analysis is based on the assumption of linearity.

The good correlation between the numerically calculated frequency changes and the experimentally observed frequency changes of a plate with clamped BC are shown in Table 5.1. Note that the eigenfrequency changes of modes number 3, 6 and 10, which are identified to be most sensitive to impact damage in the present test configuration, are well reproduced by the numerical model. An increase of the natural frequencies of symmetric bending modes, e.g. the first eigenmode, cannot be simulated because the local increase of the plate thickness in the damaged region is not taken into account by the numerical model.

When the numerically calculated eigenfrequency change is compared to the measured one under free BC, a similar agreement is obtained as for the clamped BC. This study clearly shows that the delamination pattern used in the present model is sufficient to explain most of the observed frequency changes and thus the change of the natural frequencies can

			Relative eigenfrequency changes							
Mode	Mode shape	Freq. [Hz]	Num. [%]	Exp. [%]	Num. [%]	Exp. [%]	Num. [%]	Exp. [%]	Num. [%]	Exp. [%]
	Impact energy :		3.4 J		5.1 J		6.8 J (1)		6.8 J (2)	
1	B20	476	0.00	0.03	-0.02	0.03	-0.03	-0.11	-0.03	-0.04
2	T21	525	-0.02	-0.03	-0.03	-0.01	-0.03	-0.12	-0.05	-0.10
3	B30	1289	-0.43	-0.42	-0.94	-0.99	-1.10	-0.96	-1.18	-1.28
4	T31	1357	-0.02	-0.03	-0.03	-0.05	-0.04	-0.15	-0.06	-0.13
5	B22	1366	-0.06	0.10	-0.19	0.12	-0.28	0.15	-0.34	0.05
6	B32	1967	-0.44	-0.43	-0.92	-0.80	-1.12	-1.09	-1.16	-1.32
7	B40	2473	-0.10	0.05	-0.45	-0.13	-0.77	-0.54	-0.75	-0.33
8	T41	2546	-0.03	-0.03	-0.06	-0.04	-0.06	-0.22	-0.09	-0.12
9	B42	3024	-0.24	-0.06	-1.01	-0.51	-0.24	-0.94	-1.05	-1.05
10	B23	3310	-2.79	-2.54	-6.55	-6.34	-6.58	-8.58	-7.33	-9.53

Table 5.1: Comparison between numerical and experimental relative eigenfrequency changes.

mainly be attributed to a delamination type of damage.

5.4.2 Homogenised damage model

A simplified FE model including a continuum damage approximation is created to reduce the computation time of the numerical solver and to dispose of a simple damage model based on a few parameters only. The shape of the damage is approximated and the material properties and the damage are homogenised. Referring to the projected damage shape shown in Figure 5.8 and also the shape observed in literature [125], it is reasonable to approximate it by a rhombic area (cf. Figure 5.8). The parameters of the continuum damage model described hereafter are identified via mixed numerical-experimental optimisation.

Since the principal directions of the orthotropic damage are known to coincide with the symmetry axes of the plate configuration, a diagonal damage tensor D is introduced [126–133]. According to the damage mechanisms observed in the computed tomography images, only delamination damage is taken into account whereby only the transverse shear moduli G_{13} and G_{23} are affected. A degeneration of the longitudinal and transverse moduli E_1 and E_2 is not introduced in the model because no fibre fracture and almost no intralaminar cracks are seen in the tomography images. For the same reason, the in-plane shear modulus G_{12} is kept constant. Additionally, the initial values of Poisson's ratios and

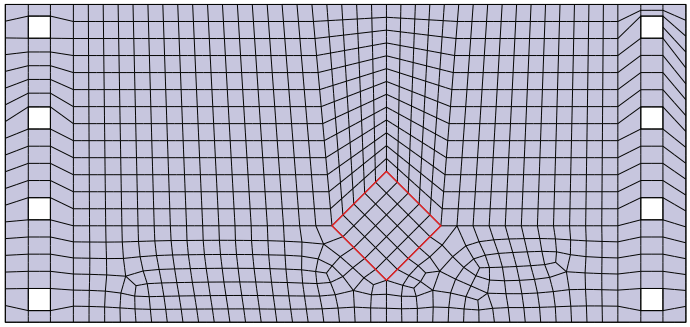

Figure 5.12: Mesh of the plate with a homogenised damage and a rhombic damage shape.

through-the-thickness Young's modulus E_3 are retained, because it can be shown that the eigenfrequencies of the plate are marginally sensitive to these material parameters.

Two damage factors are chosen to describe the loss of transverse shear stiffness due to the delaminations. A similar delamination model is considered by Johnson, et al. [134] and the reductions of the through-the-thickness shear moduli G_{13} and G_{23} are expressed in terms of the damage factors D_{13} and D_{23} by

$$\begin{aligned} \hat{G}_{13} &= (1 - D_{13})\, G_{13} \\ \hat{G}_{23} &= (1 - D_{23})\, G_{23} \end{aligned} \tag{5.4}$$

When D_{13} and D_{23} are equal to zero, the reference case for the intact plate is defined.

The FE model is meshed using 20 nodes quadratic brick elements with a reduced integration scheme, called C3D20R in Abaqus FEA 6.8.2. The mesh is regular and has n_3^e elements in the through-the-thickness direction and a general element size of W^e in the in-plane direction. The mesh in Figure 5.12 consists of three elements in the through-the-thickness direction and has an in-plane element size of 7 mm.

5.4.3 Damage factors of the homogenised damage model

The damage factors D_{13} and D_{23} are identified for different experimentally measured damage sizes by reducing the discrepancy between numerically calculated and experimentally measured eigenfrequency changes. The Levenberg-Marquardt algorithm, presented in Section 6.5.2, is used for the minimisation of the objective function (6.2) defined in Section 6.3. A sensitivity analysis of the homogenised damage model and the error norm to the damage factors D_{13} and D_{23} is also made in sections 6.4.1 and 6.4.2, respectively.

This study is based on the experimental results of 4 plates impacted at energies ranging from 3.4 J to 6.8 J. The size of the rhombic damage area is determined using the X-ray

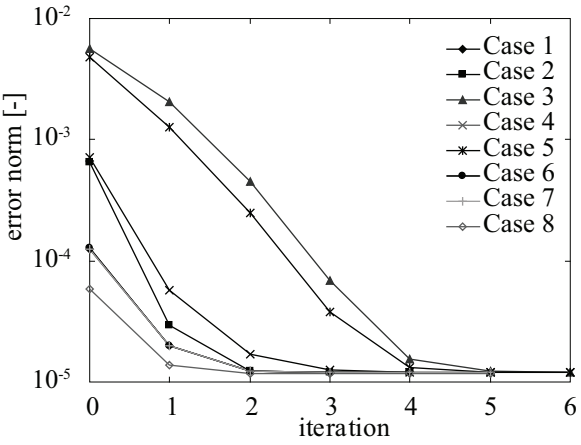

Figure 5.13: Convergence graph of the error norm for different initial values of the damage factors.

CT images shown in Figure 5.8. The robustness of the optimisation procedure is tested by using different initial values for the damage factors. Furthermore, the influence of the mesh size on the solutions is studied by varying the number of elements in the through-the-thickness direction from 1 to 6 and the in-plane element size from 10 mm to 4 mm. The residual tolerance of the optimisation algorithm is set to a low value of $1{\cdot}10^{-8}$ so that it is never met and the convergence tolerance is set to $1{\cdot}10^{-4}$. The latter tolerance is in all cases the stopping criterion for the optimisation. Depending on the initial values, 4 – 6 iterations were needed until convergence (Figure 5.13), whereas no significant improvement of the error norm could be noticed in the last 2 – 3 iterations.

Table 5.2 shows the results of the identification of the damage factors for a plate impacted with an energy of 3.4 J. The choice of the initial guess for the damage values does not, and the mesh only marginally, influence the solution of the optimisation procedure. A mesh with a single element in the through-the-thickness direction is not recommended because no faithful representation of the shear stiffness is obtained. The element size in the in-plane direction does not influence the results as long as the mesh size is regular and smaller than 4 times the plate thickness. The reference eigenfrequencies of the intact plate must be computed with a similar mesh size than the ongoing optimisation evaluations of the numerical model.

Table 5.3 summarises the experimentally determined damage sizes of the four different plates and the results of the damage factor identification. The slight increase of the damage factors with increasing impact energy can be attributed to a higher damage concentration inside the damage zone, however it remains relatively insignificant compared to the uncertainties and variability of the estimated damage area. Moreover, after identification, the

Case	Damage size W_1 [mm]	W_2 [mm]	Mesh size W^e [mm]	n_3^e	Initial guess D_{13} [%]	D_{23} [%]	Solution D_{13} [%]	D_{23} [%]	Residual norm [-]
1	56.74	37.82	7	3	90	90	83.42	85.46	$1.2128{\cdot}10^{-5}$
2	56.74	37.82	7	3	10	10	83.40	85.46	$1.2128{\cdot}10^{-5}$
3	56.74	37.82	7	3	98	98	83.43	85.46	$1.2129{\cdot}10^{-5}$
4	56.74	37.82	7	3	98	10	83.46	85.46	$1.2129{\cdot}10^{-5}$
5	56.74	37.82	7	3	10	98	83.37	85.47	$1.2128{\cdot}10^{-5}$
6	56.74	37.82	4	6	90	90	83.50	85.43	$1.2132{\cdot}10^{-5}$
7	56.74	37.82	10	3	90	90	83.39	85.49	$1.2107{\cdot}10^{-5}$
8	56.74	37.82	10	1	90	90	84.92	87.21	$1.1640{\cdot}10^{-5}$

Table 5.2: Robustness study of the algorithm to different initial values of the damage factors and sensitivity to mesh size. W^e is the in-plane element size of the elements and n_3^e is the number of elements in the through-the-thickness direction.

residual error norm based on the numerically calculated relative changes of eigenfrequencies and experimentally measured relative changes of eigenfrequencies is small. The standard deviation of the eigenfrequency changes is about 0.04 % which is very small compared to the measured eigenfrequency changes of up to 9.5 %.

Impact energy [J]:	3.4	5.1	6.8 (1)	6.8 (2)
W_1 [mm]	56.7	72.0	81.6	87.4
W_2 [mm]	37.8	47.2	47.3	47.3
D_{13} [%]	83.4	87.6	88.4	91.9
D_{23} [%]	85.5	91.7	92.5	93.9

Table 5.3: Damage factors obtained from numerical-experimental identification on 4 different specimens.

5.4.4 Validation of the homogenised damage model

The homogenised damage model is used to predict the eigenfrequency changes of the plate with a known damage size. The eigenfrequency changes of the clamped plate are measured with embedded FBG sensors as described in Section 3.3.4. The size of the rhombic damage area is varied between 56 mm and 57 mm in width and 88 mm to 90 mm in length to account for measurement uncertainties. Regarding the damage factors D_{13} and D_{23} found for the plates impacted with energy of 6.8 J, they are chosen between 92.5 % – 93.9 % and 88.4 % – 91.9 %, respectively (cf. Table 5.3).

The good agreement between the predicted relative changes of the natural frequencies

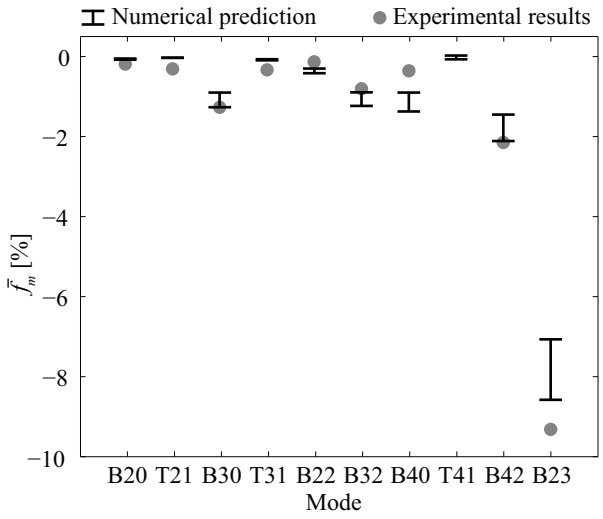

Figure 5.14: Comparison of predicted natural frequency changes to experimentally measured eigenfrequency changes of plate with embedded FBG sensors impacted with energy of 6.8 J.

and the experimentally measured changes is presented in Figure 5.14. Note here that the measurements have not been sensitive to mode 8 (T41) due to the positioning of the two FBG sensors. The homogenised damage model with constant damage factors for transverse shear moduli is found to be sufficient to reproduce the eigenfrequency changes observed in experiments.

5.4.5 Discussion

The detailed delamination model including the three-dimensional damage information obtained by X-ray CT demonstrates that the eigenfrequency changes are mainly due to delamination damage. Even though the intra-laminar cracks are not accounted for, the model allows to reproduce the eigenfrequency changes due to damage under free and clamped BCs.

A simplified homogenised damage model based on two damage factors is found to be sufficient to model the loss of transverse shear stiffness and the corresponding reduction of the eigenfrequencies. The damage factors of the homogenised damage model are identified for different experimentally measured damage sizes. The mesh used in the FE model needs to be similar when modelling the intact and damaged plated to eliminate its influence on the eigenfrequencies. Values between 85.4 % and 93.9 % are found for both factors. It has to be mentioned that, a priori, these values are only valid for the studied laminate and a

damage produced by a transverse impact with an energy in the studied range.

5.5 Conclusion

The experimental study reveals that for the studied range of energies the eigenfrequency changes of the clamped and free plates are almost proportional to the incident impact energy and the damage surface. The modal damping coefficients also change drastically but the results are not reproducible for a given impact energy in the studied configuration. A change in the displacement mode shape can only be observed if the shape is determined on a very fine, almost continuous measurement grid. Also the changes of the strain mode shape are very local and would need a lot of measurement points to be detected.

Therefore, the relative eigenfrequency changes are retained to successfully validate two numerical models, i.e. the detailed delamination model and the homogenised damage model. A value of 94 % is retained for both damage factors of the homogenised damage model. The experimentally measured relative changes of the eigenfrequencies constitute the input for the mixed numerical-experimental damage identification method presented in Chapter 6. Because the damage factors are overestimated, the damage surface is expected to be underestimated in case of low energy impacts.

Chapter 6

Inverse numerical-experimental identification

6.1 Generalities

In this chapter, a mixed numerical-experimental optimisation method for the identification of damage is presented. During the optimisation, the parameters of a numerical model are adjusted to fit the numerical results to experimental data. Such a model should allow a faithful representation of the matter under investigation and be solved in a reasonable time because multiple model evaluations are necessary in the optimisation procedure. A model of the plate with delamination damage has been presented and validated in Section 5.4.2. The parameters of this homogenised damage model are the damage factors D_{13} and D_{23}, the damage sizes W_1 and W_2 and the damage position coordinates x_1 and x_2. The general parameter vector needed to construct the entire model is denoted $\boldsymbol{\alpha}$.

It can be presumed that the damage factors and damage size are indirectly dependent in terms of a unique solution to the identification problem. This means that two different damage sizes may lead to the same relative eigenfrequency changes when the accordant damage factors are used. The scope of this work is the identification of damage size and position which are comprehensible characteristics of damage. Therefore, the damage factors have to be fixed. In a preliminary study, the damage factors D_{13} and D_{23} are evaluated from experimental data for a given composite lay-up with different damage sizes and they are finally both set to a value of 94 %. This value being the highest value obtained for the different damage sizes, it is expected that the damage size will consequently be underestimated by the identification.

The objective of the identification is the adjustment of the damage size and position to reduce the discrepancy between the numerical predictions and the experimental results. The applied criterion is called objective function or residual and is an error vector defined as a function of the experimental data and the corresponding numerical results. In Section 5.2 it is concluded that the experimental data sufficiently sensitive to damage are the normalised frequency changes

$$\bar{f}_m^{exp} = \frac{f_m^{damaged} - f_m^{intact}}{f_m^{intact}} \tag{6.1}$$

where f_m^{intact} and $f_m^{damaged}$ are the experimentally measured eigenfrequencies of mode m of the intact and damaged plate, respectively. The eigenfrequencies are determined by experimental modal analysis. In Chapter 3 it is shown that this can be done using FBG sensors and non-destructive hammer excitation. The measurement grid has a size of about 5×3 points and should be chosen as a function of the plate size and the number of modes of interest. The numerical relative eigenfrequency changes are defined with respect to the numerical eigenfrequencies of the intact plate. This accounts for the fact that initially the numerical eigenfrequencies of the intact FE model do not coincide perfectly with the experimental eigenfrequencies, but the FE model allows to study the relative effect of a parameter on the model output.

In the following sections, the numerical model is parametrised and its sensitivity to the parameters is studied. The objective function, an error measure between the numerical results and the experimental data, is defined and the sensitivity of the error norm to the parameters is also investigated. Within the error vector, cost functions are implemented to prevent insensitive parameters to deviate during the optimisation. Taking into account the findings from the sensitivity analysis (Section 6.4), an algorithm for the minimisation of the objective function is proposed. Finally, the robustness of the algorithm is tested with numerical data and the damage identification method is validated with experimental data.

6.2 Parametric model

In order to allow a simple reproduction of the numerical model with different geometrical and material parameters, a parametric numerical model is constructed using Python programming language including the modules from Abaqus CAE. The execution of the Python script, as well as the integration of all the user supplied parameters (Figure 6.1) is carried out via Matlab routines. This versatility is advantageous for the parametrical studies and the inverse numerical-experimental optimisation method. The user interface

and the corresponding functions are inspired by the work of Matter [96] and Cugnoni [94]. The parameters of the model are

- the damage surface $A = {}^1\!/_2\,(W_1 W_2)$, where W_1 and W_2 are the in-plane sizes of the damage,
- the damage aspect ratio $r_W = {}^{W_2}\!/_{W_1}$,
- the damage position $\left(x_1^{\mathrm{d}}, x_2^{\mathrm{d}}\right)$,
- the damage factors D_{13} and D_{23},
- the homogenised material properties,
- the geometric parameters of the plate.

The output of the model are the eigenfrequencies $\boldsymbol{f}\,(\boldsymbol{\alpha})$, a coarse 2-dimensional plane mesh and the associated mode shapes $\boldsymbol{\beta}\,(\boldsymbol{\alpha})$. By default, the extracted mode shapes are defined on a grid of 12×12 nodes, which is a subset of the FE model mesh. This grid size should be adapted to the number of modes considered during the identification procedure. In fact, the mode shapes are used to match the eigenfrequencies of the numerical model to the corresponding eigenfrequencies of an experiment or another numerical model. The readout from the numerical results is also performed with a Python script using the Abaqus ODB module. The complete procedure for the numerical model execution is illustrated in a block diagram in Figure 6.2. The construction of the model with a mesh of approximately 2400 elements, the eigenvalue and eigenmode extraction of the first 15 modes and the postprocessing takes about 20 s on a computer with 4 processors (2.83 GHz) and a memory of 8 GB.

6.3 Objective function

The experimental data available with high accuracy are the eigenfrequencies of the plate and the data of interest are the relative eigenfrequency changes between the intact and the damaged plate $\bar{f}_m^{exp}$. These data are used to construct the error vector that defines the accordance of the numerical and experimental results

$$\begin{aligned} E_m\,(\boldsymbol{\alpha}) &= \bar{f}_m^{exp} - \bar{f}_m\,(\boldsymbol{\alpha}) \\ \boldsymbol{E}\,(\boldsymbol{\alpha}) &= \bar{\boldsymbol{f}}^{exp} - \bar{\boldsymbol{f}}\,(\boldsymbol{\alpha}) \end{aligned} \tag{6.2}$$

where $\boldsymbol{\alpha} = \left[D_{13}, D_{23}, W_1, W_2, x_1^d, x_2^d, \ldots\right]$ is the vector with the parameters of the homogenised damage model including the material properties and the geometrical information

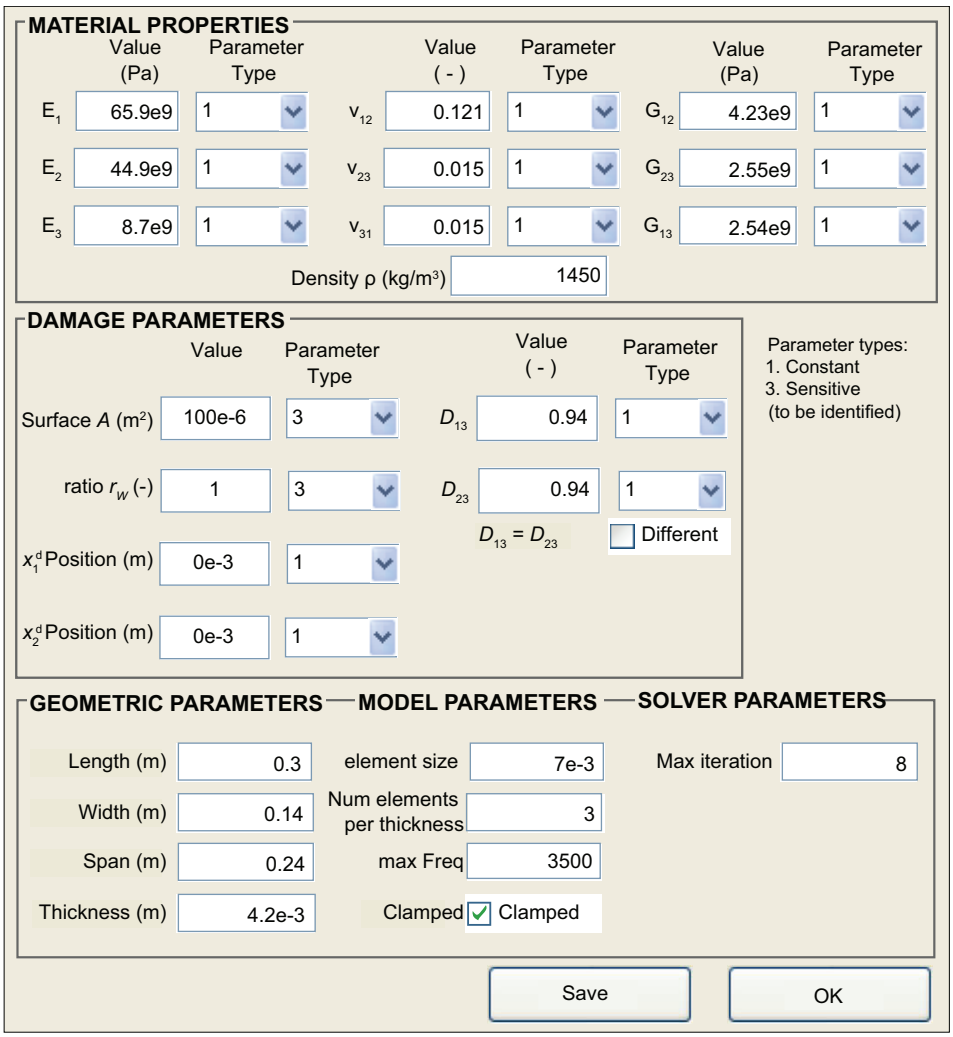

Figure 6.1: Matlab user interface for parameter supply to the FE model.

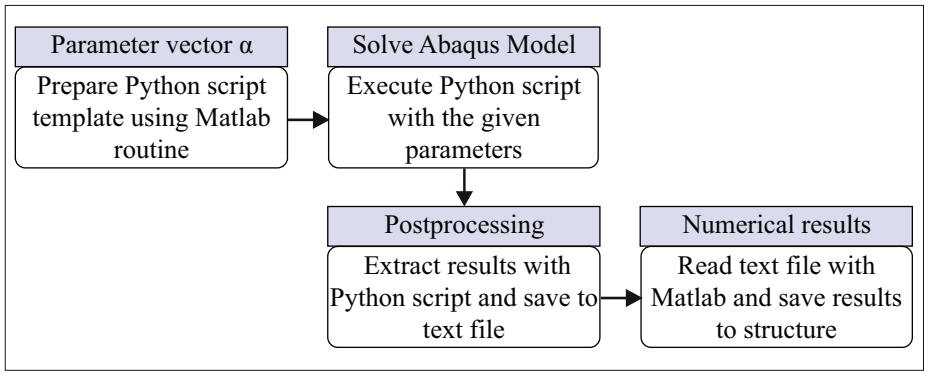

Figure 6.2: Block diagram of the FE model execution and the readout of the results.

and $\bar{\boldsymbol{f}}(\boldsymbol{\alpha})$ is the array of numerical relative eigenfrequency changes

$$\bar{\boldsymbol{f}}(\boldsymbol{\alpha}) = \frac{\boldsymbol{f}\left(D_{13}, D_{23}, W_1, W_2, x_1^d, x_2^d, \ldots\right) - \boldsymbol{f}\left(D_{13}=0, D_{23}=0, \ldots\right)}{\boldsymbol{f}\left(D_{13}=0, D_{23}=0, \ldots\right)} \tag{6.3}$$

which are normalised by the numerically calculated eigenfrequencies of the intact plate. Instead of comparing the eigenfrequencies of the numerical model directly to the experimentally measured eigenfrequencies of the damaged plate, the numerical and experimental eigenfrequency changes between the intact and damage state are compared. This allows to account for the relatively small effect of damage on the eigenfrequencies without the need to initially adjust the numerical model of the intact plate exactly to the experimentally measured eigenfrequencies of the intact plate. The normalised eigenfrequency changes are used instead of the absolute eigenfrequency change because it diminishes the weight of high frequencies and increases the weight of low frequencies on the error norm. The absolute change of high eigenfrequencies is in general much bigger and may therefore be exclusively dominating the error function if the change is not normalised by the eigenfrequency of the intact plate.

The error norm used in the minimisation algorithm is defined by

$$\left\|\boldsymbol{E}(\boldsymbol{\alpha})\right\|_2^2 = E_m(\boldsymbol{\alpha})\, E_m(\boldsymbol{\alpha}) \tag{6.4}$$

where $\|\cdot\|_2$ is the Euclidean norm. The implicit summation notation is employed in this equation. The error function is evaluated in a Matlab routine after solving and postprocessing of the numerical model. The experimental data $\bar{f}_m^{exp}$ has to be loaded into a Matlab array before the calculation of the objective function can be done. The numerical model of the intact plate has to be solved at first and a permutation matrix has to be fed manually to the routine to attribute an experimental mode to a numerical mode. This is necessary when eigenfrequencies of two different modes are very close and the order of the experimental eigenfrequencies is different from the numerical ones. The objective function is finally evaluated by carrying out the following steps:

1. $\bar{\boldsymbol{f}}^{exp}$, $\boldsymbol{P}$

   Supply the experimental normalized frequency changes $\bar{\boldsymbol{f}}^{exp}$ and a permutation matrix $\boldsymbol{P}$ attributing each experimental mode to a numerically calculated mode.

2. $\boldsymbol{\beta}_k^{\text{intact}}$, $\boldsymbol{f}^{\text{intact}}$

   Provide the numerically calculated mode shapes $\boldsymbol{\beta}_k^{\text{intact}}$ and eigenfrequencies $\boldsymbol{f}^{\text{intact}}$ of the intact plate (with $D_{13} = D_{23} = 0$).

3. $\boldsymbol{\beta}_k(\boldsymbol{\alpha})$, $\boldsymbol{f}(\boldsymbol{\alpha})$

   Retrieve the numerically calculated, unsorted mode shapes $\boldsymbol{\beta}_k(\boldsymbol{\alpha})$ and eigenfrequencies $\boldsymbol{f}(\boldsymbol{\alpha})$ of the FE model of the damaged plate (with $D_{13} = D_{23} = 94\,\%$).

4. $\mathrm{MAC}_{kl} = \frac{\left(\boldsymbol{\beta}_k^{\mathrm{intact}} \cdot \boldsymbol{\beta}_l(\boldsymbol{\alpha})\right)^2}{\left(\boldsymbol{\beta}_k^{\mathrm{intact}} \cdot \boldsymbol{\beta}_k^{\mathrm{intact}}\right)(\boldsymbol{\beta}_l(\boldsymbol{\alpha}) \cdot \boldsymbol{\beta}_l(\boldsymbol{\alpha}))}$
   Calculate the modal assurance criterion MAC_{kl} between numerical mode shapes of the intact and damaged model.

5. $\overline{\mathrm{MAC}}_{kl} = \begin{cases} 0 & \text{if } \mathrm{MAC}_{kl} < 0.8 \\ 1 & \text{if } \mathrm{MAC}_{kl} \geq 0.8 \end{cases}$
   Round the modal assurance criterion to the values zero and one.

6. $\boldsymbol{f}(\boldsymbol{\alpha}) \leftarrow \boldsymbol{P}\, \overline{\mathbf{MAC}} \cdot \boldsymbol{f}(\boldsymbol{\alpha})$
   Reorder the numerically calculated eigenfrequencies of the damaged plate.

7. $\bar{\boldsymbol{f}}(\boldsymbol{\alpha}) = \frac{\boldsymbol{f}(\boldsymbol{\alpha}) - \boldsymbol{f}^{\mathrm{intact}}}{\boldsymbol{f}^{\mathrm{intact}}}$
   Calculate the numerical normalized eigenfrequency changes $\bar{\boldsymbol{f}}(\boldsymbol{\alpha})$ between intact and damaged model.

8. $\boldsymbol{E}(\boldsymbol{\alpha}) = \bar{\boldsymbol{f}}^{exp} - \bar{\boldsymbol{f}}(\boldsymbol{\alpha})$
   Determine the residual vector $\boldsymbol{E}(\boldsymbol{\alpha})$.

6.4 Sensitivity analysis

In the current section, the sensitivity of the numerical homogenised damage model to the constitutive parameters is studied. The parameters are the damage factors D_{13} and D_{23}, the damage size W_1 and W_2 and the damage position defined by x_1^{d} and x_2^{d}. The influence of the parameters on the model output, i.e. the eigenfrequencies of the damaged plate relative to the eigenfrequencies of the intact plate, is investigated. This analysis allows to better understand which parameters strongly influence the results of the numerical model and may therefore be more rapidly and accurately identifiable.

6.4.1 Sensitivity of the numerical model

In order to study how sensitive the model results are to the parameters, the reference parameters are perturbed by a small increment and the variation of the model output is observed. The perturbation of the parameters is chosen to be 2 % from the reference values. In case of the damage position coordinates x_1^{d} and x_2^{d}, 2 % of the damage sizes W_1 and W_2 are considered respectively. The sensitivity of the eigenfrequency m to a parameter α_j is

defined as follows:

$$\begin{aligned} S_m\left(\alpha_j^0, \delta\alpha_j\right) &= \frac{\frac{f_m\left(\alpha_j^0+\delta\alpha_j\right)-f_m\left(\alpha_j^0\right)}{f_m^{intact}}}{\delta\alpha_j} \\ &= \frac{\bar{f}_m\left(\alpha_j^0+\delta\alpha_j\right)-\bar{f}_m\left(\alpha_j^0\right)}{\delta\alpha_j} \\ &= \frac{E_m\left(\alpha_j^0+\delta\alpha_j\right)-E_m\left(\alpha_j^0\right)}{\delta\alpha_j} \end{aligned} \tag{6.5}$$

where α_j^0 and $\delta\alpha_j$ represent the reference value and a small increment of the parameter.

The following three sections describe the sensitivity analysis of the three different types of parameters, which are the damage factors, damage size and damage position coordinates.

Sensitivity of the model to the damage factors

The reference values considered herein for the damage factors D_{13} and D_{23} are 0.834 and 0.855 and the damage sizes W_1 and W_2 are 56.7 mm and 37.4 mm, respectively. In fact, the results from this reference model agree very well with the experimental data from an experiment with an impact energy of 3.4 J. In order to ascertain the modes whose eigenfrequencies are mostly affected by the damage, different damage positions and damage sizes are accounted for. Throughout the analysis, the following observations are made:

- The eigenfrequencies of modes where the damage is located on a nodal displacement line are most sensitive to the damage factors. If this nodal line is oriented perpendicular to the x_1-direction (x_2-direction) the eigenfrequency of the corresponding mode is most sensitive to D_{13} (D_{23}). In fact, at the nodal displacement line of eigenmodes, the shear strain component in a plane perpendicular to this nodal line is maximal. This means that, in case of a central damage location for example, asymmetric bending modes are mostly affected. The sensitivity of mode 6 and 9 to the damage factors D_{13} and D_{23} is indicated as a function of the damage position in Figure 6.3. It can for example be seen in Figure 6.3b that the eigenfrequency of mode 9 decreases by -3.8 % when the damage factor D_{13} of a damage located at position $\left(x_1^{\mathrm{d}}, x_2^{\mathrm{d}}\right) = (-45\,\mathrm{mm}, 0\,\mathrm{mm})$ is varied by 2 %, i.e. from 0.834 to 0.851.
- When the characteristic size of the damage is bigger than half the wavelength of the mode, its eigenfrequency is also affected considerably by the damage factors D_{13} (D_{23}) if the damage is located between to nodal lines perpendicular to the x_1-direction (x_2-direction). If the damage size is small compared to the mode wavelength, the corresponding eigenfrequency is not or only slightly sensitive to the damage severity.

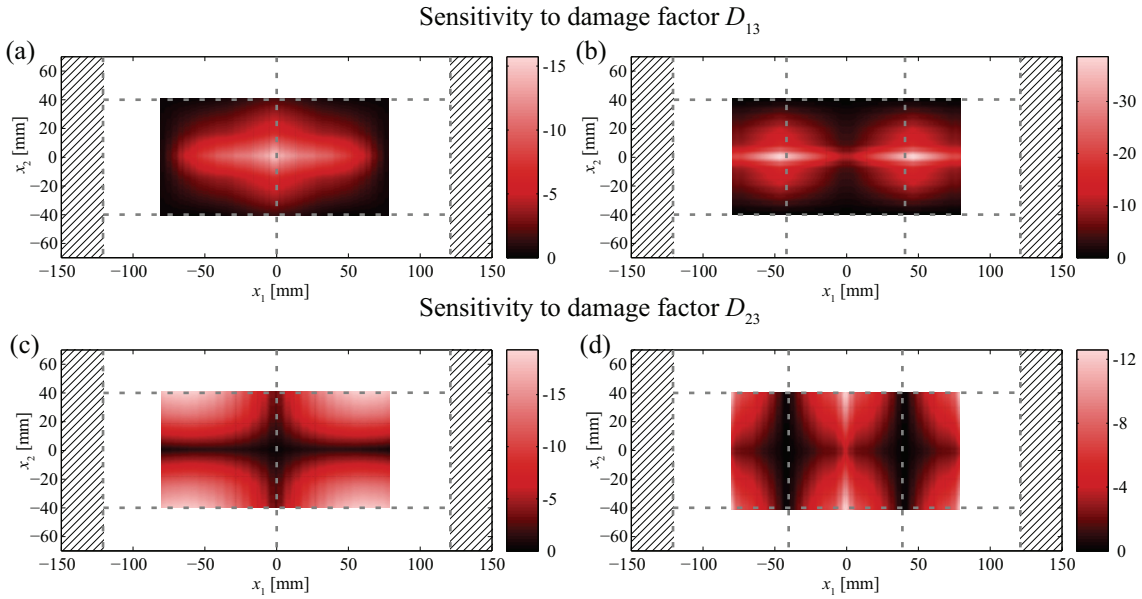

Figure 6.3: Variation of numerical eigenfrequencies [‰] of modes 6 (a,c) and 9 (b,d) with respect to a perturbation of 2 % of the damage factors D_{13} and D_{23}, respectively. Nodal lines are indicated by dashed grey lines. The clamped surface is indicated by an oblique striped pattern.

This means that, in the case of a central location of a damage with a length of 1/3 of the span, also the eigenfrequencies of the second longitudinal symmetric bending mode is affected.

- Eigenmodes with higher frequencies and smaller wavelengths are more sensitive to damage.

- When the damage is located at the intersection of 2 perpendicular nodal displacement lines of a mode, the corresponding eigenfrequency is nearly independent of the damage factors. At the intersection of two nodal displacement lines, the through-the-thickness shear strain components are close to zero. This means that, in the case of a central damage location, the eigenfrequencies of torsion modes with an odd number of nodal lines in both directions are almost not affected.

Based on the results of this study, it can be deduced that a total number of 10 modes is sufficient for the given ratio between the damage and plate sizes to have at least one mode that is very sensitive to the damage factors or to have several modes with sufficient sensitivity. In general, an eigenfrequency is sensitive to damage when the mode shape is such that shear deformation appears at the location of the damage.

Sensitivity of the model to the damage size

The same values as mentioned in the previous section are taken as a reference for the damage factors D_{13} and D_{23} and the damage sizes W_1 and W_2. The sensitivity of the plate's eigenfrequencies to the damage size is again calculated by relative finite variation using a damage size increment of 2 % which corresponds to about 1 mm. The influence of the reference damage position and size on the sensitivity to the damage size is also evaluated.

- The sensitivity of the eigenfrequencies to the damage size behaves similarly than their sensitivity to the damage factors.
- The modes where the damage is located on a single nodal displacement line are most affected. When the damage is located on a nodal line parallel to the 1-direction (2-direction) the eigenfrequency is only slightly more sensitive to the damage size $W_1(W_2)$.
- When the damage is located in-between two nodal lines, the eigenfrequency is affected when the damage size is of the order of half the mode wavelength.
- When the damage is located on the intersection of two perpendicular nodal lines, the eigenfrequency of the corresponding mode is almost independent of the damage size.

Furthermore, it can be noticed that the normalised scalar product of both sensitivity vectors $S_m\left(W_1^0, \delta W_1\right)$ and $S_m\left(W_2^0, \delta W_2\right)$, with m taking the values of all considered mode numbers, is bigger than 0.9, meaning that both vectors are almost collinear. These two parameters may not be completely independent in terms of unique solution of the optimisation and, hence, may complicate a simultaneous identification. Therefore, the damage size ratio r_W and surface A are introduced in order to evaluate the sensitivity of the model to these parameters

$$A = \frac{W_1 \times W_2}{2} \tag{6.6}$$

$$r_W = \frac{W_2}{W_1} \tag{6.7}$$

The reference values A^0 and r_W^0, corresponding to the reference damage sizes W_1^0 and W_2^0, equal to 56.7 mm and 37.4 mm, are 10.6 cm^2 and 0.66, respectively. The sensitivity of the normalised eigenfrequencies to the damage surface A and damage size ratio r_W can be

formulated with respect to the sensitivities $S_m\left(W_1^0, \delta W_1\right)$ and $S_m\left(W_2^0, \delta W_2\right)$

$$S_m\left(A^0, \delta A\right) = \left[S_m\left(W_1^0, \delta W_1\right)\frac{\partial W_1}{\partial A} + S_m\left(W_2^0, \delta W_2\right)\frac{\partial W_2}{\partial A}\right] \tag{6.8}$$

$$S_m\left(r_W^0, \delta r_W\right) = \left[S_m\left(W_1^0, \delta W_1\right)\frac{\partial W_1}{\partial r_W} + S_m\left(W_2^0, \delta W_2\right)\frac{\partial W_2}{\partial r_W}\right] \tag{6.9}$$

These equations can be developed by calculating the partial derivatives of W_1 and W_2 with respect to A and r_W. When expressing the sensitivity of the model to the damage area A, a constant size ratio r_W is supposed. Analogously, the damage area A is supposed to be constant when the sensitivity of the model to the damage size ratio r_W is defined. Under these conditions, the sensitivity of the eigenfrequencies to the damage surface and aspect ratio can be expressed by

$$S_m\left(A^0, \delta A\right) = \left[S_m\left(W_1^0, \delta W_1\right)W_2 + S_m\left(W_2^0, \delta W_2\right)W_1\right] \tag{6.10}$$

$$S_m\left(r_W^0, \delta r_W\right) = \left[S_m\left(W_1^0, \delta W_1\right)\frac{1}{W_2} + S_m\left(W_2^0, \delta W_2\right)\frac{1}{W_1}\right] \tag{6.11}$$

With the assumption of a constant aspect ratio r_W, a simultaneous variation of the damage sizes W_1 and W_2 of 2 % results in a relative change of the damage area of ∼4 % and an absolute increment δA of 0.43 cm^2. With the assumption of a constant damage area A, a simultaneous decrease and increase of the damage sizes W_1 and W_2 of 2 % results in a relative change of the damage ratio of ∼4 % and an absolute increment δr_W of ∼ 0.026.

Figure 6.4 shows the variation of the relative eigenfrequency variations $\bar{f}_m$ as a function of the damage surface A in case of a central damage position. The relative decrease of the eigenfrequencies with increasing damage size shows a similar trend than the experimentally measured eigenfrequency changes to the increasing impact energy as shown in Figure 5.1. The sensitivity $S_m\left(A^0, \delta A\right)$ of the eigenfrequency of mode m to the damage surface is the slope of the curve of mode m in Figure 6.4 calculated by finite difference at the reference damage surface A^0.

Table 6.1 compares the relative variation of the eigenfrequencies for an absolute increment of $\delta A = A^0\left({}^{\delta W_1}/_{W_1} + {}^{\delta W_2}/_{W_2}\right)$ and $\delta r_W = r_W^0\left(-{}^{\delta W_1}/_{W_1} + {}^{\delta W_2}/_{W_2}\right)$ equivalent to damage size increments $\left|{}^{\delta W_1}/_{W_1}\right|$ and $\left|{}^{\delta W_2}/_{W_2}\right|$ of 2 %. It can be noticed that the eigenfrequencies are 2 to 25 times more sensitive to a damage surface change than to a damage aspect ratio change. Regarding other damage positions, similar observations are made. Based on these findings, it can be deduced that a simultaneous identification of the damage surface A and the damage aspect ratio r_W may lead to erroneous results for r_W.

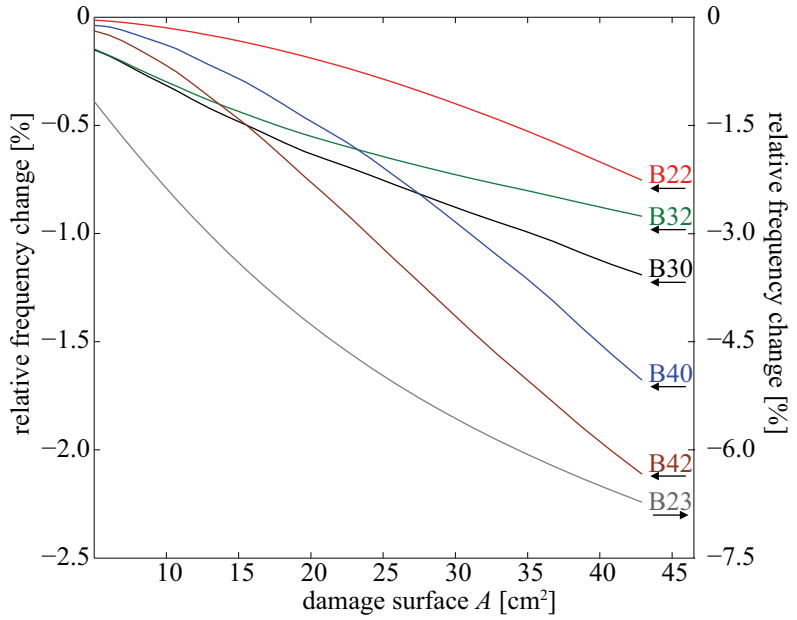

Figure 6.4: Relative eigenfrequency changes $\bar{f}_m$ of a plate with a central damage location as a function of the damage surface A.

	$S_m(W_1) \cdot \delta W_1$ [‰]	$S_m(W_2) \cdot \delta W_2$ [‰]	$S_m(A) \cdot \delta A$ [‰]	$S_m(r_W) \cdot \delta r_W$ [‰]
B20	-0.005	-0.005	-0.010	-0.001
T21	-0.004	-0.002	-0.007	0.001
B30	-0.047	-0.143	-0.163	-0.086
T31	-0.005	-0.013	-0.016	-0.007
B22	-0.014	-0.040	-0.047	-0.024
B32	-0.044	-0.102	-0.129	-0.056
B40	-0.064	-0.073	-0.130	-0.024
T41	-0.005	-0.005	-0.010	-0.001
B42	-0.099	-0.119	-0.204	-0.041
B23	-0.559	-0.421	-0.961	-0.037

Table 6.1: Sensitivity of the homogenised damage model with central damage location to the damage size.

Sensitivity of the model to the damage position

In order to study the sensitivity of the numerically calculated eigenfrequencies of a plate to the location of the damage on this plate, an important number of models are solved. For each one of these models, a damage with reference sizes $W_1 = 56.7\,\text{mm}$ and $W_2 = 37.4\,\text{mm}$ is considered and the position $\left(x_1^{\text{d}}, x_2^{\text{d}}\right)$ is translated over a grid of different locations. The sensitivities of the model to the damage position coordinates x_1^{d} and x_2^{d} are computed by finite difference calculation, Equation (6.5). A position increment δx_1^{d} or δx_2^{d} corresponding to 2 % of the reference damage sizes W_1 and W_2 are used for the finite difference calculation. Figures 6.5 and 6.6 show a mapping of the sensitivity of the normalised eigenfrequencies to the damage position coordinates in $‰/\text{mm}$.

- The sensitivity to the position coordinate x_1^{d} (x_2^{d}) is small when the damage is located on a nodal line oriented in the x_2-direction (x_1-direction).
- The sensitivity to the position coordinate x_1^{d} (x_2^{d}) is also small when the damage is located on a line in-between and parallel to two nodal lines oriented in the x_2-direction (x_1-direction). The exact distance from this line to the nodal lines may be dependent from the damage size and its proximity to the boundary of the plate.
- Outside of the aforementioned locations, the sensitivity of the different eigenfrequencies to the damage position presents multiple zones where it is comparable to the sensitivity of the eigenfrequencies to the damage size.
- For high mode numbers, the sensitivity is higher and the size of the zones where the sensitivity is most important is smaller.

Based on these results it can be deduced that an error norm based on the eigenfrequencies of the plate has multiple local minima.

6.4.2 Sensitivity of the error norm

The sensitivity of the error function is defined as the gradient of the error norm, Equation (6.4), calculated by finite difference at the reference parameters α_j^0

$$\begin{aligned} S^{\|\boldsymbol{E}\|}\left(\alpha_j^0, \delta\alpha_j\right) &= \frac{\left\|\boldsymbol{E}\left(\alpha_j^0 + \delta\alpha_j\right)\right\|_2^2 - \left\|\boldsymbol{E}\left(\alpha_j^0\right)\right\|_2^2}{\delta\alpha_j} \\ &= \frac{E_m\left(\alpha_j^0 + \delta\alpha_j\right) - E_m\left(\alpha_j^0\right)}{\delta\alpha_j} \cdot \left[E_m\left(\alpha_j^0 + \delta\alpha_j\right) + E_m\left(\alpha_j^0\right)\right] \end{aligned} \tag{6.12}$$

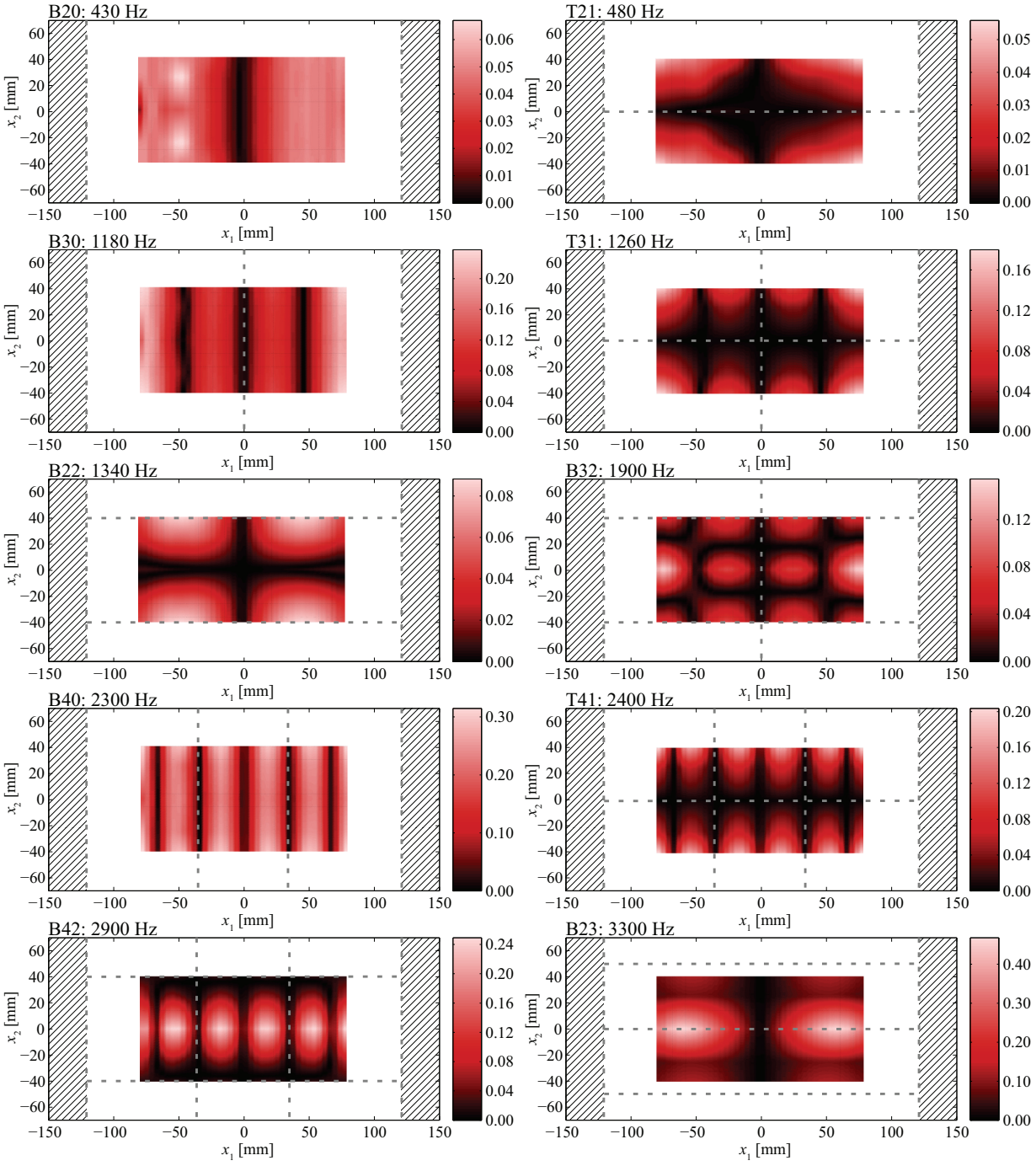

Figure 6.5: Absolute value of the sensitivity [‰/mm] of eigenfrequencies to the damage position coordinate x_1^{d}. Nodal lines are indicated by dashed grey lines. The clamped surface is indicated by an oblique striped pattern.

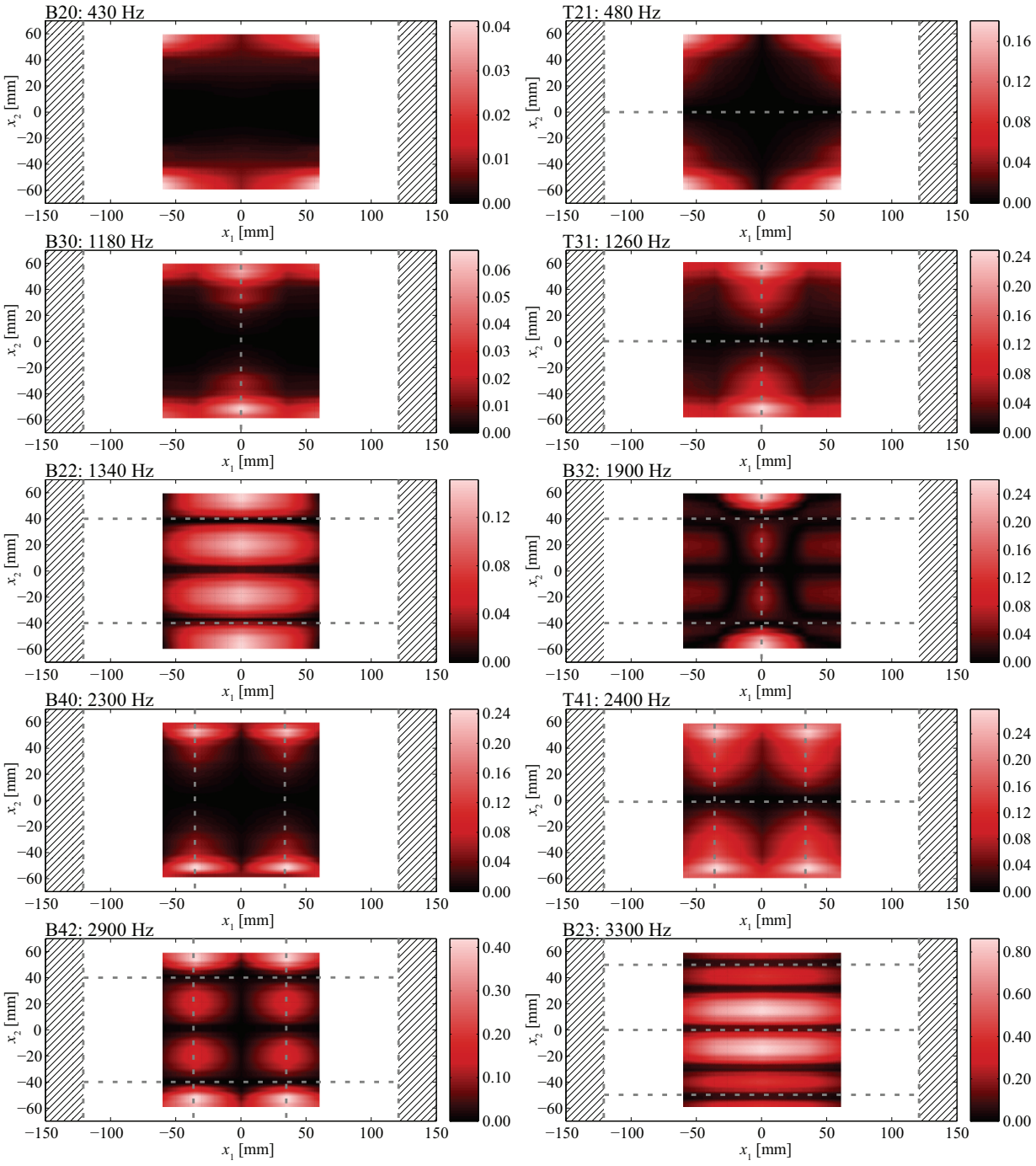

Figure 6.6: Absolute value of the sensitivity [‰/mm] of eigenfrequencies to the damage position coordinate x_2^{d}. Nodal lines are indicated by dashed grey lines. The clamped surface is indicated by an oblique striped pattern.

In order to study the error norm, α_j^0 is considered to be the solution for the minimum of the error function and the solution is considered to be perfect so that the error norm is zero. This assumption means that the numerically calculated frequency change equals the experimentally measured frequency change.

$$\begin{aligned} \bar{f}_m\left(\alpha_j^0\right) &= \bar{f}_m^{exp} \\ E_m\left(\alpha_j^0\right) &= 0 \end{aligned} \tag{6.13}$$

Under this assumption, Equation (6.12) can be rewritten as follows using the definition of the sensitivity of the model to a parameter α_j, Equation (6.5), and the definition of the error vector, Equation (6.2),

$$\begin{aligned} S^{\|\boldsymbol{E}\|}\left(\alpha_j^0, \delta\alpha_j\right) &= \frac{E_m\left(\alpha_j^0 + \delta\alpha_j\right)}{\delta\alpha_j} E_m\left(\alpha_j^0 + \delta\alpha_j\right) \\ &= \frac{\bar{f}_m^{exp} - \bar{f}_m\left(\alpha_j^0 + \delta\alpha_j\right)}{\delta\alpha_j}\left[\bar{f}_m^{exp} - \bar{f}_m\left(\alpha_j^0 + \delta\alpha_j\right)\right] \\ &= S_m\left(\alpha_j^0, \delta\alpha_j\right) S_m\left(\alpha_j^0, \delta\alpha_j\right) \delta\alpha_j \end{aligned} \tag{6.14}$$

For the sensitivity analysis of the error norm the first 10 eigenfrequencies are considered.

Sensitivity of error norm to the damage factors

Different reference values for the damage position are considered to evaluate the sensitivity of the error norm to the damage parameters D_{13} and D_{23}. It can be observed that the sensitivities to both parameters stay in the same order of magnitude over the studied damage positions. Hence, a sufficient amount of modes are studied and, depending on the position of the damage, either one eigenfrequency may dominate the behaviour of the error norm or several modes may interact on the error gradient.

The error norm as a function of the damage factors D_{13} and D_{23} is shown in Figure 6.7, where it is plotted for one of the parameters fixed and the other varying from 80 % to 108 % relative to the reference parameters. Both curves being almost parabolic, they have a perfect behaviour for a minimisation algorithm.

Sensitivity of error norm to the damage size

The sensitivity of the error norm to the damage surface A is studied while considering different damage positions. It could be observed that it varies up to a factor 8 regarding different reference positions. Analogously to the previous paragraph it can be stated that

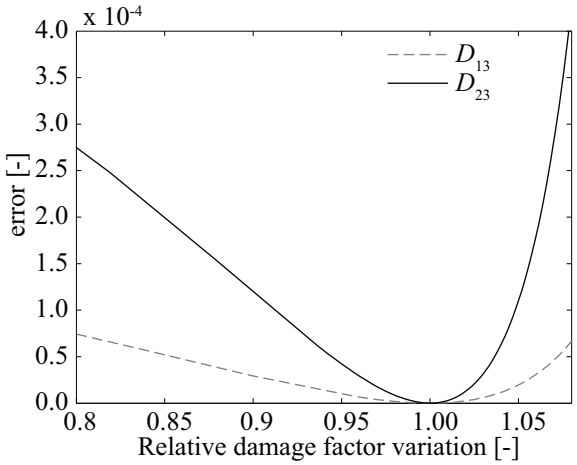

Figure 6.7: Error norm as a function of the damage factors D_{13} and D_{23} relative to their reference values in case of a centrally located damage.

a sufficient number of modes are studied so that at least one of them, or a combination of a few modes are sensitive to the damage. Again, an almost quadratic relation of the error norm to the damage area can be observed in Figure 6.8.

In order to compare the sensitivity of the error norm to the damage surface A to the one of the damage ratio r_W, an increased damage surface of $(102\,\%)^2$ under constant damage ratio and an increased damage ratio of $^{102\,\%}/_{98\,\%}$ under constant damage surface are considered, respectively. The sensitivity of the error norm to the damage size ratio is

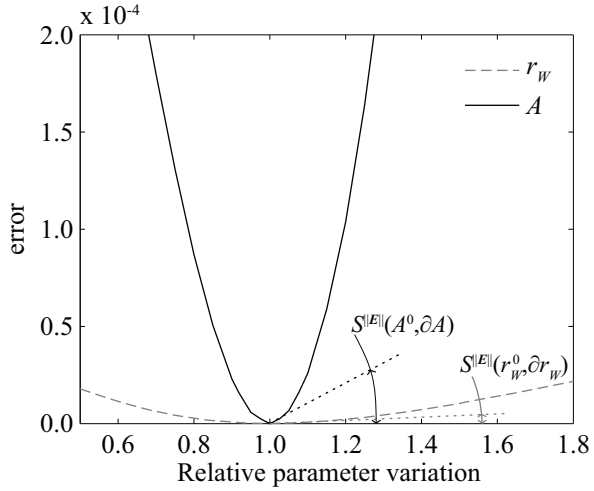

Figure 6.8: Error norm as a function of the damage aspect ratio r_W and surface A relative to their reference values in case of a centrally located damage.

between 5 and 100 times lower than the sensitivity to the damage surface. This indicates a comparatively low sensitivity to the damage size ratio at several damage locations. It is therefore suggested to apply bounds to the damage ratio in an optimisation algorithm in order to prevent it from deviating. Furthermore, it could be useful to identify first the damage surface using a unitary damage size ratio and, in a second step, optimise for a better solution of the damage size ratio.

Sensitivity of error norm to the damage position

The sensitivity of the error norm to the damage position is studied over a part of the plate. It is shown in Figure 6.9 that the sensitivity of the error function to the damage position is about 150 times lower on the symmetry axes than the maximum sensitivity. Furthermore it is noticed that the overall sensitivity surface over the domain is wavy. This may suggest that the error function may present local minima over the domain and that in some positions a good initial guess for the damage position coordinates x_1^{d} and x_2^{d} is needed. The sensitivity to the damage position coordinates is between 1 and 250 times lower than the sensitivity to the damage area. An identification procedure in two or more steps may therefore be appropriate in order to prevent the damage position coordinates

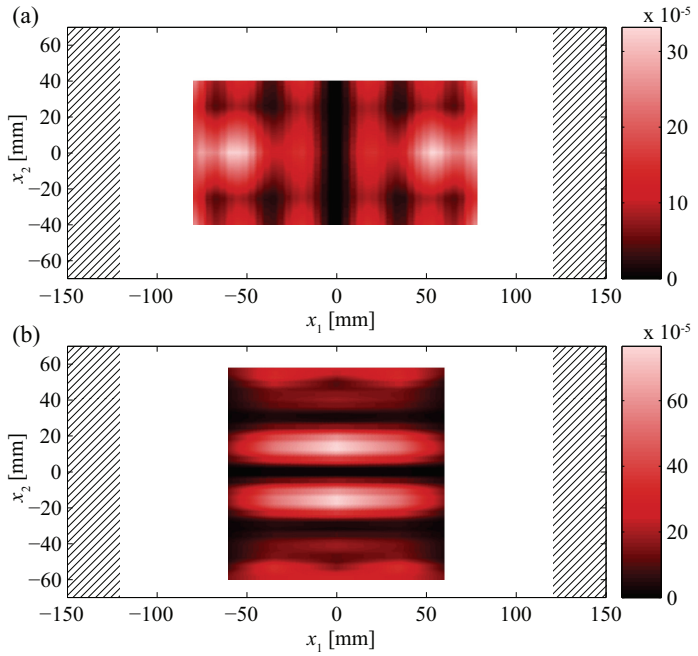

Figure 6.9: Sensitivity [‰/mm] (absolute value) of error norm to damage position coordinates x_1^{d} (a) and x_2^{d} (b).

from diverging while the error norm is mainly sensitive to the damage surface.

6.4.3 Summary of the sensitivity analysis

A list of findings during the sensitivity analysis is retained and constitutes the foundation for the development of the optimisation algorithm.

- The sensitivity to the damage factors is good and equilibrated between both factors D_{13} and D_{23}. The error norm has an almost quadratic relation to the damage factors.
- A high sensitivity to the damage surface A is observed.
- The numerically calculated eigenfrequencies vary almost linearly with the damage surface. This agrees well with the experimental findings in Section 5.2.
- The sensitivity of the error norm to the damage aspect ratio r_W is small compared to the one to the damage surface.
- The error norm presumably presents local minima as a function of the damage positions x_1^{d} and x_2^{d}. Beyond the locations of the local minima, the sensitivity of the error norm to the position is comparable to the one to the damage surface.

6.5 Optimisation algorithm

In order to solve non-linear minimisation problems, different algorithms are used in the literature. The most basic minimisation algorithm is the global search method which identifies the optimal values by evaluating the objective function over the whole domain of parameters. Very common iterative algorithms are the gradient-descent, Gauss-Newton or Levenberg-Marquardt algorithms [135]. Whereas the gradient-descent method advances in the direction of the gradient of the error norm, the modified quasi-Newton method accounts for an approximation of the Hessian matrix. The Gauss-Newton algorithm is based on a linear approximation of the residual vector. The Levenberg-Marquardt algorithm modifies the Gauss-Newton descent direction to be closer to the gradient of the error norm and has an increased robustness. In order to guarantee a reduction of the error norm at each step, line search algorithms can be introduced at each iteration. Commonly used heuristic methods for non-linear optimisation problems are the Downhill-Simplex method or genetic algorithms which do not need the computation of the function gradient. A disadvantage of these methods is the increased number of iterations needed until convergence, in particular

if the number of parameters is higher than two. An advantage of the genetic algorithm is its ability to converge to the absolute minimum via mutation of the parameter population.

For the optimisation of the damage factors, surface and aspect ratio, an iterative method is the most appropriate because of the error norm's nearly ideal parabolic form. The Levenberg-Marquardt algorithm presents in general the best trade-off between robustness and fast convergence. In function of the damage position coordinates x_1^{d} and x_2^{d}, the objective function may present local minima (mentioned in Section 6.4.2). The initial guess obtained from the localisation method has, however, an uncertainty of maximum 16 mm in radius. In order to prevent the optimisation algorithm to diverge to a local minimum that is not the correct solution, a procedure is needed that may enhance the initial guess for the damage position. A global search method over the domain of all parameters, i.e. the damage surface and aspect ratio and the damage positions within the radius of uncertainty, would need too many numerical model evaluations.

The method presented in this section is a hybrid global and iterative optimisation method. It relies on the almost linear relation between the damage surface and the normalised eigenfrequency changes, accounts for the small sensitivity to the damage aspect ratio and maximises the robustness to the damage position. The minimisation of the error norm is therefore performed in 3 steps and bounds are set for the parameters.

6.5.1 Confidence bounds for the parameters

The sensitivity analysis reveals that some parameters may be more difficult to identify than others. In particular the damage aspect ratio has little effect on the error norm. Furthermore some parameters have only a physical meaning in a particular range of values. Outside of this range the FE model execution will fail. For this reason, cost functions are added to the error vector for each parameter. Table 6.2 summarises the bounds implemented for each parameter.

Expression		Lower bound	Upper bound
D_{13}	[%]	0	1
D_{23}	[%]	0	1
$\sqrt{\left(x_{1l}^d - x_1^d\right)^2 + \left(x_{2l}^d - x_2^d\right)^2}$	[mm]	0	30
r_w	[-]	0.4	2.5

Table 6.2: Confidence bounds of the parameters.

The cost function takes a value of $1{\cdot}10^{-3}$ at the bounds and is exponentially increasing

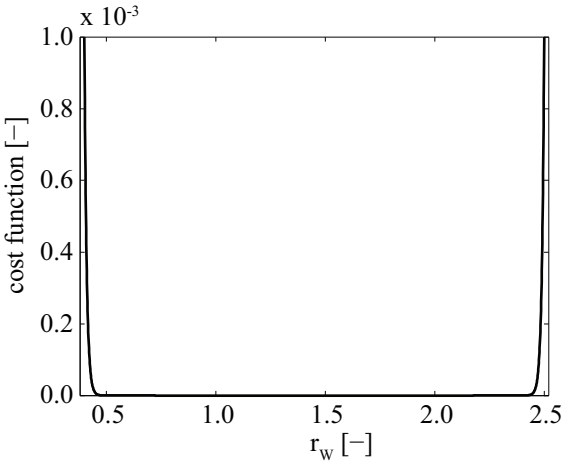

Figure 6.10: Cost function for the damage aspect ratio.

outside of these constraints. The function is increasing with an exponent of 300 for the damage factors, 100 for the damage aspect ratio and 20 for the confidence radius of the damage position. The latter has a less steeper cost function in order to prevent the error function gradient to be exclusively dominated by the cost function at the bounding values. In this case and if the actual damage position estimate is close to this bound, the optimisation algorithm would not be able to improve the damage position along the boundary of the confidence domain, nor the other parameters. The cost function for the damage aspect ratio is illustrated in Figure 6.10.

6.5.2 Levenberg-Marquardt algorithm

As mentioned in the preamble of this section, the optimisation algorithm relies on a gradient-descent method to estimate the damage surface. The minimisation of the objective function (6.2) is a least square problem defined by

$$\min_{\alpha} \|\boldsymbol{E}(\boldsymbol{\alpha})\|_2^2 = \min_{\alpha} \left\|\bar{\boldsymbol{f}}^{exp} - \bar{\boldsymbol{f}}(\boldsymbol{\alpha})\right\|_2^2 \tag{6.15}$$

The parameter vector $\boldsymbol{\alpha}$ is replaced by an estimate $\boldsymbol{\alpha} + \boldsymbol{d}$, where the increment $\boldsymbol{d}$ is determined by linearisation of the model output

$$\bar{\boldsymbol{f}}(\boldsymbol{\alpha} + \boldsymbol{d}) \approx \bar{\boldsymbol{f}}(\boldsymbol{\alpha}) + \boldsymbol{J}\boldsymbol{d} \tag{6.16}$$

In this equation, $\boldsymbol{J}$ is the gradient of $\bar{\boldsymbol{f}}$ with respect to the parameter vector $\boldsymbol{\alpha}$, expressed by

$$\boldsymbol{J} = \frac{\partial \bar{\boldsymbol{f}}}{\partial \boldsymbol{\alpha}} \tag{6.17}$$

The error norm at $\boldsymbol{\alpha} + \boldsymbol{d}$ can now be approximated by

$$\|\boldsymbol{E}(\boldsymbol{\alpha} + \boldsymbol{d})\|_2^2 \approx \left\|\bar{\boldsymbol{f}}^{exp} - \bar{\boldsymbol{f}}(\boldsymbol{\alpha}) - \boldsymbol{J}\boldsymbol{d}\right\|_2^2 \tag{6.18}$$

The minimum of the approximated error at the new estimate $\boldsymbol{\alpha} + \boldsymbol{d}$ is found by differentiating Equation (6.18) with respect to $\boldsymbol{d}$ and setting it to zero

$$\boldsymbol{J}^T\boldsymbol{J}\boldsymbol{d} = \boldsymbol{J}^T\left[\bar{\boldsymbol{f}}^{exp} - \bar{\boldsymbol{f}}(\boldsymbol{\alpha})\right] \tag{6.19}$$

Multiplying this equation by $\left(\boldsymbol{J}^T\boldsymbol{J}\right)^{-1}$ allows to determine the increment $\boldsymbol{d}$.

By introducing the coefficient λ and the identity matrix I, Levenberg's formulation is expressed by

$$\left(\boldsymbol{J}^T\boldsymbol{J} + \lambda I\right)\boldsymbol{d} = \boldsymbol{J}^T\left[\bar{\boldsymbol{f}}^{exp} - \bar{\boldsymbol{f}}(\boldsymbol{\alpha})\right] \tag{6.20}$$

When the model is more sensitive to some parameters than to others, it may be useful to replace the identity matrix I by the diagonal of the matrix J^TJ. This change increases the step in directions where the gradient of the error function is small.

The use of a line search algorithm at each iteration forces a reduction of the error norm at each step. If $\boldsymbol{d}$ is a descent direction, it exists $\epsilon > 0$ so that

$$\|\boldsymbol{E}(\boldsymbol{\alpha} + \epsilon\boldsymbol{d})\| \leq \|\boldsymbol{E}(\boldsymbol{\alpha})\| \tag{6.21}$$

The increment $d\boldsymbol{\alpha}$ is finally obtained by

$$d\boldsymbol{\alpha} = \epsilon\boldsymbol{d} \tag{6.22}$$

The general routine for the Levenberg-Marquardt optimisation is described in Figure 6.11. The input of this routine is the experimental data, i.e. the normalised eigenfrequency changes of a damaged plate, and an initial guess of the parameters $\boldsymbol{\alpha}$. The termination of the iterative method is controlled by one or more criteria. A possible criterion, called residual tolerance, verifies that the norm of the residual error is smaller than a given tolerance which means that the model results are very close to the experimental data. However, in case of experimental data, the residual remaining after an optimal fitting depends on the quality and the scattering of the experimental data and, hence, it is complicated to estimate a priori a value for the minimum error norm. A more appropriate criterion, called convergence tolerance, verifies that the increment $d\boldsymbol{\alpha}$ for the new estimate of $\boldsymbol{\alpha}$ is smaller than a given tolerance, which means that no significant improvement of the parameter estimation is attained.

The Levenberg-Marquardt algorithm is used by the inverse numerical-experimental damage identification method, allowing to obtain the damage size, aspect ratio and position while the damage factors are fixed. This algorithm is also used in Section 5.4.2 to identify the damage factors D_{13} and D_{23} for different sizes of damage.

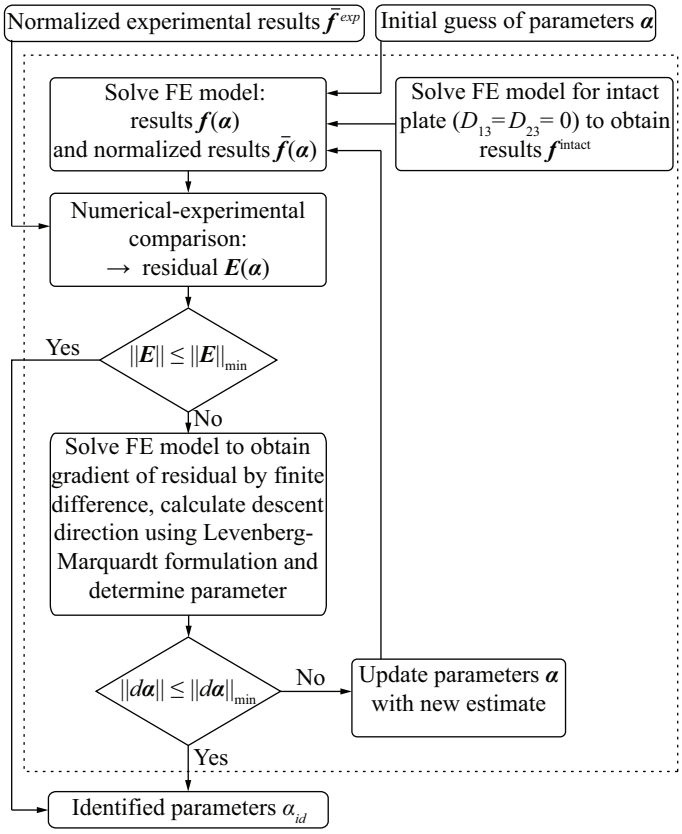

Figure 6.11: Block diagram of the Levenberg-Marquardt optimisation algorithm.

6.5.3 Implementation of algorithm

Whereas the Levenberg-Marquardt algorithm is well suited to identify the damage surface, the same risks to diverge to a local minimum of the error norm when a bad initial damage position is used. After the estimation of the damage surface via the Levenberg-Marquardt algorithm, a global search method looks for the optimal damage position within an uncertainty radius of 15 mm around the guess obtained from the impact localisation method. Then, the Levenberg-Marquardt algorithm is again used to simultaneously identify all the parameters. Figure 6.12 shows a flow chart of the hybrid global and iterative optimisation method.

The procedure of the optimisation in 3 steps is the following: (a) First a rough estimation of the damage area A_1 is made with the Levenberg-Marquardt optimisation algorithm. It is initialised with the impact location $\left(x^{\mathrm{d}}_{1,\mathrm{loc}}, x^{\mathrm{d}}_{2,\mathrm{loc}}\right)$, obtained from the localisation method, as well as a damage surface A_0 and aspect ratio $r_{w0} = 1$. (b) Secondly, a global search is performed during which the best departure point for the damage position

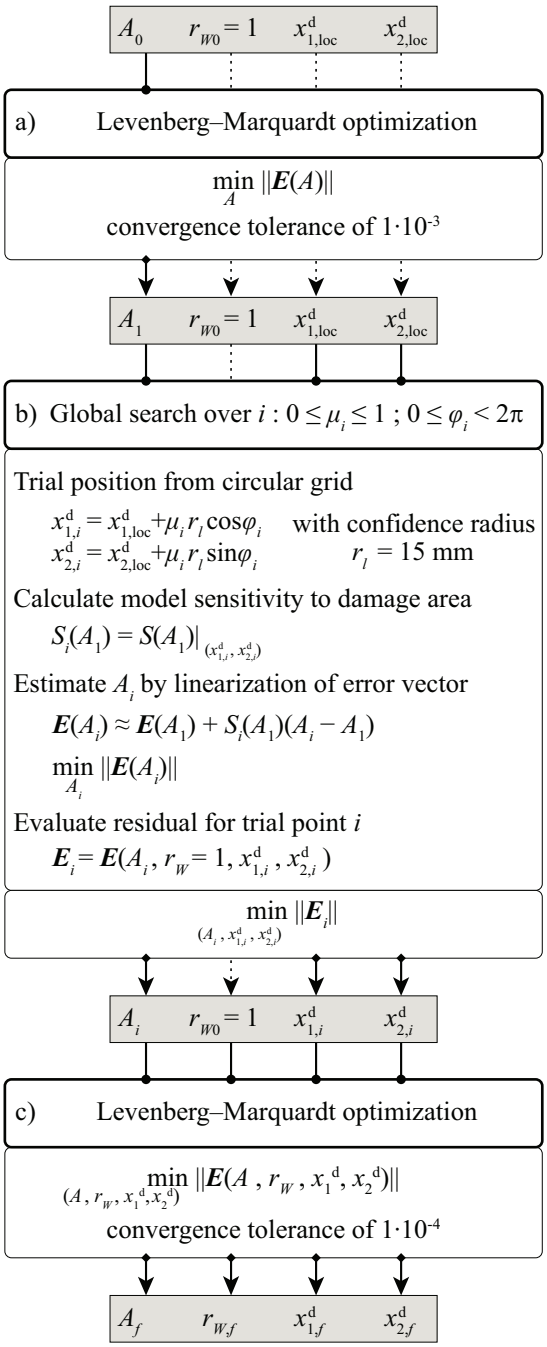

Figure 6.12: Block diagram illustrating the implementation of the hybrid optimisation method for damage size and position identification.

is chosen among a cloud of trial points within a radius r_l of 15 mm to the initial guess. A better estimate of the damage surface A_i is calculated for each trial point i, using a single Gauss-Newton iteration with an initial value of the damage surface corresponding to the previously identified damage surface A_1. This iteration is very efficient because of the almost linear relation between the damage surface and the normalised eigenfrequency changes. Among these trial positions, the one with the lowest residual norm is retained. (c) Finally, this damage position as well as the corresponding damage surface estimate A_i and a unitary damage aspect ratio are used as initial values for the Levenberg-Marquardt algorithm.

In terms of FE model evaluations, this method is very efficient. Step (a), which is a Levenberg-Marquardt optimisation of an almost parabolic function, converges in less than 4 iterations when a convergence tolerance of 1 ‰ is chosen. Each iteration requires at least 2 FE model evaluations whereof one for the gradient calculation and at least one for the error calculation for the next increment. Step (b), which is a global search method, requires 3 x *number of evaluated positions* FE model evaluations. A grid of 17 points are sufficient to cover enough points in the domain of possible damage positions. Because of the good initial guess of all parameters, the last step (c), which is a Levenberg-Marquardt optimisation with 4 parameters, converges in about $6 - 8$ iterations. These iterations require each at least 5 FE model evaluations, whereof 4 for the gradient calculation and at least one for the residual calculation of the new estimate. In total, about 100 FE model evaluations are required, taking approximately half an hour on the previously specified computer.

6.6 Validation of the damage identification method

6.6.1 Definition of the problem

The damage identification method presented in the previous section and its robustness to different initial guesses of the parameters is tested. The identification procedure described in Figure 6.12 is applied in order to identify the position $\left(x_1^{\mathrm{d}}, x_2^{\mathrm{d}}\right)$, the surface A and the aspect ratio r_W of a potential damage in a composite plate. The input for the optimisation algorithm is a vector of relative eigenfrequency changes originating from the damage.

In the first step of the optimisation procedure, a rough estimation of the damage surface is made. Different initial values of the damage surface are tested within this first optimisation step. In order to test the robustness of the complete damage identification procedure, initial damage positions $\left(x_{1i}^{\mathrm{d}}, x_{1i}^{\mathrm{d}}\right)$ are chosen arbitrarily within a radius of

30 mm of the exact location. The initial positions tested here are chosen within a limited region because it is shown in Chapter 4 that the impact localisation method permits to supply the impact location with an accuracy better than 16 mm. The initial damage aspect ratio is always set to one because it is already anticipated in Section 6.4 that the model is not very sensitive to this parameter.

Numerically generated test problems

First, the optimisation procedure is tested with numerically generated data obtained from the detailed delamination model presented in Section 5.4.1. The model of the plate has dimensions of 300 mm × 140 mm and is clamped on the two short sides. An experimentally determined delamination pattern (cf. Section 5.3) is introduced at different locations. Damage locations $\left(x_1^{\mathrm{d}}, x_2^{\mathrm{d}}\right)$ of the numerical examples are chosen arbitrarily and are listed together with the damage surfaces in Table 6.3. During the identification procedure, the numerically generated eigenfrequency changes of the first 10 modes are considered as an input.

Total damage surface [cm^2]	Projected damage surface [cm^2]	Damage aspect ratio [-]	Damage position x_1^{d} [mm]	x_2^{d} [mm]
40.58	10.73	0.66	30	13
58.95	15.95	0.66	55	3
70.43	20.60	0.58	70	33
70.43	20.60	0.58	4	24
70.43	20.60	0.58	22	40

Table 6.3: Numerically generated data with arbitrary damage positions and different damage sizes.

Experimental test problems

Secondly, the method is validated by experiments. A set of plates with dimensions of 300 mm × 140 mm are impacted with different energies at different positions. The projected damage size is determined by visually inspecting the plate's face opposite of the impact location. The damage position is known with a precision of approximately ±1 mm as the impact weight is well guided. The experimentally measured damage surface and the impact position coordinates x_1^{d} and x_2^{d} are given in Table 6.4. The experimentally measured eigenfrequency changes of the first 10 modes are used to identify the damage.

Impact energy [J]	Projected damage surface [cm^2]	Damage aspect ratio [-]	Impact position x_1^{d} [mm]	x_2^{d} [mm]
1.7	7.6 ($\pm$1.0)	0.86 ($\pm$0.05)	75 ($\pm$1)	40 ($\pm$1)
3.4	15.4 ($\pm$1.0)	0.75 ($\pm$0.05)	25 ($\pm$1)	20 ($\pm$1)
5.1	13.9 ($\pm$1.0)	0.60 ($\pm$0.05)	0 ($\pm$1)	35 ($\pm$1)

Table 6.4: Damage positions and measured damage sizes from impact experiments.

Test problem generalised to a plate with larger dimensions

Finally, the damage identification method is tested on a plate with larger dimensions. Therefore, the detailed delamination model built in Section 5.4.1 is again used to numerically generate the eigenfrequency changes that are due to the presence of delamination damage. A plate with dimensions of 400 mm $\times$ 300 mm is modelled and a delamination pattern with a projected damage surface of 20.60 cm^2 is introduced at an off-centre position of (90 mm,70 mm) (Figure 6.13).

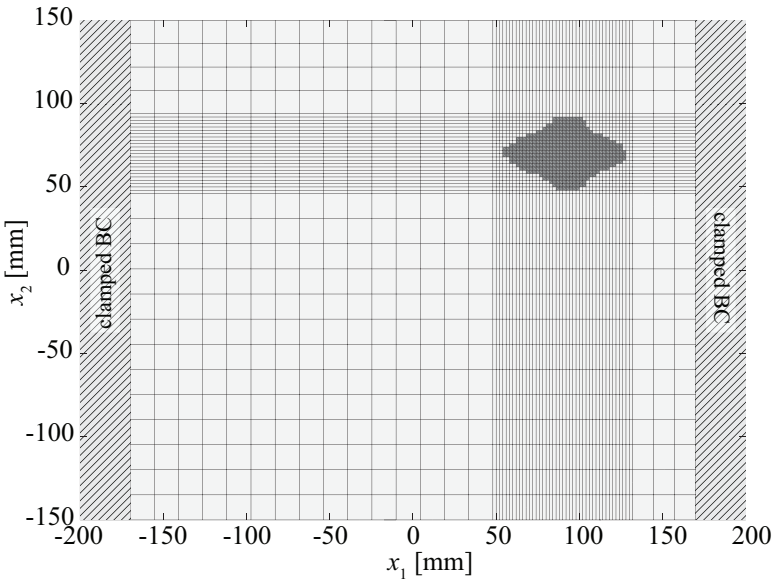

Figure 6.13: Mesh of the detailed delamination model of a large plate with dimensions of 400 mm $\times$ 300 mm.

The eigenfrequency changes of the first 10 modes are small compared to the achievable precision attributed to the eigenfrequency determination technique. Higher eigenfrequencies with eigenmodes having a shorter spatial wavelength see relative changes of 1 % or more. To identify the damage in this larger plate, the first 24 eigenfrequencies, comprised in a range of 3 000 Hz, are considered as an input to the optimisation method.

6.6.2 Results of the validation

Several tests have shown that the guess of the initial damage surface is not important because the first optimisation step in the identification procedure consists in a rough Levenberg-Marquardt optimisation with a single parameter, converging within less than 4 iterations to a good estimate of the damage surface. Any reasonable surface bigger than zero and smaller than the plate size can be used as an initial guess. In further tests, the initial value for the damage surface is set to $1\,\mathrm{cm}^2$.

Results of the numerically generated test problems

Table 6.5 shows the results of the identification procedure in case of the numerical examples that have a plate size of 300 mm × 140 mm. The solutions for the damage position are located within a radius of 5 mm to the exact position. As anticipated in Section 5.4.3, the damage size is underestimated by 8.3 % up to 37 %. The optimisation procedure converges to the same values, independently of the initial guess of the damage position and indepentently of the initial guess of the damage surface. In case the initial guess of the damage position is located close to a symmetry line of the plate, the predicted damage position may however be found beyond the wrong side of the symmetry line. The damage aspect ratio can not be identified in some of the examples. It is important to notice that the value of the aspect ratio does not diverge to meaningless values. In fact, it never reaches the confidence bounds defined in Section 6.5.1. The residual after identification is between $5.7{\cdot}10^{-7}$ and $2.4{\cdot}10^{-5}$, meaning that the standard deviations from the adjusted eigenfrequency changes are between 0.02 % and 0.16 %. The numerical model fits the experimental results very well and it demonstrates that the homogenised damage model faithfully represents the stiffness loss due to delamination damage.

Results of the experimental test problems

Table 6.6 shows the results in case of the experimental validation tests. Here, the prediction of the position is also very good. In the worst case, the error is within a radius of less than 7 mm to the exact position. This distance corresponds to merely 10 % or less of the damage size. The damage surface is identified with a maximum error of -30 %. It has been expected that the damage surface is underestimated because the damage factors have been chosen among the highest values listed in Table 5.3. It is also anticipated in the sensitivity analysis in Section 6.4.2 that the damage aspect ratio is not always correctly identified. The residual error after the convergence of the optimisation algorithm is small with values

Initial guess		Identification results				
x^{d}_{1i} [mm]	x^{d}_{2i} [mm]	x^{d}_{1} [mm]	x^{d}_{2} [mm]	A [cm^2]	r_W [-]	Residual [-]
	Reference:	30.00	13.00	10.73	0.66	
15.0	13.0	30.61	14.65	6.78	1.00	$5.72{\cdot}10^{-7}$
18.0	20.0	29.57	15.06	6.85	0.98	$7.28{\cdot}10^{-7}$
25.0	3.0	30.62	14.65	6.79	1.00	$5.72{\cdot}10^{-7}$
25.0	-2.0	30.65	-14.64	6.79	1.00	$5.72{\cdot}10^{-7}$
31.0	12.0	29.59	15.12	6.91	1.00	$6.92{\cdot}10^{-7}$
40.0	26.0	30.64	14.65	6.79	1.00	$5.72{\cdot}10^{-7}$
42.0	8.0	30.63	14.65	6.79	1.00	$5.72{\cdot}10^{-7}$
	Reference:	55.00	3.00	15.95	0.66	
55.0	3.0	53.98	-1.41	13.95	0.74	$1.59{\cdot}10^{-6}$
50.0	10.0	53.23	0.89	13.75	0.74	$1.11{\cdot}10^{-6}$
46.0	0.0	53.68	-0.53	13.86	0.74	$1.32{\cdot}10^{-6}$
40.0	1.0	54.63	0.42	14.09	0.74	$2.20{\cdot}10^{-6}$
62.0	-2.0	54.02	-1.21	13.95	0.74	$1.61{\cdot}10^{-6}$
61.0	8.0	54.42	-0.21	14.04	0.74	$1.95{\cdot}10^{-6}$
	Reference:	70.00	33.00	20.60	0.58	
70.0	33.0	65.81	32.89	17.04	0.96	$4.39{\cdot}10^{-6}$
60.0	32.0	65.90	32.12	17.06	0.96	$4.18{\cdot}10^{-6}$
64.0	36.0	65.84	32.02	17.09	1.00	$4.11{\cdot}10^{-6}$
75.0	29.0	66.14	32.23	17.18	0.99	$4.23{\cdot}10^{-6}$
79.0	21.0	65.82	32.06	17.07	1.02	$4.15{\cdot}10^{-6}$
71.0	45.0	65.83	32.13	17.09	1.02	$4.16{\cdot}10^{-6}$
	Reference:	4.00	24.00	20.60	0.58	
4.0	24.0	-0.74	19.36	16.94	0.65	$2.45{\cdot}10^{-5}$
-5.0	32.0	0.43	19.27	16.85	0.64	$2.43{\cdot}10^{-5}$
2.0	14.0	0.47	19.21	16.85	0.65	$2.42{\cdot}10^{-5}$
0.0	29.0	-1.17	19.15	16.79	0.62	$2.42{\cdot}10^{-5}$
9.0	30.0	-0.52	19.33	16.92	0.64	$2.44{\cdot}10^{-5}$
16.0	22.0	-0.04	19.27	16.88	0.65	$2.43{\cdot}10^{-5}$
	Reference:	22.00	40.00	20.60	0.58	
22.0	40.0	23.46	40.55	16.59	0.77	$6.24{\cdot}10^{-6}$
19.0	47.0	23.44	40.30	16.59	0.78	$6.17{\cdot}10^{-6}$
10.0	36.0	23.58	40.66	16.54	0.77	$6.38{\cdot}10^{-6}$
28.0	29.0	23.44	39.73	16.78	0.78	$6.41{\cdot}10^{-6}$
30.0	31.0	23.37	40.29	16.66	0.78	$6.23{\cdot}10^{-6}$
26.0	53.0	23.36	40.50	16.57	0.78	$6.17{\cdot}10^{-6}$

Table 6.5: Results of the identification of the numerically generated data.

Initial guess		Identification results				
x_{1i}^{d} [mm]	x_{2i}^{d} [mm]	x_1^{d} [mm]	x_2^{d} [mm]	A [cm^2]	r_W [-]	Residual [-]
	Reference:	75.00	40.00	7.56	0.86	
95.00	60.00	71.66	38.43	5.47	1.54	$1.75{\cdot}10^{-6}$
55.00	20.00	71.78	38.62	5.71	1.29	$1.90{\cdot}10^{-6}$
95.00	20.00	71.17	38.09	5.40	1.53	$1.83{\cdot}10^{-6}$
55.00	60.00	71.53	38.38	5.52	1.45	$1.83{\cdot}10^{-6}$
	Reference:	25.00	20.00	15.36	0.75	
15.00	10.00	21.98	23.55	12.00	0.74	$1.21{\cdot}10^{-5}$
15.00	30.00	21.93	23.62	12.04	0.74	$1.18{\cdot}10^{-5}$
35.00	10.00	21.86	23.78	12.10	0.75	$1.23{\cdot}10^{-5}$
35.00	30.00	21.99	23.74	12.10	0.73	$1.21{\cdot}10^{-5}$
5.00	0.00	22.10	-23.45	11.98	0.73	$1.15{\cdot}10^{-5}$
* 5.00	40.00	21.94	23.63	12.04	0.73	$1.23{\cdot}10^{-5}$
45.00	0.00	23.35	-23.38	12.12	0.64	$1.21{\cdot}10^{-5}$
45.00	40.00	21.84	23.79	12.10	0.75	$1.21{\cdot}10^{-5}$
	Reference:	0.00	35.00	13.94	0.6	
-20.00	15.00	7.56	35.66	9.59	0.45	$8.22{\cdot}10^{-5}$
-20.00	55.00	2.12	35.44	9.68	0.44	$8.18{\cdot}10^{-5}$
20.00	55.00	6.34	35.40	9.68	0.48	$8.22{\cdot}10^{-5}$
20.00	15.00	5.34	35.50	9.74	0.46	$8.20{\cdot}10^{-5}$

Table 6.6: Results of the identification of the experimental data. The convergence to the solutions in the row with a (*) is illustrated in Figure 6.14

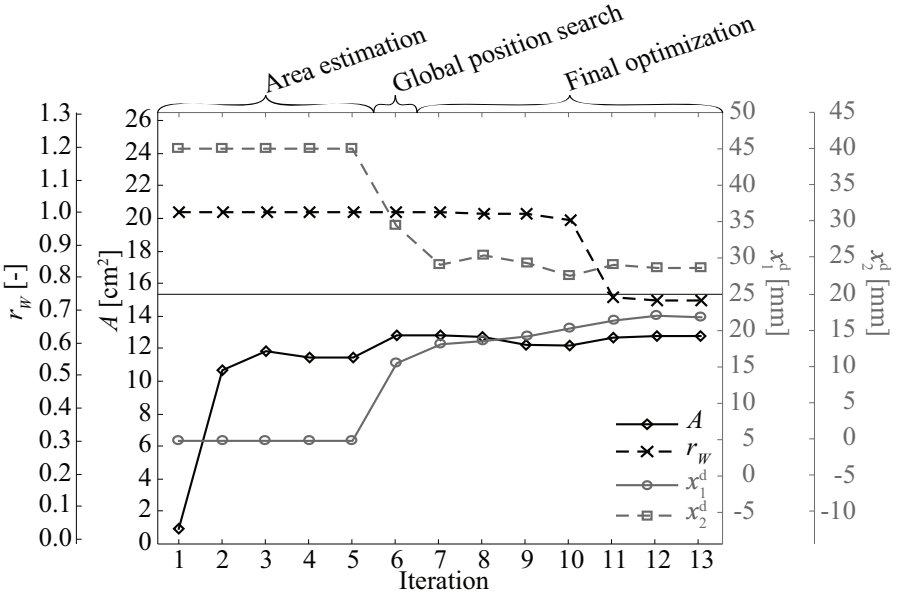

Figure 6.14: Convergence graph of all the parameters during the identification procedure. The horizontal axis indicates the experimentally measured values.

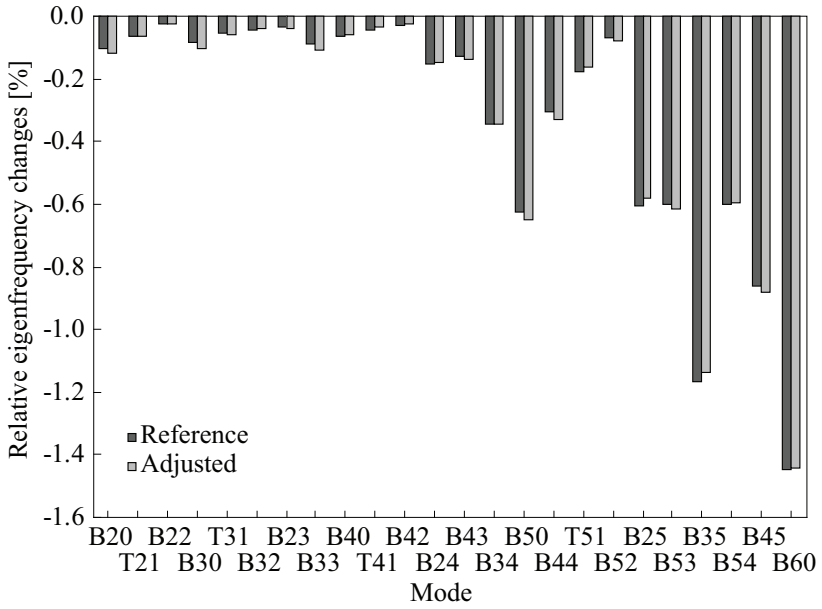

Figure 6.15: Residuals of optimisation in case of a large plate. Comparison of the adjusted to the reference eigenfrequency changes of the large plate.

between $1.75{\cdot}10^{-6}$ and $8.2{\cdot}10^{-5}$ and gives evidence of the good quality of the identified results and the model.

The convergence of the four parameters identified throughout the optimisation procedure is illustrated in Figure 6.14. The convergence graph corresponds to the row marked by a (*) from Table 6.6. During the first step of the optimisation, it is noticed that a good estimate of the damage surface is already achieved. In the next step, the damage position is considerably improved if, like in this case, the initial guess is far from the solution. This global search step also allows to get an even better estimate of the damage surface. During the last step, the final optimisation, all the parameters are jointly fine-tuned until convergence of the iterative optimisation algorithm.

Results of the generalised test problem with larger plate dimensions

In a plate with dimensions of 400 mm × 300 mm, the eigenfrequency changes of the first 24 modes are considered to identify the size and position of the damage. This amount of input data is sufficient for the optimisation method to be robust and converge to an accurate solution. Independently on the initial guess of the damage position, the algorithm converges to a good estimate of the damage surface and position. The results are summarised in Table 6.7. The eigenfrequency changes of the final, adjusted numerical model coincide well

Initial guess		Identification results				
x^{d}_{1i} [mm]	x^{d}_{2i} [mm]	x^{d}_{1} [mm]	x^{d}_{2} [mm]	A [cm^2]	r_W [-]	Residual [-]
	Reference:	90.00	70.00	20.60	0.58	
110.0	50.0	92.03	69.63	14.95	0.99	$4.95{\cdot}10^{-7}$
110.0	90.0	91.91	69.54	14.93	0.99	$5.08{\cdot}10^{-7}$
70.0	50.0	91.99	69.99	14.98	0.97	$4.46{\cdot}10^{-7}$
70.0	90.0	91.98	69.72	14.95	0.99	$4.83{\cdot}10^{-7}$

Table 6.7: Results of the damage identification in a large plate.

with the reference input data (see Figure 6.15). An average standard deviation of only 0.015 % is obtained after the optimisation.

6.7 Summary and conclusion

The homogenised damage model built in Section 5.4.2 is used in a inverse numerical-experimental optimisation procedure. The parameters of the damage model are the damage position, surface and aspect ratio. These parameters have the advantage of being a comprehensible measure of a potential damage. Before the numerical model is used in the inverse damage identification procedure, damage factors of the continuum damage model were determined. The damage factors define the reduction of transverse shear stiffness of the laminate in the damage region. This reduction is supposed to be homogeneous within the damage zone which is approximated by a rhomb. In the range of low energies studied in this work, damage factors of 94 % are determined for the composite lay-up presented in Section 2.2.2.

The algorithm for the identification of the damage size needs initial values for the damage surface, aspect ratio and position. For simplicity reasons, the aspect ratio is initially set to a value of one. The first guess for the damage surface can have any reasonable value bigger than zero and smaller than the plate size. A good estimate of the damage surface is already obtained throughout a first optimisation step. The initial guess for the damage position needs to be more precise. When the initial guess of the damage position is far from the exact position, the algorithm may diverge to a wrong position. The tolerated distance between the initial guess and the exact position depends on the amount of eigenmodes considered during the identification, but it has not been evaluated during this study. However, it could be shown in the robustness analysis that the identification procedure converges to the same solution when the initial value for the damage position is within a radius of 30 mm. A guess with such a precision can be obtained from the

localisation method presented in Chapter 4.

The accuracy of the identified parameters is good. During the validation tests, the damage size is underestimated with an error smaller than 30 %. The damage position also converges to a location that is within a radius of about 7 mm to the exact position. This error corresponds to a distance less than 10 % of the damage size.

In case the damage is to be identified in a plate with a bigger size, the input data supplied to the identification procedure has to be chosen appropriately. The relative eigenfrequency changes originating from damage have to be higher than the achievable measurement accuracy of the frequencies which is about 0.06 %. The larger the plate, the higher the eigenfrequencies that are considerably affected by the damage. Eigenmodes with a wavelength in the order of twice the size of the damage or shorter are sufficiently sensitive to damage. When the number of available eigenfrequency changes is sufficient, the damage is identified correctly.

Chapter 7

Application of impact localisation and damage identification method

In this chapter, the usage and implementation of the impact localisation and damage identification method based on dynamic FBG measurements is summarised. In the previous chapters, the different tools necessary for the detection and localisation of an impact event and the characterisation of damage have been developed.

An improved and high rate FBG interrogation method has been presented, calibrated and validated (Chapter 3). An interpolation-based impact localisation method has been developed, tested and validated (Chapter 4). A precision of a few millimetres has been attested to the prediction of the impact location. The type of damage occurring in the CFRP plates during a low-velocity impact has been fully characterised and its influence on the vibration properties of a plate studied. A homogenised damage model has been built and validated (Chapter 5). An inverse numerical-experimental optimisation method has been developed to identify the size and the position of damage (Chapter 6). The impact position predicted by the localisation method provides a good initial guess of the damage position to the proposed optimisation algorithm.

The different tasks of the structural health monitoring method have been validated individually. At this point, the impact localisation and damage identification method is applied to a complete experiment.

7.1 Summary of the method

Before a complete experiment is presented in the next section, the procedure adopted for the method is summarised. At first, the composite plate monitored during the experiment needs to be equipped with embedded or surface-glued FBG sensors. A minimum of three sensors is required for the localisation method. Further sensors enhance the precision of the impact location prediction. The sensors should be placed so that they delimit the periphery of the region monitored for impact events and that they are sufficiently sensitive to the first eigenmodes of the plate. The sequence of operations developed for the impact detection and damage characterisation method is the following:

- Before impact, reference measurements are performed by using non-destructive impacts on a grid of known locations.
    1. The variable intensity signal of the FBG sensors is acquired at a rate of 1 GHz.
    2. The arrival time delays of the waves originating from the non-destructive impacts and arriving at the different sensors are determined. These data constitute the reference set for the interpolation-based localisation method.
    3. The calibrated strain signal of the FBG sensors is acquired at a rate of 100 kHz.
    4. FRFs are calculated and the eigenfrequencies of the intact plate are determined.
    5. An FE model of the intact plate is built and validated with the experimentally measured eigenfrequencies.
- During impact, the response of the FGB sensors is monitored.
    1. The variable intensity signal of the FBG sensors is acquired at a rate of 1 GHz.
    2. The arrival time delays of the waves originating from the impact and arriving at the different sensors are determined. The impact location can be predicted.
    3. The calibrated strain signal of the FBG sensors is acquired at a rate of 100 kHz.
    4. The amplitude and duration of the strain signal indicate the existence or not of an impact event.
- After impact, the plate is again dynamically excited by non-destructive impacts.
    1. The calibrated strain signal of the FBG sensors is acquired at a rate of 100 kHz.
    2. FRFs are calculated and the eigenfrequencies of the damaged plate are determined.

3. The relative changes of the eigenfrequencies before and after impact serve as an input to the inverse numerical-experimental damage size and position identification procedure. The predicted impact location is used as an initial guess for the damage position.

7.2 Application of the method

7.2.1 Specimen preparation

A CFRP plate with a symmetric $[0\,°_2, 90\,°_2, 0\,°_2, 90\,°_2, 0\,°_2, 90\,°_2, 0\,°_2]_s$ stacking sequence is produced. Two FBG sensors are embedded between the ultimate and penultimate ply in the direction of the reinforcing fibres. The plate is cured in autoclave during 17 h at a temperature of up to 80 °C. The cured plate is cut to a size of 300 mm × 140 mm and holes are drilled in the plate for the bolts of the fixture mechanism. Two other FBG sensors are glued on the surface of the plate in an oblique direction. The plate is clamped on the basis of the impact tower with the optical fibres on the lower side. The configuration of the clamped plate with FBG sensors is illustrated in Figure 7.1.

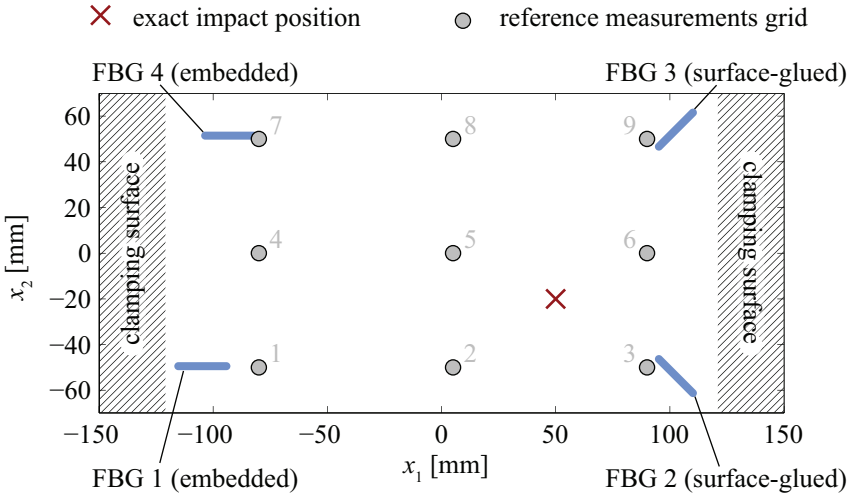

Figure 7.1: Schematic of the clamped plate with four FBG sensors.

7.2.2 Reference measurements

During reference measurements, the dynamic strain response of the FBG sensors to non-destructive impacts is acquired using the two fast FBG interrogation methods presented

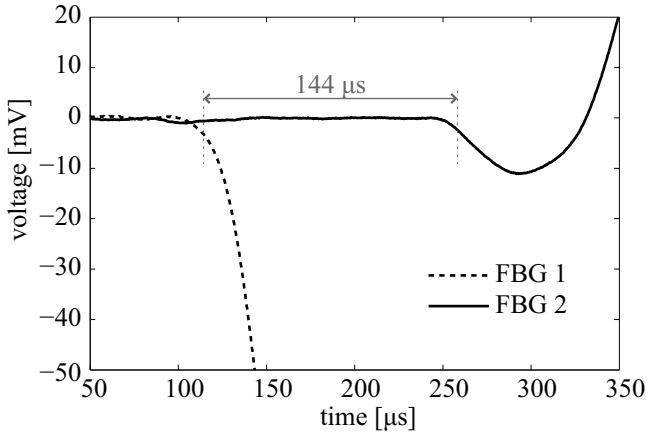

Figure 7.2: High rate signals from FBG 1 and FBG 2 during a non-destructive impact on reference point 1.

in Chapter 3. The excitation is done using hammer impact on a grid of 9 points $\left(x_1^R, x_2^R\right)$. The data serve as a reference for the interpolation-based impact localisation method and for determining the eigenfrequencies of the intact plate. Fast and highly sensitive intensity measurements are done for the localisation, and calibrated strain measurements for the experimental modal analysis. Note here that only two optical channels with sufficient sensitivity are available for this very low amplitude signals due to the configuration of the equipment. Therefore, each measurement is performed four times — once for each of the four different couples of sensors. The arrival times of the wave at the sensors are determined using a threshold method. Figure 7.2 shows the signals of FBG 1 and FBG 2 during a non-destructive hit on reference point 1.

	Position [mm]		Arrival time delays [µs]			
Point	x_1^R	x_2^R	Δt_{12}^R	Δt_{23}^R	Δt_{34}^R	Δt_{41}^R
1	-80	-50	(*)144	29	-27	-127
2	5	-50	-16	37	26	-60
3	90	-50	-149	73	79	-46
4	-80	-50	102	24	-61	-25
5	5	0	-12	4	41	-22
6	90	0	-110	7	153	-13
7	-80	0	57	-5	-143	95
8	5	50	-8	-27	11	53
9	90	50	-65	-50	159	17

Table 7.1: Reference measurements of wave arrival time delays.

The arrival time delays $\left[\Delta t_{12}^R, \Delta t_{23}^R, \Delta t_{34}^R, \Delta t_{41}^R\right]$ of four different couples of sensors as a function of the reference position $(x_1, x_2)^R$ are shown in Table 7.1. The (*) indicates the value obtained from the signals in Figure 7.2. It can be noticed that the sum of the arrival time delays expressed by

$$\Delta t_{12}^R + \Delta t_{23}^R + \Delta t_{34}^R + \Delta t_{41}^R = \left(t_2^R - t_1^R\right) + \left(t_3^R - t_2^R\right) + \left(t_4^R - t_3^R\right) + \left(t_1^R - t_4^R\right) \tag{7.1}$$

is not equal to zero as it would be expected. This is due to the fact that the signals are not recorded synchronously and that the arrival time delays are subject to errors. The reference data set $\left\{\left[\Delta t_{12}^R, \Delta t_{23}^R, \Delta t_{34}^R, \Delta t_{41}^R\right]; \left(x_1^R, x_2^R\right)\right\}$ allows to compute the interpolated response surfaces $\left[\widehat{\Delta t}_{12}^R(x_1, x_2), \widehat{\Delta t}_{23}^R(x_1, x_2), \widehat{\Delta t}_{34}^R(x_1, x_2), \widehat{\Delta t}_{41}^R(x_1, x_2)\right]$.

The dynamic strain measurements done with the FBG sensors are also used to calculate the FRFs of the reference points. The signal-to-noise ratio is good and hence the FRFs present a high dynamic range as shown in Figure 7.3. The eigenfrequencies of the intact plate are determined from the FRFs using the modal curve fitting software ME'scope. The natural frequencies of the first ten modes are obtained with a relative precision of about 0.07 % (cf. Section 3.3.4) and are listed in Table 7.2.

The natural frequencies serve for validation of the FE model of the intact plate. The FE model corresponds to the homogenised damage model presented in Chapter 5 with the damage factors D_{13} and D_{23} equal to zero.

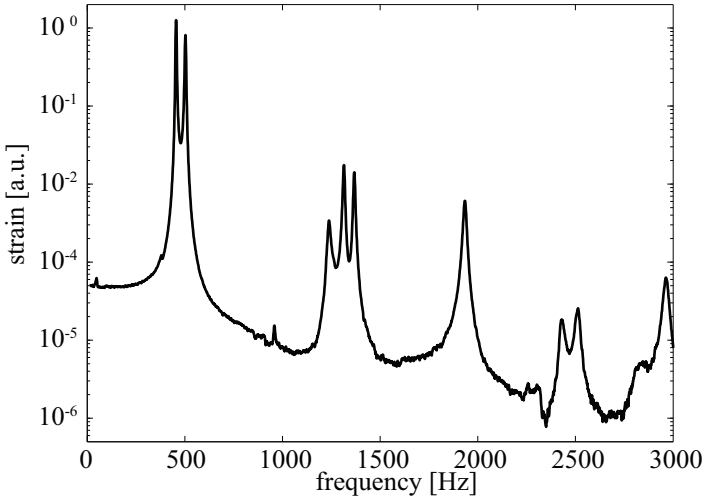

Figure 7.3: Average FRF of intact plate measured with FBG sensors.

Mode	Shape	Frequency [Hz]
1	B20	456.03
2	T21	508.81
3	B30	1237.92
4	T31	1318.29
5	B22	1387.15
6	B32	1960.95
7	B40	2450.96
8	T41	2522.28
9	B42	2991.67
10	B23	3371.46

Table 7.2: Eigenfrequencies of the intact plate.

7.2.3 Low velocity impact

The plate is impacted at the position $(x_1^i, x_2^i) = (50\,\text{mm}, -20\,\text{mm})$ with an energy of 3.4 J. During the impact, the two different acquisition modes for the intensity signals are used. Calibrated measurements of the strain signals are done to have an indication about the amplitude of the impact. The strain signals of FBG 1 and FBG 2 are acquired with the two high sensitivity channels. FBG 3 and FBG 4 are interrogated synchronously with the two high range channels. The first 20 ms of the strain signals of all four sensors are shown in Figure 7.4. It can be seen that the signal of sensor FBG 1 is out of range during the first milliseconds of the impact. Maximum strain levels of up to 1 000 $\mu\varepsilon$ are reached during the first 5 ms of the impact. The high spectral content of the signals may indicate the initiation and propagation of damage. After 5 ms, the response obviously consists of a superposition of modal vibrations.

7.2.4 Impact localisation

Fast and highly sensitive intensity measurements are done for the localisation of the impact. Figure 7.5 shows the first 700 microseconds of the intensity signal (Figure 7.4) acquired during the impact. This signal allows to determine the arrival time delays of the waves at the four different sensors. Table 7.3 gives the arrival time delays $\left[\Delta t_{12}^P, \Delta t_{23}^P, \Delta t_{34}^P, \Delta t_{41}^P\right]$ determined using a threshold method. These values are used to predict the impact location with the localisation method described in Chapter 4. A negative value is for example obtained for the arrival time delay Δt_{12}^P because the wavefront arrives at the sensor S_2 before it arrives at sensor S_1, and hence $t_1^P > t_2^P$.

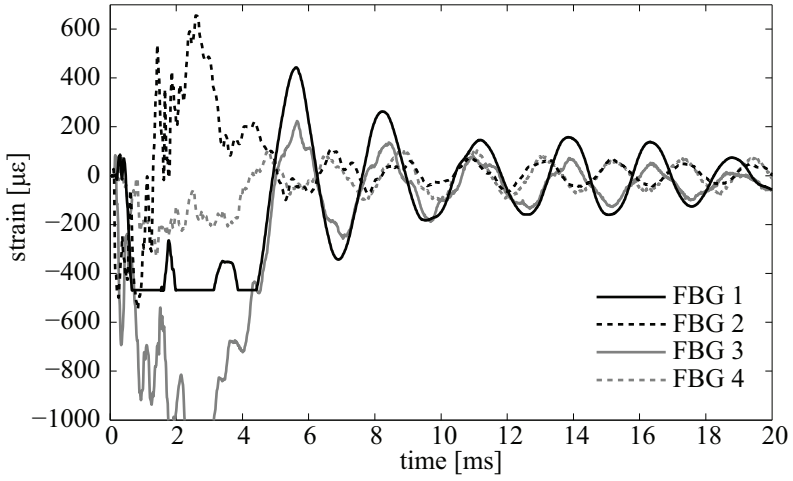

Figure 7.4: Strain signals during impact with energy of 3.4 J.

The isolines L_{12}, L_{23}, L_{34} and L_{41} are the lines where the interpolated response surfaces $\left[\widehat{\Delta t}^{R}_{12}(x_1,x_2), \widehat{\Delta t}^{R}_{23}(x_1,x_2), \widehat{\Delta t}^{R}_{34}(x_1,x_2), \widehat{\Delta t}^{R}_{41}(x_1,x_2)\right]$ take the values of arrival time delays $\left[\Delta t^{P}_{12} = -78\,\mu\text{s}, \Delta t^{P}_{23} = -20\,\mu\text{s}, \Delta t^{P}_{34} = 91\,\mu\text{s}, \Delta t^{P}_{41} = 7\,\mu\text{s}\right]$, respectively. These isolines are indicated in Figure 7.6. The intersections of the pairs of isolines (L_{12}, L_{23}), (L_{23}, L_{34}), (L_{34}, L_{41}) and (L_{41}, L_{12}) are calculated. The predicted location of the impact corresponds to the average of these four intersections, which is also shown in this figure. The coordinates of the predicted impact position are $\left(x^{l}_1, x^{l}_2\right) = (52.95\,\text{mm}, -24.69\,\text{mm})$. The distance between the predicted and exact location is 5.5 mm which is very small compared to the smallest plate dimension (4 %). This location constitutes the initial guess of

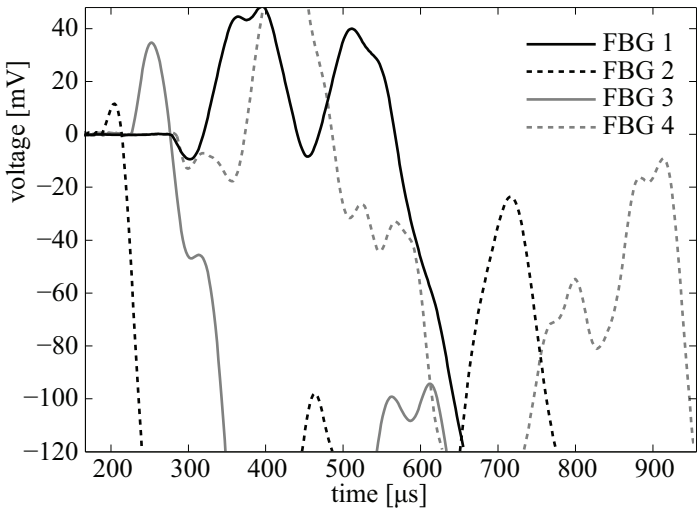

Figure 7.5: Intensity signals from FBG sensors.

Position [mm]		Arrival time delays [µs]			
x_1	x_2	Δt_{12}^P	Δt_{23}^P	Δt_{34}^P	Δt_{41}^P
50.0	-20.0	-78	-20	91	7

Table 7.3: Arrival time delays determined in the case of the impact with an energy of 3.4 J.

the damage position for the inverse numerical-experimental damage identification method.

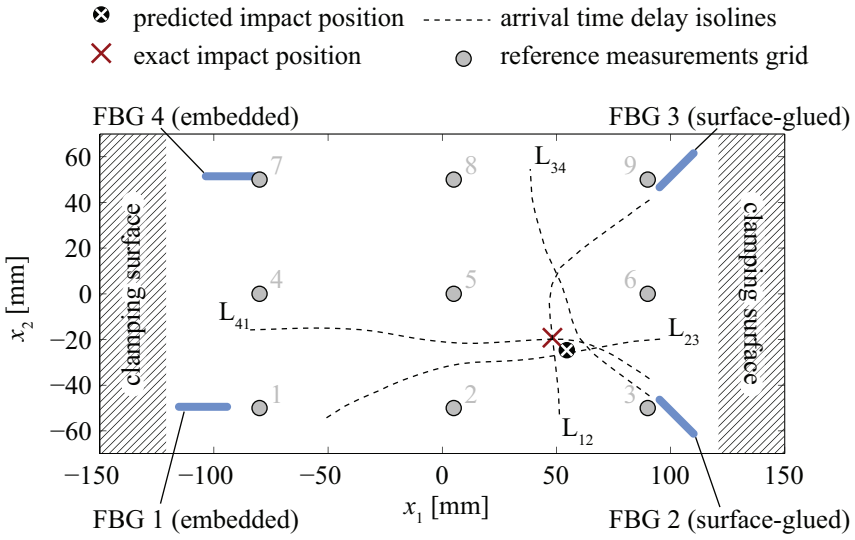

Figure 7.6: Predicted impact location.

7.2.5 Post-impact measurements

After the impact, an experimental modal analysis of the damaged plate is carried out using non-destructive impacts. The FRFs are again computed from the dynamic strain signal obtained by FBG sensors. The eigenfrequencies of the damaged plate are obtained by modal curve fitting and can be compared to those of the intact plate.

For the current damage position and size, eigenfrequency changes of around -1 % are noticed. These eigenfrequency changes are considerably higher than the accuracy of the eigenfrequency measurements. The relative eigenfrequency changes due to the damage are listed in Table 7.4. These data are used to adjust the parameters of the homogenised damage model. The parameters are the damage size and position. The shape of the damage is approximated by a rhomb and the damaged region is governed by a reduction of the transverse shear moduli G_{13} and G_{23}. Damage factors $D_{13} = D_{23} = 94\,\%$ have

Mode	Shape	Frequency [Hz]	Frequency change [%]
1	B20	450.99	-0.45
2	T21	507.54	-0.25
3	B30	1236.56	-0.11
4	T31	1316.84	-0.11
5	B22	1380.35	-0.49
6	B32	1946.05	-0.76
7	B40	2414.44	-1.49
8	T41	2513.70	-0.34
9	B42	2962.65	-0.97
10	B23	3332.01	-1.17

Table 7.4: Eigenfrequency changes due to damage.

been determined in Chapter 5 for the type of damage occuring within this range of impact energies.

7.2.6 Damage identification

Damage surface and damage position are identified using the numerical-experimental optimisation method presented in Chapter 6. The initial value chosen for the damage surface A is $1\,\mathrm{cm}^2$ and the aspect ratio r_W is set to one. The impact location $\left(x_1^l, x_2^l\right)$ predicted by the localisation method is used as the initial guess for the damage position $\left(x_1^d, x_2^d\right)$.

The optimisation procedure is performed in three steps. First, a rough estimation of the damage surface is made. Secondly, a global search is performed over different damage positions within a radius of 15 mm around the predicted impact location. Finally, the damage surface, aspect ratio and position are jointly identified using an iterative algorithm.

A total of 92 numerical model evaluations are needed. The optimisation takes about 25 minutes on a computer with 4 CPUs (2.83 GHz) and 8 GB memory. Figure 7.7a shows the convergence of the four parameters. The rough estimation of the damage surface requires four iterations. It has to be noticed that in this case, the global search step does not contribute to an improvement because the predicted impact location, used as an initial guess, is close the the final solution of the damage position. The final optimisation algorithm of the last step converges again fast in only two iterations.

The identified parameters are given in Table 7.5 where they are compared to the experimentally measured data. The exact damage position is known and the projected damage

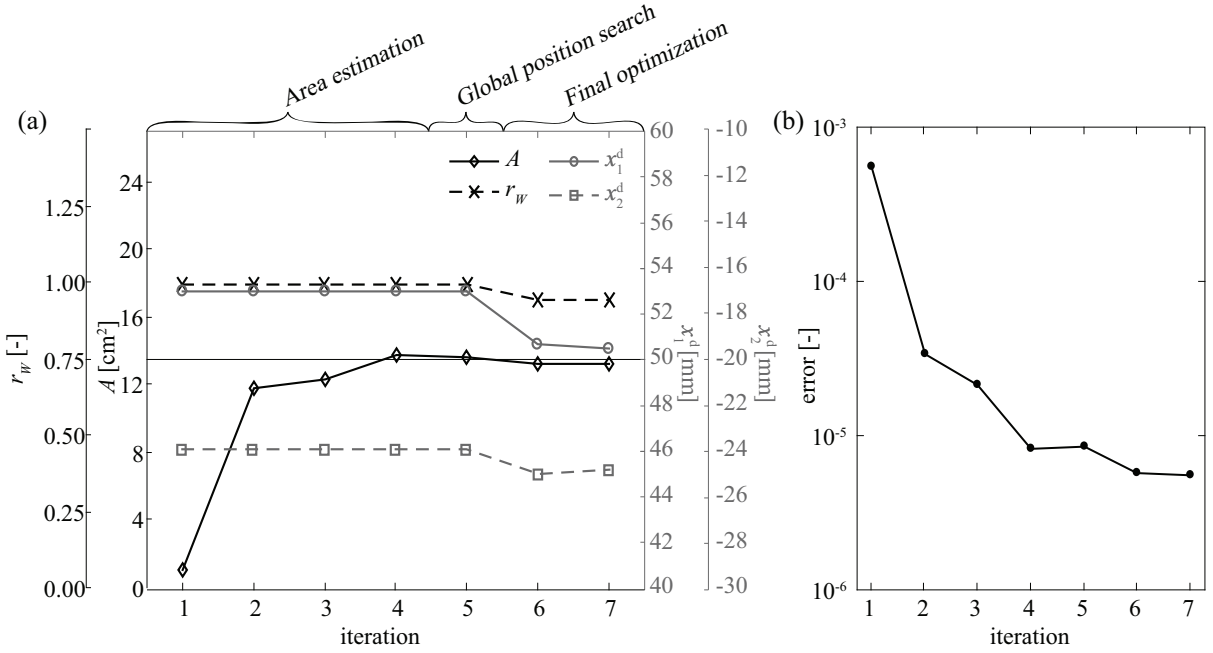

Figure 7.7: (a) Convergence of the parameters during the optimisation procedure. (b) Convergence of the error norm.

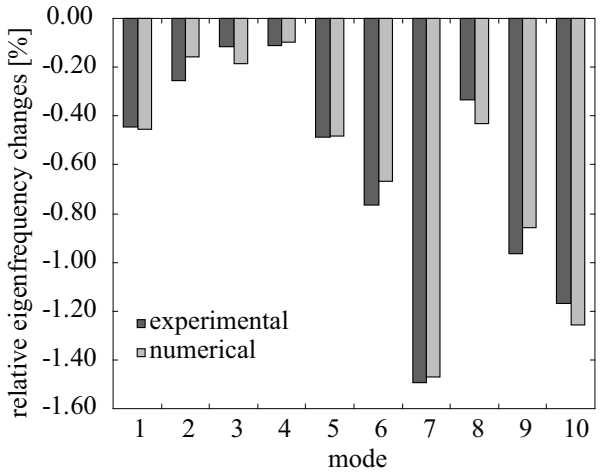

Figure 7.8: Numerical and experimental eigenfrequency changes.

	Damage surface [cm^2]	Aspect ratio [-]	Position x_1^d [mm]	x_2^d [mm]
measured	13.50	0.75	50.00	-20.00
identified	13.36	0.96	50.81	-25.43

Table 7.5: Results of the identification procedure.

surface is determined by visual inspection. The experimental error related to this way of determining the damage surface is of about 10 %. The final prediction error of the damage position is only 5.5 mm which is very small compared to the damage size. In this case, the optimisation algorithm could not improve the initial guess obtained from the impact localization method because this prediction has already been very close to the exact damage position. The damage surface estimation is also good compared to the measurement precision.

Figure 7.7b shows the convergence graph of the error norm. The norm of the residual is small with a value of $5.57 \cdot 10^{-6}$, which corresponds to a standard deviation of 0.07 % of the numerical relative eigenfrequency changes to the experimental ones. The relative eigenfrequency changes of the final numerical model are compared to the experimental ones in Figure 7.8. It can be seen that all the eigenfrequency changes are well fitted by the model.

Chapter 8

Conclusions

8.1 Synthesis and conclusions

A high rate FBG interrogation method has been elaborated and enhanced in order to permit the use of FBG sensors for dynamic strain measurements with sufficiently low noise. The interrogation system has been thoroughly calibrated so that quantitative strain measurements can be done at rates up to 250 kHz. It allows to capture the maximum local internal deformation in the laminate and the high frequency content of the strain signals during an impact. Moreover it has been demonstrated that FBG sensors can be employed for experimental modal analysis of composite plates excited by non-destructive hammer impacts. The eigenfrequencies can be determined with a similar precision than the one obtained with traditional sensors. An auxiliary acquisition mode with a high sensitivity and a sampling rate of 1 GHz permits the use of FBG sensors for sensing acoustic waves.

A versatile interpolation-based impact localisation method has been developed. The arrival time delays of acoustic waves originating from the impact and arriving at the FBG sensors can be determined with an accuracy of a few microseconds and serve for the localisation of an impact. The method does neither require the a priori knowledge of the wave propagation velocity nor the exact position of the sensors within the laminate. A reference data set produced by non-destructive hammer impacts on a coarse measurement grid is needed. Via interpolation of the reference data, the impact location can be predicted with an accuracy of a few millimetres. The error sources of the prediction have been evaluated and are found to be mainly independent of the plate size.

The effect of low impact energy induced damage on the vibrational behaviour of a laminate has been investigated. Therefore, a set of CP plates have been impacted with

energies ranging from 1.7 to 6.8 J. A systematic, almost linear decrease of the eigenfrequencies is observed with increasing impact energy. Considerable changes of the modal damping factors can be observed but no reproducible trend identified. The local changes of the mode shapes are only noticeable when a very fine measurement grid is employed during experimental modal analysis. A three-dimensional representation of the damage pattern has been produced by high resolution X-ray computed tomography and validated by microscopic images and ultrasonic C-scan. This method is time-consuming but gives a very accurate picture of the damage. In case of the investigated impact energy range, the damage mainly consists of delamination damage and only a few intra-laminar cracks are found just beneath the impact point. An almost linear relation between delaminated surface and incident impact energy is noticed. Consequently, the eigenfrequencies decrease almost linearly with increasing damage surface.

Numerical modal analysis with a detailed delamination model confirms that the eigenfrequency changes of the plate can mainly be attributed to delamination damage. A simplified damage model, based on material properties and damage homogenisation as well as damage shape approximation has been built and validated. The continuum damage model relies on two damage factors reducing the transverse shear moduli of the laminate. Damage factors of approximately 94 % have been determined on the basis of experimental data for the given laminate and the studied impact energy range. Despite its simplicity, this model constitutes a faithful representation of the damage and the associated stiffness loss of the laminate. The parameters of the model, i.e. damage position, surface and aspect ratio, are comprehensible characteristics and their number is reduced to a minimum to ease their identification.

An inverse numerical-experimental optimisation method has been developed to identify these parameters. The minimisation algorithm reduces the discrepancy between numerically calculated and experimentally measured eigenfrequency changes. The proposed optimisation algorithm is performed in three steps to improve consecutively the estimation of the damage surface, position and aspect ratio. The robustness of the optimisation algorithm to various initial values of the damage surface and position could be verified successfully. The eigenfrequency changes of the first 10 modes are considered in the validation examples. Due to the limited amount of experimental input data, a good initial guess of the damage position is needed. Such a guess can be obtained from the impact localisation method. In the case of the studied configuration it has been shown that the damage position is identified within a radius of a few millimetres when its initial guess is no more than 30 mm away from the exact position. This error corresponds to less than 10 % of the damage size. A good estimate of the damage surface is obtained and, because the damage factors of the homogenised damage model are chosen amongst the highest experimentally

determined values, the surface is consistently underestimated. Throughout several tests it has been found that an optimisation procedure in 2 steps would also converge to the same results in most of the cases. When the plate under test is large, more eigenfrequencies must be considered to have sufficient exploitable data for the identification of the damage. Indeed, an eigenfrequency change of a mode is significant compared to the measurement precision obtained with FBG sensors when the wavelength of an eigenmode is shorter or in the order of 4 times the damage size.

A comprehensive experiment has demonstrated the successful application of FBG sensors for impact localisation and damage identification in CFRP plates. The location of a destructive impact has been predicted with a good accuracy and could be used as an initial guess of the damage position in the inverse numerical-experimental optimisation method. The damage surface and position have been identified with an excellent accuracy.

8.2 Perspective

The applicability of FBG sensors for SHM depends largely on the quality of the acquisition signals. Beyond the modifications and improvements already made to the FBG interrogation method throughout this work, it might possible to enhance the quality of the measurements. Compared to the dynamic range of traditional sensors used for dynamic measurements, the signals obtained from FBG sensors still show room for further improvement in terms of signal-to-noise ratio. Following is a list of modifications that might contribute to a reduction of the noise:

- Use an acquisition card with a built-in analogue low-pass filter for the acquisition of the intensity signals.
- Use an acquisition card with a higher analogue input resolution. The actual data acquisition card has a 14 bit resolution.
- Reduce the optical coupling between the interrogation channels to a maximum. Use a circulator instead of a coupler to deviate the Bragg reflection peak to the photodiodes.
- Reduce the electrical noise by employing a better stabilised voltage source and low-noise amplifiers for the photodiodes.

Despite the good results obtained from the impact localisation and damage identification method, the prediction might be upgraded by considering more experimental data. Moreover it is of interest to generalise the method to a large variety of composite laminates and experimentally validate its applicability for different configurations.

- Further study the effect of damage on the damping characteristics of a plate or structure and the use of modal damping ratios to contribute to the damage identification. A high sensitivity of the modal damping factors is noticed but no reproducible trend could be observed within this work.
- Multiplexed optical fibres with several Bragg gratings along the length of the fibre can be used in low frequency vibrations to increase the number of measurement points. The strain mode shapes and their sensitivity to a local decrease of the laminate stiffness may contribute to the identification of damage. Forthcoming progress in optics technology might allow the use of long Bragg gratings for distributed, dynamic strain measurements.
- The homogenised damage model and especially the values of the damage factors has to be validated for different materials. If needed, the model has to be generalised for different materials, stacking sequences, thicknesses and damage types.
- The damage identification method has to be experimentally validated for larger composite panels and can be extended to real structures. It has been discussed on the basis of a numerical analysis that a higher number of eigenfrequencies has to be considered for the damage identification in a larger structure. The dynamic excitation of the structure as well as the number of sensors may have to be adapted to these circumstances.
- The influence of temperature and other environmental conditions on the modal parameters, in particular the eigenfrequencies, has to be checked because these effects may falsify the prediction of impact damage.
- In order to increase the efficiency of the numerical-experimental identification procedure, the finite element model of the damage plate can be adapted to shell elements based on higher-order shear deformation theory.

In order to realise an integrated system for damage identification with embedded FBG sensors, further extended developments need to be achieved. The following modifications might be considered in the development approach:

- The dynamic excitation of the plate or structure may be done by integrated actuators. Piezoelectric transducers might allow a controlled excitation of a laminate.
- The modal parameter extraction may also rely on ambient excitation of the structure if the frequency range of interest is excited with a sufficient amplitude and may be performed by operational modal analysis.
- It might be of interest to exploit furthermore the information obtained from embed-

ded FBG sensors and the dynamic or static internal strain measurements that can be performed with. Once it is planed to integrate FBG sensors in a structure, they can also be used to monitor the curing process of the composite, check the residual strains and their evolution over the life-time of the laminate and monitor the static and dynamic loading history of the structure.

- The transient response of the FBG sensors may be used to estimate the impact force and position via modal decomposition.

The numerous opportunities for potential future developments and the actual research effort invested by many other groups in the fields of optical sensors and structural health monitoring confirms the interest in the present research work. From my personal point of view the present project has been a very interesting experience because of its actual relevance and its multidisciplinary character. The work gave a deep insight and required a extensive comprehension in the fields of optics, continuum mechanics, dynamics and physics of wave propagation. Moreover it demonstrates again that the combined use of both numerical and experimental, methods permits efficient approaches in engineering.

Publications

[i] J. Frieden, J. Cugnoni, J. Botsis, Th. Gmür, D. Coric. High-speed internal strain measurements in composite structures under dynamic load using embedded FBG sensors. *Composite Structures*, 92(8):1905–1912, 2010.

[ii] J. Frieden, J. Cugnoni, J. Botsis, Th. Gmür. Vibration-based characterization of impact induced delamination in composite plates using embedded FBG sensors and numerical modelling. *Composites Part B*, 42(4):607–613, 2011.

[iii] J. Frieden, J. Cugnoni, J. Botsis, Th. Gmür. Low energy impact damage monitoring of composites using dynamic strain signals from FBG sensors – Part I: Impact detection and localization. *Composite Structures*, *submitted*.

[iv] J. Frieden, J. Cugnoni, J. Botsis, Th. Gmür. Low energy impact damage monitoring of composites using dynamic strain signals from FBG sensors – Part II: Damage identification. *Composite Structures*, *submitted*.

[v] J. Frieden, J. Cugnoni, J. Botsis, Th. Gmür. Characterization of impact damage in fibre reinforced composite plates using embedded FBG sensors. *In: Proceedings of the 5th International Conference on Composites Testing and Model Identification, CompTest*, 157–158, 2011.

[vi] J. Frieden, J. Cugnoni, J. Botsis, Th. Gmür. Damage assessment in carbon fibre reinforced polymer plates based on dynamic measurements with fibre Bragg grating sensors. *In: Proceedings of the Tenth International Conference on Computational Structures Technology, Civil-Comp Press*, P87, 2010.

[vii] J. Frieden, J. Cugnoni, J. Botsis, Th. Gmür. Internal strain measurements in CFRP plates subjected to impact load using FBG sensors. *In: Proceedings of the 17th International Conference on Composite Materials ICCM-17, The British Composites Society*, 2009.

[viii] J. Frieden, J. Cugnoni, J. Botsis, Th. Gmür. Characterization of dynamic response of composite plates with embedded FBG sensors. *In: Proceedings of the 4th International Conference on Composites Testing and Model Identification, CompTest*, P1–3, 2008.

[ix] J. Frieden, J. Cugnoni, Th. Gmür, J. Botsis. Dynamic strain measurements of composite materials using embedded fibre Bragg grating sensors. *In: Proceedings of the 5th International Conference on Fracture of Polymers, Composites and Adhesives (5th ESIS TC4 Conference)*, P023, 2008.

Bibliography

[1] J. N. Reddy. *Mechanics of Laminated Composite Plates*. CRC Press, Boca Raton, USA, 1996.

[2] S. Abrate. Impact on laminated composite materials. *Applied Mechanics Review*, 44(4):155–190, 1991.

[3] S. Abrate. Impact on laminated composites: Recent advances. *Applied Mechanics Review*, 47(11):517–545, 1994.

[4] S. Abrate. Modeling of impacts on composite structures. *Composite Structures*, 51(2):129–138, 2001.

[5] W. J. Cantwell and J. Morton. The impact resistance of composite materials – A review. *Composites*, 22(5):347–362, 1991.

[6] G. A. O. Davies, D. Hitchings, and J. Wang. Prediction of threshold impact energy for onset of delamination in quasi-isotropic carbon/epoxy composite laminates under low-velocity impact. *Composites Science and Technology*, 60(1):1–7, 2000.

[7] M. O. W. Richardson and M. J. Wisheart. Review of low-velocity impact properties of composite materials. *Composites Part A: Applied Science and Manufacturing*, 27(12):1123–1131, 1996.

[8] J. Degrieck and W. Van Paepegem. Fatigue damage modeling of fibre-reinforced composite materials: Review. *Applied Mechanics Reviews*, 54(4):279–300, 2001.

[9] M. Q. Nguyen, D. J. Elder, J. Bayandor, R. S. Thomson, and M. L. Scott. A review of explicit finite element software for composite impact analysis. *Journal of Composite Materials*, 39(4):375–386, 2005.

[10] I. M. Daniel. Failure of composite materials. *Strain*, 43(1):4–12, 2007.

[11] P. D. Soden, M. J. Hinton, and A. S. Kaddour. A comparison of the predictive capabilities of current failure theories for composite laminates. *Composites Science and Technology*, 58(7):1225–1254, 1998.

[12] M. J. Hinton, A. S. Kaddour, and P. D. Soden. A further assessment of the predictive capabilities of current failure theories for composite laminates: Comparison with experimental evidence. *Composites Science and Technology*, 64(3-4):549–588, 2004.

[13] G. A. O. Davies and X. Zhang. Impact damage prediction in carbon composite structures. *International Journal of Impact Engineering*, 16(1):149–170, 1995.

[14] G. P. Zhao and C. D. Cho. Damage initiation and propagation in composite shells subjected to impact. *Composite Structures*, 78(1):91–100, 2007.

[15] R. D. Adams and P. Cawley. A review of defect types and nondestructive testing techniques for composites and bonded joints. *NDT International*, 21(4):208–222, 1988.

[16] A. S. Birks, R. E. Green, and P. McIntire. *Ultrasonic Testing*, volume 7 of *Nondestructive Testing Handbook. Second Edition.* American Society for Nondestructive Testing, United States of America, 1991.

[17] S. L. Gao and J. K. Kim. Three-dimensional characterization of impact damage in CFRPs. In *Impact Response and Dynamic Failure of Composites and Laminate Materials, Pts 1 and 2*, volume 141-1 of *Key Engineering Materials*, pages 35–53. Trans Tech Publications Ltd, Stafa-Zurich, 1998.

[18] P. Wright, X. Fu, I. Sinclair, and S. M. Spearing. Ultra high resolution computed tomography of damage in notched carbon fiber-epoxy composites. *Journal of Composite Materials*, 42(19):1993–2002, 2008.

[19] S. R. Stock, T. M. Breunig, A. Guvenilir, J. H. Kimmey, and M. C. Nichols. Nondestructive X-ray tomographic microscopy of damage in various continuous-fiber metal matrix composites. In J. E. Masters, editor, *Damage Detection in Composite Materials*, volume STP 1128, pages 25–34. ASTM, Philadelphia, 1992.

[20] A. P. Marshall and H. Bouadi. Low-velocity impact damage on thick-section graphite/epoxy laminated plates. *Journal of Reinforced Plastics and Composites*, 12(12):1281–1294, 1993.

[21] W. J. Cantwell and J. Morton. Geometrical effects in the low velocity impact response of CFRP. *Composite Structures*, 12(1):39–59, 1989.

[22] F. K. Chang. Ultra reliable and super safe structures for the new century. In D. L. Balageas, editor, *Proceedings of the First European Workshop on Structural Health Monitoring*, pages 3–12. DEStech Publications, Inc., Lancaster, 2002.

[23] E. L. Kirkby, V. J. Michaud, J. A. E. Månson, N. R. Sottos, and S. R. White. Performance of self-healing epoxy with microencapsulated healing agent and shape memory alloy wires. *Polymer*, 50(23):5533–5538, 2009.

[24] D. L. Balageas. *Proceedings of the first European Workshop on Structural Health Monitoring*. DEStech Publications, Lancaster, 2002.

[25] G. R. Kirikera, J. W. Lee, M. J. Schulz, A. Ghoshal, M. J. Sundaresan, R. J. Allemang, V. N. Shanov, and H. Westheider. Initial evaluation of an active/passive structural neural system for health monitoring of composite materials. *Smart Materials and Structures*, 15(5):1275, 2006.

[26] W. J. Staszewski, S. Mahzan, and R. Traynor. Health monitoring of aerospace composite structures - active and passive approach. *Composites Science and Technology*, 69(11-12):1678–1685, 2009.

[27] M. A. Mannan, P. McHargue, and M. H. Richardson. Continuous monitoring of modal parameters to quantify structural damage. In *International Modal Analysis Conference*, volume 2251, page 59. Proceedings of SPIE, 1993.

[28] R. K. Miller and P. McIntire. *Acoustic Emission Testing*, volume 5 of *Nondestructive Testing Handbook. Second Edition.* American Society for Nondestructive Testing, United States of America, 1987.

[29] T. Kundu, S. Das, S. A. Martin, and K. V. Jata. Locating point of impact in anisotropic fiber reinforced composite plates. *Ultrasonics*, 48(3):193–201, 2008.

[30] T. Kundu, S. Das, and K. V. Jata. Detection of the point of impact on a stiffened plate by the acoustic emission technique. *Smart Materials and Structures*, 18(3):035006–9, 2009.

[31] V. Giurgiutiu. *Structural Health Monitoring with Piezoelectric Wafer Active Sensors*. Academic Press, Amsterdam, 2008.

[32] W. Lestari and P. Qiao. Application of wave propagation analysis for damage identification in composite laminated beams. *Journal of Composite Materials*, 39(22):1967–1984, 2005.

[33] S. W. Doebling, C. R. Farrar, M. B. Prime, and D. W. Shevitz. Damage identification and health monitoring of structural and mechanical systems from changes in their vibration characteristics: A literature review. Technical Report LA–13070-MS, 1996.

[34] Y. Zou, L. Tong, and G. P. Steven. Vibration-based model-dependent damage (delamination) identification and health monitoring for composite structures – A review. *Journal of Sound and Vibration*, 230(2):357–378, 2000.

[35] C. N. Della and D. Shu. Vibration of delaminated composite laminates: A review. *Applied Mechanics Reviews*, 60(1):1–20, 2007.

[36] I. Bovio and L. Lecce. *Health monitoring: New techniques based on vibrations measurements and identification algorithms*, volume 2005. Big Sky, MT, 2005.

[37] J. V. Araújo dos Santos, C. M. Mota Soares, C. A. Mota Soares, and N. M. M. Maia. Structural damage identification in laminated structures using frf data. *Composite Structures*, 67(2):239–249, 2005.

[38] M. J. Schulz, P. F. Pai, A. S. Naser, S. K. Thyagarajan, G. R. Brannon, and J. Chung. Locating structural damage using frequency response reference functions and curvatures. In F. K. Chang, editor, *Structural Health Monitoring - Current Status and Perspectives*, pages 690–701. Technomic Publ Co Inc, Lancaster, 1997.

[39] S. S. Kessler, S. M. Spearing, M. J. Atalla, C. E. S. Cesnik, and C. Soutis. Damage detection in composite materials using frequency response methods. *Composites Part B: Engineering*, 33(1):87–95, 2002.

[40] S. Underwood, D. Koester, and D. E. Adams. Damage detection in sandwich composite materials using laser vibrometry in conjunction with nonlinear system identification. volume 7295 of *Health Monitoring of Structural and Biological Systems 2009*, San Diego, CA, 2009.

[41] A. K. Pandey, M. Biswas, and M. M. Samman. Damage detection from changes in curvature mode shapes. *Journal of Sound and Vibration*, 145(2):321–332, 1991.

[42] P. Qiao, W. Lestari, M. G. Shah, and J. Wang. Damage detection algorithms and sensor systems for laminate composite beams. In *Earth and Space*, volume 188, pages 175–175, League City/Houston, Texas, USA, 2006. ASCE.

[43] V. K. Sharma, M. Ruzzene, and S. Hanagud. Perturbation methods for the analysis of the dynamic behavior of damaged plates. *International Journal of Solids and Structures*, 43(16):4648–4672, 2006.

[44] G. J. Yun, S. Shang, and P. Qiao. Fast inverse identification of delamination of e-glass/epoxy laminated composite panels. volume 7294 of *Nondestructive Characterization for Composite Materials, Aerospace Engineering, Civil Infrastructure, and Homeland Security 2009*, San Diego, CA, 2009.

[45] H. Luo and S. Hanagud. An integral equation for changes in the structural dynamics characteristics of damaged structures. *International Journal of Solids and Structures*, 34(35-36):4557–4579, 1997.

[46] P. Qiao, W. Lestari, M. G. Shah, and J. Wang. Dynamics-based damage detection of composite laminated beams using contact and noncontact measurement systems. *Journal of Composite Materials*, 41(10):1217–1252, 2007.

[47] W. Lestari and P. Qiao. Damage detection of fiber-reinforced polymer honeycomb sandwich beams. *Composite Structures*, 67(3):365–373, 2005.

[48] P. Cawley and R. Adams. The location of defects in structures from measurements of natural frequencies. *The Journal of Strain Analysis for Engineering Design*, 14(2):49–57, 1979.

[49] J. E. Grady and E. H. Meyn. Vibration testing of impact-damaged composite laminates. *NASA Technical Memorandum*, 4115:11, 1989.

[50] L. H. Tenek, E. G. Henneke Ii, and M. D. Gunzburger. Vibration of delaminated composite plates and some applications to non-destructive testing. *Composite Structures*, 23(3):253–262, 1993.

[51] J. J. Tracy and G. C. Pardoen. Effect of delamination on the natural frequencies of composite laminates. *Journal of Composite Materials*, 23(12):1200–1215, 1989.

[52] K. H. Hsieh, M. W. Halling, and P. J. Barr. Overview of vibrational structural health monitoring with representative case studies. *Journal of Bridge Engineering*, 11(6):707–715, 2006.

[53] A. Shahdin, J. Morlier, and Y. Gourinat. Correlating low-energy impact damage with changes in modal parameters: A preliminary study on composite beams. *Structural Health Monitoring*, 8(6):523–536, 2009.

[54] B. Moaveni, X. He, J. P. Conte, and R. A. De Callafon. Damage identification of a composite beam using finite element model updating. *Computer-Aided Civil and Infrastructure Engineering*, 23(5):339–359, 2008.

[55] S. Keye, M. Rose, and D. Sachau. Localizing delamination damages in aircraft panels from modal damping parameters. *Proceedings of the International Modal Analysis Conference - IMAC*, 1:412–417, 2001.

[56] C. Kyriazoglou, B. H. Le Page, and F. J. Guild. Vibration damping for crack detection in composite laminates. *Composites Part A: Applied Science and Manufacturing*, 35(7-8):945–953, 2004.

[57] N. A. Chrysochoidis and D. A. Saravanos. Assessing the effects of delamination on the damped dynamic response of composite beams with piezoelectric actuators and sensors. *Smart Materials and Structures*, 13(4):733–742, 2004.

[58] D. A. Saravanos and D. A. Hopkins. Effects of delaminations on the damped dynamic characteristics of composite laminates: Analysis and experiments. *Journal of Sound and Vibration*, 192(5):977–993, 1996.

[59] A. Shahdin, J. Morlier, and Y. Gourinat. Significance of low energy impact damage on modal parameters of composite beams by design of experiments. *Journal of Physics: Conference Series*, 181(1):012045, 2009.

[60] D. Montalvão, A. M. R. Ribeiro, and J. Duarte-Silva. A method for the localization of damage in a CFRP plate using damping. *Mechanical Systems and Signal Processing*, 23(6):1846–1854, 2009.

[61] N. A. Chrysohoidis and D. A. Saravanos. Effects of delaminations on the damped dynamic response of composite laminates with piezoelectric sensors. In D. L. Balageas, editor, *Proceedings of the First European Workshop on Structural Health Monitoring*, pages 179–186. DEStech Publications, Lancaster, 2002.

[62] K. O. Hill and G. Meltz. Fiber bragg grating technology fundamentals and overview. *Lightwave Technology, Journal of*, 15(8):1263–1276, 1997.

[63] R. M. Measures. *Structural Monitoring with fiber optic technology*. Academic Press, San Diego, 2001.

[64] M. Majumder, T. K. Gangopadhyay, A. K. Chakraborty, K. Dasgupta, and D. K. Bhattacharya. Fibre Bragg gratings in structural health monitoring – Present status and applications. *Sensors and Actuators A: Physical*, 147(1):150–164, 2008.

[65] J. Leng and A. Asundi. Structural health monitoring of smart composite materials by using EFPI and FBG sensors. *Sensors and Actuators A: Physical*, 103(3):330–340, 2003.

[66] G. M. Kamath, R. Sundaram, N. Gupta, and M. Rao. Damage studies in composite structures for structural health monitoring using strain sensors. *Structural Health Monitoring*, 9(6):497–512, 2010.

[67] F. Colpo. *Residual Stress Characterization in a Single Fiber Composite Specimen Using FBG sensor and the OLCR Technique*. PhD thesis, École polytechnique fédérale de Lausanne (N° 3533), 2006.

[68] A. R. Chambers, M. C. Mowlem, and L. Dokos. Evaluating impact damage in CFRP using fibre optic sensors. *Composites Science and Technology*, 67(6):1235–1242, 2007.

[69] K. S. C. Kuang, R. Kenny, M. P. Whelan, W. J. Cantwell, and P. R. Chalker. Residual strain measurement and impact response of optical fibre Bragg grating sensors in fibre metal laminates. *Smart Materials and Structures*, 10(2):338–346, 2001.

[70] T. Okabe, R. Mizutani, R. Tsuji, and N. Takeda. Identification of crack locations in composites using fiber Bragg grating sensors. In D. L. Balageas, editor, *Proceedings of the First European Workshop on Strutural Health Monitoring*, pages 517–523. DEStech Publications, Lancaster, 2002.

[71] S. Yashiro, T. Okabe, N. Toyama, and N. Takeda. Monitoring damage in holed CFRP laminates using embedded chirped FBG sensors. *International Journal of Solids and Structures*, 44(2):603–613, 2007.

[72] S. Stutz, J. Cugnoni, and J. Botsis. Studies of mode I delamination in monotonic and fatigue loading using FBG wavelength multiplexing and numerical analysis. *Composites Science and Technology*, 71(4):443–449, 2011.

[73] D. C. Betz, W. J. Staszewski, G. Thursby, and B. Culshaw. Structural damage identification using multifunctional Bragg grating sensors: II. Damage detection results and analysis. *Smart Materials and Structures*, 15(5):1313–1322, 2006.

[74] D. C. Betz, G. Thursby, B. Culshaw, and W. J. Staszewski. Structural damage location with fiber Bragg grating rosettes and Lamb waves. *Structural Health Monitoring*, 6(4):299–308, 2007.

[75] H. Tsuda. Ultrasound and damage detection in CFRP using fiber Bragg grating sensors. *Composites Science and Technology*, 66(5):676–683, 2006.

[76] N. Takeda, Y. Okabe, J. Kuwahara, S. Kojima, and T. Ogisu. Development of smart composite structures with small-diameter fiber Bragg grating sensors for damage detection: Quantitative evaluation of delamination length in CFRP laminates using Lamb wave sensing. *Composites Science and Technology*, 65(15-16):2575–2587, 2005.

[77] E. Kirkby. *Active Sensing and Repair Composites*. PhD thesis, École polytechnique fédérale de Lausanne (N° 4409), 2009.

[78] E. Kosters and T. J. Van Els. Structural health monitoring and impact detection for primary aircraft structures. In *Proceedings of SPIE*, volume 7677, pages 1–3, Orlando, Florida, USA, 2010.

[79] B. L. Chen and C. S. Shin. Fiber bragg gratings array for structural health monitoring. *Materials and Manufacturing Processes*, 25(4):255–258, 2010.

[80] P. Capoluongo, C. Ambrosino, S. Campopiano, A. Cutolo, M. Giordano, I. Bovio, L. Lecce, and A. Cusano. Modal analysis and damage detection by fiber bragg grating sensors. *Sensors and Actuators A: Physical*, 133(2):415–424, 2007.

[81] A. Cusano, P. Capoluongo, S. Campopiano, A. Cutolo, M. Giordano, F. Felli, A. Paolozzi, and M. Caponero. Experimental modal analysis of an aircraft model wing by embedded fiber bragg grating sensors. *Sensors Journal, IEEE*, 6(1):67–77, 2006.

[82] D. Tosi. Dynamic strain measurement system with fiber Bragg gratings and noise mitigation techniques. *Measurement Science and Technology*, 20(6):065203–9, 2009.

[83] J. M. A. Silva, T. C. Devezas, A. P. Silva, and J. A. M. Ferreira. Mechanical characterization of composites with embedded optical fibers. *Journal of Composite Materials*, 39(14):1261–1281, 2005.

[84] B. S. Jeon, J. J. Lee, J. K. Kim, and J. S. Huh. Low velocity impact and delamination buckling behavior of composite laminates with embedded optical fibers. *Smart Materials and Structures*, 8(1):41–48, 1999.

[85] R. Isago and K. Nakamura. A high reading rate fiber Bragg grating sensor system using a high-speed swept light source based on fiber vibrations. *Measurement Science and Technology*, 20(3):034021–5, 2009.

[86] B. Soller, D. Gifford, M. Wolfe, and M. Froggatt. High resolution optical frequency domain reflectometry for characterization of components and assemblies. *Optics Express*, 13(2):666–674, 2005.

[87] M. D. Todd, J. M. Nichols, S. T. Trickey, M. Seaver, C. J. Nichols, and L. N. Virgin. Bragg grating-based fibre optic sensors in structural health monitoring. *Philosophical Transactions of the Royal Society*, 365(1851):317–343, 2007.

[88] C. Park, K. Peters, M. Zikry, T. Haber, S. Schultz, and R. Selfridge. Peak wavelength interrogation of fiber Bragg grating sensors during impact events. *Smart Materials and Structures*, 19(4):045015–7, 2010.

[89] H. Tsuda and J.-R. Lee. Strain and damage monitoring of CFRP in impact loading using a fiber Bragg grating sensor system. *Composites Science and Technology*, 67(7-8):1353–1361, 2007.

[90] D. C. Betz, G. Thursby, B. Culshaw, and W. J. Staszewski. Acousto-ultrasonic sensing using fiber bragg gratings. *Smart Materials and Structures*, 12(1):122–128, 2003.

[91] T. Vella. Full-spectrum interrogation of fiber Bragg gratings at 100 khz for detection of impact loading. *Measurement Science and Technology*, 21(9):094009–6, 2010.

[92] H. Y. Fu, H. L. Liu, X. Dong, H. Y. Tam, P. K. A. Wai, and C. Lu. High-speed fibre bragg grating sensor interrogation using dispersion-compensation fibre. *Electronics Letters*, 44(10):618–619, 2008.

[93] B. W. Lee, M. S. Seo, H. G. Oh, and C. Y. Park. High-speed wavelength interrogator of fiber Bragg gratings for capturing impulsive strain waveforms. *Advanced Materials Research*, 123-125:867–870, 2010.

[94] J. Cugnoni. *Identification par récalage modal et fréquentiel des propriétés constitutives de coques en matériaux composites*. PhD thesis, École polytechnique fédérale de Lausanne (N° 3109), 2004.

[95] J. Cugnoni, T. Gmür, and A. Schorderet. Inverse method based on modal analysis for characterizing the constitutive properties of thick composite plates. *Computers and Structures*, 85(17-18):1310–1320, 2007.

[96] M. Matter. *Identification modale numérique-expérimentale des propriétés élastiques et dissipatives de matériaux composites*. PhD thesis, École polytechnique fédérale de Lausanne (N° 4215), 2008.

[97] M. Matter, T. Gmür, J. e. l. Cugnoni, and A. Schorderet. A PSDT shell finite element formulation including structural damping. *Computers and Structures*, 88(15-16):902–908, 2010.

[98] F. Bosia, P. Giaccari, J. Botsis, M. Facchini, H. G. Limberger, and R. e. P. Salathé. Characterization of the response of fibre Bragg grating sensors subjected to a two-dimensional strain field. *Smart Materials and Structures*, 12(6):925–934, 2003.

[99] W. Y. Li, C. C. Cheng, and Y. L. Lo. Investigation of strain transmission of surface-bonded FBGs used as strain sensors. *Sensors and Actuators A: Physical*, 149(2):201–207, 2009.

[100] C.-C. Cheng, Y.-L. Lo, B. S. Pun, Y. M. Chang, and W. Y. Li. An investigation of bonding-layer characteristics of substrate-bonded fiber Bragg grating. *Journal of Lightwave Technology*, 23(11):3907–3915, 2005.

[101] D. J. Elder, R. S. Thomson, M. Q. Nguyen, and M. L. Scott. Review of delamination predictive methods for low speed impact of composite laminates. *Composite Structures*, 66(1-4):677–683, 2004.

[102] B. R. K. Blackman, J. P. Dear, A. J. Kinloch, H. MacGillivray, Y. Wang, J. G. Williams, and P. Yayla. The failure of fibre composites and adhesively bonded fibre composites under high rates of test. *Journal of Materials Science*, 31(17):4467–4477, 1996.

[103] G. Caprino, I. Crivelli Visconti, and A. Di Ilio. Elastic behaviour of composite structures under low velocity impact. *Composites*, 15(3):231–234, 1984.

[104] P. Robinson and G. A. O. Davies. Impactor mass and specimen geometry effects in low velocity impact of laminated composites. *International Journal of Impact Engineering*, 12(2):189–207, 1992.

[105] T. Gmür. *Dynamique des structures - Analyse modal numérique*. Presses polytechniques et universitaires romandes, Lausanne, 1997.

[106] J. S. Sun, K. H. Lee, and H. P. Lee. Comparison of implicit and explicit finite element methods for dynamic problems. *Journal of Materials Processing Technology*, 105(1-2):110–118, 2000.

[107] T. C. Haber, J. L. Mock, and J. Kraus. Method and apparatus for high frequency optical sensor interrogation. *US Patent*, No. 20080106745, 2008.

[108] R. R. J. Maier, W. N. MacPherson, J. S. Barton, J. D. C. Jones, S. McCulloch, and G. Burnell. Temperature dependence of the stress response of fibre bragg gratings. *Measurement Science and Technology*, 15(8):1601, 2004.

[109] K. Worden and W. J. Staszewski. Impact location and quantification on a composite panel using neural networks and a genetic algorithm. *Strain*, 36(2):61–68, 2000.

[110] F. Ciampa and M. Meo. Acoustic emission source localization and velocity determination of the fundamental mode A(0) using wavelet analysis and a Newton-based optimization technique. *Smart Materials and Structures*, 19(4):045027–14, 2010.

[111] D. C. Betz, G. Thursby, B. Culshaw, and W. J. Staszewski. Advanced layout of a fiber Bragg grating strain gauge rosette. *Journal of Lightwave Technology*, 24(2):1019–1026, 2006.

[112] D. C. Betz, G. Thursby, B. Culshaw, and W. J. Staszewski. Identification of structural damage using multifunctional Bragg grating sensors: I. Theory and implementation. *Smart Materials and Structures*, 15(5):1305–1312, 2006.

[113] H. Tsutsui, A. Kawamata, T. Sanda, and N. Takeda. Detection of impact damage of stiffened composite panels using embedded small-diameter optical fibers. *Smart Materials and Structures*, 13(6):1284–1290, 2004.

[114] H. Jeong and Y.-S. Jang. Wavelet analysis of plate wave propagation in composite laminates. *Composite Structures*, 49(4):443–450, 2000.

[115] S. M. Ziola and M. R. Gorman. Source location in thin plates using cross-correlation. *The Journal of the Acoustical Society of America*, 90(5):2551–2556, 1991.

[116] A. Tobias. Acoustic-emission source location in two dimensions by an array of three sensors. *Non-Destructive Testing*, 9(1):9–12, 1976.

[117] T. Kundu, S. Das, and K. V. Jata. Point of impact prediction in isotropic and anisotropic plates from the acoustic emission data. *The Journal of the Acoustical Society of America*, 122(4):2057–2066, 2007.

[118] J. Haywood, P. T. Coverley, W. J. Staszewski, and K. Worden. An automatic impact monitor for a composite panel employing smart sensor technology. *Smart Materials and Structures*, 14(1):265–271, 2005.

[119] J. R. LeClerc, K. Worden, W. J. Staszewski, and J. Haywood. Impact detection in an aircraft composite panel – A neural-network approach. *Journal of Sound and Vibration*, 299(3):672–682, 2007.

[120] Z. Su and L. Ye. *Identification of damage using Lamb waves: From fundamentals to applications*, volume 48 of *Lecture Notes in Applied and Computational Mechanics*. Springer, Heidelberg, 2009.

[121] J. L. Rose. *Ultrasonic Waves in Solid Media*. Cambridge University Press, New York, 2004.

[122] F. Aymerich, F. Dore, and P. Priolo. Simulation of multiple delaminations in impacted cross-ply laminates using a finite element model based on cohesive interface elements. *Composites Science and Technology*, 69(11-12):1699–1709, 2009.

[123] C. F. Li, N. Hu, Y. J. Yin, H. Sekine, and H. Fukunaga. Low-velocity impact-induced damage of continuous fiber-reinforced composite laminates. Part I. An FEM numerical model. *Composites Part A: Applied Science and Manufacturing*, 33(8):1055–1062, 2002.

[124] R. J. Allemang. The modal assurance criterion – Twenty years of use and abuse. *Sound and Vibration*, 37(8):14–23, 2003.

[125] H. Kaczmarek and S. Maison. Comparative ultrasonic analysis of damage in CFRP under static indentation and low-velocity impact. *Composites Science and Technology*, 51(1):11–26, 1994.

[126] A. Burr, F. Hild, and F. A. Leckie. Micro-mechanics and continuum damage mechanics. *Archive of Applied Mechanics (Ingenieur Archiv)*, 65(7):437–456, 1995.

[127] J. Lemaitre. How to use damage mechanics. *Nuclear Engineering and Design*, 80(2):233–245, 1984.

[128] J. Lemaitre and J. Dufailly. Damage measurements. *Engineering Fracture Mechanics*, 28(5-6):643–661, 1987.

[129] Z. Hashin. Analysis of stiffness reduction of cracked cross-ply laminates. *Engineering Fracture Mechanics*, 25(5-6):771–778, 1986.

[130] T. J. Lu and C. L. Chow. On constitutive equations of inelastic solids with anisotropic damage. *Theoretical and Applied Fracture Mechanics*, 14(3):187–218, 1990.

[131] T. J. Lu and C. L. Chow. A constitutive theory of matrix cracking and interply delamination in orthotropic laminated composites. *Journal of Reinforced Plastics and Composites*, 11(5):494–536, 1992.

[132] G. Z. Voyiadjis and P. I. Kattan. *Damage Mechanics*. CRC Press, Boca Raton, USA, 2005.

[133] C. S. Lopes, P. P. Camanho, Z. Gürdal, P. Maimí, and E. V. González. Low-velocity impact damage on dispersed stacking sequence laminates. Part II: Numerical simulations. *Composites Science and Technology*, 69(7-8):937–947, 2009.

[134] A. F. Johnson and M. Holzapfel. Influence of delamination on impact damage in composite structures. *Composites Science and Technology*, 66(6):807–815, 2006.

[135] H. Ramsin and P. A. Wedin. A comparison of some algorithms for the nonlinear least squares problem. *BIT Numerical Mathematics*, 17(1):72–90, 1977.

Curriculum Vitæ

Jeannot Frieden
born on 11 July 1983,
in Luxembourg (Grand Duchy of Luxembourg).

Education:

2007–2011: École polytechnique fédérale de Lausanne, Switzerland
PhD thesis at the doctoral school of Mechanics

2002–2007: École polytechnique fédérale de Lausanne, Switzerland
MSc in mechanical engineering

1995–2002: Lycée Classique d'Echternach, Luxembourg
Diplôme de fin d'études secondaires
(sciences - mathematiques - latin)

Work experience:

2002, 2005: Internship at Paul Wurth S.A., Luxembourg
Thermal and structural analysis of a rabble arm of a multiple stage furnace.
Development of a VBA program to facilitate human resource managing.

2005–2010: École polytechnique fédérale de Lausanne, Switzerland
Teaching assistant for the courses
"Mécanique des structures" (Prof. J. Botsis),
"Mécanique des milieux continus" (Prof. J. Botsis),
"Mécanique vibratoire" (Prof. Th. Gmür),
"Méthode des éléments finis" (Prof. Th. Gmür) and
"Techniques de mesure" (Dr. T.-V. Truong).